

**DEVELOPMENT OF NEAR SURFACE FLOW
PATTERN AND WATER MASS DISTRIBUTION
IN ARABIAN SEA IN RESPONSE TO
MONSOONAL FORCINGS**

Dissertation submitted to

GOA UNIVERSITY

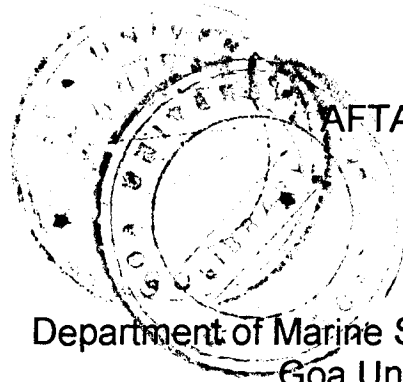
For the degree of Doctor philosophy

in

MARINE SCIENCES

By

AFTAB A CAN



Department of Marine Sciences and Biotechnology
Goa University, Goa
October, 2001

574.92
CP11.21

~~T-213~~

T-213

Statement

As required under the University ordinance 0.19.8(VI), I state that this thesis entitled "*Development of Near-Surface flow pattern and Water Mass Distribution in Arabian Sea in response to monsoonal forcings*" is my original contribution and it has not been submitted on any previous occasion.

The literature related to the problem investigated has been cited. Due acknowledgement have been made wherever facilities and suggestion have been availed of.

Goa University, Goa
October 2001




Aftab A. Can

Certificate

This is to certify that the thesis entitled "*Development of Near-Surface flow pattern and Water Mass distribution in Arabian Sea in response to monsoonal forcing*", submitted by Aftab A. Can to Goa University for the degree of Doctor of Philosophy, is based on his original studies carried out under my supervision. The thesis or any part thereof has not been previously submitted for any other degree or diploma in any University or institution.


Harilal B. Menon 24/10/01

Goa University, Goa
October 2001

Reader
Dept. of Marine Science
and Biotechnology

Certified and no correction.

X. Jayala Reddy

2/4/02.

Acknowledgements

I bow to Thee, oh! Almighty.

The constant guidance and encouragement for the work was always coming from Dr. H. B. Menon, without whose help the work would not have taken the shape of the thesis. I place my deep sense of sincere gratitude to my guide.

I wish to express my thanks to Prof. U. M. X. Sangodkar, Head, Department of Marine Sciences and Biotechnology, for his support in carrying out this work. I am grateful to Dr. G. N. Nayak for all his help. My sincere thanks are also for Prof. B. S. Sonde, Vice-Chancellor, Goa University, for his help.

I owe lots to Dr. S. U. Upadhyay, Goa University, for all his help. The help from Dr. P. C. Pandey, Director, National Center for Ocean and Antarctic Research, Dr L. V. G. Rao, National Institute of Oceanography, Dr. Ramesh Kumar, NIO and Dr. G. R. Bhat has largely contributed to the success. I am indeed highly grateful to them.

My thanks are also to Dr. C. L. Rodrigues, Dr. C. U. Rivonkar, Dr. V. M. Matta for their help. The suggestions from Dr V. Agarwal, Dr. Pranav Desai, Dr P. K. Pal, Dr. S. K. Basu, Dr. M. M. Ali, Mr. P. Thapliyal, and Mrs. R. Sharma of Space Applications Center, ISRO, Ahmedabad has been highly useful. I place my gratefulness to them.

My thanks are also to Dr. Ehrlich Desa, the Director, and Mr. Albert Gouveia for providing the advance computing facilities.

The fellowship for carrying out work, in the initial phase, was provided by Council of Scientific and Industrial Research, New Delhi. I acknowledge CSIR for this. I also thank the University of Texas for providing the sea surface height

anomaly data derived from satellite altimeter. I am grateful to the US-Joint Global Ocean Flux programmers for providing the high accuracy hydrographic data.

I place my thanks to Shri. Shashikant Parab and non-teaching staff of Marine Sciences and Biotechnology, Goa University, for their help. I am also very grateful to Mr. Vasudev Narvekar. My sincere thanks are also for Dr. Altaf Nadaf for the prompt help. The support from M. Sc. students had been coming in small and big way. I thank them all.

I owe a great deal of gratitude to all my family members, especially parents, for their sacrifices and encouragement in my endeavor.

Aftab A. Can

*Goa University, Goa
October 2001*

Contents

I	List of figures	
II	Abbreviations	
I	<i>Introduction</i>	1
1.1	The forcing regimes of the region	1
1.1.1	Lower tropospheric regime	1
1.1.2	The Marginal Seas	3
1.1.3	The Equatorial Indian Ocean	5
1.2	Arabian Sea response to seasonal forcing	5
1.2.1	The Arabian Sea Dynamics during Northeast Monsoon	5
1.2.2	The Arabian Sea Dynamics during Southwest Monsoon	6
1.2.3	Transitional variations	9
1.2.4	Water Masses in the region	10
1.3	Objectives of the present work	10
1.3	Layout of the thesis	11
II	<i>Data and Methods of Analysis</i>	12
2.1	Data Used	12
2.1.1	Winds and fluxes at the air-sea interface	12
2.1.2	Hydrographic data	13
2.1.3	Satellite data	13
2.2	Methodology	14
2.2.1	Climatological hydrography and water mass mapping	14
	Potential Density computations	14
	Buoyancy Flux	14
	Meteorological forcings	14
	Water mass mapping	14

2.2.2	<i>Hydrography and water mass mapping during 1995</i>	15
	<i>Mixed Layer Depth</i>	15
	<i>Computation of Stability</i>	16
	<i>Computation of water type density</i>	16
2.2.3	<i>Geostrophic flow from Satellite altimeter data</i>	17
III	<i>Lower Tropospheric Forcings and ocean response</i>	19
3.1	Lower Tropospheric Wind Regime	19
3.2	Fluxes At The Air-Sea Boundary	20
3.2.1	<i>Influx of short wave radiations</i>	20
3.2.2	<i>Outward flux through long wave radiations</i>	21
3.2.3	<i>Sensible heat flux</i>	22
3.2.4	<i>Latent heat flux</i>	23
3.2.5	<i>Net heat flux</i>	24
3.2.6	<i>Buoyancy flux</i>	25
3.3	Arabian Sea Hydrographic Regime	27
3.3.1	<i>Winter variability in thermal regime</i>	27
3.3.2	<i>Winter variability in haline regime</i>	28
3.3.3	<i>Winter to summer transitional variability in thermal regime</i>	28
3.3.4	<i>Winter to summer transitional variability in haline regime</i>	28
3.3.5	<i>Summer variability in thermal regime</i>	29
3.3.6	<i>Summer variability in haline regime</i>	30
3.3.7	<i>Summer to winter transitional variability in thermal regime</i>	30
3.3.8	<i>Summer to winter transitional variability in haline regime</i>	31
3.3.9	<i>Thermal and haline variability at intermediate depths</i>	31
3.3.10	<i>Density field of the study area</i>	32
3.4	Mapping Of Water Masses In Arabian Sea	32
IV	<i>Seasonal hydrographic regime and stability</i>	37

4.1	Seasonal winds during 1995	37
4.2	The Hydrographic Regime	37
4.2.1	<i>Distribution of Temperature and Salinity along the northern and southern transects during January</i>	38
4.2.2	<i>Distribution of Temperature and Salinity along the northern and southern transects during March-April</i>	40
4.2.3	<i>Distribution of Temperature and Salinity along the northern and southern transects during July-August</i>	42
4.2.4	<i>Distribution of Temperature and Salinity along the northern and southern transects during August-September</i>	44
4.2.5	<i>Distribution of Temperature and Salinity along the northern and southern transects during December</i>	45
4.3	The water column stability in response to the seasons	47
4.3	Seasonal impact on hydrography in terms of Water Type Density	49
V	<i>Sea surface height anomaly, Surface flow characteristics and kinetic energy from satellite altimeter</i>	50
5.1	Sea Level Anomaly, Circulation and Kinetic Energy during winter	50
5.2	Sea Level Anomaly, Circulation and Kinetic Energy during winter to Summer transition	53
5.3	Sea Level Anomaly, Circulation and Kinetic Energy during summer	53
5.4	Sea Level Anomaly, Circulation and Kinetic Energy during summer to winter transition	54
VI	<i>Discussion</i>	56
VII	<i>Summary and Conclusions</i>	74
	<i>Bibliography</i>	

List of Figures

- 1.1 Study area showing the CTD stations
- 3.1 Wind stress (N/m^2) and Curl of stress (N/m^3)
- 3.2 Flux of Short Wave Radiation (Wm^{-2})
- 3.3 Flux of Long Wave Radiation (Wm^{-2})
- 3.4 Sensible Heat flux (Wm^{-2})
- 3.5 Latent Heat flux (Wm^{-2})
- 3.6 Net Heat flux (Wm^{-2})
- 3.7 Buoyancy Flux ($kgm^{-1}s^{-3}$)
- 3.8 Horizontal Temperature Distribution at different depths during December
- 3.9 Horizontal Temperature Distribution at different depths during January
- 3.10 Horizontal Temperature Distribution at different depths during February
- 3.11 Horizontal Temperature Distribution at different depths during March
- 3.12 Horizontal Salinity distribution at different depths during December
- 3.13 Horizontal Salinity distribution at different depths during January
- 3.14 Horizontal Salinity distribution at different depths during February
- 3.15 Horizontal Salinity distribution at different depths during March
- 3.16 Horizontal Temperature Distribution at different depths during April
- 3.17 Horizontal Temperature Distribution at different depths during May
- 3.18 Horizontal Salinity distribution at different depths during April
- 3.19 Horizontal Salinity distribution at different depths during May
- 3.20 Horizontal Temperature Distribution at different depths during June
- 3.21 Horizontal Temperature Distribution at different depths during July
- 3.22 Horizontal Temperature Distribution at different depths during August
- 3.23 Horizontal Temperature Distribution at different depths during September
- 3.24 Horizontal Salinity distribution at different depths during June
- 3.25 Horizontal Salinity distribution at different depths during July
- 3.26 Horizontal Salinity distribution at different depths during August
- 3.27 Horizontal Salinity distribution at different depths during September
- 3.28 Horizontal Temperature Distribution at different depths during October

- 3.29 Horizontal Temperature Distribution at different depths during November
- 3.30 Horizontal Salinity distribution at different depths during October
- 3.31 Horizontal Salinity distribution at different depths during November
- 3.32 Horizontal Temperature Distribution at deeper levels during February
- 3.33 Horizontal Salinity Distribution at deeper levels during February
- 3.34 Horizontal Temperature Distribution at deeper levels depths during August
- 3.35 Horizontal Salinity Distribution at deeper levels during August
- 3.36 Horizontal Density Distribution at different levels during January and July
- 3.37 Spread of Arabian Sea and Bay of Bengal Water Masses
- 3.38 Spread of Persian Gulf and Red Sea Water Masses
- 4.1 Wind stress (N/m^2) and Curl (N/m^3)
- 4.2 Vertical sections of (a) Potential temperature and (b) Salinity along northern transect during January
- 4.3 Vertical sections of (a) Potential temperature and (b) Salinity along southern transect during January
- 4.4 T-S profiles at different stations along the two transects during January
- 4.5 Vertical sections of (a) Potential temperature and (b) Salinity along northern transect during March
- 4.6 Vertical sections of (a) Potential temperature and (b) Salinity along southern transect during March-April
- 4.7 T-S profiles at different stations along the two transects during March-April
- 4.8 Vertical sections of (a) Potential temperature and (b) Salinity along northern transect during July
- 4.9 Vertical sections of (a) Potential temperature and (b) Salinity along southern transect during July-August
- 4.10 T-S profiles at different stations along the two transects during July-August
- 4.11 Vertical sections of (a) Potential temperature and (b) Salinity along northern transect during August
- 4.12 Vertical sections of (a) Potential temperature and (b) Salinity along southern transect August-September
- 4.13 T-S profiles at different stations along the two transects during August-

September

- 4.14 Vertical sections of (a) Potential temperature and (b) Salinity along northern transect during December
- 4.15 Vertical sections of (a) Potential temperature and (b) Salinity along southern transect during December
- 4.16 Vertical sections of (a) Potential temperature and (b) Salinity along southern transect during December
- 4.17 Stability (m^{-1}) of water column at different stations during January
- 4.18 Stability (m^{-1}) of water column at different stations during March-April
- 4.19 Stability (m^{-1}) of water column at different stations during July-August
- 4.20 Stability (m^{-1}) of water column at different stations during August-September
- 4.21 Stability of water column at different stations during December (m^{-1})
- 4.22 Water Type Density at different stations
- 5.1 Sea surface height anomaly (cm) during winter
- 5.2 Geostrophic Velocity ($cm\ s^{-1}$) during winter
- 5.3 Kinetic Energy ($cm^2\ s^{-2}$) during winter
- 5.4 Sea surface height anomaly (cm) during winter to summer transition
- 5.5 Geostrophic Velocity ($cm\ s^{-1}$) during winter to summer transition
- 5.6 Kinetic Energy ($cm^2\ s^{-2}$) during winter to summer transition
- 5.7 Sea surface height anomaly (cm) during summer
- 5.8 Geostrophic Velocity ($cm\ s^{-1}$) during summer
- 5.9 Kinetic Energy ($cm^2\ s^{-2}$) during summer
- 5.10 Sea surface height anomaly (cm) during summer to winter transition
- 5.11 Geostrophic Velocity ($cm\ s^{-1}$) during summer to winter transition
- 5.12 Kinetic Energy ($cm^2\ s^{-2}$) during summer to winter transition

ABBREVIATIONS

ASWM	Arabian Sea Water Mass
KE	Kinetic Energy
MLD	Mixed Layer Depth
NEM	Northeast Monsoon
NT	Northern Transect
PGWM	Persian Gulf Water Mass
RSWM	Red Sea Water Mass
SLA	Sea Level anomaly
ST	Southern Transect
SWM	Southwest Monsoon
WTD	Water Type Density

Chapter - I

Introduction

Arabian Sea forms the northwestern part of the Indian Ocean and is bounded by Persian Gulf, Red Sea at the west, Equatorial Indian Ocean at south and Asiatic continent at north and east. The differential heating and cooling between the Tibetan Plateau/Indian subcontinent and the large volume of ocean surrounding it results in the seasonality of winds over the region and hence the air mass characteristics in the lower tropospheric winds over the Arabian Sea (Prell 1984; Webster 1987). The area experiences monsoons annually viz. a weaker Northeast Monsoon (NEM) - December to March, and a stronger Southwest Monsoon (SWM) - June to September. This leads to variability in the North Indian Ocean circulation and in the hydrographic structure extending as south as 20° S (Tchernia, 1980). The seasonality in circulation in the north Indian Ocean (Arabian Sea and Bay of Bengal) leads to change in the pelagic ecosystem. The study region is the Arabian Sea to the north of 8° N (Fig. 1).

1.1 The forcing regimes of the region

The interaction of marginal seas, equatorial region in conjunction with the overlying atmospheric forcing evolves a dynamic hydrographic structure and flow characteristics in the Arabian Sea that plays an important role in the biogeochemical cycling and the global climate (Smith et al., 1998). These interacting regimes show seasonality in their characteristics.

1.1.1 Lower tropospheric regime

During the northern winter, cooling of Siberia, Central Asia and Tibet generally surpasses that of the neighbouring oceans (northwest Pacific and the Indian). These continental regions then become centers of atmospheric high, resulting in the dry air blowing from the land to sea. A mooring study

revealed that the Northeast Monsoon is a season of dry, steady and moderate winds with typical speed of 5 ms^{-1} , clear skies and heat and evaporative losses to the atmosphere (Rudnick et al., 1997; Weller et al., 1998).

A low pressure that develops over Tibetan plateau and a high pressure over the ocean, during the summer, cause the lower level tropospheric winds to flow from equatorial zone to the Tibetan plateau. The Coriolis force influences these winds that are first directed towards Africa near the equator and then towards Tibet. The mountainous regions of Kenya, Ethiopia and Yemen further deflect the winds (Knox 1987, Krishnamurti 1987). The winds first proceed along east Africa and then along the center of Arabian Sea to the Indian subcontinent. This atmospheric flow across the Arabian Sea, takes the form of an intense low-level jet known as Findlater Jet (Findlater, 1969). The timing of the onset of the jet depends on the timing of the heating of the Tibetan Plateau (Smith et al., 1998). Records of the Merchant vessels during the last century show that the winds associated with the Findalter jet over the Arabian Sea begin within a few days of May in 60% of years (Fieux and Stommel, 1977). Recent observations from a moored buoy located at $15^{\circ} 30' \text{ N}$, $61^{\circ} 30' \text{ E}$ and lying along the axis of the jet shows typical wind speed greater than 10 ms^{-1} throughout the southwest monsoon and sometimes exceeding 15 ms^{-1} .

The stress during the SWM was roughly four times that during the NEM (Rudnick et al., 1997). The response of Arabian Sea to the sustained southwest winds of high intensity shows a high degree of coupling. The increase in wind speed and the change in wind direction have important implications on the upper ocean. In their study of hydrography and circulation, off the west coast of India, during the southwest monsoon of 1987, Shetye et al. (1990) observed that the winds varied between west-northwesterly near the southern end of the coast to west-southwesterly near the northern end with an average speed of 8 ms^{-1} .

Rameshbabu et al. (1992) found a negative net surface heat balance ($\sim 70 \text{ Wm}^{-2}$) during May 1988. This was attributed to excessive latent heat loss over the incoming radiation. While during August, September 1988, it was

positive on account of decrease in evaporative heat flux by about 25% of that during May ($\sim 240 \text{ Wm}^{-2}$). The lowering of specific humidity gradient by 1.5 from May to September is mainly responsible for lower evaporation rates during the later period. The monsoonal cooling (approximately 87 Wm^{-2}) confines to upper 100 m layer and the heat gain at an average rate of about 160 Wm^{-2} . The evaporation rates on a seasonal scale were found to be same over the Arabian Sea irrespective of the monsoonal activity over the Indian Subcontinent.

1.1.2 *The Marginal Seas*

The marginal seas - Persian Gulf and Red Sea are the source regions for two of the most saline water masses, namely Red Sea Water Mass (RSWM) and Persian Gulf Water Mass (PGWM), found in the World Ocean (Rochford 1964). The maximum salinity of Persian Gulf water over most of the gulf is 40.0-40.5, while that of Red Sea water is 40-41 and it can exceed 50 in limited areas (Wyrki, 1971; Brewer et al., 1978; John et al., 1990; Chao et al., 1992). The high evaporation rates ($1.5\text{-}5 \text{ myr}^{-1}$, Chao et al., 1992), less rainfall and river inflow, restricted exchange with the open ocean and the shallowness of the Persian Gulf lead to the formation of high saline, dense water (John et al., 1990). The dense, saline Red Sea water and Persian Gulf water enter the Indian Ocean in exchange flows through narrow, shallow straits such as Bab-al-Mandeb Strait, and Strait of Hormuz (Fig.1). The sill depth of Bab-al-Mandeb is $\sim 160 \text{ m}$ and that of Strait of Hormuz is $\sim 80 \text{ m}$.

The high salinity water exits the straits as dense bottom currents, cascading down the continental slope and entraining less dense water until they reach neutral buoyancy and spread laterally into the Indian Ocean (Chao et al., 1992). Estimates of the mean annual transport of Red Sea water and Persian Gulf water through their respective straits are $\sim 0.4 \text{ Sv}$ and $\sim 0.2 \text{ Sv}$ (Ahmad and Sultan, 1991). Recent observations (Bower et al., 2000) from ADCP moored in the Strait of Hormuz indicate no strong seasonal variations in the outflow transport, and an annual mean of about $0.20 - 0.25 \text{ Sv}$.

Densification of the water in the Persian Gulf drives an exchange flow through the Strait of Hormuz, where less saline Arabian Sea water flows into

the Persian Gulf at the surface on the northern side of the Strait and the high saline Persian Gulf water exits at the bottom on the southern side of the Strait (Brewer et al., 1978; Horton et al., 1994). The most saline water is cooler by several degrees during February - June (~19 - 22.5°C) compared to July - January (22 - 25°C) and is only partially compensated by salinity, resulting in less dense source water in summer (Bower et al., 2000). The winter decrease /increase in outflow temperature /salinity results in a substantial winter/summer difference in outflow density of almost 1.3 kgm⁻³.

The Red Sea water and Persian Gulf water can be traced at intermediate depths over large portions of the Indian Ocean, due to their extreme temperature-salinity characteristics (Wyrki, 1971; Varma et al., 1980; Premchand et al., 1986; Shapiro and Meshchanov, 1991; Beal et al., 1999). Bower et al. (2000) used historical hydrographic data from the US Naval Oceanographic Office and a Numerical Model has been developed to investigate the transformation, dynamics and initial spreading pathways of the Red Sea and the Persian Gulf outflows where they enter the Indian Ocean. They concluded that RSWM and PGWM are the only two "native" intermediate water masses in the Indian Ocean.

The outflow from the Red Sea is the highest from October to May and occurs in a relatively strong two-layer exchange through Bab-al-Mandeb Strait. The high saline, dense RSWM flows out in the lower layer, and less saline Gulf of Aden water enters the Red Sea in the upper layer. Minimum outflow occurs during summer (June-September), when the prevailing winds from the north-northwest drive a surface flow out of the Red Sea. The Gulf of Aden water flows into the Red Sea in an intermediate layer sandwiched between the surface layer and the out flowing Red Sea water layer. Current meter and Acoustic Doppler Current Profiler observations at the Hamish Sill indicate a typical outflow transport of about 0.6 Sv in winter and 0.05 Sv in summer (Murray and Johns, 1997). Maximum outflow speeds of 1 ms⁻¹ were observed in late February, and outflow transport ceased completely for short periods during summer.

Observations made by Wyrki (1971), Brewer et al. (1978) and

Morrison et al. (1998) found that both Red Sea water and Persian Gulf water affect the stratification in the upper water column by injecting higher oxygen water into the oxygen minimum layer of Arabian Sea.

1.1.3 *The Equatorial Indian Ocean*

During NEM, water movements at the north of the equator is from east to west and is referred as 'North East Monsoon Current' (Wyrтки, 1973) or 'North Equatorial Current (Tomczac and Godfrey, 1994). This current sets in by November and attains peak by February before subsiding in April. Southward flow along the Somali coast during the northeast monsoon is limited to the region south of 10° N. It first occurs in early December near the equator and expands rapidly north in January with velocities of 0.7 - 1.0 ms⁻¹. In March the southward flow contracts again to 4° N, until the surface flow reverses in April (Tomczac and Godfrey, 1994). The waters of southward Somali current cross the equator before forming part of the Equatorial Counter Current. In November and December the Equatorial Counter Current flows along either side of the equator – between 3° N and 5° S. From January through April the Equatorial Counter Current further shifts to south up to 10° S.

With the onset of southwest monsoon a more vigorous ocean circulation develops. The poleward Somali current feeds the clockwise gyre to the northeast up to the coast of India before merging with the 'SWM Drift Current' (Wyrтки, 1973) or 'Indian Monsoon Current' (Molinari et al., 1990), flowing east between 5° N and 10° N. The Equatorial Counter Current shifts north and joins the Indian Monsoon Current.

1.2 *Arabian Sea response to seasonal forcings*

The oscillating atmospheric forcing is coupled to the hydrographic property fields and circulation structure. The surface currents and the seasonality is given in Cutler and Swallow (1984) and Molinari et al. (1990) while the water masses are compiled in the hydrographic atlas by Wyrтки (1971) on the basis of International Indian Ocean Expedition (IIOE).

1.2.1 *The Arabian Sea Dynamics during Northeast Monsoon*

The latent heat release during the relative calm winter (November-

February) monsoon, driven by cool, dry continental air from the north results in increased density of the surface layer. The excess evaporation over precipitation, turbulent heat loss exceeding the radiative heat gain, cools the surface waters of the northern Arabian Sea leading to formation of Arabian Sea High Salinity Water (Prasanna Kumar and Prasad, 1996). The study was based on monthly mean climatology of temperature and salinity in Arabian Sea north of the equator and west of 80° E, on a 2° x 2° grid. They observed that the Arabian Sea High Salinity Water spreads southwards along 24 sigma-t surface against the prevailing weak zonal currents. The eastern extent of the core is limited by the northward current that flows along the west coast of India as a branch of NEC. The high dense surface waters, while spreading southward from 10° N to 5° S sink beneath less dense warmer water that move poleward and forms a subsurface salinity maxima located near 100 to 150 m depth (Tchernia, 1980).

The poleward current carries water of Bay of Bengal to the eastern Arabian Sea and persists till January with a width of nearly 400 km and a depth of about 200 m at 10° N. It becomes narrow and deeper as it flows along the continental slope. The poleward flow is against the weak winds that have an average speed of 3 ms⁻¹ and is driven by pressure gradient, which forms along this coast during the northeast monsoon due to either thermohaline forcing and due to the effect of Kelvin waves that comes from the Bay of Bengal (Shetye et al., 1984). The eastern Arabian Sea, during NEM is also characterised by subsurface equatorward flow and downwelling. Studies on surface circulation based on TOPEX/POSEIDON altimeter data reveal the sea surface height variations (Prasanna Kumar et al., 1998).

1.2.2 *The Arabian Sea Dynamics during Southwest Monsoon*

During summer period, coastal upwelling occurs along both - the Arabian and Somali coasts (Schott, 1983; Currie, 1992), and open-ocean upwelling occurs in 500 km wide belt and is associated with positive wind stress curl (Swallow, 1984; Bauer et al., 1991). The Somali current, with maximum speed of 3.5 ms⁻¹ along the African coast leads to upwelling at several places in the Arabian Sea (Swallow and Bruce, 1966). On the basis of observations made during International Indian Ocean Expedition, Currie

(1992) found that under the influence of the southwest monsoon a pronounced geostrophic current develops off Arabia up to 1000 km in May and the strong southwesterly wind brings about offshore transport of the surface layer between 55° E and 60° E.

The development of the northward flow can be divided into two phases of different dynamics (Tomczac and Godfrey, 1994). In May, during the first phase of SWM (the second transition or inter-monsoon period) the Somali current is first established as a response to the wind reversal along the African coast, as well as to remote westerly winds just north of the equator. Lighthill (1969) concluded that a wind stress located 500 km away from the coast could generate a western boundary flux within a month, if baroclinic modes were taken into account. This result is also observed in data collected during the Monsoon Experiment MONEX, 1979 (Luyten, 1982). Measurements made in 1964 during the International Indian Ocean Expedition (1962-1965) show that the flow pattern of the Somali current is far more complicated than the continuous northward or southward flow as seen in climatological atlases (Schott, 1983). This current, observed during the Indian Ocean Experiment (INDEX) carried out during 1976 to 1979, develops into an intense jet with extreme velocities of 2.0 ms^{-1} for mid-May and greater than 3.5 ms^{-1} for June.

Along the western boundary, water is upwelled to the continental shelf from depths of about 150 m and this creates a strong negative sea surface temperature anomaly along the coast, reaching maxima in July – August. With the decline of the monsoon winds upwelling ceases in September. The distribution of the upwelled water was related to the direction of the wind and coastline, and the seabed topography. The upwelling along the coast of Arabia and Somali produces Ekman transport away from the coast (Tomczac and Godfrey, 1994). The signature of the resulting cold, upwelled waters extend to areas as far as the coast of India.

Observations made by Shetye et al. (1990) revealed the presence of surface equatorward flow, subsurface poleward flow and upwelling off the west coast of India during the southwest monsoon (Shetye, 1984). Though weak, the current is dynamically similar to the wind-driven eastern boundary

currents found elsewhere in the oceans. Local wind driving is also important to the coastal circulation off western Indian coast during the southwest monsoon (Shetye et al., 1994).

During the southwest monsoon, studies pertaining to this region indicate the presence of a two-gyre system - the Great Whirl between 5°N and 10°N with clockwise rotation, and a secondary eddy towards its south. Ali (1990) studied one of the most striking features of Arabian Sea – the Socotra eddy using INSAT –IB with very high-resolution digital data. Satellite imageries of Arabian Sea show eddy circulation at surface. These eddies intensify and persists locally during the SWM dominated by upwelling along the Arabia coast. The eddies, with horizontal dimensions of 200-500 km, extent to few hundreds of meters, and with typical speed of 26-30 cms^{-1} has been reported (Swallow, 1984). The eddy circulation is also evident in the studies of Prasanna Kumar et al. (1998).

The changes in the upper ocean temperature are particularly important in the Northern Indian Ocean, where the annual monsoon cycle causes rapid changes in its circulation, mixed layer development and adjustment of the density. The cooling which occurs through air-sea heat exchange during the high-wind periods known as Arabian Sea cooling is most intense during the SWM when the northern and western Arabian Sea are dominated by upwelling (Duing and Leetmaa, 1980, McCreary and Kundu, 1989). From May to September, coastal temperatures are lower by 5° C (Tomczac and Godfrey, 1994). Water of several degrees colder than that offshore can be localised within few 10s to 100 km off the coast. This small spatial scale in the sea surface temperature is in turn reflected in the sensible heat flux field. This low sea surface temperature during the summer is unique to Arabian Sea (Rudnick et al., 1997).

In the central Arabian Sea there is a mid summer decrease in sea surface temperature collocated with the wind maximum associated with increased evaporative cooling (McCreary and Kundu, 1989). Along Somalia, strong long-shore currents and cooler Sea surface temperature associated with local upwelling are found (McCreary and Kundu, 1989; Hastenrath and

Greischar, 1991).

While analysing the mixed layer, Rao et al. (1989) found that the surface cooling of 2.3°C in the central Arabian Sea with the onset and sway of the summer monsoon over five weeks, was mostly due to the net ocean surface losses as compared with the contribution of entrainment and advection of colder water. A major portion of corresponding mixed layer deepening of 55 m is explained by the one-dimensional forcing of surface cooling leading to convective turnover. Babu et al. (1991) studied the hydrographic structure in the east central Arabian Sea during premonsoon period and found that it undergoes temperature rises by approximately 0.5°C on an average in the upper 100 m, from May to June.

The major contribution in increasing the surface layer temperature comes from surface heat exchange processes while the horizontal advective process tends to remove the heat from the upper layer. They further found that the geostrophic flow patterns are similar from May to June in the major part of their study area while in the coastal areas off Goa a southerly current sets in June in response to coastal upwelling.

During the SWM, the northern part of the core of Arabian Sea high Salinity Water Mass shoals under the influence of Findlater jet, while the southern extent deepens. Throughout the year, the southern extent of the ASHSW is inhibited by the equatorial currents (Prasanna Kumar and Prasad, 1996). The most biologically productive period in the Arabian Sea is summer monsoon. Prevailing winds cause nutrient rich subsurface waters to flow toward the surface during this season.

1.2.3 *Transitional variations*

The NEM and SWM are separated by transition periods or monsoon lulls during which the winds are weaker and variable (Rudnick et al., 1997).

During summer to winter transition, the Arabian Sea shows a complex circulation pattern with currents off Somalia and Arabia remaining poleward while that off west coast of India are reversed (poleward) in the latter part of

the transition period. The circulation in Arabian Sea changes from anticyclonic to cyclonic. During winter to summer transition, the Arabian Sea shows development of weak anticyclonic gyres while currents off Somalia and Arabia do not show any strong definite pattern in April. In May the currents are more organised and resemble to that of southwest monsoon surface circulation. Reversal in currents precedes the winds by a couple of months and occurs when the winds are at their strongest (Shetye and Shenoi, 1988).

1.2.4 Water Masses of the region

The T-S pattern in the Arabian Sea shows the presence of Persian Gulf and Red Sea water masses at 300 and 900 m. The mixing pattern studied by constructing the triangles of mixing by Sarma et al. (1986), in the central Arabian Sea, found that the vertical mixing is dominant along the core of the Persian Gulf Water Mass.

Most of the studies of Arabian Sea are focused on the coastal region of Somalia and Arabia (Varma et al., 1980; Qasim, 1982; Swallow, 1984; Schott et al., 1990; Brock et al., 1992, Fischer et al., 1996; Stramma et al., 1996 and Smith et al., 1998) and the waters off the west coast of India (Shetye, 1984; Sarma et al., 1986; Shenoi et al., 1988; Shetye et al., 1990 and 1991; Kumar and Kumar (1996). The studies on central portion of the Arabian Sea are scarce (Luther and O'Brien 1985; Perigaud and Delecluse. 1993; Prasanna Kumar et al., 1998; Basu et al., 2000). Moreover, many of these studies involve modeling approach and give a general structure of the circulation aspects rather than the water mass structure throughout the region.

1.3 Objectives of the present work

The objectives of the present work are:

To analyse the monthly evolution of hydrography and surface circulation with special reference to the water masses.

To delineate the water masses and to analyse their spatio-temporal variability in response to meteorological forcings.

To study the role of eddies on the hydrography in response to monsoonal forcings.

To quantify the influence of marginal sea outflows and monsoonal

effect on the stability.

To detect the presence of mode waters of Arabian Sea origin.

1.4 *Layout of the thesis*

The work is presented in seven chapters. The first chapter deals with a literature review of the studies related to the topic of investigation. The second chapter explains data and methodology. The spatial and temporal quantitative distribution and development of water masses, delineation of forcings is considered in chapter three. The chapter four deals with hydrography, stability and mode water using a high quality CTD data along the two transects that are repeatedly covered during different periods. The sea surface height anomaly variations, geostrophic currents and kinetic energy are dealt with in chapter five. The whole work explaining the study region as a system is discussed in chapter six while summary and conclusions are presented in seventh chapter. Bibliography is given at the end.

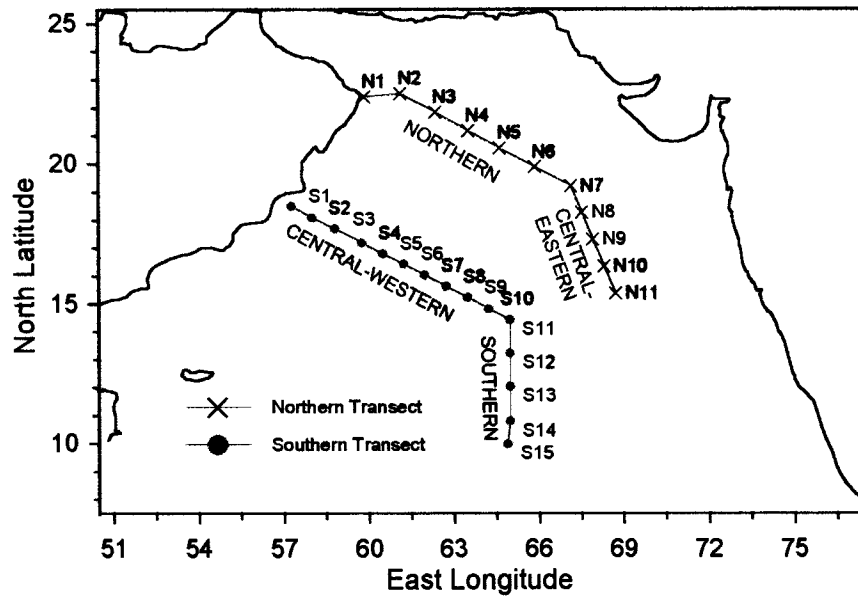


Fig. 1. Study area showing the CTD stations

Chapter - II

Data and Methods of Analysis

The anatomy of Arabian Sea through the analysis of water mass structure, current pattern and sea level variations in response to different forcings is the theme of the present work. Figure 1 represents the study area. To achieve the objectives the climatological perspective of the generation/decay of water masses, their spatial extent associated with temporal variability have been carried out. Further to this, the vertical variability of stability, identification of mode water in association with hydrography and water mass has also been carried out. As detailed analysis of the geometry of the sea surface is all the more important, quasi-synoptic sea level variability, the geostrophic flow pattern and the kinetic energy have also been dealt with using satellite data.

2.1 Data Used

The air-sea fluxes, hydrographic and satellite altimeter data used to accomplish the task are described below.

2.1.1 Winds and Fluxes at the air-sea interface

The climatological monthly winds from Hellerman and Rosenstien (1983), with spatial resolution (x and y directions) $2^{\circ} \times 2^{\circ}$, are also used. The climatological data of fluxes of short wave, long wave radiations, sensible, latent and net heat are used to delineate the forcings that are associated with the hydrography (Da Silva 1994). The buoyancy flux (Da Silva 1994) is used to study the variability of flux associated with the heat and salt, over the entire region. The data is climatological and monthly. It is defined for 0.5° latitudinal and longitudinal resolution.

Winds of the year 1995, obtained from SSM/I (Special Sensor Microwave Imager) flown on board US Navy's Defense Meteorological Satellite

Programme (DMSP), are used. As the temporal resolution is 6 hourly, monthly averaged data is estimated. The spatial resolution is 2.5 x 2.0 degree in x and y directions.

2.1.2 Hydrographic data

To study the monthly evolution of hydrography and for the delineation of spatial extent of water masses, temperature and salinity from Levitus data set (Levitus et al., 1994a and 1994b) are used. Temporally the data are defined for every month while spatially the resolution is different in the horizontal and vertical directions. The horizontal resolution is 1° x 1° and in z direction it is spread over nineteen levels. From surface to 30 m the resolution is 10 m. The next level is at 50 m and 25 m resolution exists between 50 to 150 m. From 150 to 300 m it's 50 m and 100 m resolution is below 300 m to 1000 m.

Though climatological data evolve a general understanding of the hydrography and the water masses of the study area, with it's tumultuous nature, a small-scale feature in the Arabian Sea can cause a large impact on the atmosphere. Hence, further analysis of the area is carried out using the high vertical resolution CTD data, generated as a part of Joint Global Ocean Flux (JGOFS) campaign. These data are collected onboard US research vessel Thomas G Thompson during 1995. The details of the data are presented in table I. The stations form two transects – northern and southern, are repeatedly covered during different periods of 1995. The stations of the northern transect (NT) are named from N1 to N11 while that of southern transect (ST) are from S1 to S15 (Fig. 1).

2.1.3 Satellite data

The sea surface height anomaly, generated from Topex/Poseidon, procured from University of Texas is used. These deviations are with respect to four year period (October 1992 to October 1996). The data spans with 1° x 1° in x and y directions and has a temporal resolution of approximately 10 days (9.915625 days) corresponding to the cycle period of Topex/Poseidon. The period of the different cycles are shown in table II. The data corresponding to cycle 118 is not available.

2.2 Methodology

The procedures involved in accomplishing the objectives are given below.

2.2.1 Climatological fluxes, hydrography and water mass mapping

Potential Density computations.

The spreading of the water masses depends on the density structure of the water. The spread waters in turn affect the density of the ambient waters. Hence, potential density computations are carried out following Fofonoff and Millard (1983).

Buoyancy Flux

The dynamics in association with the high degree of meteorological variability presents its impact on the water characteristics. The heat and salt fluxes are given as Buoyancy flux. The buoyancy forcings are analysed during the different months to determine the net flux associated with the water mass formation. Further analysis of the components of buoyancy flux lead to the study of meteorological forcings.

Meteorological forcings

The climatological monthly winds, short wave and long wave radiations, sensible heat and latent heat fluxes are analysed for every month. To study the temporal variations of the hydrography of the region of concern, horizontal sections of potential temperature (hereafter referred as temperature), salinity and potential density are plotted at all the nineteen levels during the different months. Those sections that do not show significant features are not presented for brevity.

Water mass mapping

By analyzing the data used for the present study and on the basis of studies by Varma et al. (1980), Quadfasel and Schott (1982), Molinari et al. (1986); Brock and Mc Cain (1992), Stramma et al. (1996), Morrison et al.

(1998) and Prasanna Kumar and Prasad (1999), the annual mean properties ascribed to the different water masses in the present study are given in table III.

While mapping the spatial distribution of water masses at deeper levels the property distribution in terms of its variation is meager. Hence care is taken to identify the water masses on the basis of its equilibrated property.

On the basis of the above conservative properties, the grids covered by different water masses are then identified for the time series analysis. The grids occupied by Arabian Sea Water, Persian Gulf Water, Red sea water and the Bay of Bengal water masses are depicted in different colours to map their spatial extent.

2.2.3 Hydrography, water masses, stability and mode water

Mixed Layer Depth

The high quality CTD data of the year 1995 are used to study the seasonality associated with the hydrography. Various criteria are used for MLD identification. These criteria include change in temperature of 0.1°C or 1°C from surface. Also, MLD is determined on the basis of change in density. In the present study area preliminary analysis of the sections reveal that temperature may not show any significant variation while drastic salinity variation is seen (for example, in March at eastern and southern stations). Also at the second station (S2) of the southern transect during January. The temperature section indicates a MLD of 90 m. However, from salinity section significant variations in MLD is seen in this layer. In southern transect, during July, salinity at the coastal stations are fairly constant with depth, but temperature variations exists. Thus both properties do not always remain constant. Therefore, MLD is considered as a depth up to which weak gradient is seen in temperature and salinity.

To have an insight into the different water masses prevailing and their spatial variability, T-S diagrams are plotted. Only those profiles showing remarkable variations are presented.

Computation of Stability

The analysis of the hydrographic properties along the two transects reveal a high degree of anomaly at the western region compared to the eastern region. This anomaly is depicted in the weak/absence of thermocline and halocline, which are responsible for development of high stability of the water column. Thus the anomaly is represented by the decrease in stability of the water column. Hence, to quantify this, the stability parameter is examined throughout the two transects.

The stability is computed using.

$$E = \alpha \left(\frac{\partial T}{\partial z} \right) + \beta \left(\frac{\partial S}{\partial z} \right) \text{ m}^{-1}$$

is coefficient of thermal expansion and

$$\alpha = -\frac{1}{\rho} \left(\frac{\partial \rho}{\partial T} \right)_{s,p}$$

is coefficient of haline expansion

$$\beta = \frac{1}{\rho} \left(\frac{\partial \rho}{\partial S} \right)_{t,p}$$

Computation of water type density

Though T-S diagrams characterise water bodies of uniform properties, they lack characteristics of micro scale features and depth information unless special annotation of the T-S curve is included. Even then the information cannot be very detailed. There are, however, instances where continuous depth information along the T-S curve is of interest, if there is a water mass contributing to large volume. Therefore, water type density (WTD) is computed (Tomczac 1999). The mode water is characterized by low variations in WTD over a substantial vertical extent.

The water type density is defined as a normalized total property gradient along the vertical in physical space and expresses degree of homogeneity in the water mass as function of depth. The derivation for the computation of water type density is as follows.

Mathematically, and expressed in finite difference form suitable to application of hydrographic data, water type density δ_{wt} is defined as follows. Assume that a hydrographic station extends over a depth range r and the observational increment is $\Delta z = r/m$, where m is reasonably large integer. The accumulated change L_j of property p_j over the range r expressed in finite difference form, is then given by

$$L_j = \sum_{i=1}^m \left(|p_j(z_i) - p_j(z_{i-1})| \right)$$

Where Z_i ($i = 0, m$) represents the depth increments over the range r . The contribution of property p_j to δ_{wt} is then

$$\delta_j = \frac{|p_j(z_i) - p_j(z_{i-1})|}{\delta_j}$$

And the water type density δ_{wt} is found by adding the contributions from all the properties:

$$\delta_{wt} = \sum_{j=1}^n \delta_j$$

L_j can be interpreted as the length of the water mass definition curve in parameter space with respect to parameter j (as seen in Fig 1), expressed in dimensional units. Water type density is then the non dimensional contribution of the ocean layer between Z_{j-1} and Z_j to the total length L_j .

Geostrophic flow from Satellite altimeter data

To study the variability of sea surface height, it is plotted for every cycle of the year. From the sea surface height, geostrophic currents are computed adopting the below given formula (Lagerloef et al., 1999). The kinetic energy is also estimated and plotted to identify energy rich zones and their variability.

For latitude $>, = 10^\circ$

$U = - (g/f) (dh/dx)$ and

$V = (g/f) (dh/dy)$

Where u is positive eastward and v is positive northward. The units are cm/s.

dh/dy and dh/dx are the northward and eastward slopes.
 $g = 980\text{cm s}^{-2}$ is the acceleration due to gravity
 $f (= 2\Omega\sin\phi)$ is the coriolis parameter with $\Omega = 7.29 \cdot 10^{-5}$,
 ϕ is the latitude.

For Latitude less than 10°

$$U_m = \mu U + (1 - \mu) U_e \quad \text{and} \quad V_m = \mu V$$

Where $U_e = -g/\beta (d^2h/dy^2)$ and $\beta = 4\pi/86400$

$$\text{Kinetic energy} = (u^2 + v^2)/2$$

Table I : Details of the CTD data.

Transect	Ship	No. of stations	Period of observations
Northern	R V Thomas Thompson	11	Jan 08 to Jan 15, 1995
Southern	R V Thomas Thompson	15	Jan 18 to Jan 31, 1995
Northern	R V Thomas Thompson	11	Mar 14 to Mar 21, 1995
Southern	R V Thomas Thompson	15	Mar 23 to Apr 05, 1995
Northern	R V Thomas Thompson	11	Jul 18 to Jul 25, 1995
Southern	R V Thomas Thompson	15	Jul 28 to Aug 11, 1995
Northern	R V Thomas Thompson	11	Aug 18 to Aug 26, 1995
Southern	R V Thomas Thompson	13	Aug 30 to Sep 12, 1995
Northern	R V Thomas Thompson	11	Nov 30 to Dec 08, 1995
Southern	R V Thomas Thompson	15	Dec 11 to Dec 26, 1995

Table II. details of the cycles periods of Topex/Poseidon

Topex/ Poseidon Cycle No.	Cycle period	Topex/ Poseidon Cycle No.	Cycle period
84	25/12/94 to 03/01/95	103	01/07/95 to 10/07/95
85	04/01/95 to 12/01/95	104	11/07/95 to 20/07/95
86	13/01/95 to 22/01/95	105	21/07/95 to 30/07/95
87	23/01/95 to 01/02/95	106	31/07/95 to 09/08/95
88	02/02/95 to 11/02/95	107	10/08/95 to 19/08/95
89	12/02/95 to 21/02/95	108	20/08/95 to 29/08/95
90	22/02/95 to 03/03/95	119	30/08/95 to 07/09/95
91	04/03/95 to 13/03/95	110	08/09/95 to 17/09/95
92	14/03/95 to 23/03/95	111	18/09/95 to 27/09/95
93	24/03/95 to 02/04/95	112	28/09/95 to 07/10/95
94	03/04/95 to 12/04/95	113	08/10/95 to 17/10/95
95	13/04/95 to 23/04/95	114	18/10/95 to 27/10/95
96	23/04/95 to 02/05/95	115	28/10/95 to 06/11/95
97	03/05/95 to 11/05/95	116	07/11/95 to 16/11/95
98	12/05/95 to 21/05/95	117	17/11/95 to 26/11/95
99	22/05/95 to 31/05/95	118	27/11/95 to 06/12/95
100	01/06/95 to 10/06/95	129	07/12/95 to 16/12/95
101	11/06/95 to 20/06/95	120	17/12/95 to 26/12/95
102	21/06/95 to 30/06/95	121	27/12/95 to 03/01/96

Table III. Characteristics of the various water masses

Water Mass	Range of			
	Temperature (°C)		Salinity	
Arabian Sea	23.0	25.8	36.35	36.75
Persian Gulf	16.0	19.5	36.1	37.1
Red Sea	9.7	11.1	35.4	35.9
Bay of Bengal	27.5	29.5	32.6	34.6

Chapter - III

Lower Tropospheric Forcings And Ocean Response

The air-sea interaction is well manifested by the micro and macro features in the oceanic system. Based on the wind pattern over the study area, a year is classified into four categories. The summer season – June to September, transition from summer to winter – October and November, winter season - December to March and transition from winter to summer - April and May. The results of the detail analysis of the winds, heat budget, hydrographic properties and quantitative delineation of spatial extent of water masses of the study area have been dealt in the chapter. The heat budget components, helps to delineate the forcing that are responsible for the water mass formation.

3.1 Lower tropospheric wind regime

The lower tropospheric winds influence the upper ocean dynamics. Winds of the representative months of summer and winter monsoons are analysed along with that of the selected transition months that depict reversal in the winds (Fig. 3.1).

During winter the winds are northeasterly with maximum velocity in January. Further examination shows that the spatial distribution of velocity during winter, exhibits a maxima along an axis running from Gujarat to Somalia. A negative curl exists to the northern side of the axis and a positive to southern side. The magnitude of the curl ranges from 0 to $-9 \times 10^{-7} \text{ N m}^{-3}$ and

0 to $3 \times 10^{-7} \text{ N m}^{-3}$. As the season advances, the axis shifts southeastwards and the shift is more pronounced in Central Arabian Sea.

An examination of wind pattern during transition period (April and May) suggests that in April the wind pattern over the central-western region shows a change in direction with respect to that in March. Further, in May, there is a total reversal of wind over the entire region from northeast to southwest. The axis, with negative curl on northern side and positive on the southern side, shifts southeastwards. Also, in this month another axis with positive curl to the west of it and negative to the east is seen along the western boundary of the region.

Wind pattern during July shows that the winds are southwesterly and the winds stress is strong (0.4 N m^{-2}). The pattern of the wind distribution reveals a belt of intense winds that runs from Somali coast to Gujarat with positive curl on northern side and negative on southern side. Wind further strengthens in July while in August and September it weakens. During September the axis moves towards the western boundary with the development of another axis along the west coast of Indian subcontinent.

October shows change in the direction of wind from southwest-west to north-northeast while November shows northeasterly winds. The axis shifts westward and runs from Gujarat to Somalia with negative curl on the northern side and positive on the southern side during October and November.

3.2 Fluxes at the air-sea boundary

The fluxes at the air-sea interface include the short wave radiations, long wave radiations, sensible heat flux, latent heat flux, the resultant net heat flux and the buoyancy flux associated with the combined effect of heat and salt fluxes.

3.2.1 Influx of short wave radiations

The distribution pattern of short wave radiation is presented in Fig. 3.2. During winter the short wave flux shows a decreasing trend towards pole with an exception in March. The central and eastern regions, during March, show a

high flux in the form of a core, while poleward and equatorward of it the flux decreases. During April the flux ranges from 260 to 330 Wm^{-2} while in May it ranges from 235 to 360 Wm^{-2} . There is a poleward shift in the core of high flux from March to April while in May the distribution is conspicuous with absent of the core.

The short wave flux during June, July, August and September ranges from 215 to 325 Wm^{-2} , 215 to 315 Wm^{-2} , 205 to 315 Wm^{-2} and 225 to 305 Wm^{-2} , respectively. The distribution in summer shows an alignment of isolines with higher fluxes on western side than on the east, with highest intensity during August. In June the southeastern region is characterized by low flux while in July the region to the east of 66°E experiences lower flux. However in August, a core of low ($\sim 200 \text{Wm}^{-2}$) is centered around 19°N and 66°E . In September the eastern region is characterized by low flux. In October the flux varies between 210 and 275 Wm^{-2} while in November it is between 190 and 235 Wm^{-2} . Orientation of isolines to the north of 19°N , during November, is zonal in nature, showing a decrease in short wave flux at head region - a characteristic of winter.

3.2.2 Outward flux through long wave radiations

The Outgoing long wave radiation is given in figure 3.3. The flux distribution shows an approximately zonal nature during December, January and February. Detail analysis of the flux during this period reveals a lower flux on the eastern side than on the western side with an increase in poleward direction. The range of flux during December is from 51 to 82 Wm^{-2} , whereas it is from 54 to 82 Wm^{-2} during January and 54 to 75 Wm^{-2} in February. The temporal variability within the season shows that the distribution during March is different than the earlier months. A core of high flux is discernible at 18°N , 61°E . The distribution pattern further shows lower flux on eastern side than on the western side. The flux ranges from 43 to 57 Wm^{-2} and 39 to 49 Wm^{-2} during April and May. The transition period further shows that the core, seen at northwestern part of study area during March, shifts to the central region. The lowest values are in the southeastern region.

The outgoing long wave radiation ranges between 33 and 46 Wm^{-2} in

June, 29 and 46 Wm^{-2} in July, 29 and 47 Wm^{-2} in August while in September it ranges from 39 to 49 Wm^{-2} . During June to August isolines are orienting along the northwest to southeast direction till 20° N. However north of 20° N, it is aligning along the northeast to southwest. The flux is the lowest off the central west coast of India. In September a core of low flux (42 Wm^{-2}) is seen at 14° N and 60° E. The distribution of flux is such that it is lower on eastern side than on the western side. The flux ranges between 46 and 60 Wm^{-2} during October while it is between 45 and 71 Wm^{-2} during November. The transition period shows a higher gradient in flux in the southeast to northwesterly direction with lower values at southeastern region.

3.2.3 *Sensible heat flux*

The sensible heat flux in the study area is shown in Fig. 3.4. The distribution of sensible heat flux shows that the region is characterized by gain as well as loss. Positive values represent the gain while negative values represent the loss to the ocean.

In winter, a characteristic feature is the loss in sensible heat flux. The loss is between 2 and 12 Wm^{-2} during December and January, 3 to 9 Wm^{-2} in February while it is between 2 and 7 Wm^{-2} in March. The loss increases towards the head of the region. The distribution of the flux further reveals lower loss on the eastern side compared to the west. During February a core of high loss (8 Wm^{-2}) is seen centered around 16° N and 64° E. As the season advances (March), there is a decrease in the loss with a shift in the core in a southeasterly direction. The distribution of sensible heat flux during April shows a similar pattern as in the earlier month. A comparatively lower (5 Wm^{-2}) loss is associated with the core during April. The distribution pattern in May is entirely different showing a drastic reduction in loss of sensible heat flux. The loss decreases towards pole and there is no loss at the head region.

The summer season is characterized by both gain and loss at different regions of the study area. The range of sensible heat flux is between -8 and 3 Wm^{-2} during June, -8 and 8 Wm^{-2} in July, -8 and 7 Wm^{-2} in August while in September it is -4 to 6 Wm^{-2} . The region on the western side shows that the ocean gains heat energy while on the eastern side it loses. An intra-seasonal

variability is seen in the spatial extent of the region experiencing gain and loss. During July and August the maximum gain ($\sim 8 \text{ Wm}^{-2}$) is experienced in the central-western region. The region of high gain in tropical seas is associated with upwelling zones. As the month advances to October and November the ocean starts losing heat and it is in the range of 0 to 4 Wm^{-2} and 1 to 7 Wm^{-2} .

3.2.4 *Latent heat flux*

Fig. 3.5 shows the distribution of latent heat throughout the study area with values representing the loss from the ocean. The flux is ranging between 105 and 165 Wm^{-2} in December, 100 and 165 Wm^{-2} in January, 90 and 140 Wm^{-2} during February while in March it is between 80 and 115 Wm^{-2} . The winter season is characterized by low latent heat flux in the southeastern part of the study area. The distribution during December and January reveals high values of latent heat flux in the form of a belt from Somalia to Gujath with highest values in the northeastern region. On either side of the belt latent heat flux decreases. A shift in the belt, with a core of high, towards southeastwards is very clear during February and March. The flux during April ranges between 60 and 110 Wm^{-2} and while in May it is 60 and 125 Wm^{-2} . As in the previous month, distribution in April depicts a core of high energy towards southeastward region of the study area. It is weaker compared to the previous month and is absent during May. In general the latent heat flux decreases towards pole.

The range of latent heat flux during June, July, August and September is 70 to 180 Wm^{-2} , 40 to 120 Wm^{-2} , 30 to 120 Wm^{-2} and 40 to 110 Wm^{-2} , respectively. The flux distribution reveals a core of maxima (170 Wm^{-2}) centered around 12° N and 65° E during June. But in July and August it weakens ($140, 120 \text{ Wm}^{-2}$) and is located in the central-southcentral Arabian Sea. The core is absent during September but high values are seen along 67° E . The flux ranges between 70 and 100 Wm^{-2} , 80 and 150 Wm^{-2} in October and November. In October the latent heat flux is lower than during April-May. Latent heat flux during November clearly shows initial phase of winter season. The region exhibits a belt of higher flux from Somalia to Gujath.

3.2.4 *Net heat flux*

Fig. 3.6 shows the distribution of net heat flux in the study area with positive values indicating gain to ocean. During December the entire area except southeastern region experiences loss. The loss of heat energy at the head is 120 Wm^{-2} while towards the equator there is a considerable reduction in the loss (20 Wm^{-2}). The position of transition zone of gain to loss remains same from December to January. However, the loss from the entire region is reduced. In general the flux distribution during these two months show similar pattern. February depicts an entirely different pattern in the distribution of flux, with the large part of the ocean experiencing gain. The loss is seen at the head and north-central regions and depicts a tongue like feature. The southeastern region showing higher gain compared to southwestern side. Distribution during March shows gain to ocean throughout the entire region with higher input at the western side than the eastern side. The coastal region shows higher flux than the open ocean. An important feature seen during March is the gradual reduction in heat input from head to equatorial region to the west of 69° E . This variation in flux is opposite to that during previous months.

In April and May, the isolines show an approximately zonal nature with higher flux on the west compared to the east. This pattern of flux distribution is different from that of the winter season.

During June the study area is characterized by loss and gain. The loss (-20 Wm^{-2}) exhibits in the form of core centered around 11° N and 67° E . A large part of the region along the coastal boundaries shows gain to ocean with higher fluxes (180 Wm^{-2}) at the head region. A similar pattern in flux distribution is seen during July wherein the loss depicted in the form of a core that shifts northwards and exhibits a drastic reduction in intensity ($< 10 \text{ Wm}^{-2}$). In August the entire region is characterized by gain with minimum centered between 66 and 72° E . The western side shows higher gain than the eastern side. The range is between 40 and 180 Wm^{-2} . Though the pattern of flux distribution in September is similar to that of previous months, the range of gain is lower (50 to 160 Wm^{-2}). The gain is higher at the open ocean region while at the boundaries it reduces.

The pattern of net heat flux during October resembles to that of summer months while during November it resembles to that of winter months. In October the distribution shows a drastic reduction in gain in the western region. During November the northern and central part of the region shows loss (60 Wm^{-2}) from the ocean while rest of the region shows a gain with higher values at the southeastern region ($<40 \text{ Wm}^{-2}$).

3.2.4 *Buoyancy flux*

Though the heat budget reveals the exchange of mass and energy between the air and the sea, it does not account for the net flux that may be influenced by advection/ convection/ diffusion. The buoyancy flux however deals with the exchange of heat and salt between air and sea. The buoyancy flux over the study area is given in figure 3.7. The negative values indicate negative buoyancy (loss from the ocean) and vice versa. The zero value represents neutral buoyancy.

From December to February large portion of the region shows loss while in March the entire region shows gain. In December the loss ranges from 0 to $14 \text{ kg m}^{-1}\text{s}^{-3}$. The southeastern region of the study area shows neutral buoyancy flux. Off Gujrath, a well demarcated core of loss is evident. The distribution of buoyancy flux reveals that the eastern boundary experiences lower loss compared to the western boundary. During January, the buoyancy flux ranges from 2 to $-12 \text{ kg m}^{-1}\text{s}^{-3}$. In addition, the distribution of buoyancy flux shows that a large area exhibits loss with a core like pattern off Gujrath.

The southeastern region shows gain with higher values at the equatorward side. These features result in high gradient in flux along the eastern boundary of the area compared to western region. The western boundary shows loss. In February the distribution of flux shows a core of loss with a magnitude of $3 \text{ kg m}^{-1}\text{s}^{-3}$ is seen at the central eastern region. At the southeastern region the ocean experiences gain up to $4 \text{ kg m}^{-1}\text{s}^{-3}$. The gain is high during this month than the earlier months. Off Oman, the region is characterized by a weak gain. The distribution of buoyancy flux during March is entirely different from that of the earlier months of the season. The entire

region is characterized by gain ranging from 3 to 7.5 kg m⁻¹s⁻³. The buoyancy flux at the central region is lower compared to eastern and western boundaries. At the western boundary, higher flux is seen off Oman while along the eastern boundary it is higher at southeastern region. The western boundary do not show high gradient.

During April the entire area experiences gain (positive buoyancy) ranging from 5 to 12 kg m⁻¹s⁻³. The central-western regions show a uniform gain (~10 kg m⁻¹s⁻³). The variation further shows that the gain increases from equator to head region. In the month of May, the buoyancy flux distribution shows an approximately zonal nature with higher gain at the head region. The entire region is characterized by positive buoyancy and the range of flux is from 2 to 18 kg m⁻¹s⁻³. The south central region shows uniform nature in buoyancy flux distribution.

The distribution pattern of buoyancy flux over the area, during summer, reveals that the entire region is dynamic in nature. In June and July the coastal region is characterized by gain to ocean. It ranges from 0 to 14 kg m⁻¹s⁻³. Along the western boundary the offshore gradient of buoyancy flux is higher than the rest of the coastal region. The distribution of buoyancy flux further shows that in June the south central region experiences loss while in July the central region shows loss. The loss in July (2 kg m⁻¹s⁻³) is lower compared to June (4 kg m⁻¹s⁻³). Further in July, the offshore gradient is higher at the west than at the east while it is absent at the north.

During August, the entire region experiences positive buoyancy ranging up to 14 kg m⁻¹s⁻³. The western region exhibits higher gradient and is characterized by higher positive buoyancy (14 kg m⁻¹s⁻³) compared to the east (10 kg m⁻¹s⁻³). The pattern of buoyancy flux during September is different from that of the earlier months. The flux ranges from 4 to 11 kg m⁻¹s⁻³. Though the western region shows gradient in positive buoyancy it is lower compared to the earlier months. The gradient in buoyancy flux at the western boundary is higher in comparison with the eastern boundary. Another interesting feature is the depiction of large area, between 66 to 72° E, experiencing low buoyancy flux ranging between 4 and 5 kg m⁻¹s⁻³.

The distribution of buoyancy flux during October and November are different. The flux ranges from 3 to 9 kgm⁻¹s⁻³ in October and 4 to - 8 kg m¹s⁻³ in November. In October the western boundary experiences higher gain than the eastern boundary. The offshore gradient in October, along the western boundary, is less than the earlier season. In November, all along the coast of India, the region experiences gain with higher values towards the equator. Unlike the previous season, the gradient is absent along the eastern and western boundaries. The northern and central region depicts a loss in the flux.

3.3 Arabian Sea Hydrographic regime

The hydrographic regime of the study area in response to different forcings is dealt in this section. For analyzing the features associated with the meteorological forcings detail study have been presented till the depth where seasonal influence is felt. As a high degree of interaction exists between the study region and the marginal seas, property distribution is presented at those depth zones where the effect of marginal seas is felt. The spatial and temporal variability of the hydrographic properties are given below.

3.3.1 Winter variability in thermal regime

The surface temperature range in winter is from 25.5 to 29.0° C in December, 23.5 to 28.5° C in January, 23.0 to 28.5° C in February and 24.5 to 29.5° C in March (Figs. 3.8 to 3.11). The distribution of property shows similar pattern extending from surface to 30 m in December, 50 m in January while in February and March it is seen up to 75 m. This clearly shows the gradual deepening of the influence of winter with advance of season. In addition, the orientation of isotherms from December to March in the study area shows alignment in southwest - northeast direction with warm waters at the southeastern part. This warm water protrudes in the northwesterly direction.

Monthly analysis shows that in December and January the vertical extent of the warm water is 125 m while in February and March it shallows to 100 m and 75 m respectively. In December and January, a large body of water is seen in the south-central region at a depth of 75 m with temperature between 24.5 and 25.0° C. Off Oman, a well defined feature is the presence of

a front between 50 and 125 m in December, 75 and 125 m in January, 100 and 125 m in February and March, respectively. The frontal formation is due to mixing of cold water, that is remnant of the upwelling during previous summer, with ambient water. With the advance of season the gradient of front decreases.

3.3.2 Winter variability in haline regime

The salinity at the surface ranges from 33.4 to 36.6 psu in December, 34.4 to 36.6 psu in January, 33.4 to 36.8 psu in February and 34.0 to 36.6 psu in March (Figs. 3.12 to 3.15). Unlike the temperature distribution, the pattern of horizontal variation of salinity in the upper 50 m is not same throughout the season. The surface salinity distribution in the central and northern regions shows an increase in salinity from December to January. An elongated high salinity tongue like feature, in the upper 50 m during December, protrudes from northwesterly to southerly direction. Similar pattern is seen in January but extending up to 75 m. As the season advances to February and March the central Arabian Sea depicts a core of high saline water (36.4 psu) extending from surface to 50 m. However, the southward extent of the above mentioned feature is limited to central region. This is due to the prominence of low salinity water at the southeastern region, flowing in the northwesterly direction and extending to a depth of 75 m. Off the coast of Oman, between 50 and 75 m, less saline water is not distinctly seen in concurrence with temperature distribution. This is due to the fact that the outflow of the high saline water from marginal seas does not lead to drastic reduction in salinity with depth at the western region of the study area.

3.3.3 Winter to summer transitional variability in thermal regime

The thermal structure during the transition period is given in Figs. 3.16 and 3.17. The surface temperature in April ranges from 26.0 to 30.5°C while in May it is 28.0 to 30.5°C. During April, at western boundary, between 100 and 125 m, there is a presence of cold water that is similar to that of the earlier month. The distribution further reveals the presence of water of uniform temperature between 125 and 150 m, at the central Arabian Sea. During May the distribution of temperature divides the upper waters in the two vertical

zones, one from surface to 50 m with uniform pattern while the other below 50 to 150 m with a non-uniform nature. At the southeastern region, between 75 and 150 m, there is a clear depiction of gradient in temperature due to the presence of cold water. Along the western boundary, between 75 and 125 m, the isotherms are parallel and closely packed indicating presence of cold water. In the upper 30 m, the southeastern region of the study area depicts presence of warm water with greater homogeneity in May than in April.

3.3.4 Winter to summer transitional variability in haline regime

The salinity variations during the transition period are shown in Figs. 3.18 and 3.19. The surface salinity distribution in April and May indicates a range of 34.2 to 36.6 psu and 34.6 to 36.6 psu. During April and May, a well defined feature in the form of a tongue of high saline water, extending from northwest to central region, is present from surface to 30 m. Similar distribution is also seen during winter. The distribution in April, between 50 and 75 m, shows high salinity core in the central Arabian Sea while it is absent during May. At the southeastern region, the salinity decreases drastically towards equator in the depth range of 75 to 125 m.

3.3.5 Summer variability in thermal regime

The distribution of temperature during summer is given in Figs 3.20 to 3.23. The surface distribution shows that temperature ranges from 26.5 to 30.0° C in June, 24.5 to 28.5° C in July while it is 23.0 to 28.5° C in August and 24.5 to 28.5° C in September respectively. Analysis further shows that along the western boundary, there is a cold water extending from surface to 125 m in June, 150 m in July while in August and September it extends up to 200 m. Similarly, along the eastern boundary, presence of cold water is discernible between 50 and 75 m in June, 10 to 125 m in July, while it is seen from surface to 150 m in August and September.

The clustering of isotherms is more at the western boundary than at the eastern boundary. Thus it indicates that the process is stronger at the western boundary. As the season advances, in August, the feature seen at the western and the eastern boundaries extends to northern region while in September it is

absent. Further, the temperature variation shows that the gradient at the surface is highest in August revealing strong upwelling.

3.3.6 *Summer variability in haline regime*

The spatio-temporal variability in salinity during summer is shown in Figs. 3.24 to 3.27. The salinity at the surface ranges from 34.6 to 36.8 psu in June, 34.4 to 36.8 psu in July, 34.2 to 36.6 psu in August and 34.6 to 36.6 psu in September. The salinity distribution shows a feature in the form of a tongue extending from north to equatorward with a vertical extent of 125 m in June, 150 m in July and August. The salinity associated with the tongue is highest (36.6 psu) in June. In September though the tongue is absent, high salinity is seen in central region in the form of a core from surface to 125 m. Within this depth range waters along the eastern and western boundaries are characterized by low salinity. This in turn results in the formation of a haline front. The haline gradient is seen to be higher along the eastern boundary than the western boundary. Such a low gradient in salinity on the western side is due to the presence of high saline waters at the subsurface region. At the eastern boundary, the temporal variation in the gradient across the front is the strongest in August with a vertical extent from surface to 125 m.

3.3.7 *Summer to winter transitional variability in thermal regime*

The temperature distribution during the transition period is given in Figs. 3.28 and 3.29. The surface temperature in October and November ranges from 26.5 to 29.0° C. The distribution shows a decrease in surface temperature in poleward direction. There is a marked difference in distribution with respect to previous season. Such a deviation in pattern is extending up to 10 m in October while in November up to 30 m. The property distribution during October and November further shows that along the western boundary there is a presence of cold water from 20 to 150 m and 50 to 125 m respectively. This results in the formation of a front. Also, a front is seen, at the eastern boundary, between 20 and 100 m in October while in November it is between 50 and 75 m. The gradient of the front is less at the east than at the western boundary.

3.3.8 Summer to winter transitional variability in haline regime

The salinity distribution during the transition is shown in Figs. 3.30 and 3.31. The surface salinity distribution in October and November indicates a range of 34.8 to 36.8 psu and 32.8 to 36.6 psu. The distribution pattern in both the months shows a similarity from surface to 50 m. Another interesting feature is the well defined haline front at the eastern boundary with no such feature at the west. This front is the strongest during November than in October and extending vertically up to 50 m.

3.3.9 Thermal and haline variability at intermediate depths

The area near the mouth of the Persian Gulf and Red Sea is characterized by warmer and high saline water. Vertically, these waters are seen till 1000 m. The analysis of horizontal distribution of properties at different levels shows a significant feature in the depth range between 150 and 300 m and between 600 and 900 m. The feature is consistent throughout the year in the above limits and shows lower variability with depth. Therefore, the characteristics of water for representative months of the season are presented (Figs. 3.32 to 3.35).

The orientation of isolines (isotherms and isohalines) between 200 and 300 m and between 600 and 900 m reveals an outflow of warm saline waters from the Persian Gulf and Red Sea, during January (Figs. 3.32 and 3.33). These waters are characterised by temperature between 16.5 and 21° C while the salinity is greater than 35.8 psu. The orientation of the isotherms and isohalines further shows that the spreading of Persian Gulf water is equatorward and occurs along the western boundary. Further examination reveals that the flow associated with Persian Gulf water is predominant at 250 m. In July, the pattern of the isotherms and isohalines below 200 m do not show much variations than that during January (Figs. 3.34 and 3.35). However, at 150 and 200 m the isoline variations differ largely. The temperature distribution reveals cooler waters compared to January at the northern region while the salinity also decrease in salinity in the northern region at these depths.

The isotherm and isohaline variations show presence of warmer and high saline waters at the northern and western regions. The pattern also reveals a poleward spread occurring along the western and central regions. This spread is predominant at 800 m.

3.3.10 *Density field of the study area*

The potential density (hereafter density) field for the representative months of summer monsoon and winter monsoon are selected and analysed (Fig. 3.36 psu). In January and July, at 10 m level, the density increases towards pole. The density is higher at the western region while the southeastern region has the least density. The density is lower at this level during the summer month than the winter month. At 300 m, the density at the western, northern and southeastern regions is lower than the rest of the area. The lower dense water at the west and at the northwest is separated by the high dense water. These variations in density are akin to both the months. At 800 m, during both the months the density is found to be higher at the southern and eastern side in comparison with the remaining part of the study area.

3.3 *Mapping of water masses in Arabian Sea*

The water mass plays a vital role in the redistribution of environmental parameters essential for the biota thereby coupling the ocean atmospheric system. An area is influenced by different water masses with varying spatial extent. The analysis shows the presence of four water masses in the study area. These are Arabian Sea Water Mass (ASWM), Persian Gulf Water Mass (PGWM), Red Sea Water Mass (RSWM) and Bay of Bengal Water Mass (BBWM). The criterion for the properties adopted for the identification of water masses are given in table III. This section deals with the delineation of spatial extent and the associated inter and intra-seasonal variability of the water masses. The volume and area of prominence covered by different water masses during different months are presented in table IV.

The spatial extent of the water masses shows a large variability at different levels. The depth at which the horizontal spread of a water mass is higher, in comparison with that at the other levels, is referred as depth of

prominence. During certain months, for the ASWM and BBWM, the area occupied at surface is the highest. However the surface level is not considered as depth of prominence because this level is in direct contact with the highly dynamic atmosphere that influences the water properties.

Arabian Sea Water Mass

Figure 3.37 shows the area covered by Arabian Sea Water Mass (ASWM). During December, January, February and March, the presence of a water mass is well demarcated till 75 m. With depth, the area covered by water mass decreases in December, January and March while in February there is an irregular pattern. The water mass is present at the head region in the upper levels and with depth it shows equatorward spread. The water mass, in upper 30 m, is present along the central and western region while deeper to 30 m it is seen on eastern side. The highest equatorward extent is seen in central region. The eastward shift with depth is akin to all the months of the winter season. Throughout the season, the lower levels show greater equatorward extent than the levels above. In December, maximum area coverage is seen at 50 m while it is 10 m in January and 50 m in February and March. The volume occupied increases from $243 \times 10^5 \text{ km}^3$ in December to $754 \times 10^5 \text{ km}^3$ in January. With the advance of the season it decreases to $433 \times 10^5 \text{ km}^3$ in February and $396 \times 10^5 \text{ km}^3$ in March.

The spatial extent of ASWM is different in April than in May. During April, the extent of water mass is depicted from 20 to 100 m while in May it is between 30 and 100 m. This indicates the trapping of the ASWM at the subsurface region as the season advances. Further, in April and May the area covered by ASWM is the highest at 75 m. However, in the previous month larger spread is seen at 50 m. This reveals the deepening of the water mass in April and May. The eastward and equatorward extent increases during the transition period in comparison with that during winter season. However, the horizontal spread decreases. The temporal variation shows that the equatorward extent is higher in April than in May. The volume in April ($318 \times 10^5 \text{ km}^3$) is lower than March and it increases to $585 \times 10^5 \text{ km}^3$ in May.

The water mass is present during June, July and August while it is

absent in September. The area occupied by the water mass is between 30 and 100 m in June, 50 and 75 m in July and between 30 and 75 m in August. Vertical analysis of the horizontal extent reveals that the maximum horizontal extent of water mass is at 50 m in June and August while it is at 75 m in July. In comparison to the earlier months, the water mass shows eastward shift. While examining the area covered at different levels during summer, it is evident that the equatorward extent is highest at 75 m and occurs in July. As the spatial extent varies within the summer season, the volume occupied shows decrease from the transition period to July ($106 \cdot 10^5 \text{ km}^3$). However from July to August there is an increase in volume.

An Interesting feature is the depiction of water with properties of ASWM in October and the absence in September. The waters seen during October are not at the head region instead, it is present at the eastern boundary at 50 m and between 12° and 16° N along the 68° E at 75 m. In November the waters with properties of ASWM is evident at 30 and 50 m. At 30 m it is present at northwestern region while at 50 m it is at the eastern region. The depth of prominence is 75 m in November and 50 m in October.

Bay of Bengal Water Mass

The spatial distribution of BBWM is given in Fig. 3.37. The monthly analysis shows that BBWM is present only From November to April. A weak signal of BBWM is evident at southeastern region extending to 30 m in winter while in April it is seen only at 30m. The water mass spreads poleward from the southeastern region with decreasing spread with depth and it restricts along the coast. Temporal analysis shows that the poleward extent is up to 15° N, during January and February. The westward extent of the water is highest at 10 m and occurs in February and March. The depth of prominence is 10 m from December to March and in April it is 30 m. The area occupied at the level of prominence increases from $249 \cdot 10^3 \text{ km}^2$ in December to $506 \cdot 10^3 \text{ km}^2$ in March while in April it reduces drastically to $95 \cdot 10^3 \text{ km}^2$. The volume occupied by the water mass increase from $40 \cdot 10^5 \text{ km}^3$ in November to $165 \cdot 10^5 \text{ km}^3$ in January while it decrease to $22 \cdot 10^5 \text{ km}^3$ in April.

Persian Gulf Water Mass

The spatial and the associated intra-seasonal variability of PGWM are given in figure 3.38. It clearly shows the presence of the water mass between 150 and 300 m in December and 200 to 300 m in January, February and March. The area occupied at 150 m in January is negligible. Further examination reveals that the spreading is in southwest direction. In December and January the maximum area occupied by the water mass is at 250 m while in February and March it is at 300 m. The PGWM is seen between 200 and 300 m with prominence at 300 m and 250 m in April and May. The spread of PGWM is more towards the western region.

During summer, the vertical extent of the PGWM is between 150 and 300 m in June, 150 and 250 m in July, 125 to 250 m in August and from 125 to 250 m in September respectively. During winter the water mass is seen along western boundary while in summer it is present at the head region. This shows a transient nature in the spread of PGWM. A decrease in equatorward extent is clear with depth as the season advances. Also, associated with the progress of the season there is an upward lifting of PGWM. In June the water mass is more prominent at 300 m while in July to September it is predominant at 150 m. The horizontal extent is higher in June than rest of the months of the season.

The PGWM is seen to be extending from 200 to 250 m in October while in November it is between 150 and 300 m. The PGWM is more predominant at 250 m both in October and November. The water mass is confined to the western boundary. The area occupied by the water mass is more during these months compared to the earlier months. The equatorward extent and the spread are higher in November than in October. The water mass occupies highest volume in winter (January) and lowest in the summer season (June).

The variability of the area occupied by the RSWM along the different months is given in the Fig. 3.39. The monthly analysis reveals that RSWM is present between 600 and 900 m. Further the inter and intraseasonal variability do not show any significant spatial variability in the area covered by

RSWM. Hence, the figure corresponding to June alone is presented. The RSWM covers larger area of the Arabian Sea compared to the area covered by other water masses.

Red Sea Water Mass

The spatial extent of the RSWM is shown in fig. 3.39. The horizontal extent of the water mass is maximum at 700 m in December, February and March while it is at 800 m in January. The area occupied by RSWM shows that it is more predominant at 800 m from April to September and it spreads northward. At the mouth of the Red Sea the water mass is also seen at a depth of 900 m. In October and November maximum spread is at 700 m. Hence, from this it is clear that RSWM is prominent between 700 and 800 m.

The temperature and salinity decreases towards equator. Hence, the northern region of the study area is expected to have lower density than the equatorward region. Therefore the RSWM spreads northward along the western boundary and not towards the equator.

Table IV. Area at Depth of prominence of the water masses and total volume.

Water mass	ASWM			BBWM			PGWM			RSWM		
	Prominent			Prominent			Prominent			Prominent		
	Month	Depth (m)	Area 10^3 km^2	volume 10^5 km^3	Depth (m)	Area 10^3 km^2	volume 10^5 km^3	Depth (m)	Area 10^3 km^2	volume 10^5 km^3	Depth (m)	Area 10^3 km^2
Dec	50	411	234	10	249	74	250	308	487	700	212	4650
Jan	10	1022	754	10	437	165	250	461	612	800	179	4404
Feb	50	624	433	10	460	157	300	379	448	700	174	4261
Mar	50	587	395	10	506	145	300	379	514	700	220	5316
Apr	75	648	318	30	95	22	300	331	444	800	209	5077
May	75	587	334	-	-	-	250	320	497	700	183	4503
Jun	50	435	210	-	-	-	300	355	585	800	178	4421
Jul	75	247	106	-	-	-	150	213	198	800	203	4473
Aug	50	342	190	-	-	-	150	332	466	800	201	4692
Sep	-	-	-	-	-	-	150	153	210	800	183	3984
Oct	75	116	65	-	-	-	250	202	228	700	207	5255
Nov	50	152	49	10	178	40	250	366	525	700	211	4721

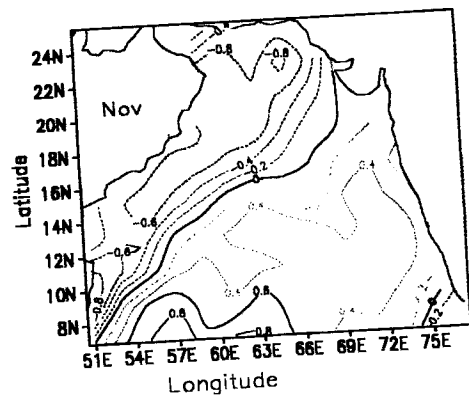
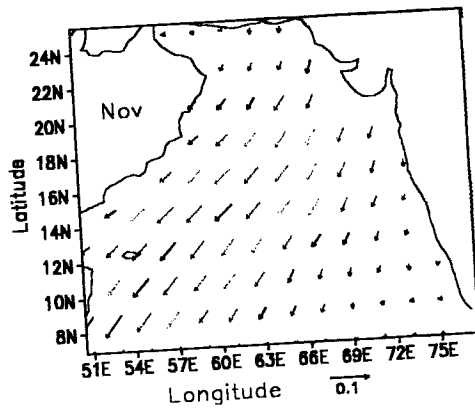
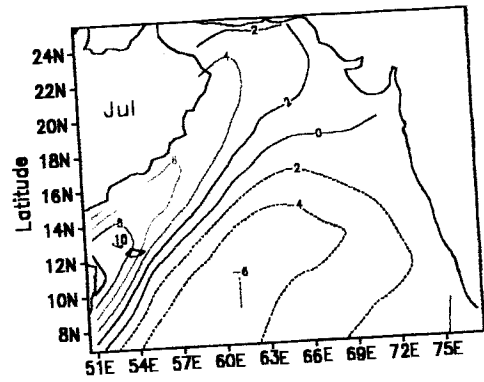
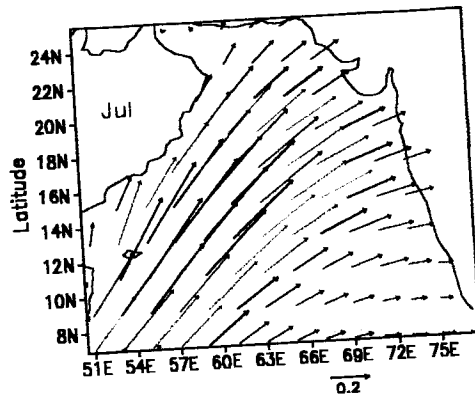
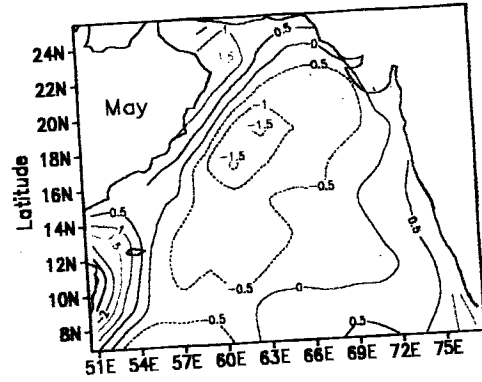
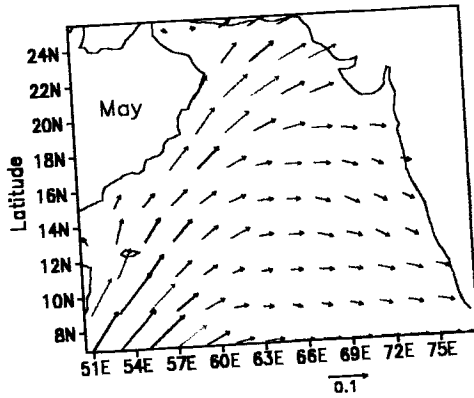
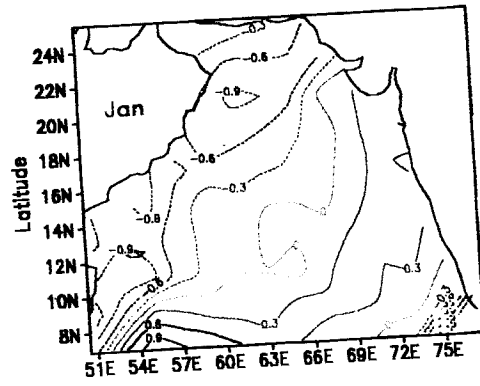
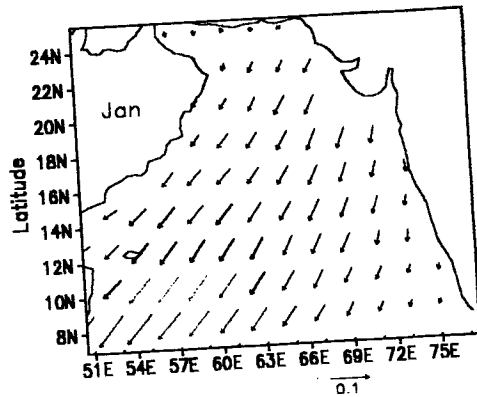


Fig.3.1 Wind stress (N/m^2) and curl of stress ($10^{-7} N/m^3$)

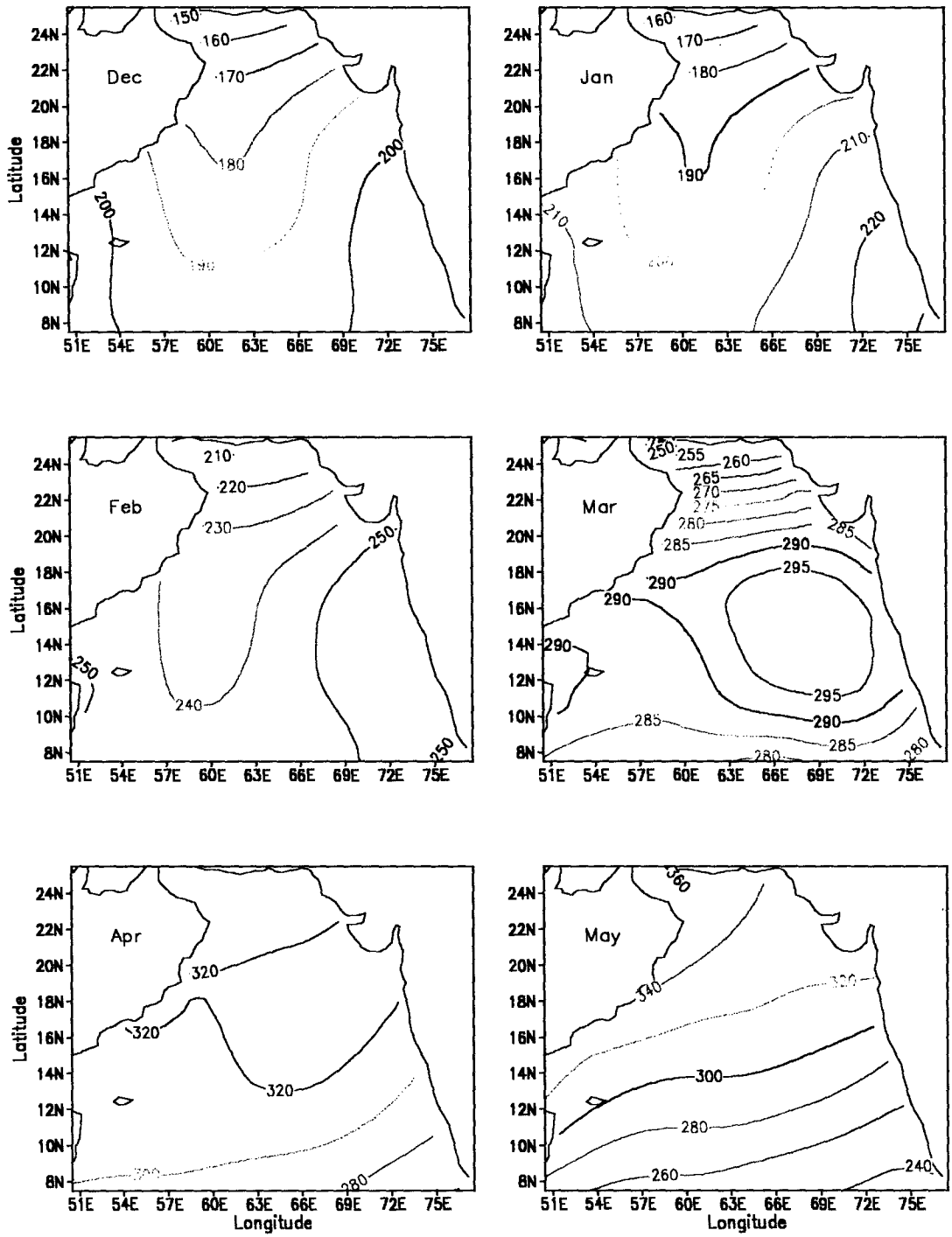


Fig. 3.2 Flux of Short Wave Radiations (W/m^2)

Contd...

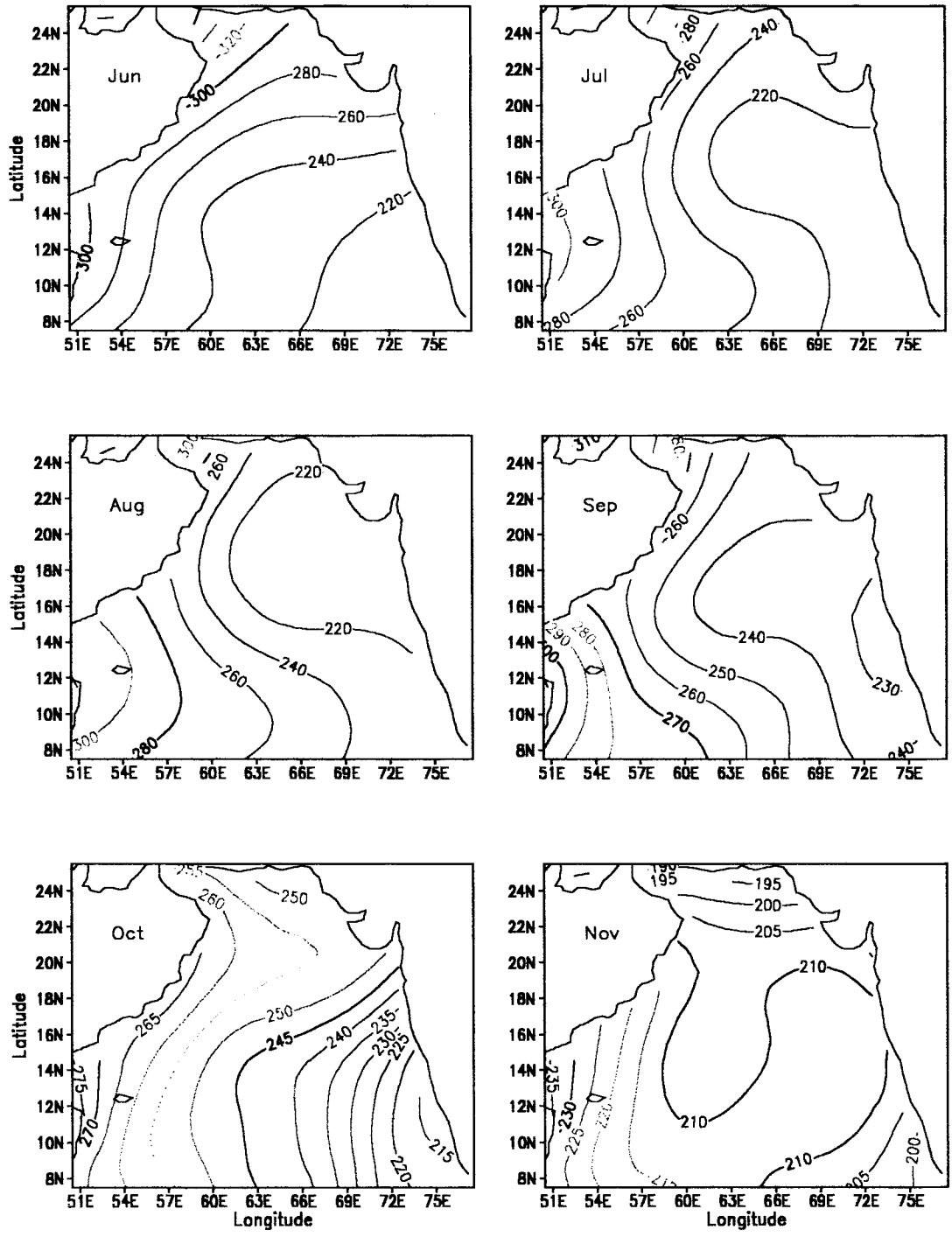


Fig. 3.2 Flux of Short Wave Radiations (W/m^2)

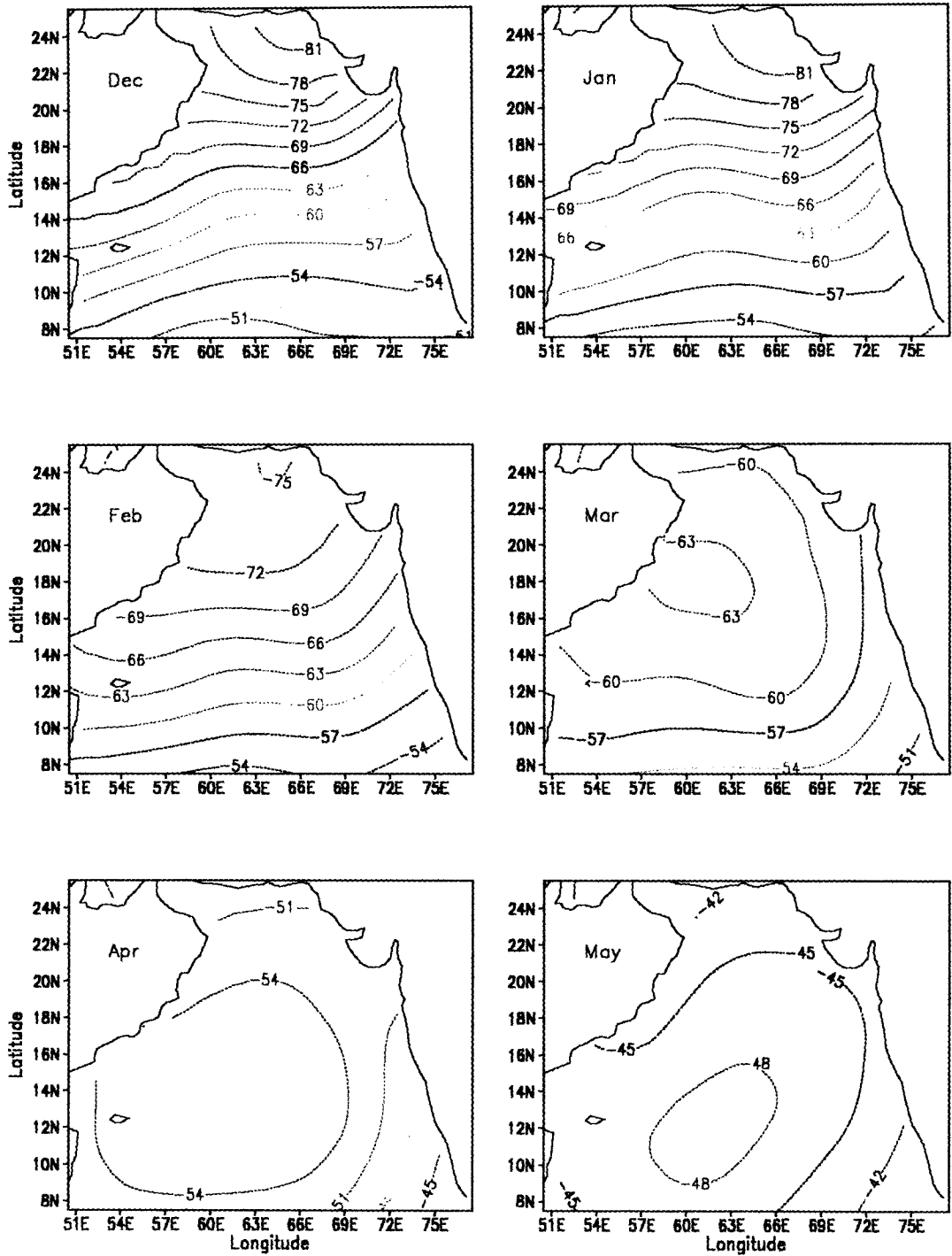


Fig. 3.3 Flux of Long Wave Radiations (W/m^2)

Contd...

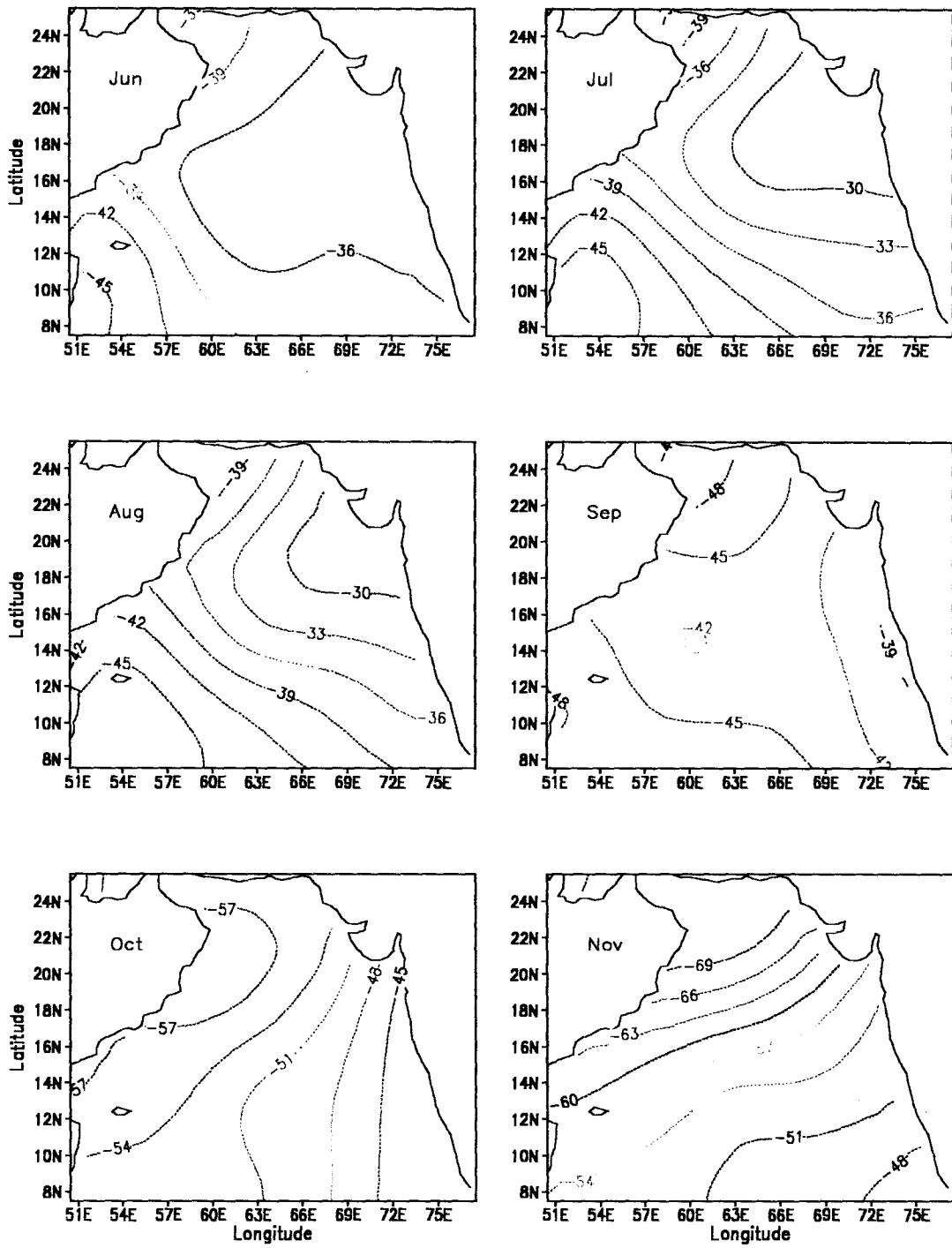


Fig. 3.3 Flux of Long Wave Radiations (W/m^2)

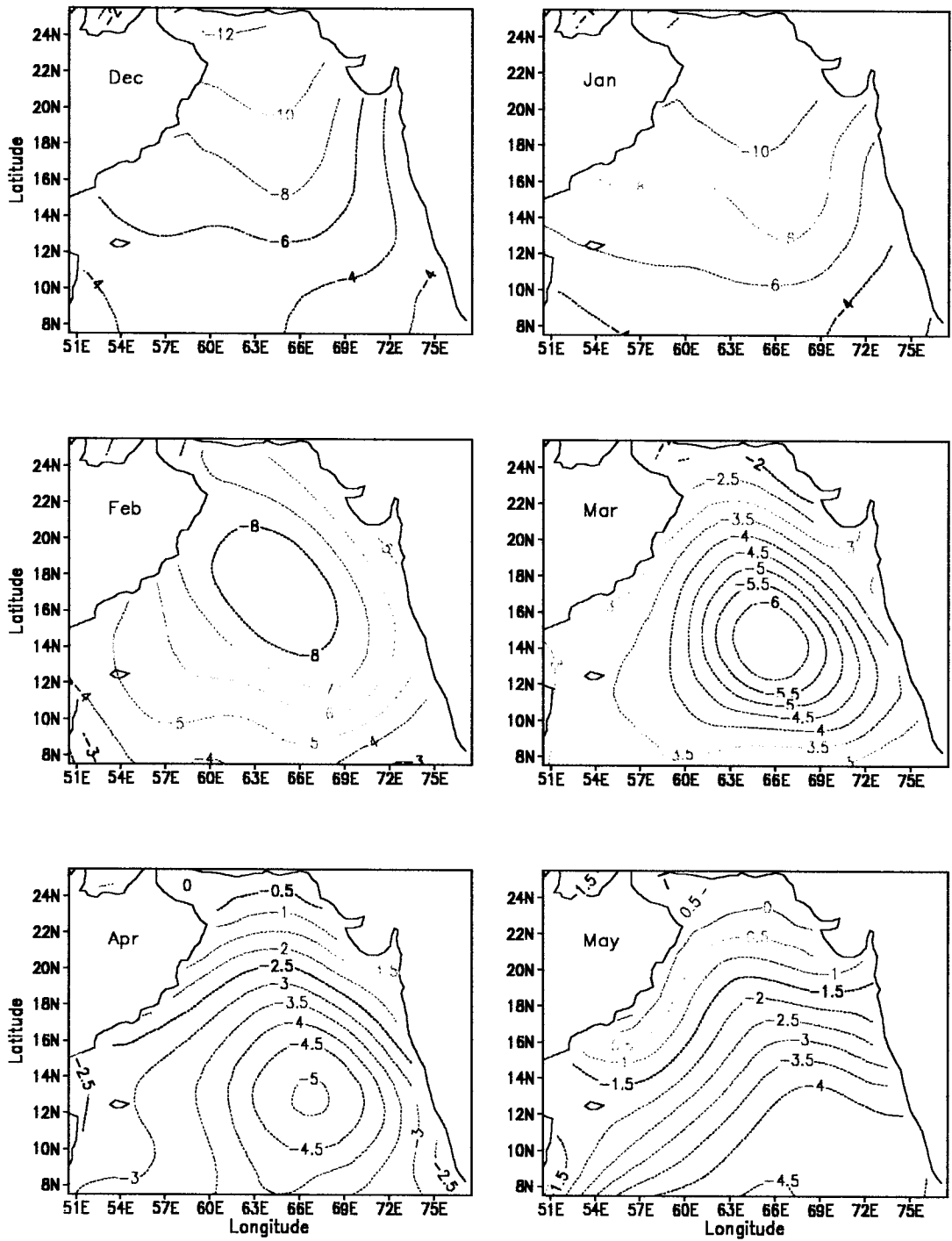


Fig. 3.4 Sensible Heat Flux (W/m²)

Contd...

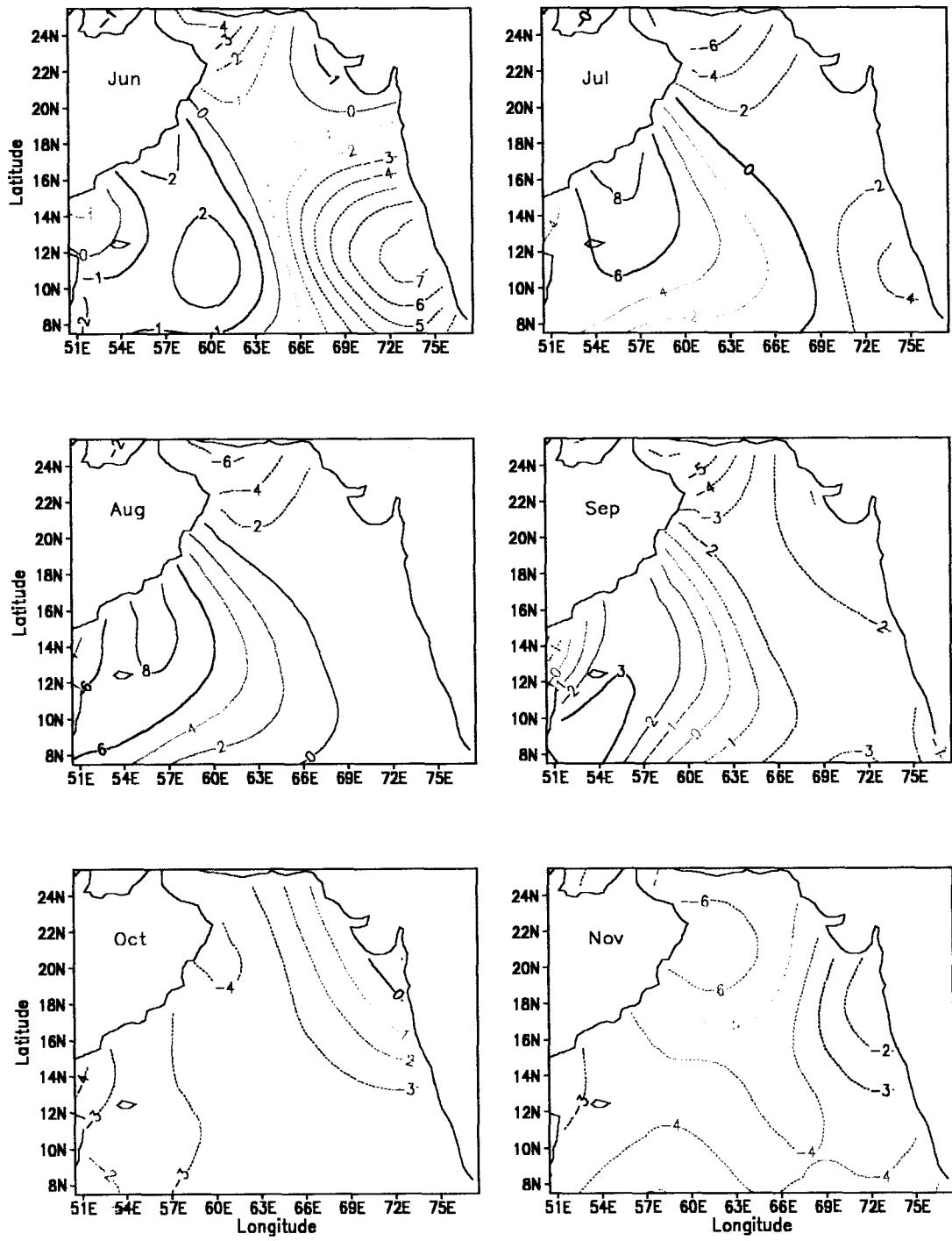


Fig. 3.4 Sensible Heat Flux (W/m^2)

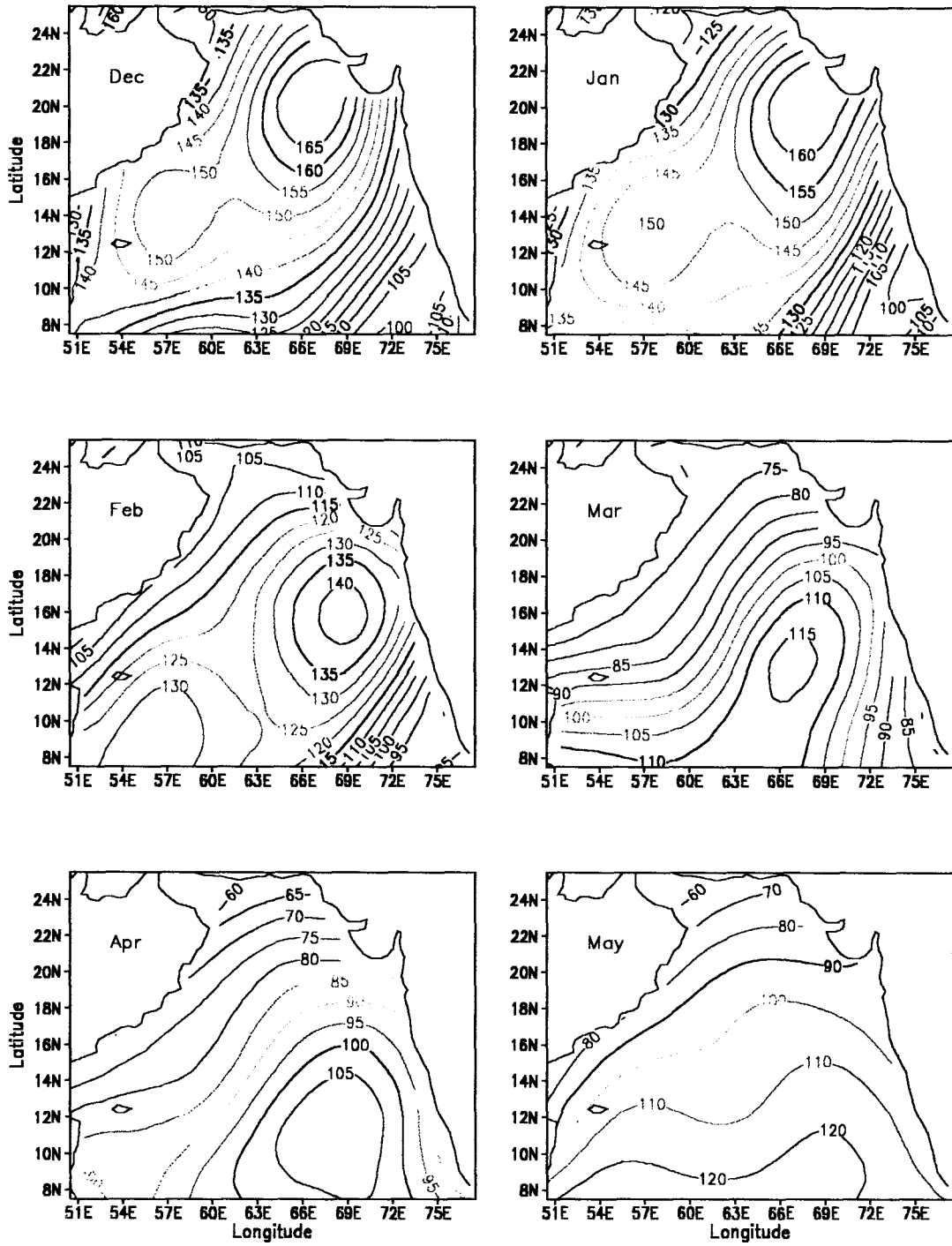


Fig. 3.5 Latent Heat Flux (W/m^2)

Contd...

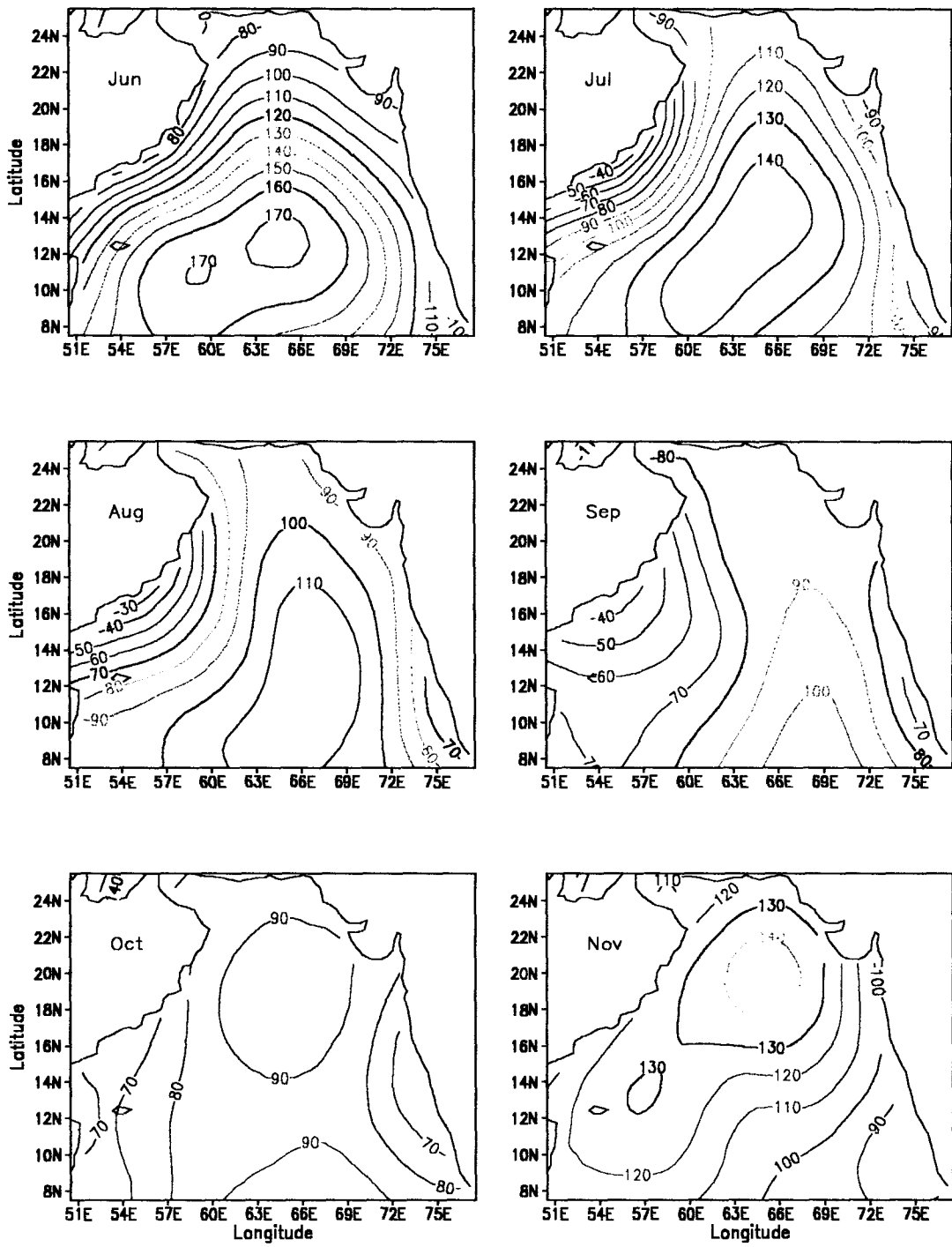


Fig. 3.5 Latent Heat Flux (W/m^2)

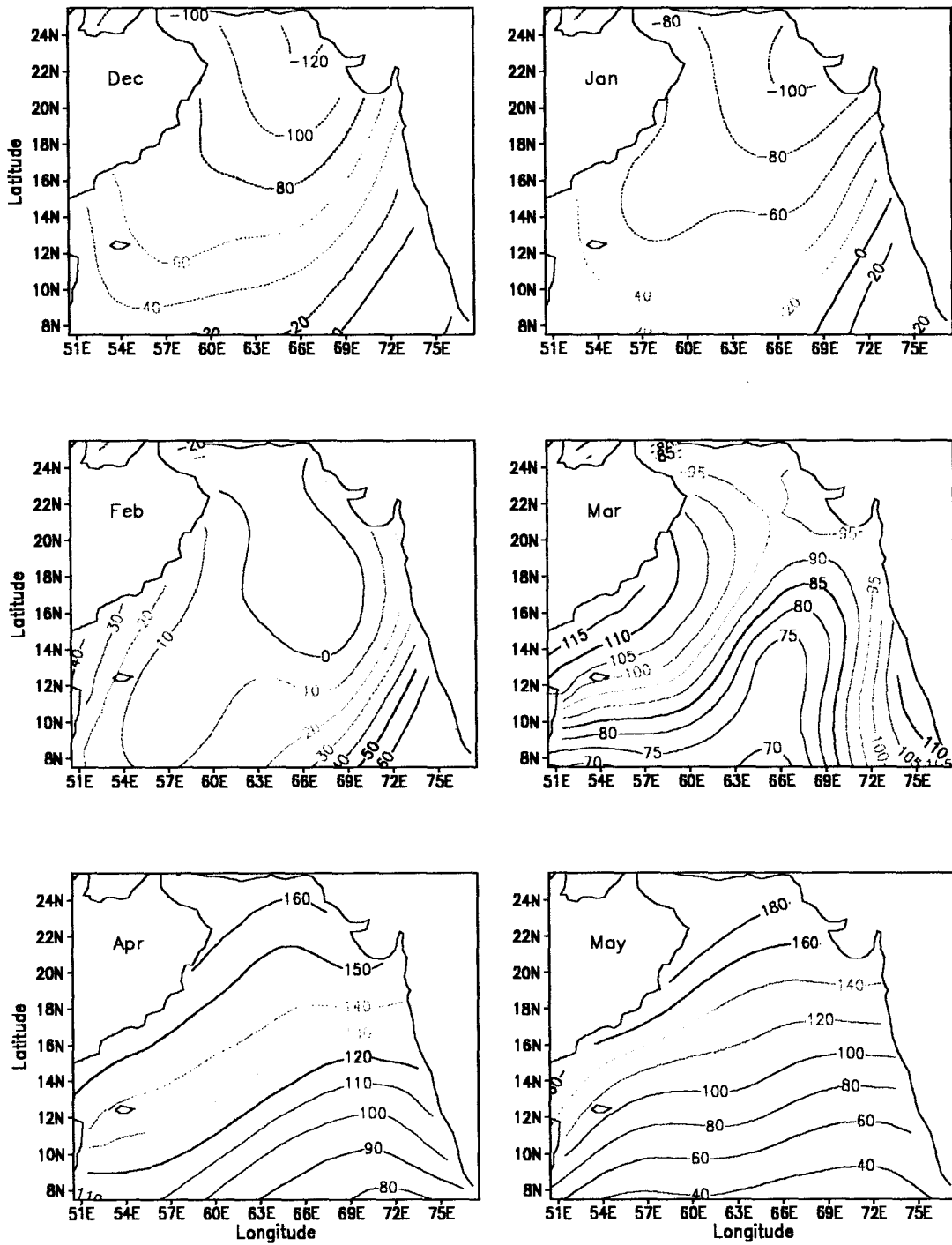


Fig. 3.6 Net Heat Flux (W/m^2)

Contd...

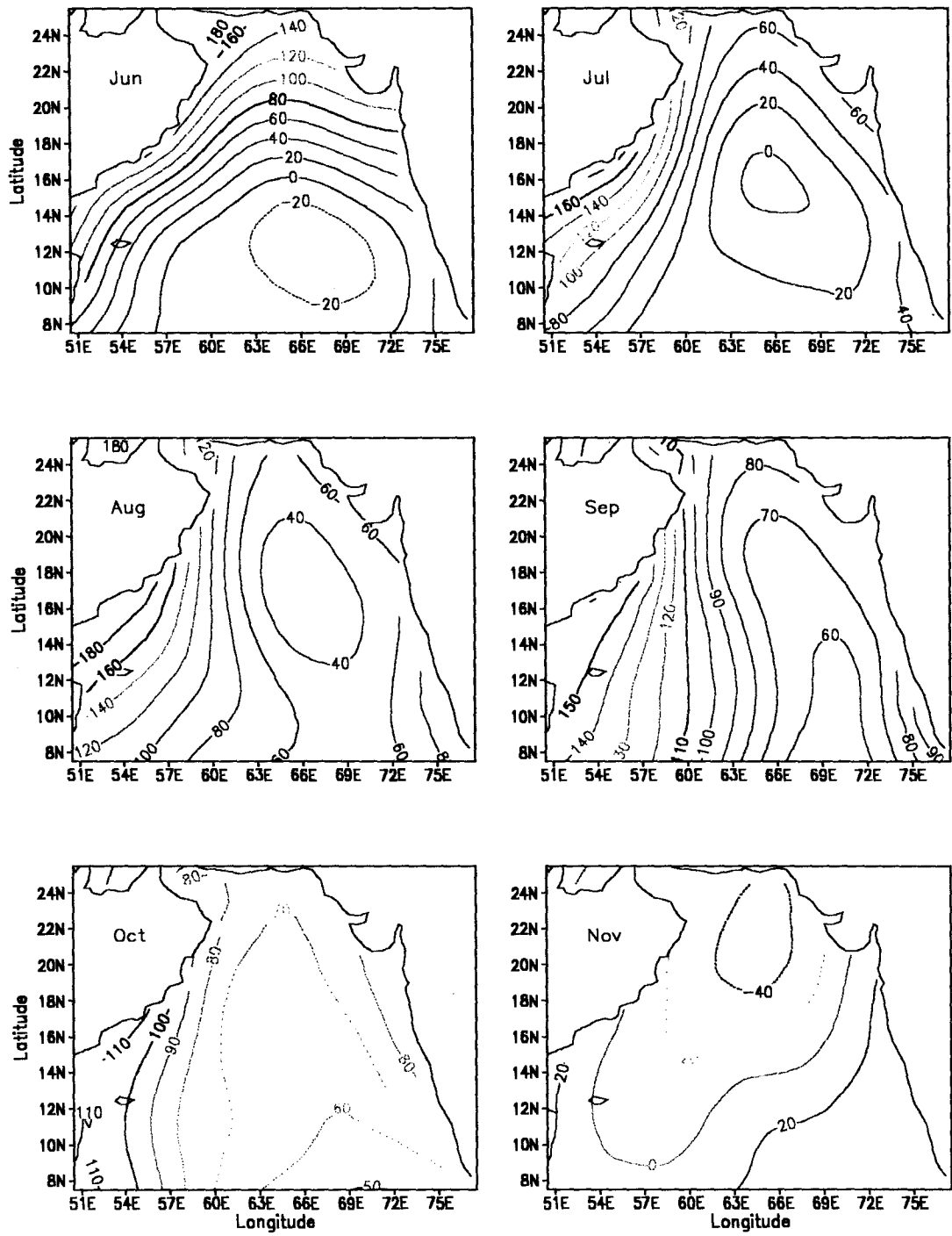


Fig. 3.6 Net Heat Flux (W/m^2)

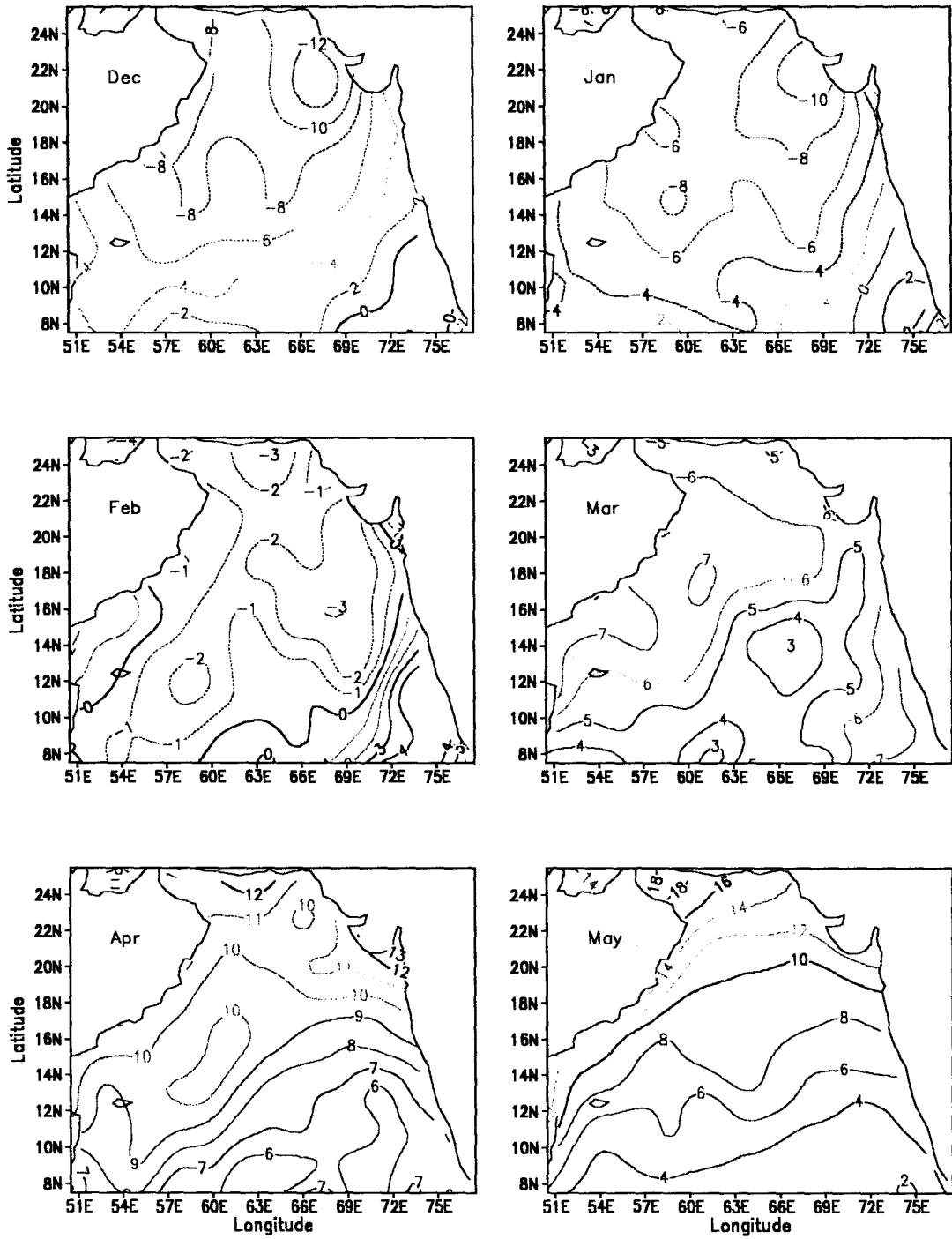


Fig 3.7 Buoyancy Flux (kg/(ms³))

Contd...

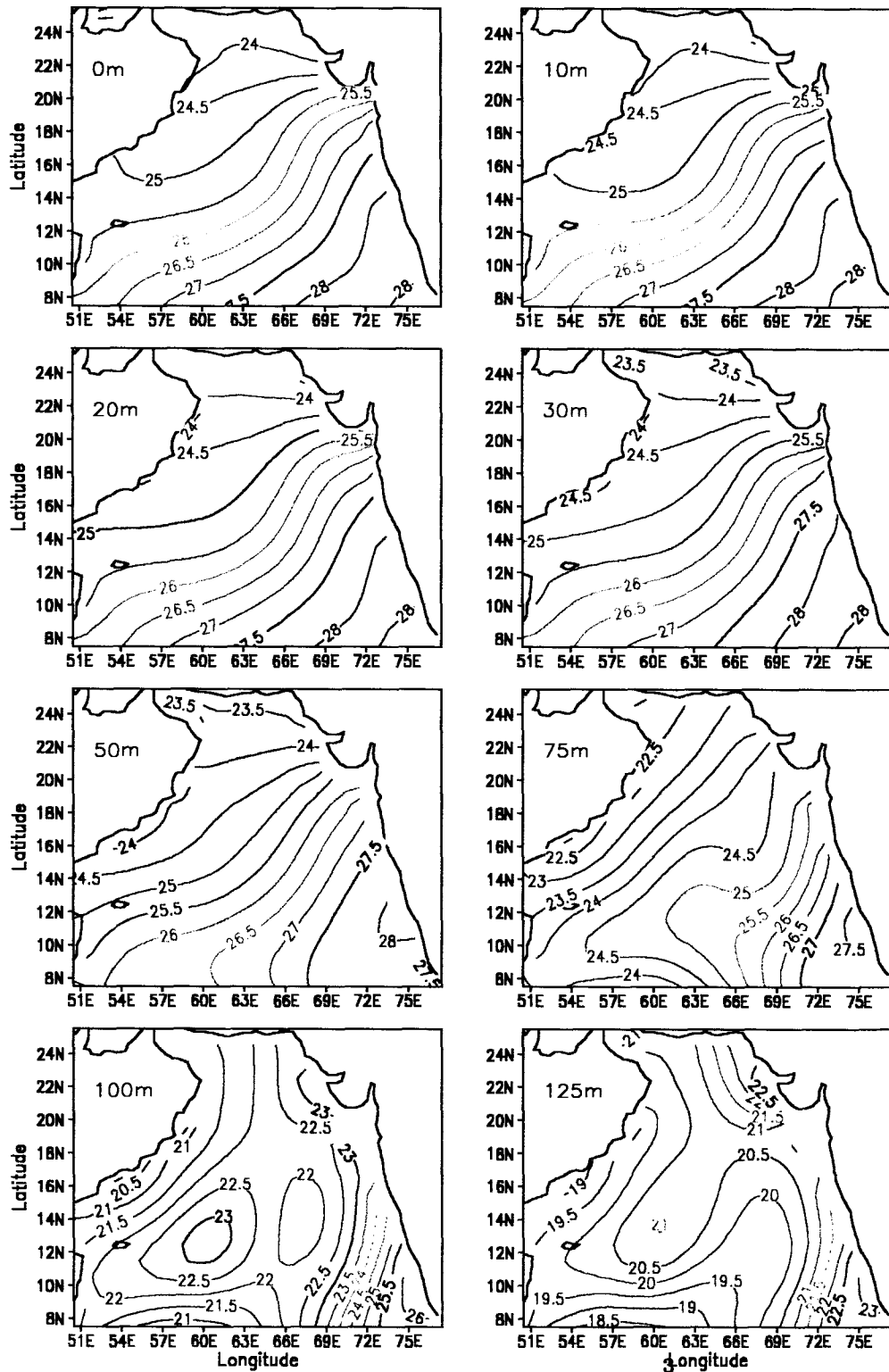


Fig. 3.9 Horizontal Temperature distribution at different depths during January

Contd...

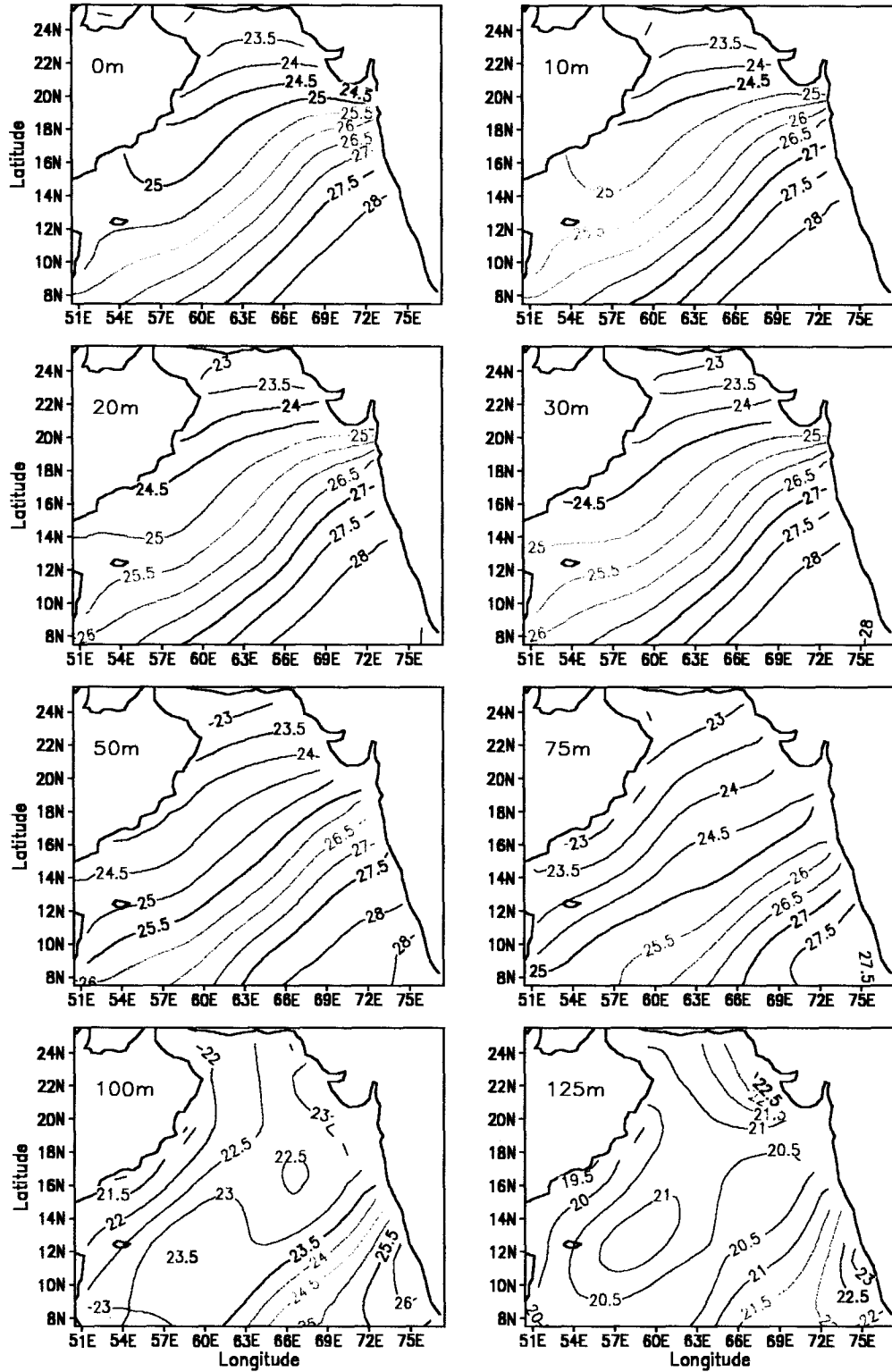


Fig. 3.10 Horizontal Temperature distribution at different depths during February

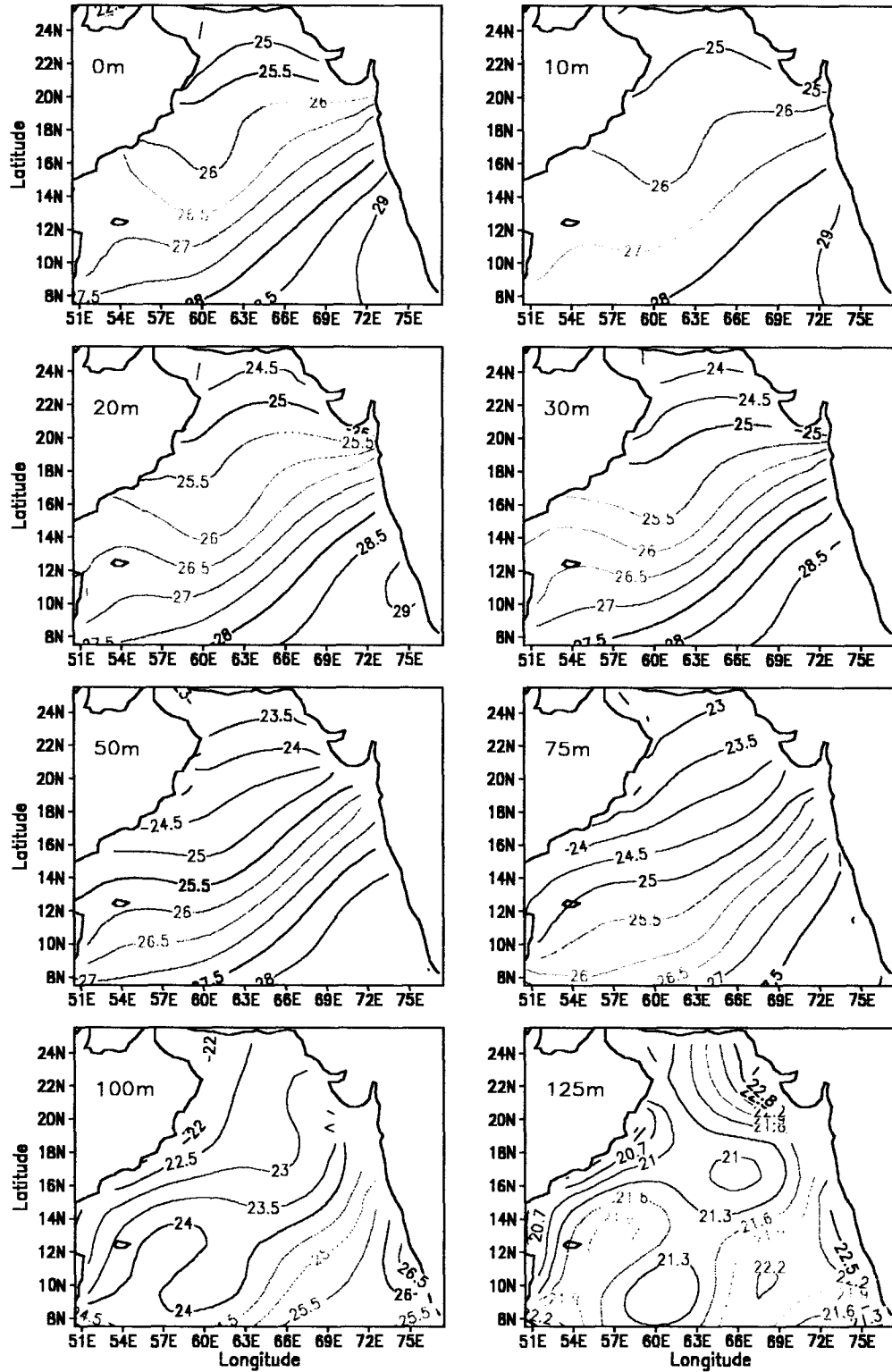


Fig. 3.11 Horizontal Temperature distribution at different depths during March

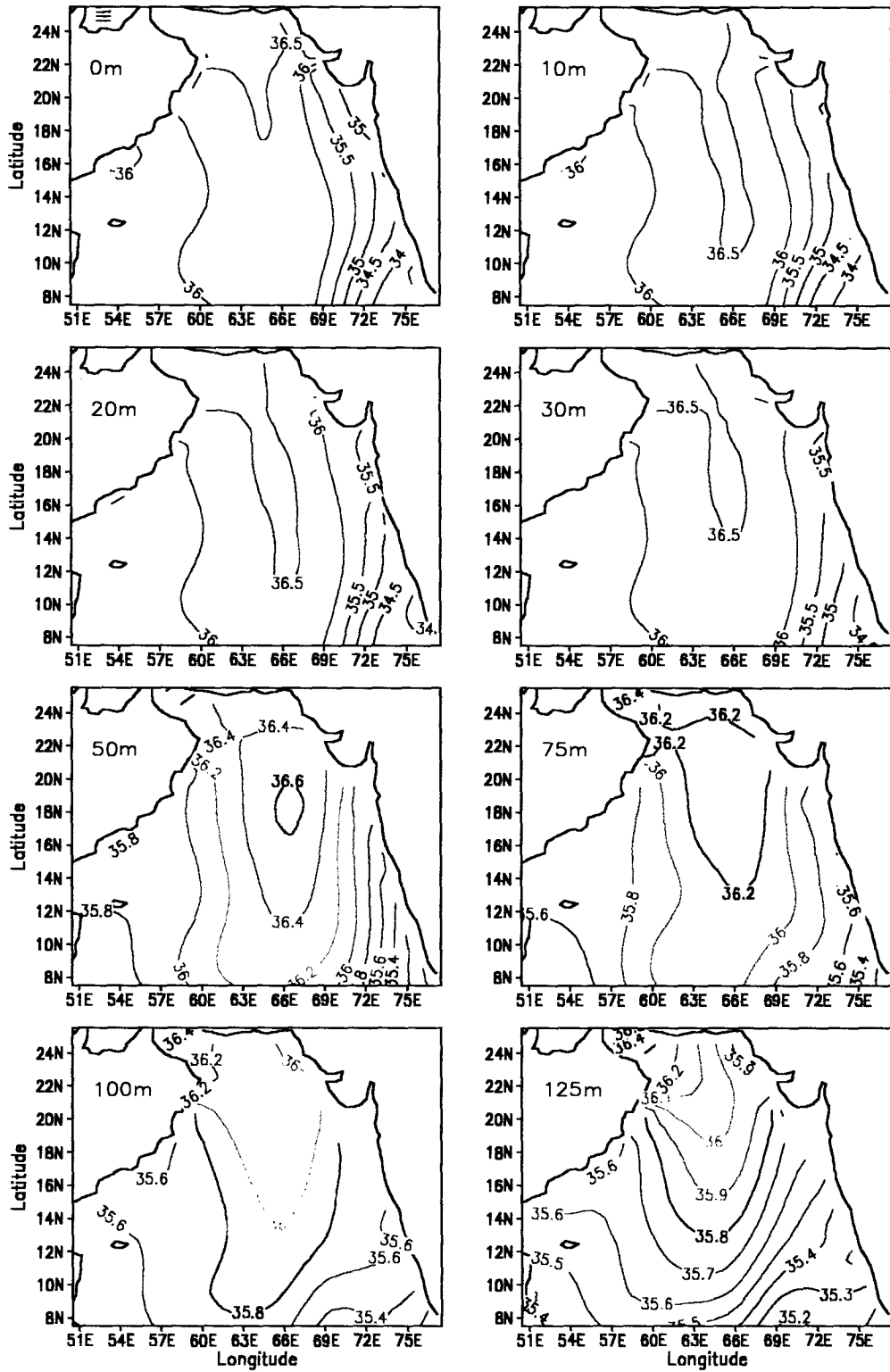


Fig. 3.12 Horizontal salinity distribution at different depths during December

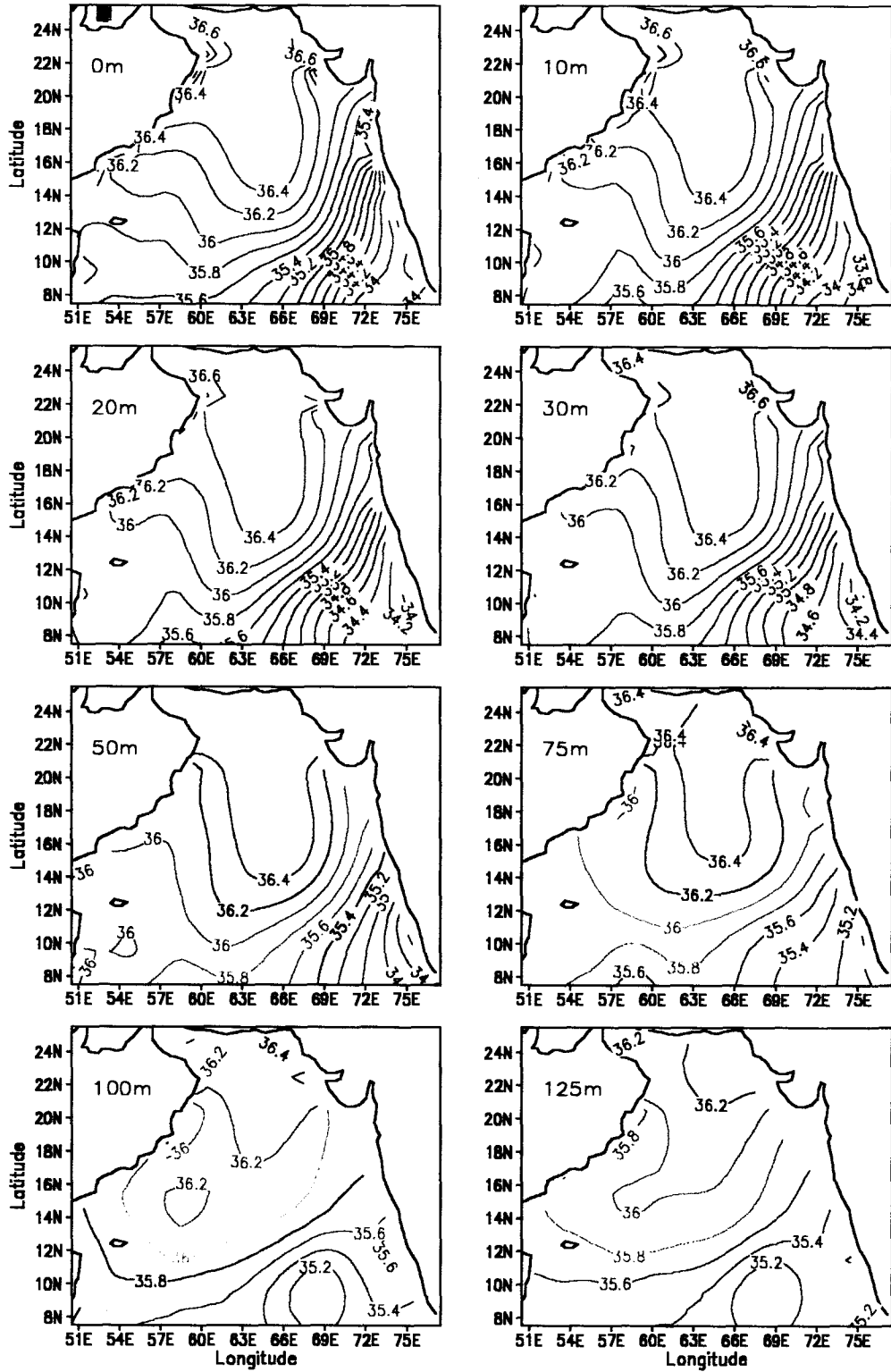


Fig. 3.13 Horizontal Salinity distribution at different depths during January

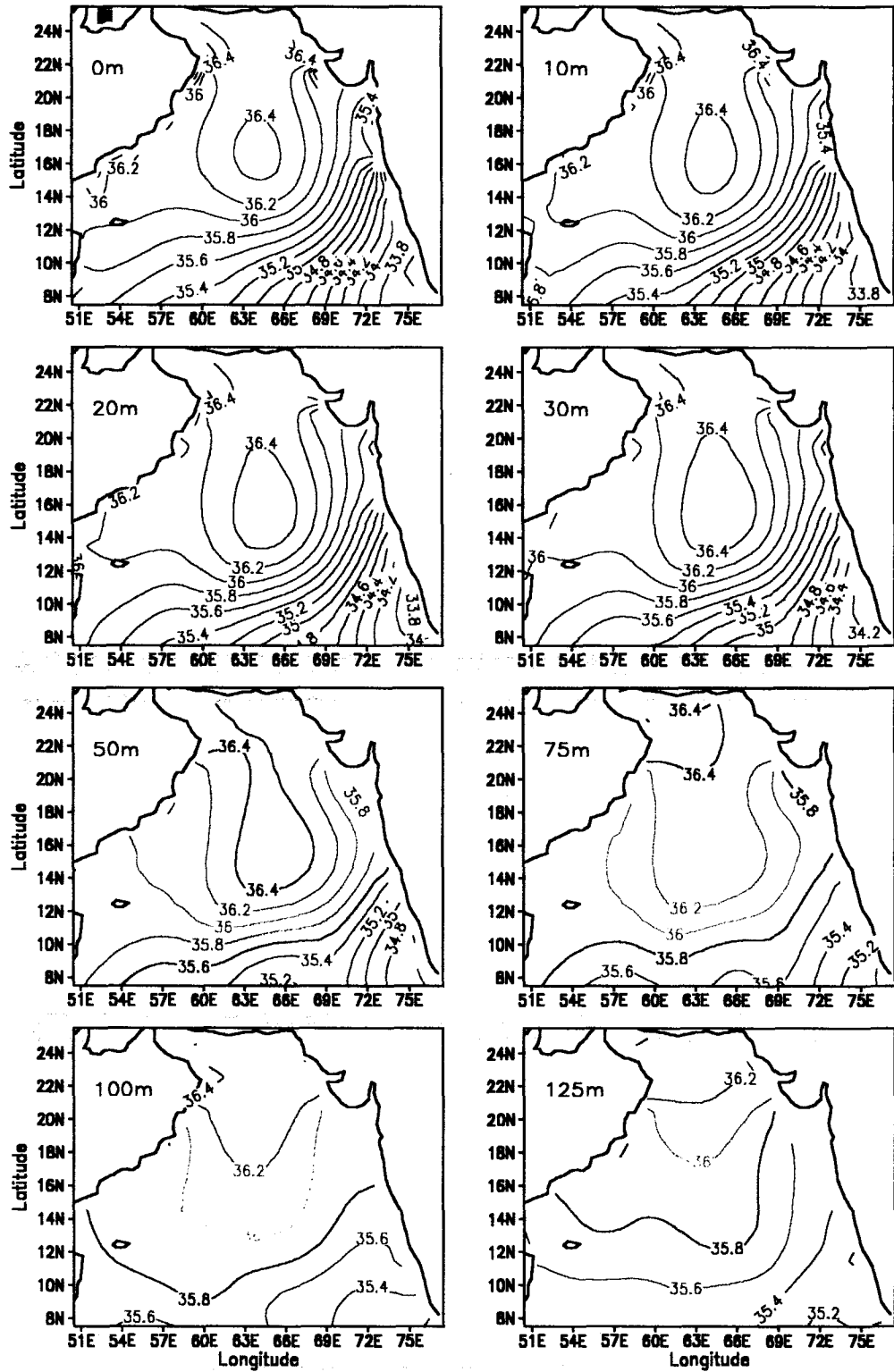


Fig. 3.14 Horizontal Salinity distribution at different depths during February

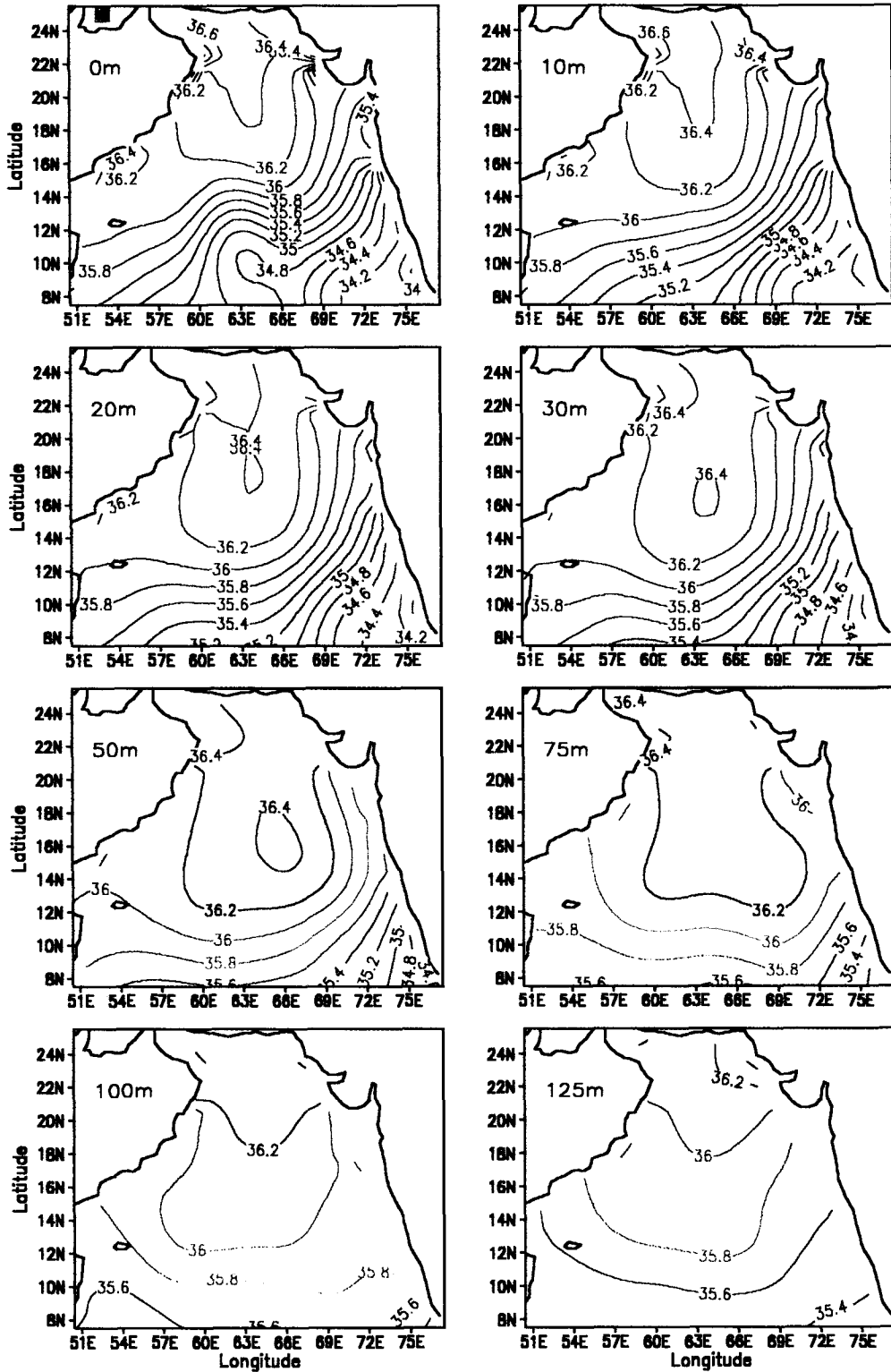


Fig. 3.15 Horizontal Salinity distribution at different depths during March

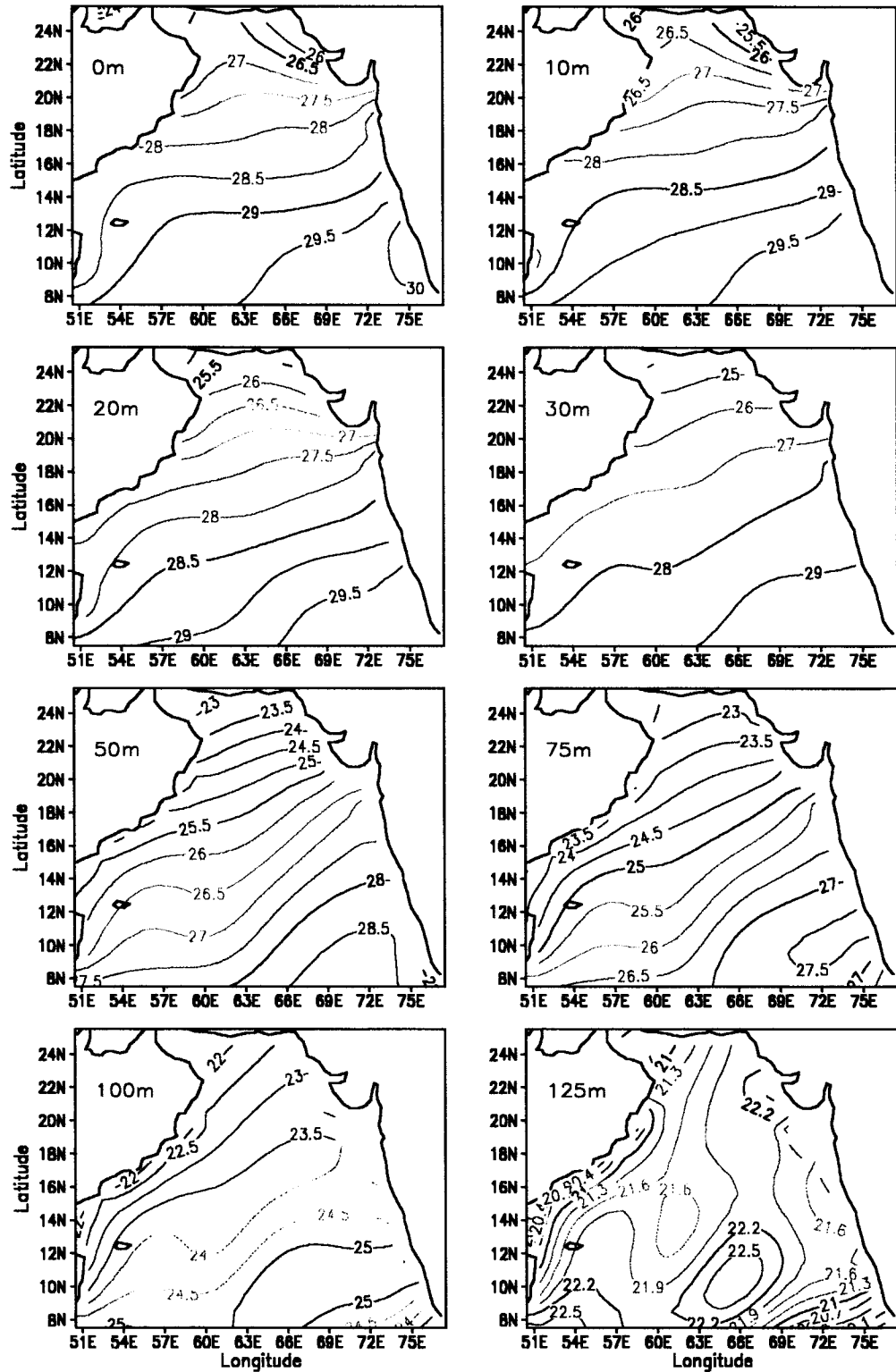


Fig. 3.16 Horizontal Temperature distribution at different depths during April

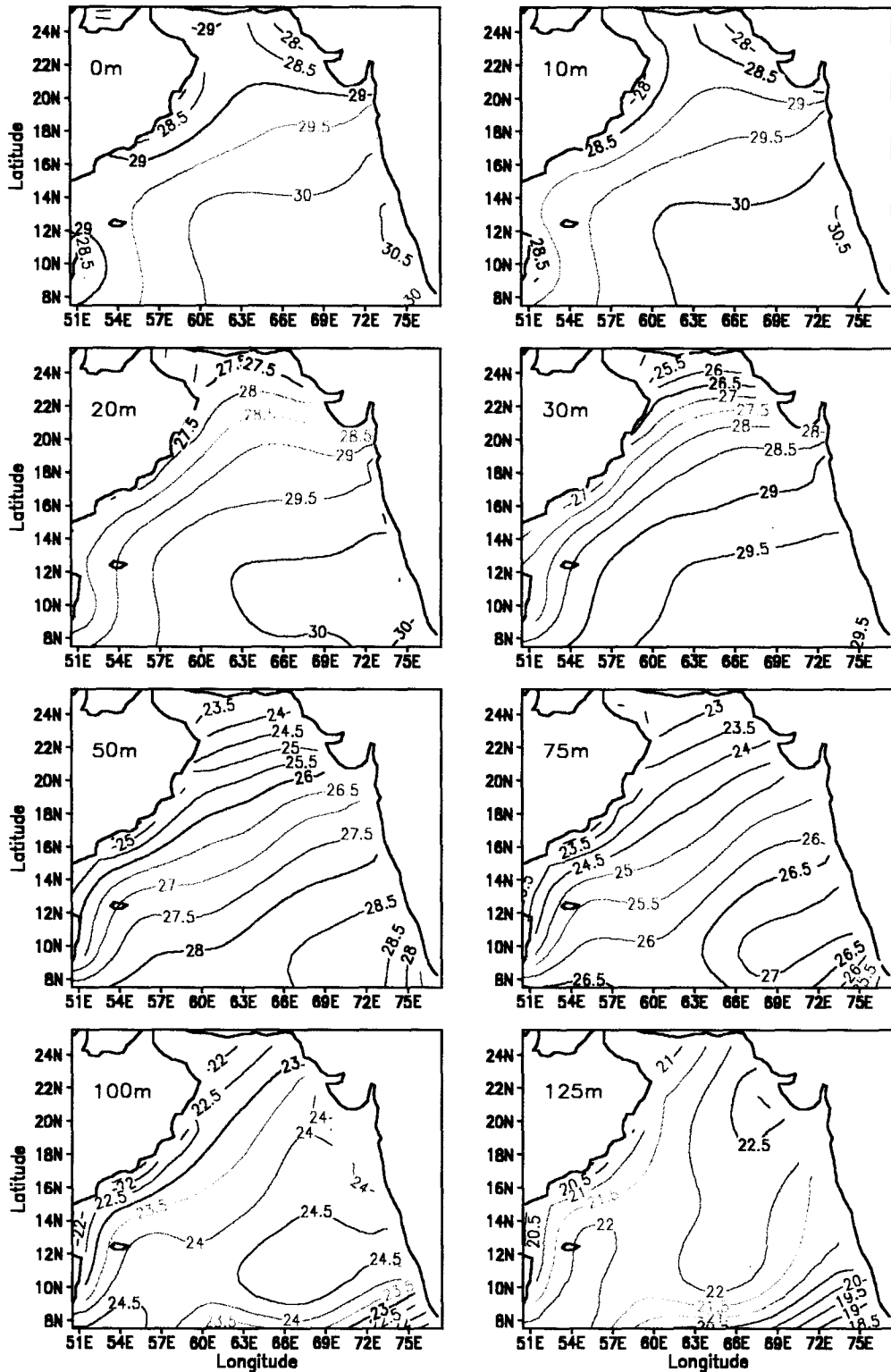


Fig. 3.17 Horizontal Temperature distribution at different depths during May

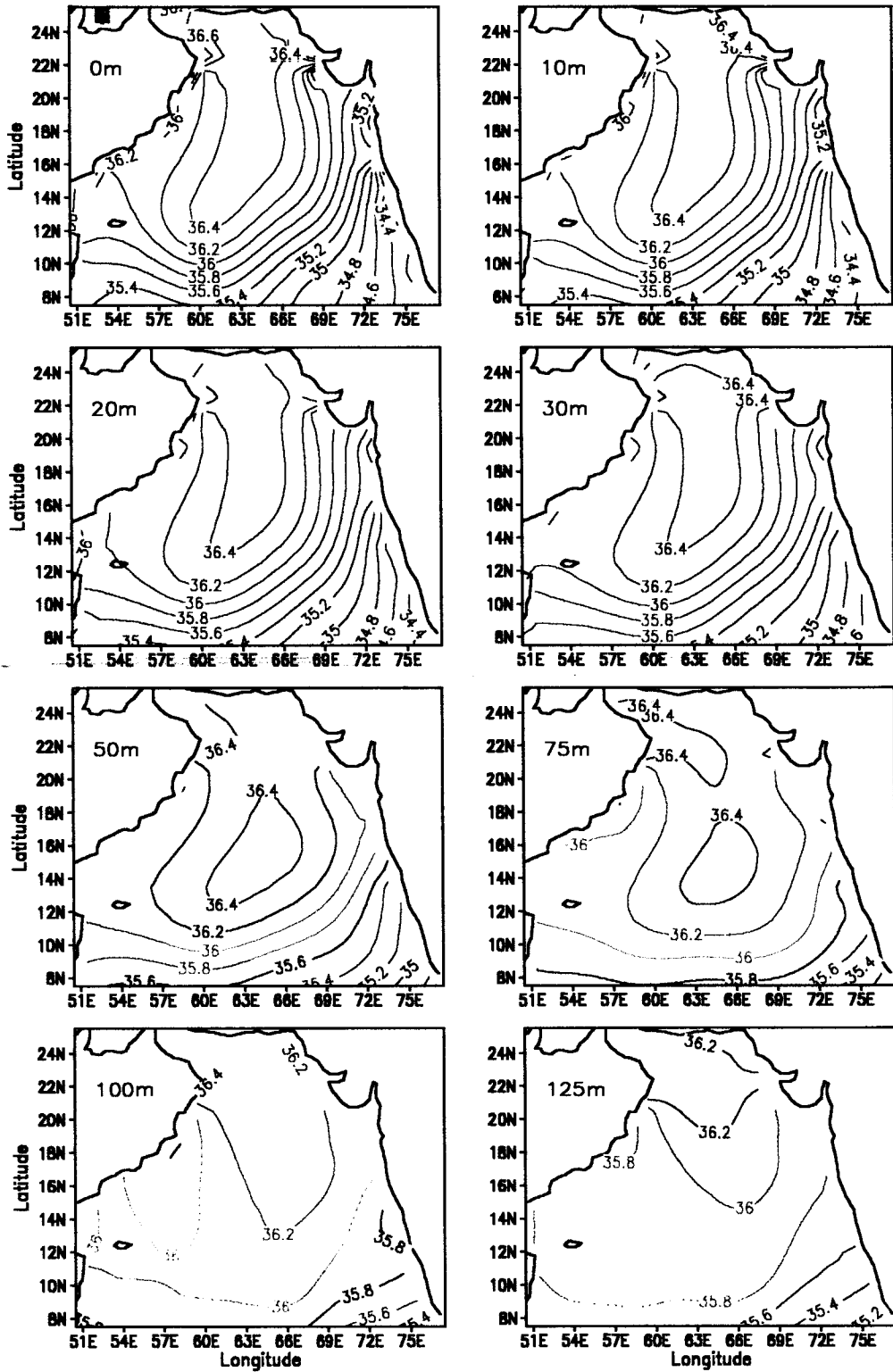


Fig. 3.18 Horizontal Salinity distribution at different depths during April

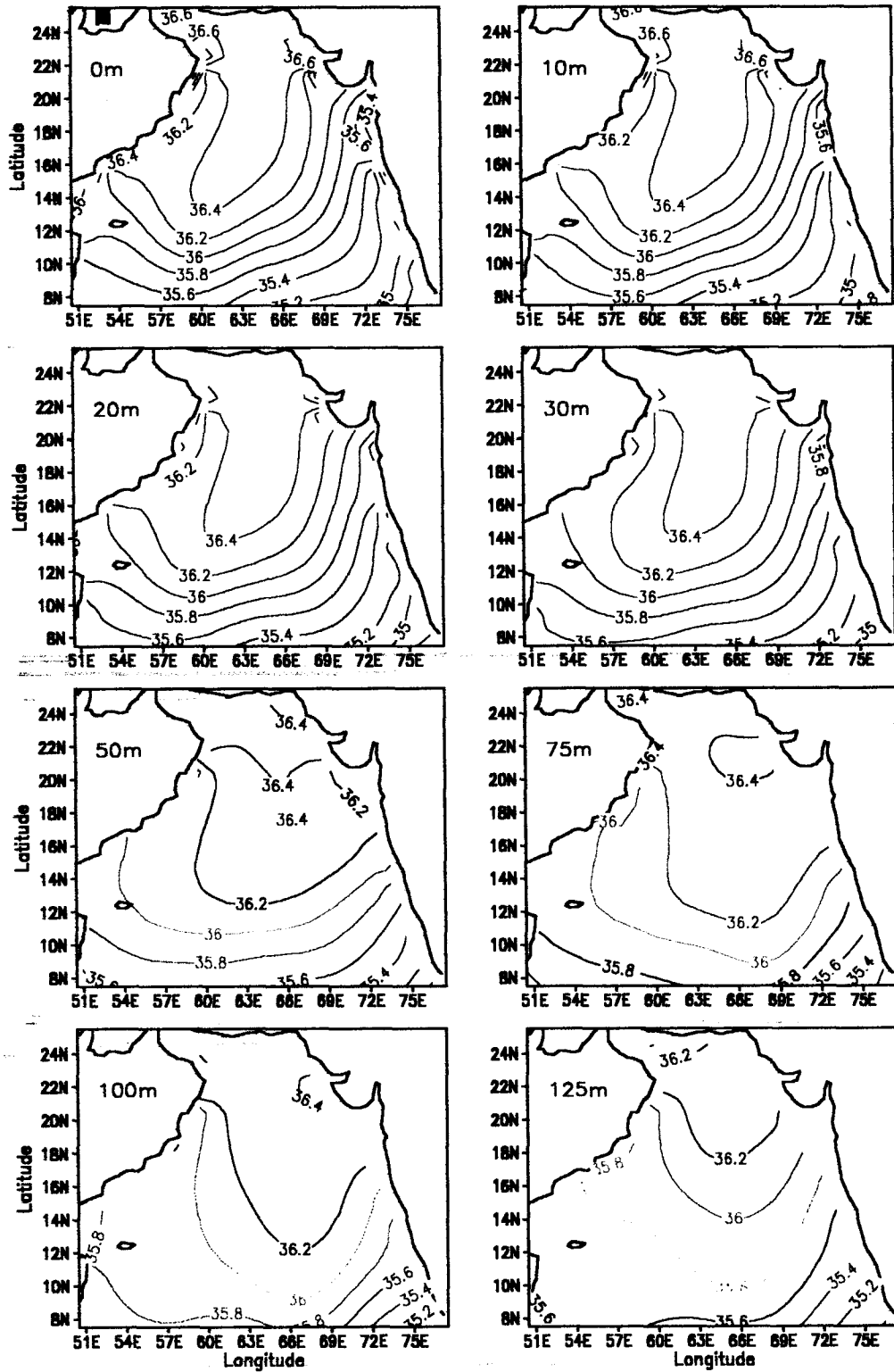


Fig. 3.19 Horizontal Salinity distribution at different depths during May

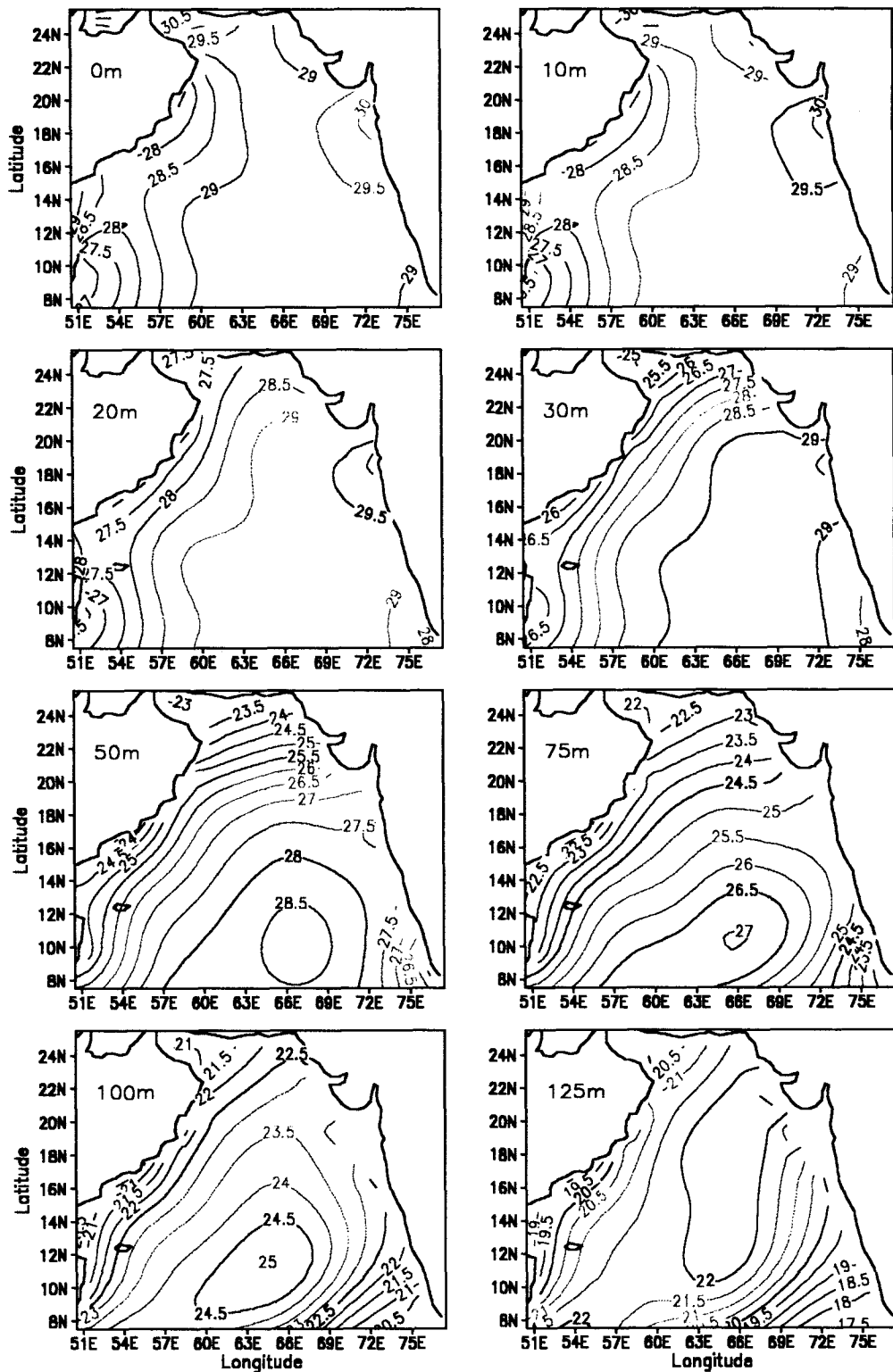


Fig. 3.20 Horizontal Temperature distribution at different depths during June

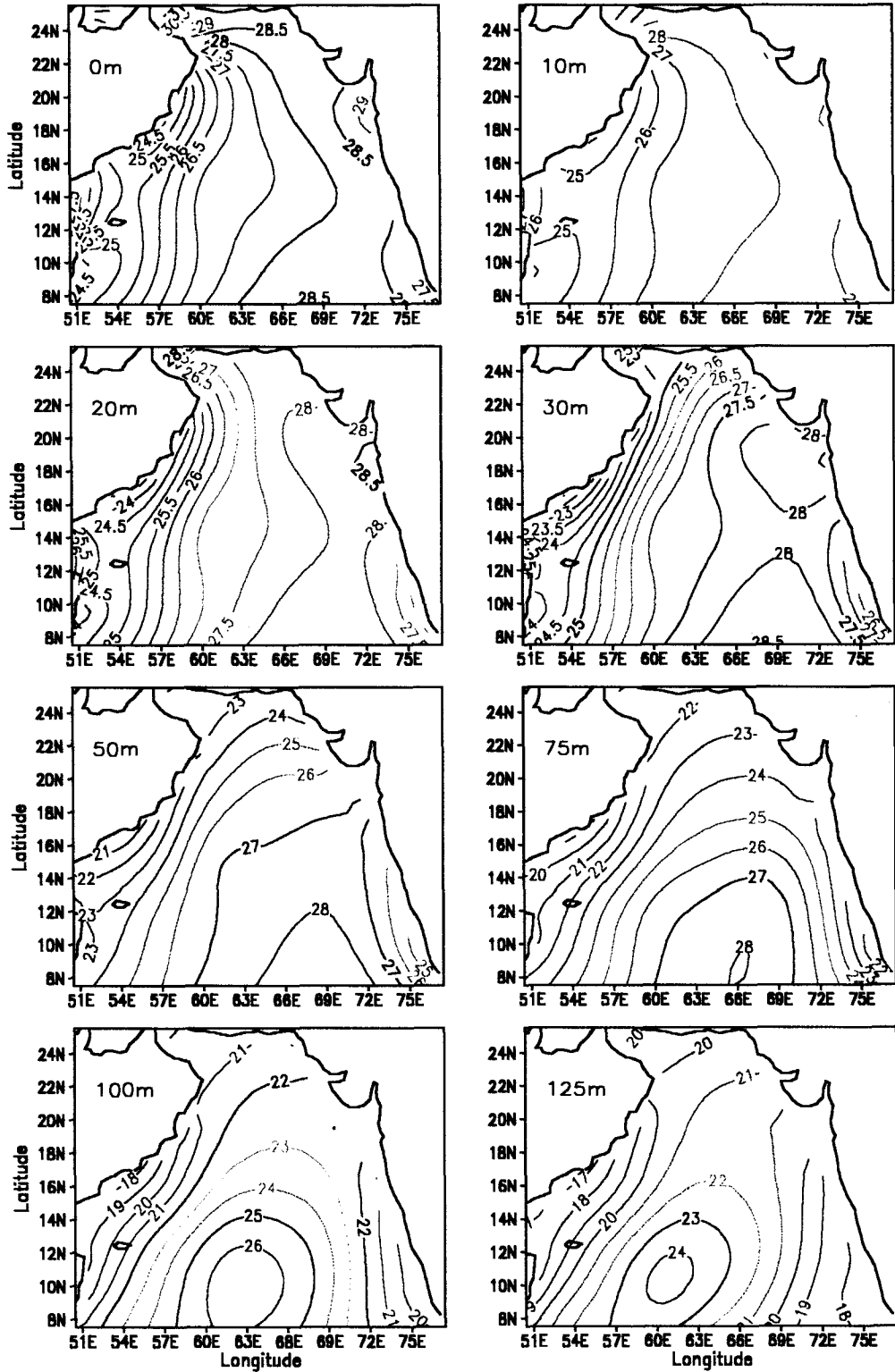


Fig. 3.21 Horizontal Temperature distribution at different depths during July

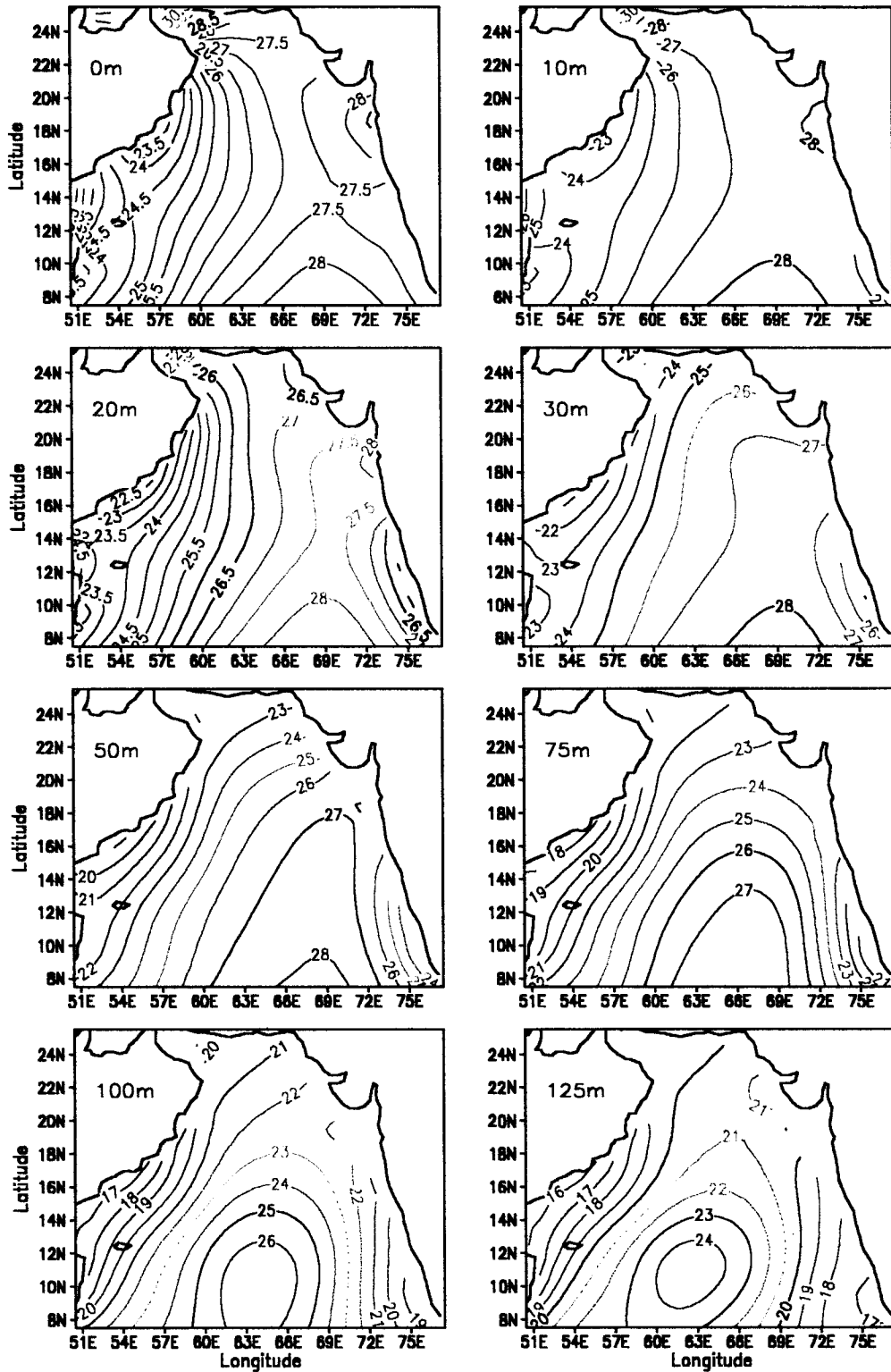


Fig. 3.22 Horizontal Temperature distribution at different depths during August

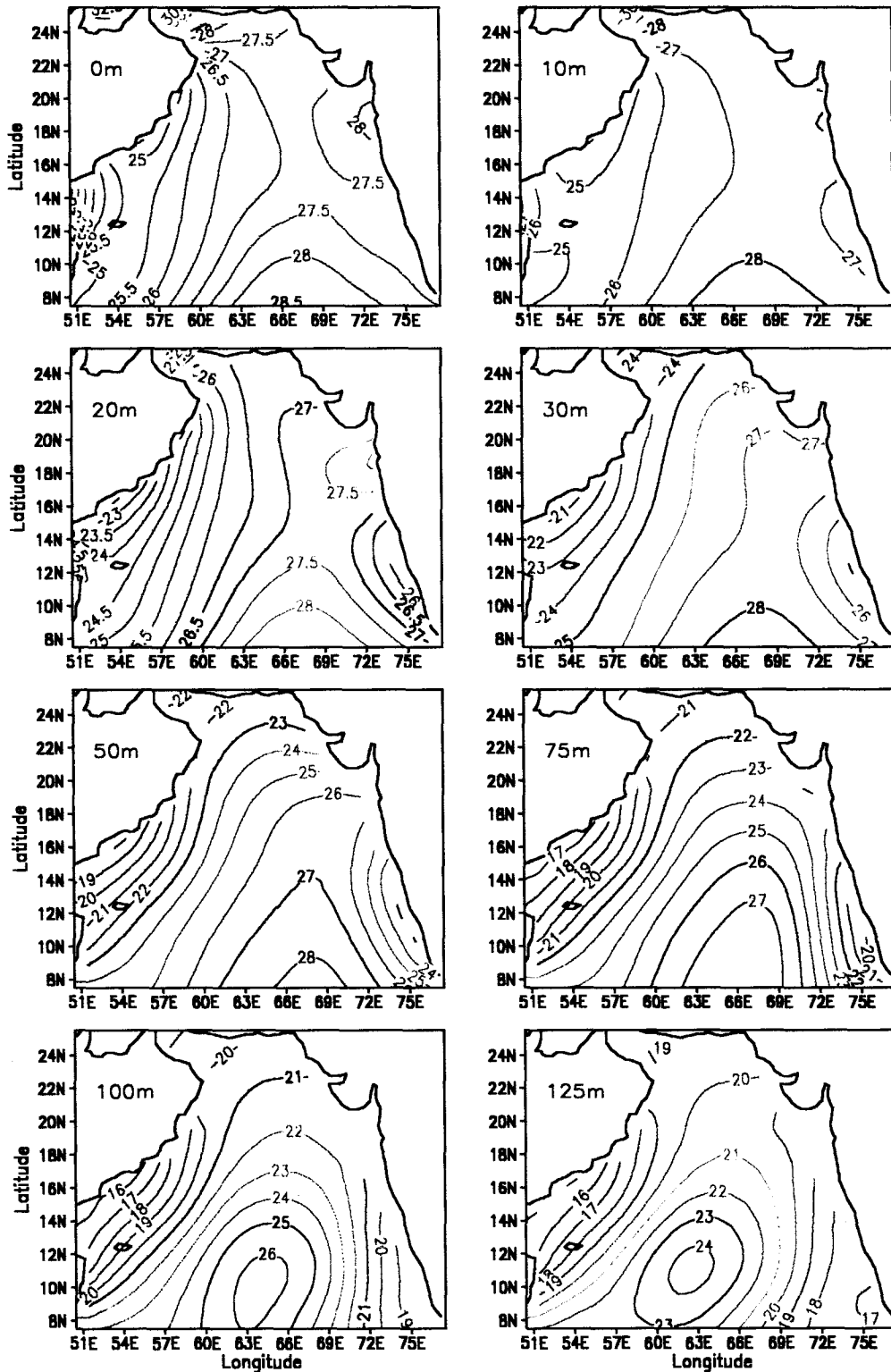


Fig. 3.23 Horizontal Temperature distribution at different depths during September

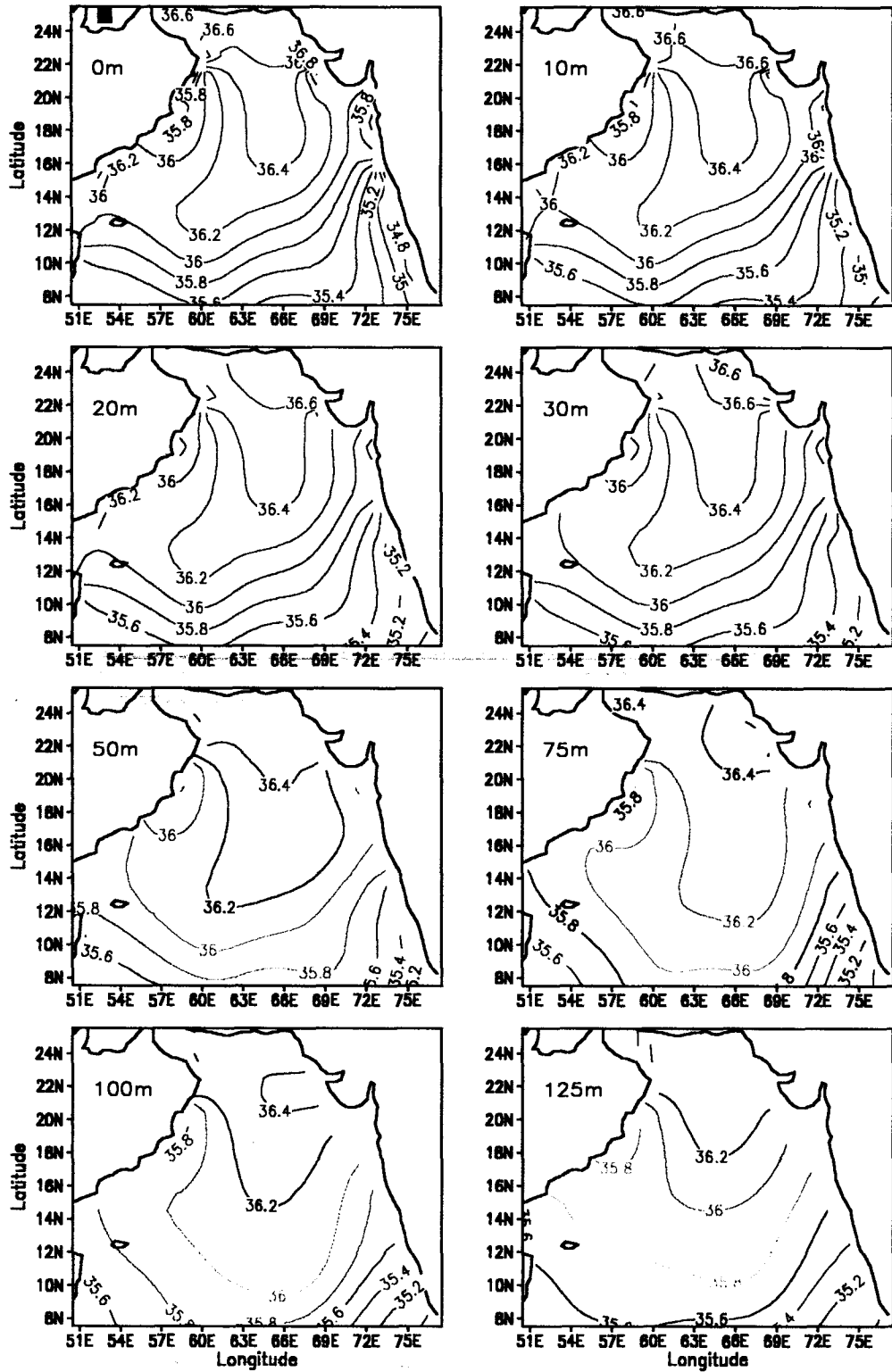


Fig. 3.24 Horizontal Salinity distribution at different depths during June

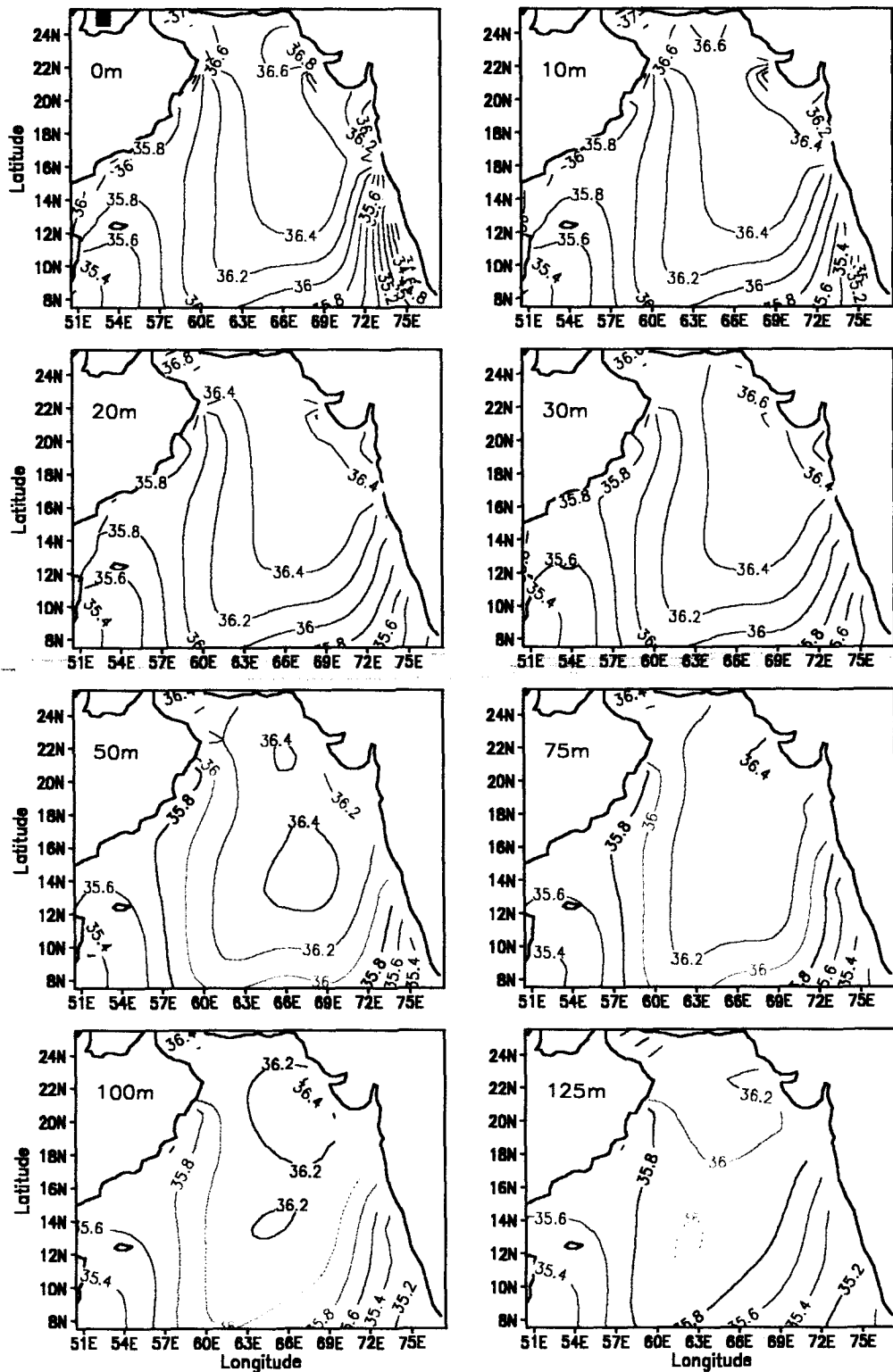


Fig. 3.25 Horizontal Salinity distribution at different depths during July

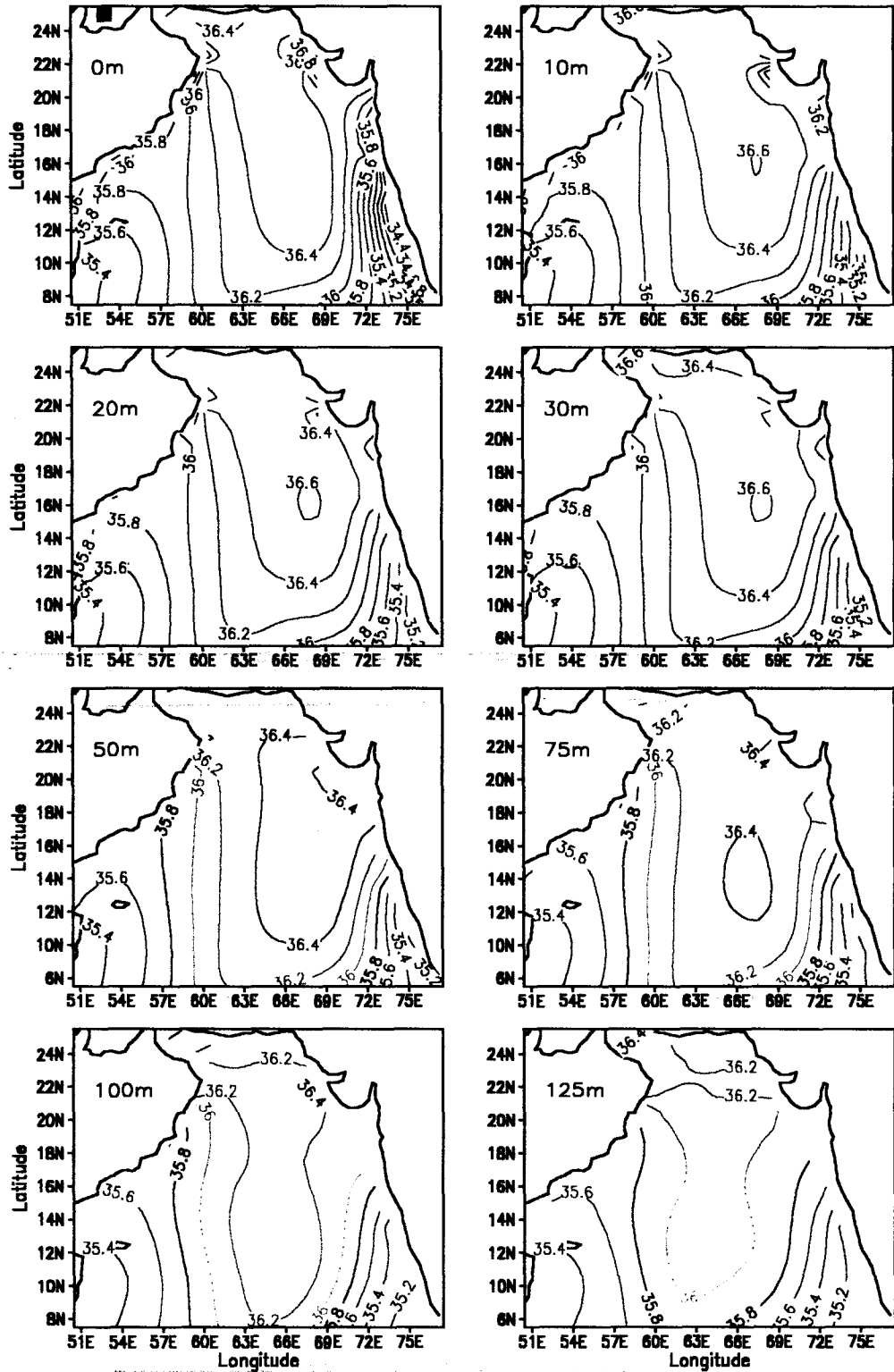


Fig. 3.26 Horizontal Salinity distribution at different depths during August

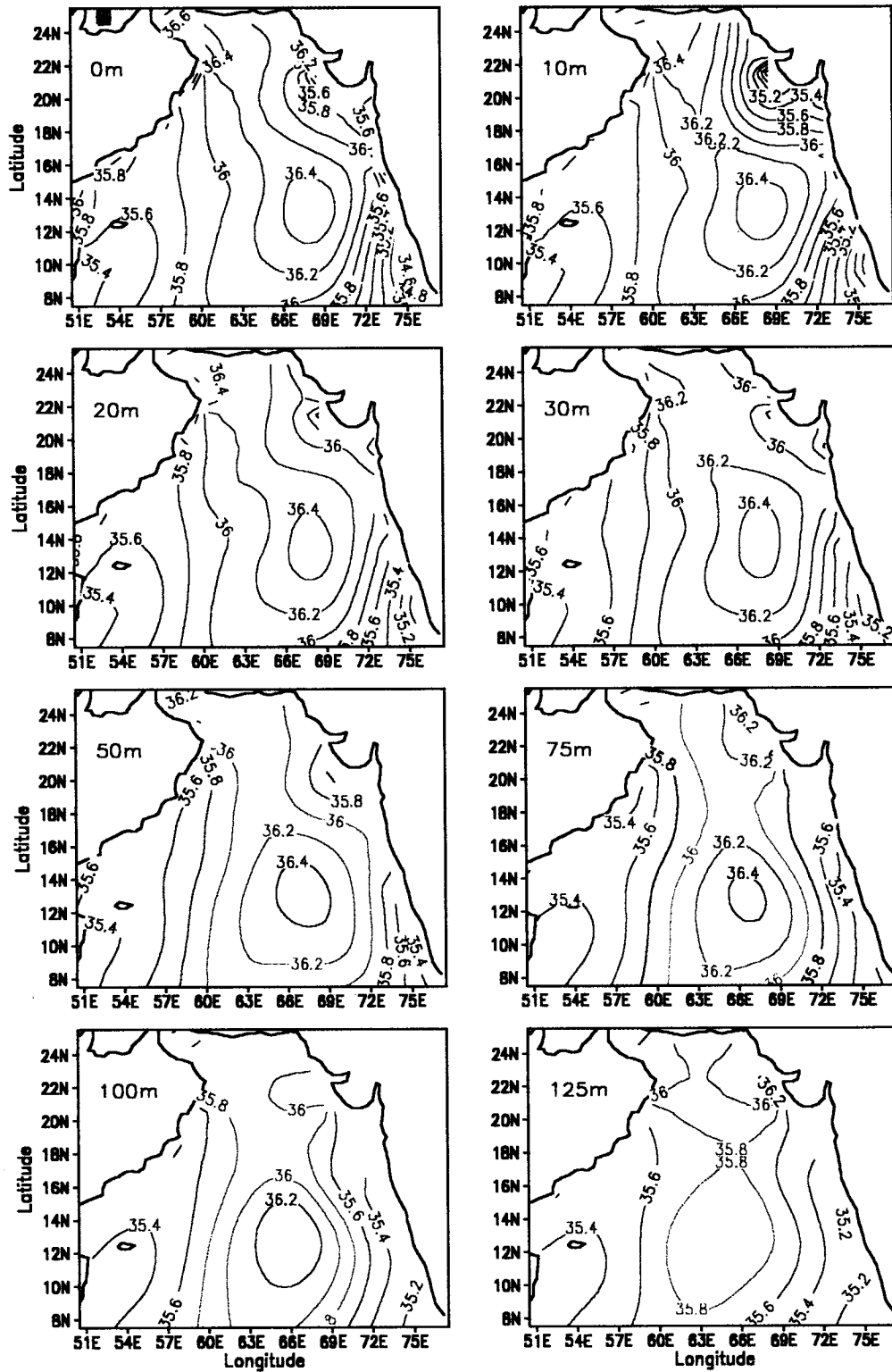


Fig. 3.27 Horizontal Salinity distribution at different depths during September

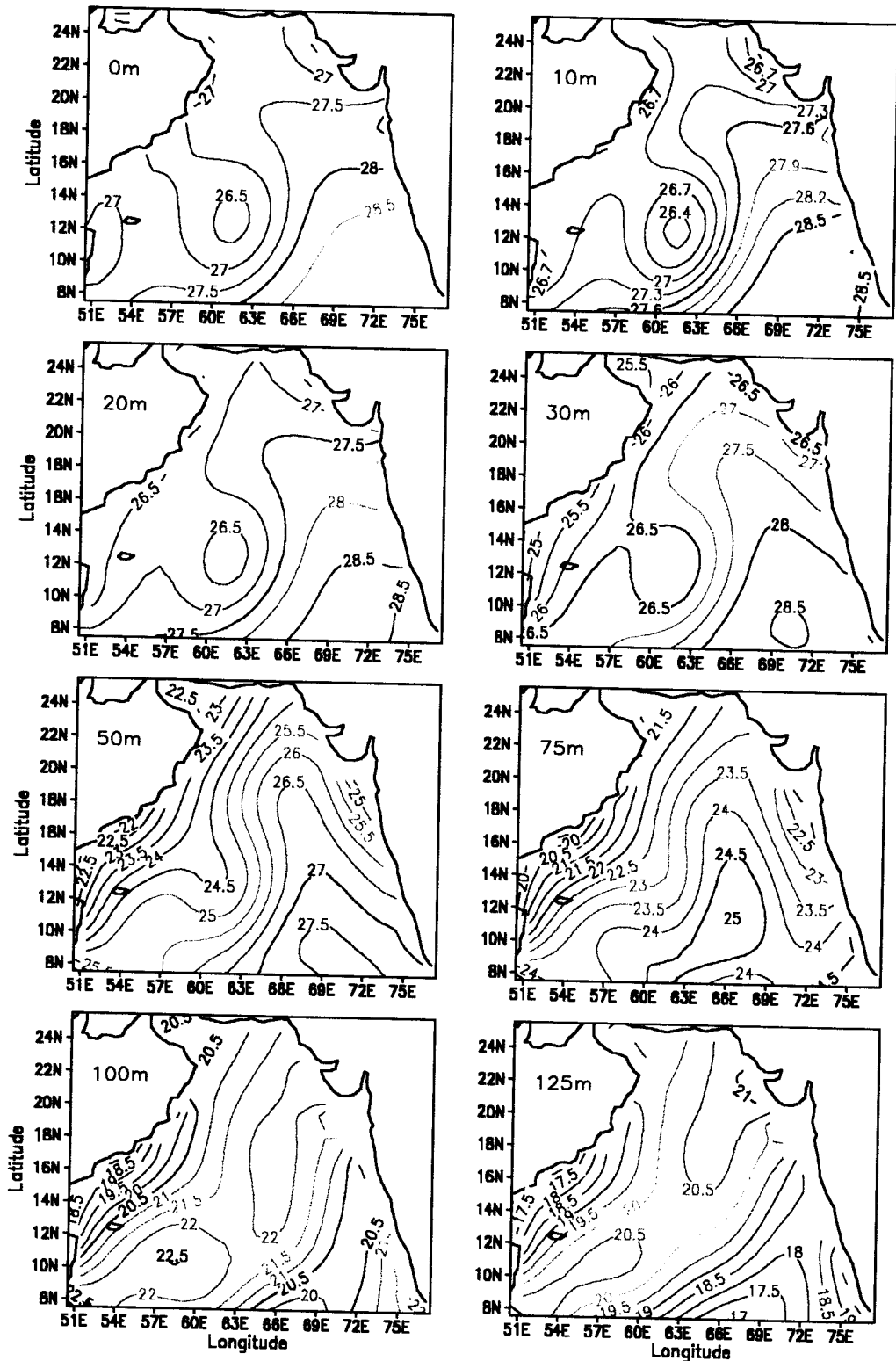


Fig. 3.29 Horizontal Temperature distribution at different depths during November

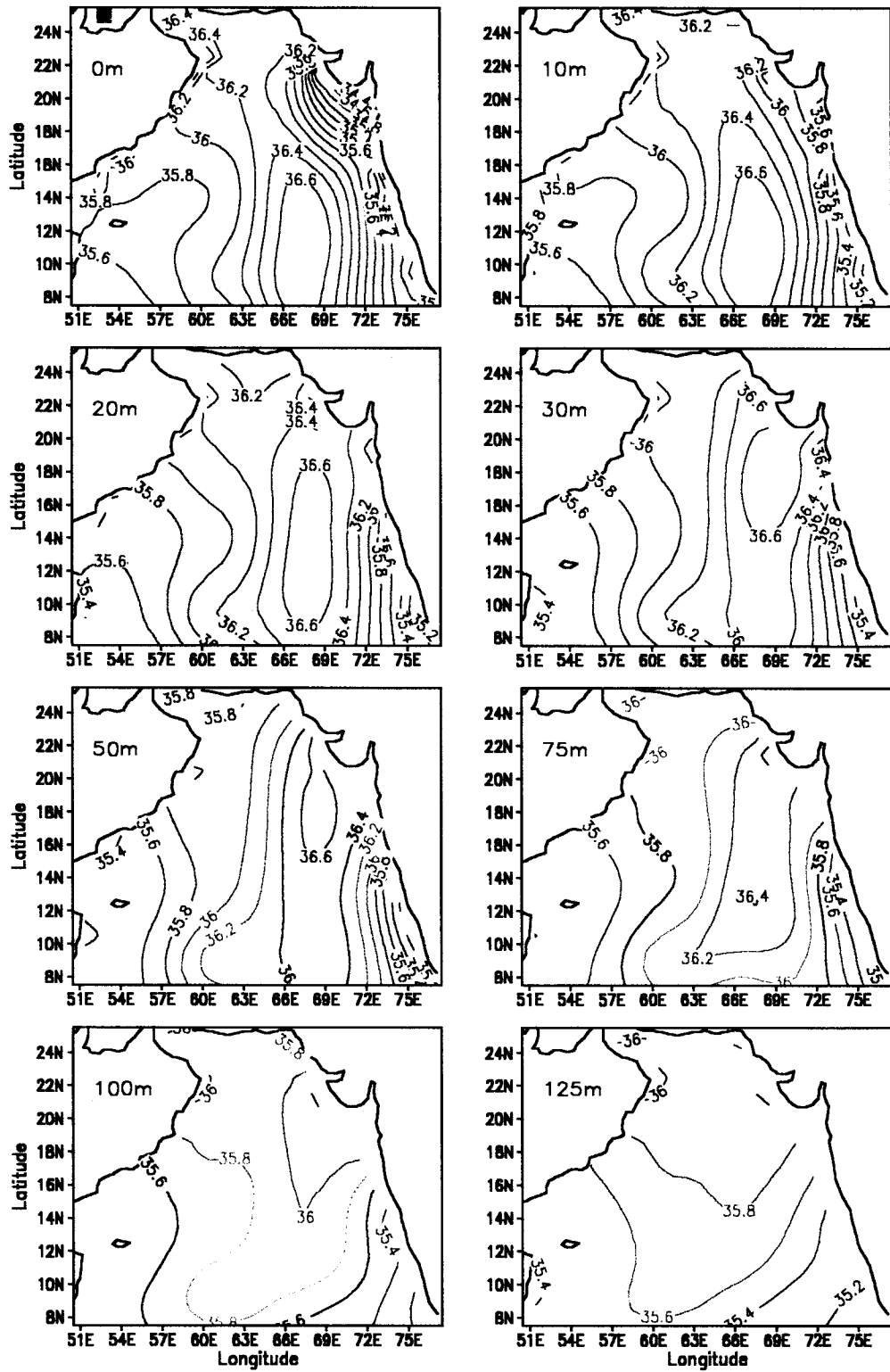


Fig. 3.30 Horizontal Salinity distribution at different depths during October

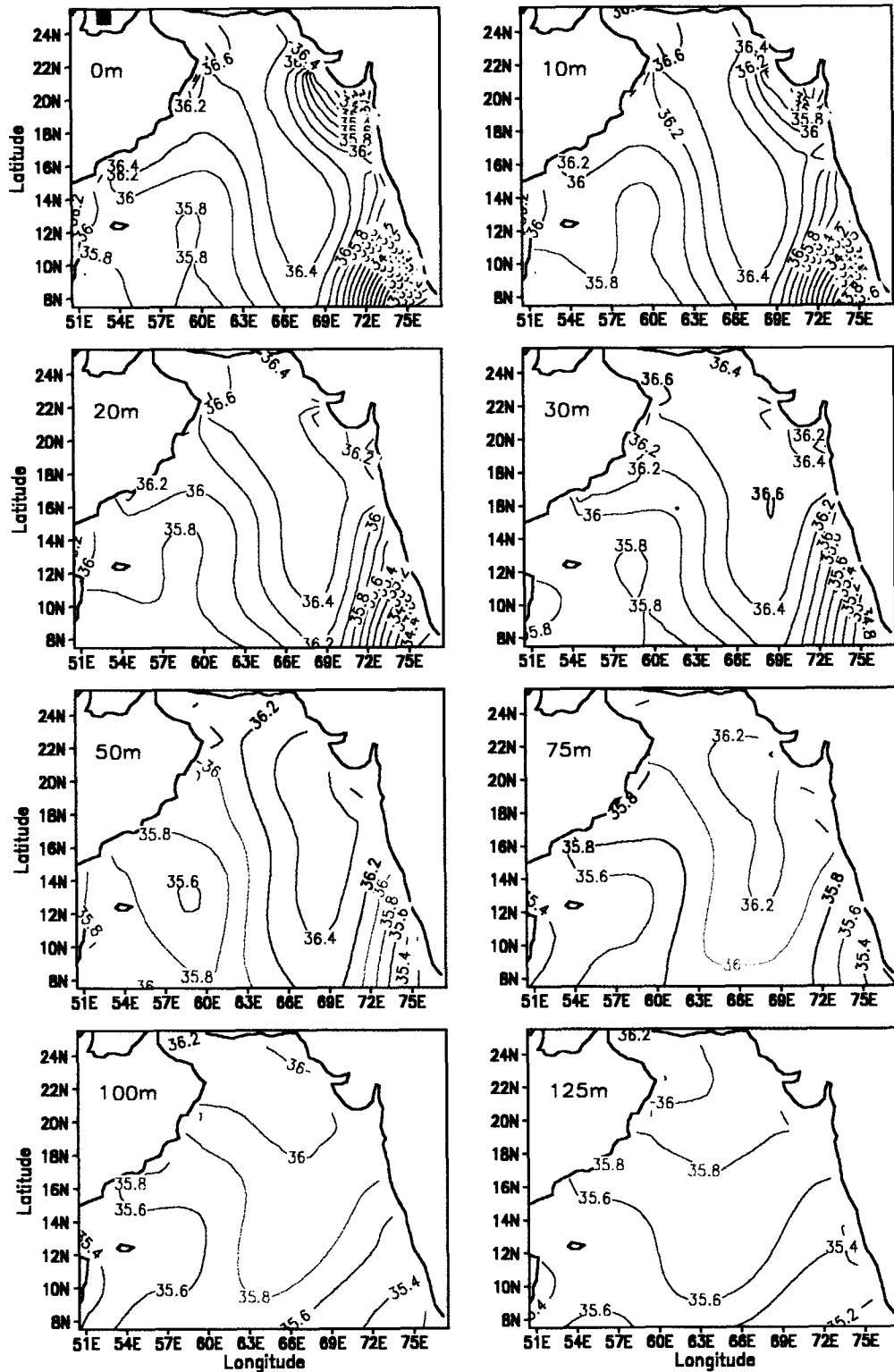


Fig. 3.31 Horizontal Salinity distribution at different depths during November

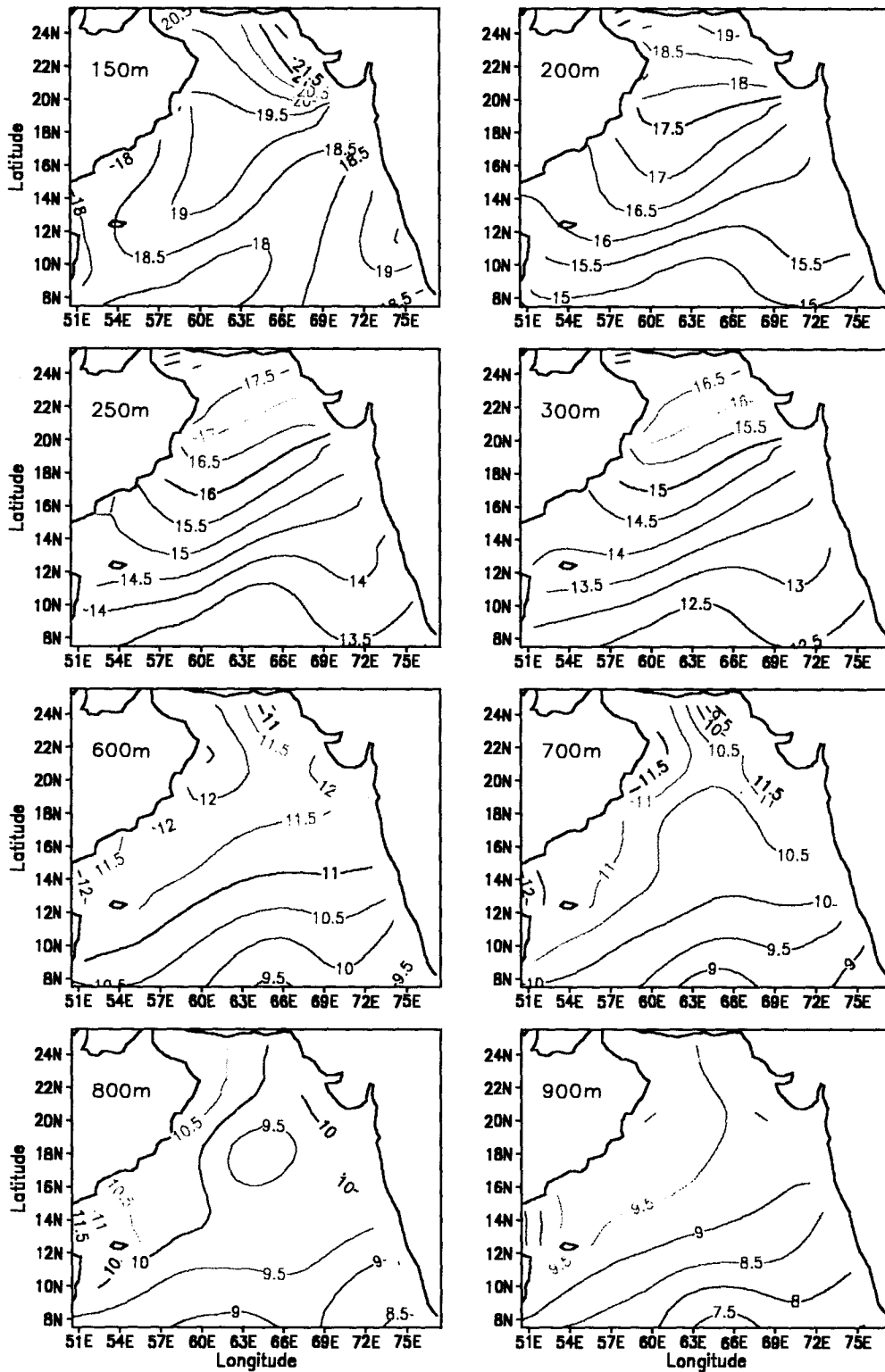


Fig.3.32 Horizontal Temperature distribution at different depths during February

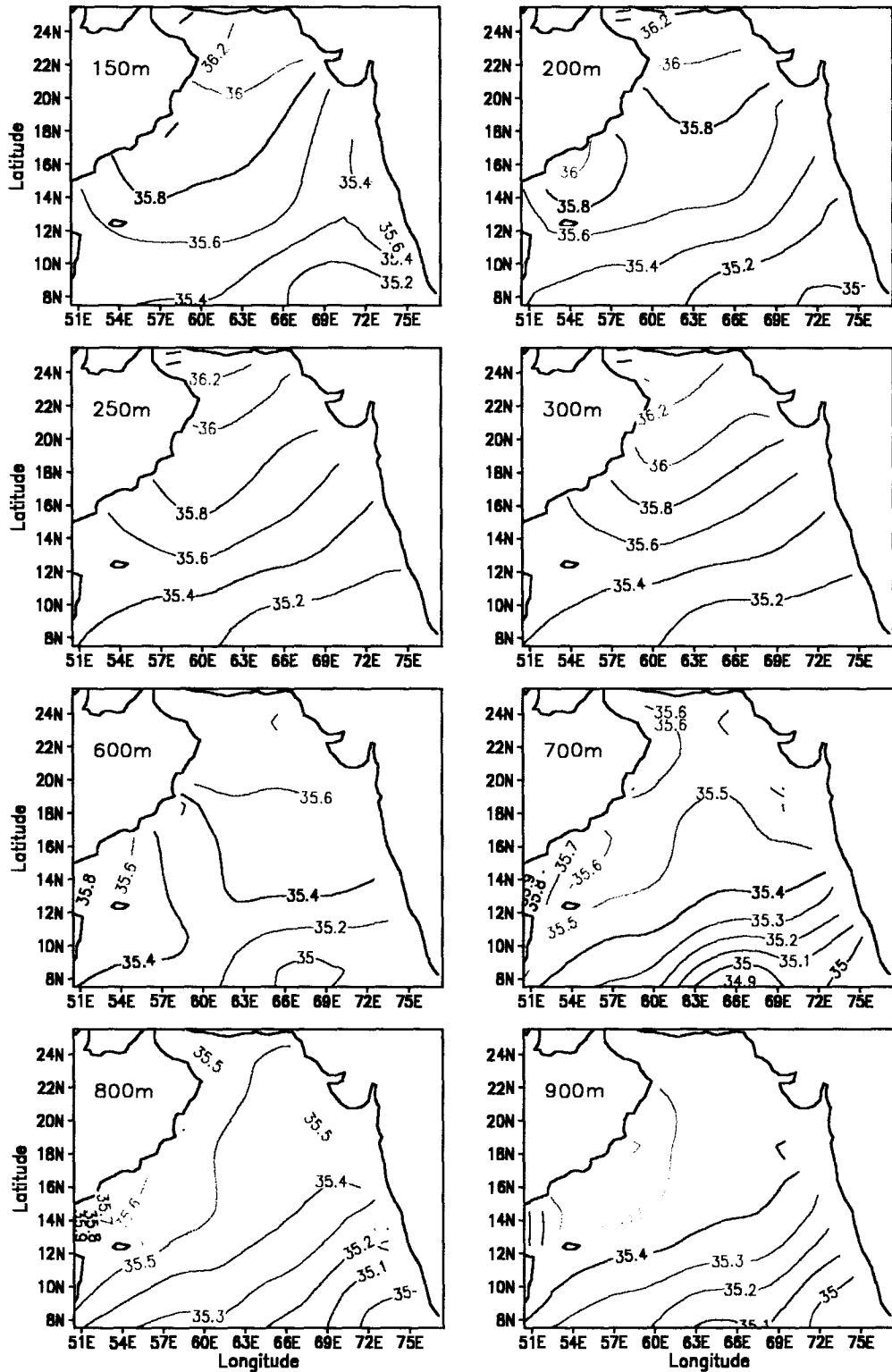


Fig.3.33 Horizontal Salinity distribution at different depths during February

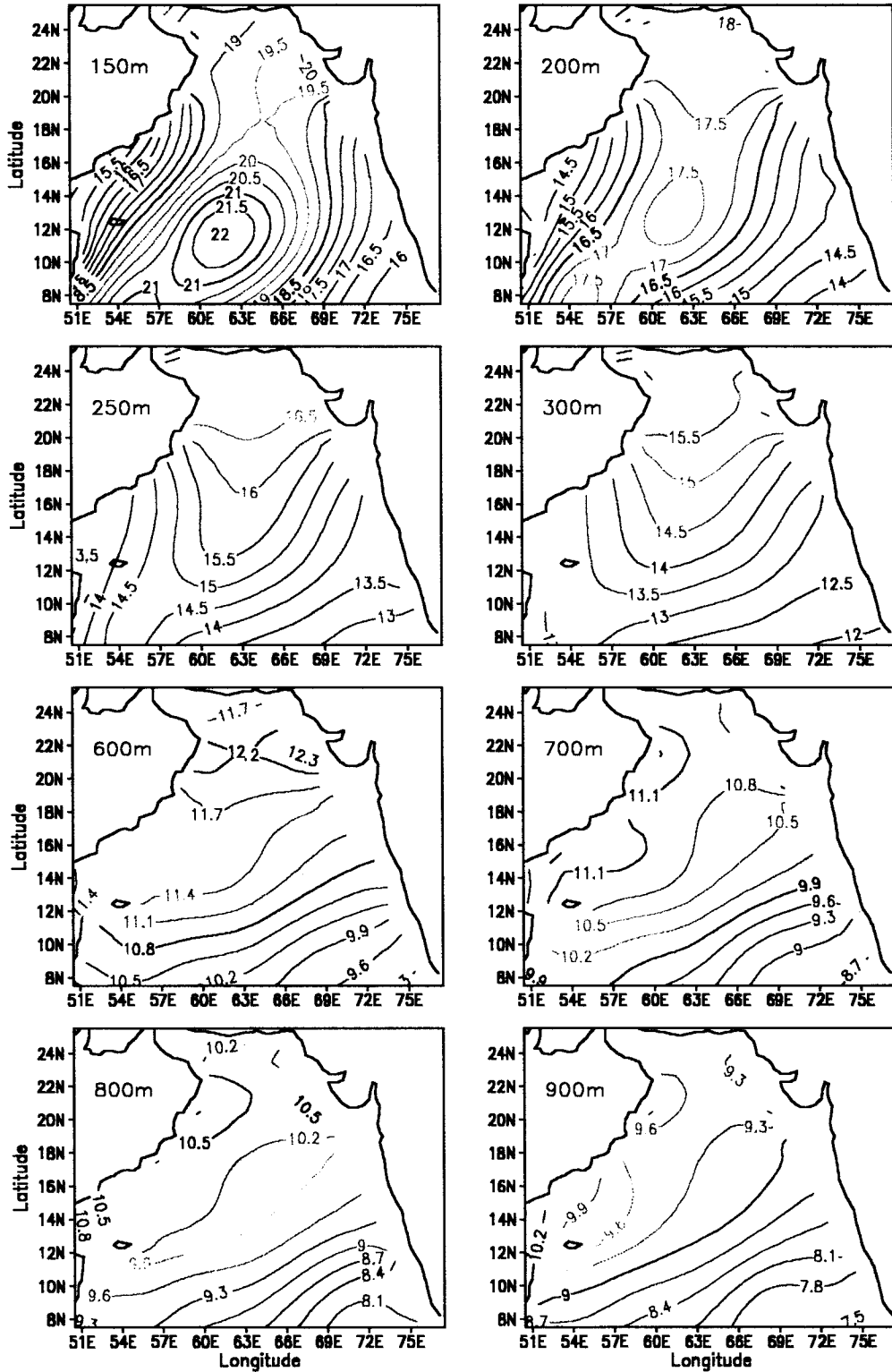


Fig 3.34 Horizontal temperature distribution at different depths during August

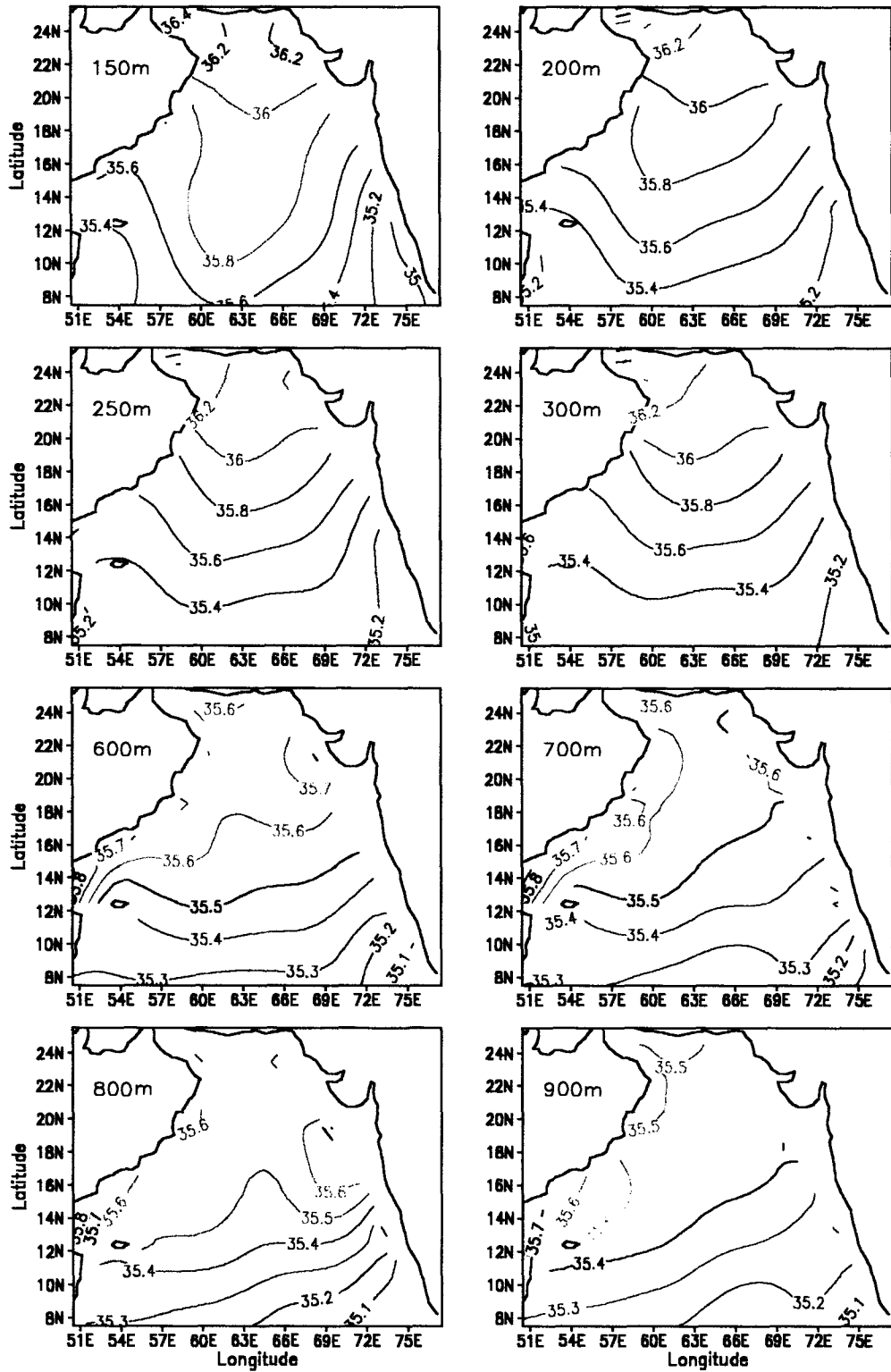


Fig. 3.35 Horizontal Salinity distribution at different depths during August

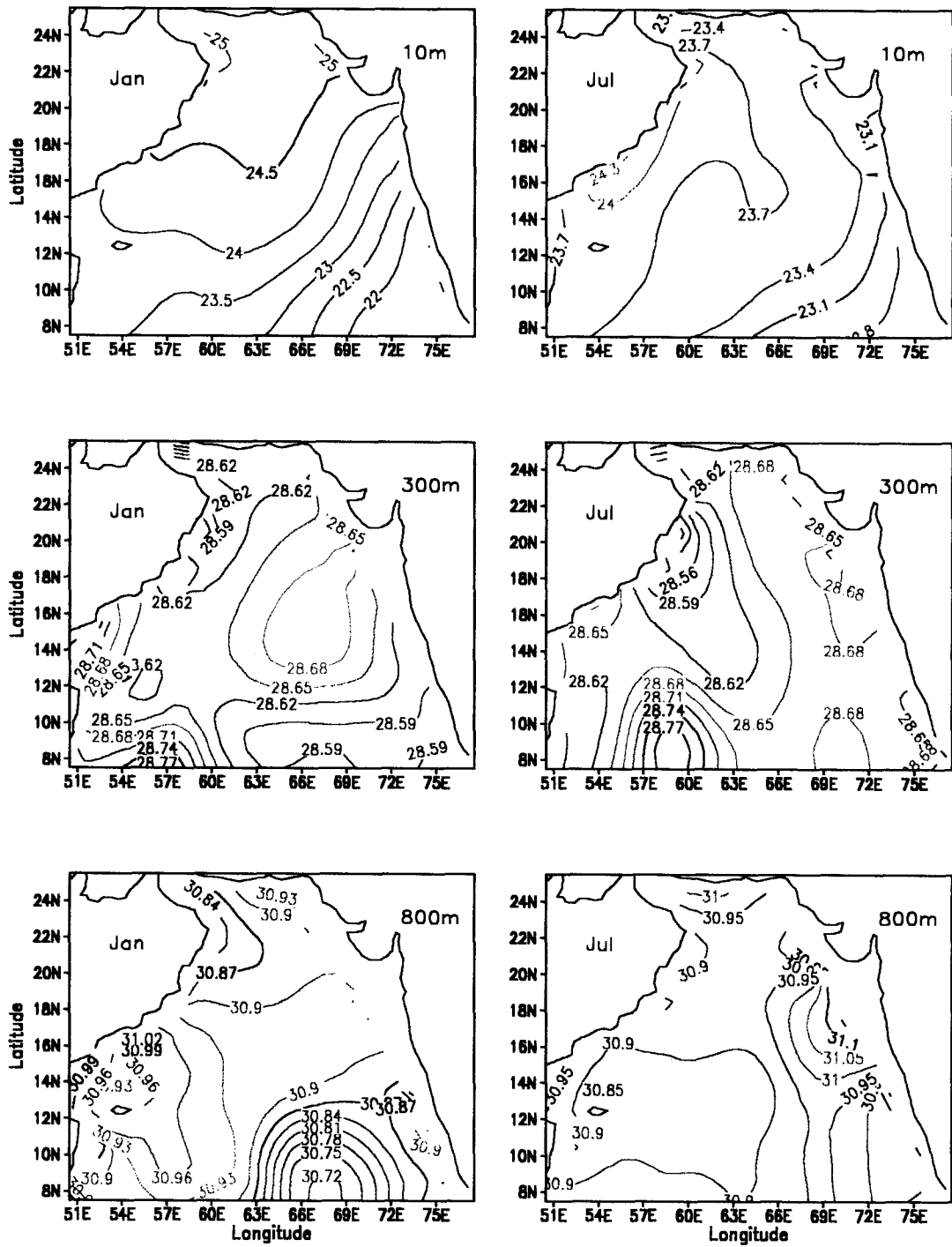


Fig 3.36 Potential Density Distribution at different levels during January and July

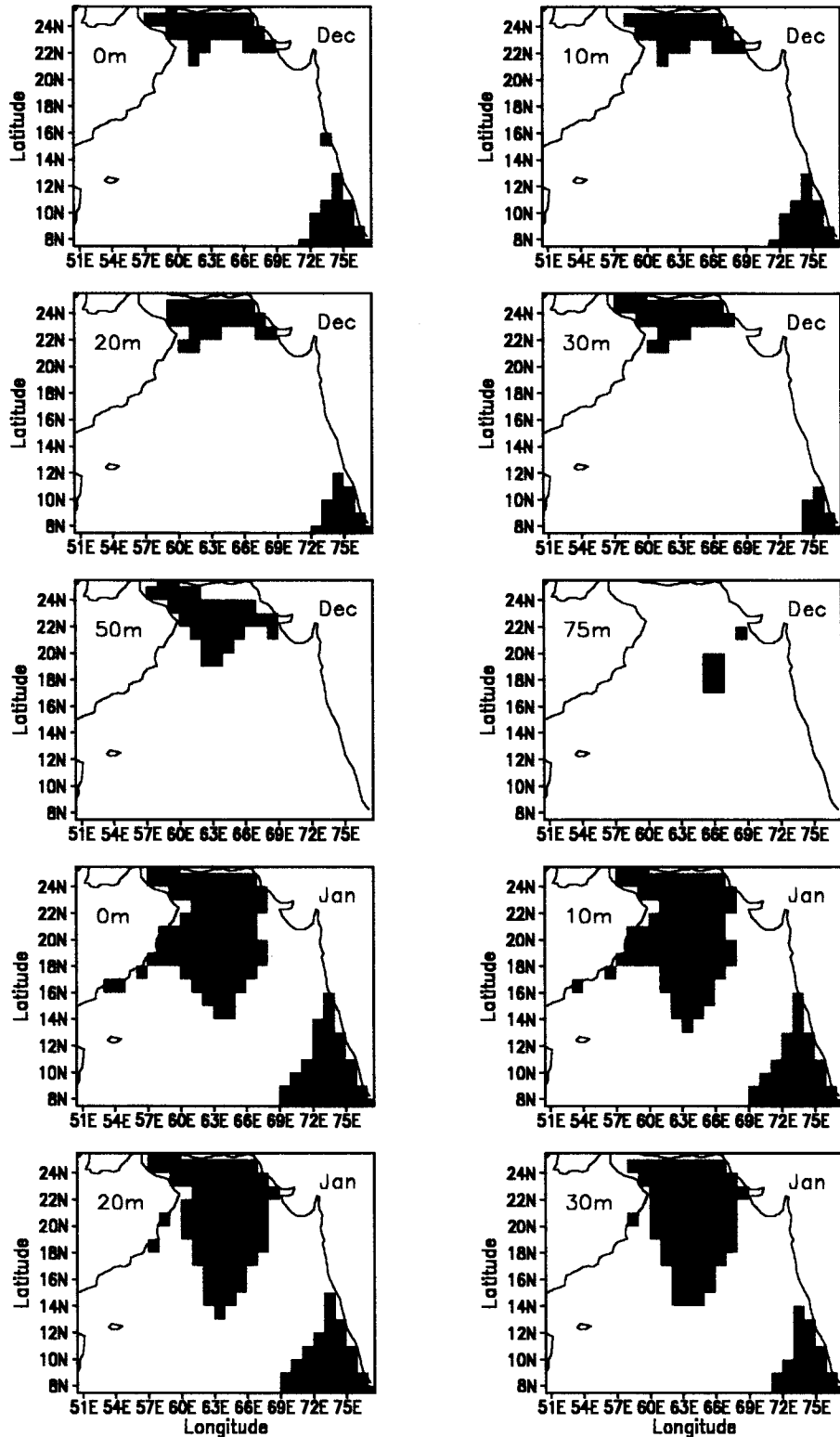


Fig.3.37 Spread of Arabian Sea and Bay of Bengal water masses
 (green for ASWM, medium blue for BBWM)

Contd...

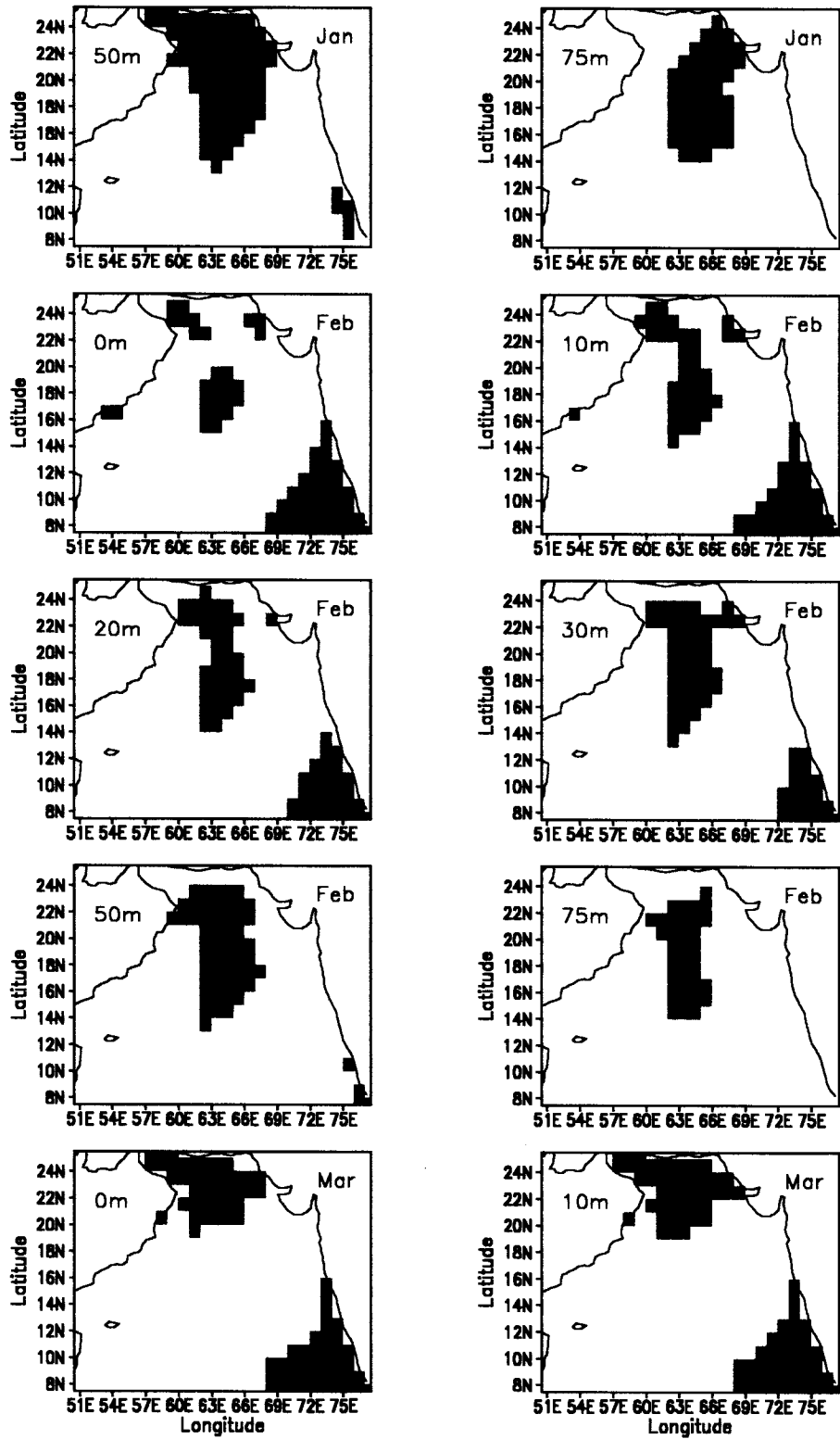


Fig.3.37 Spread of Arabian Sea and Bay of Bengal water masses
(green for ASWM, medium blue for BBWM)

Contd...

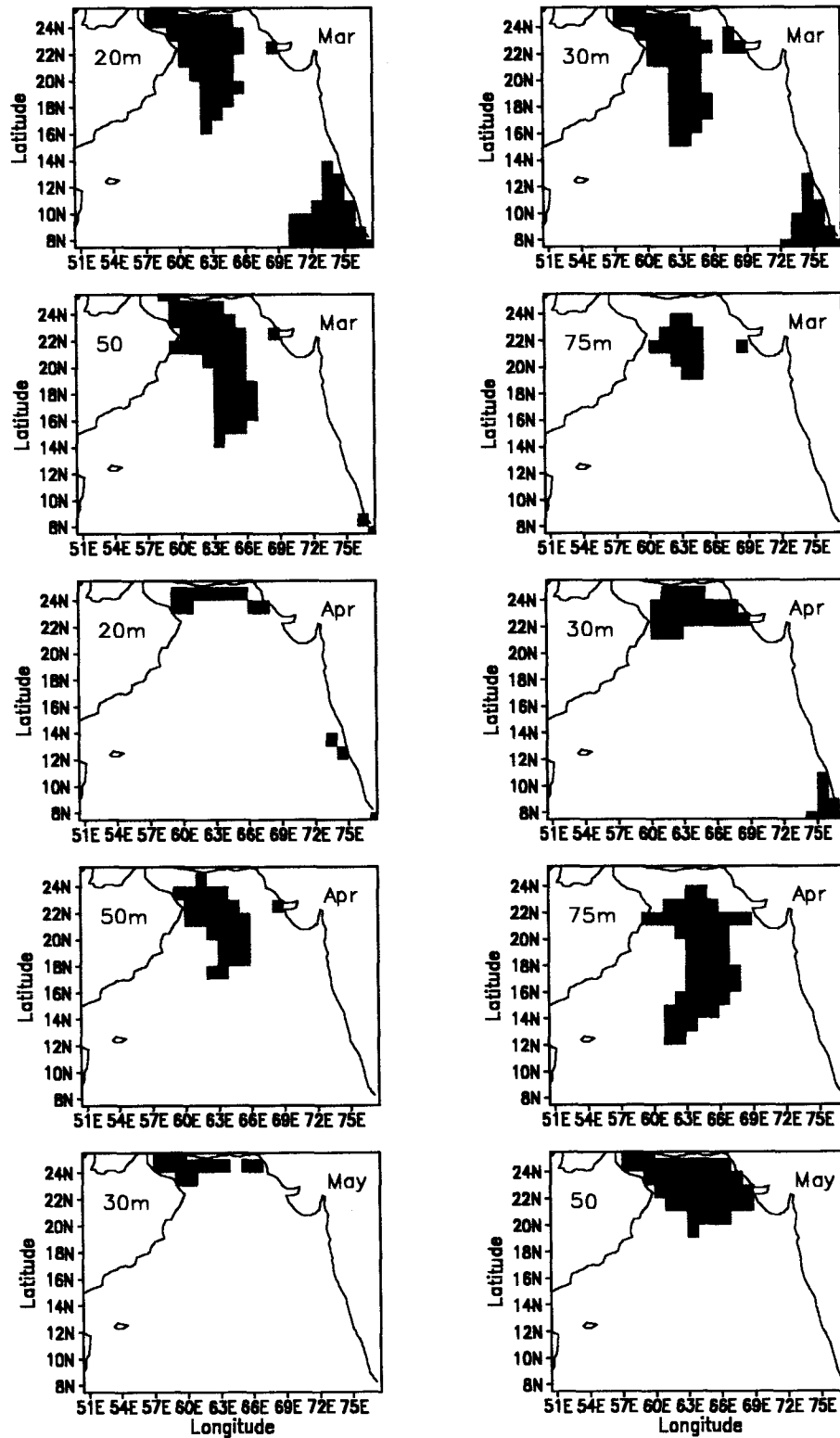


Fig.3.37 Spread of Arabian Sea and Bay of Bengal water masses
(green for ASWM, medium blue for BBWM)

Contd...

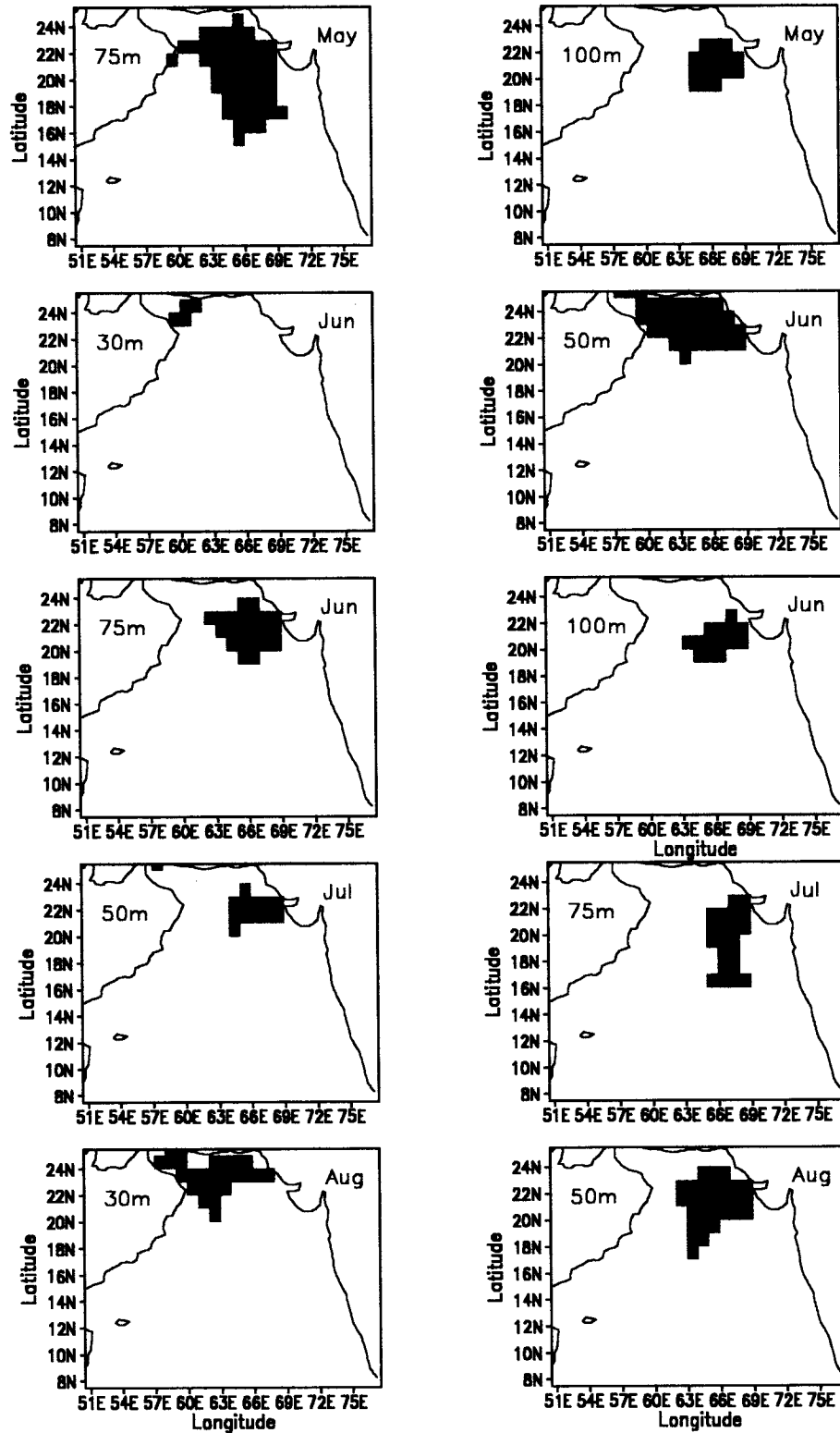


Fig.3.37 Spread of Arabian Sea and Bay of Bengal water masses
(green for ASWM, medium blue for BBWM)

Contd...

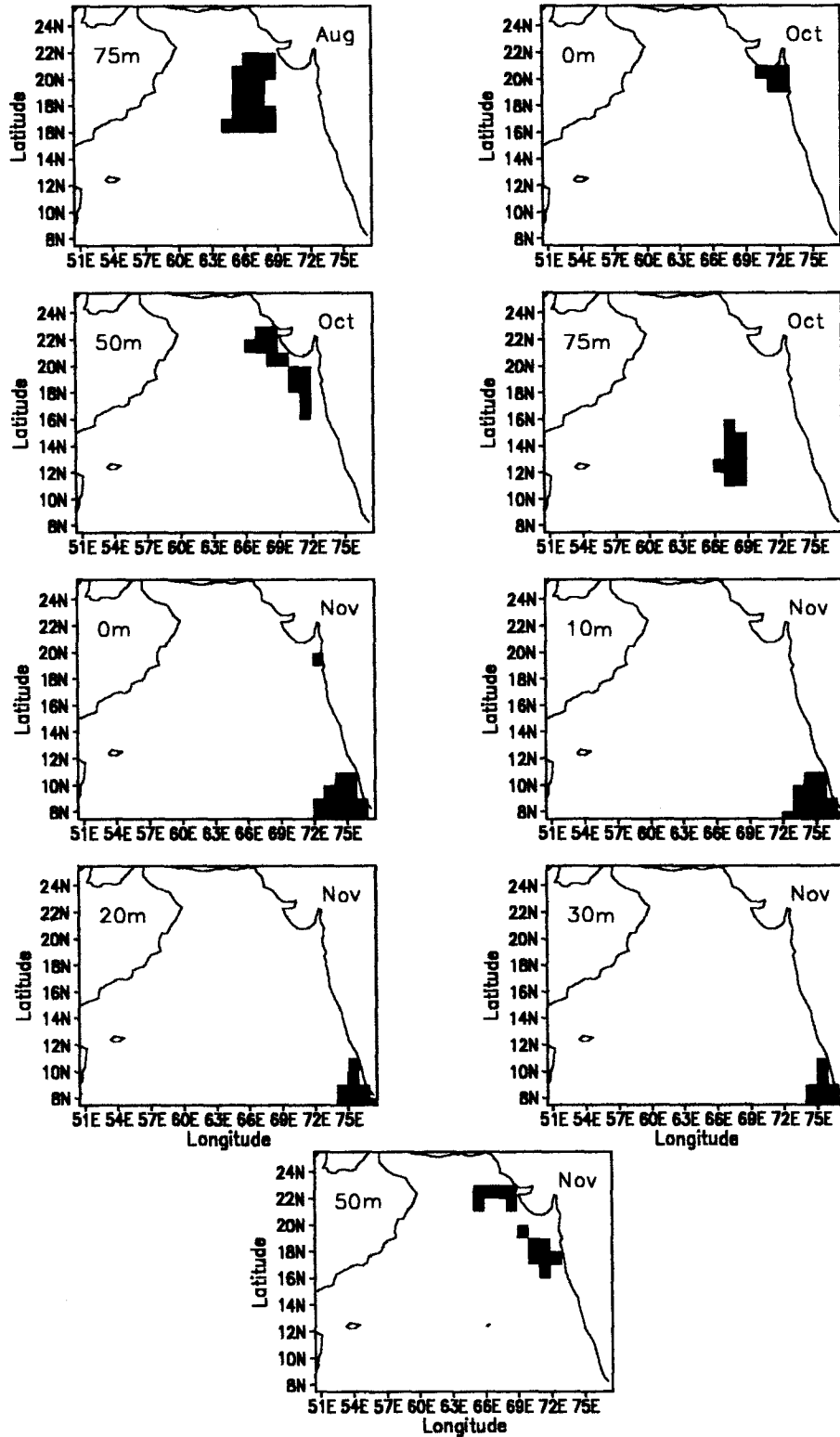


Fig.3.37 Spread of Arabian Sea and Bay of Bengal water masses
 (green for ASWM, medium blue for BBWM)

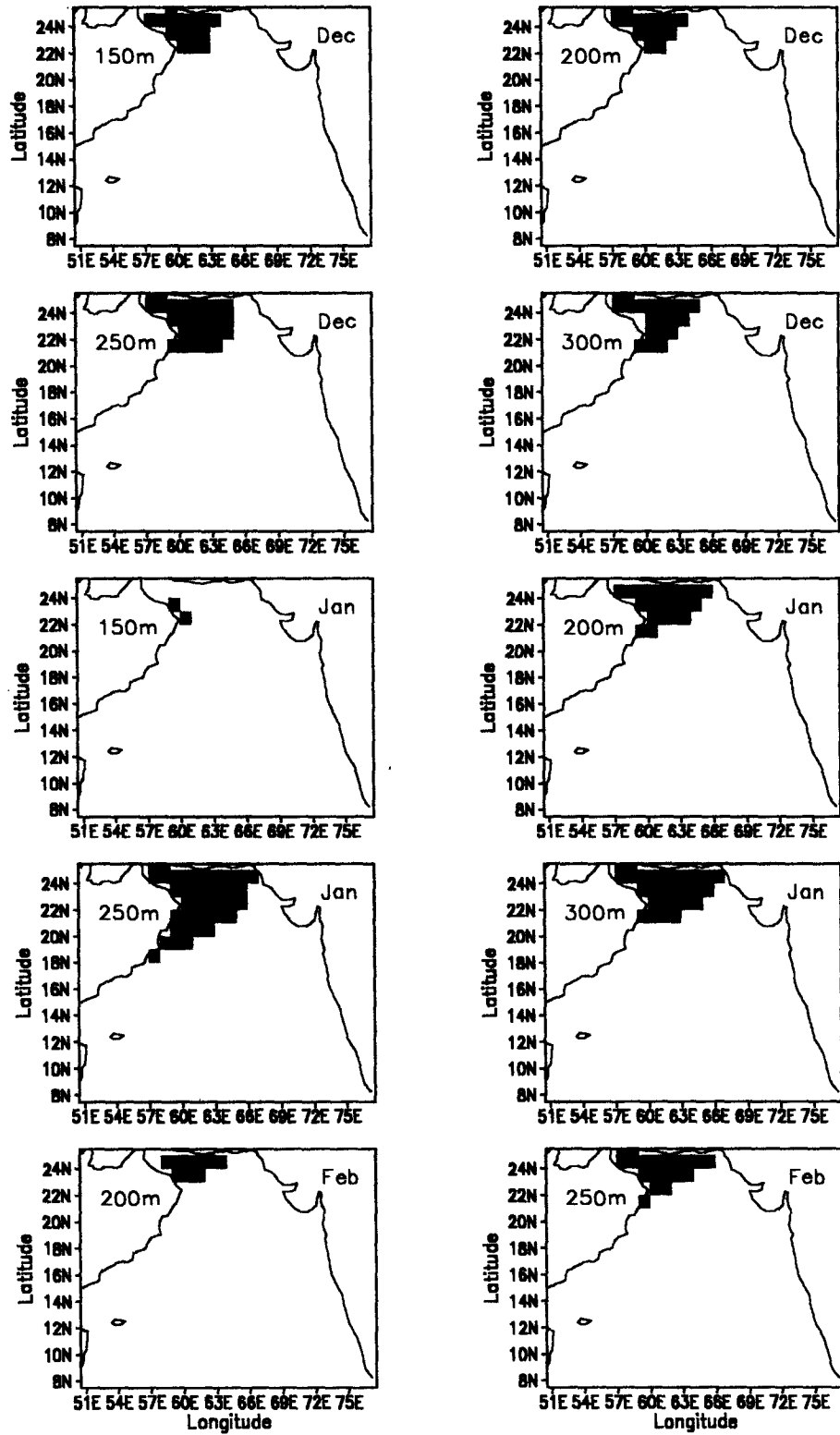


Fig.3.38 Spread of Persian Gulf Water Mass
(Maroon for PGWM)

Contd...

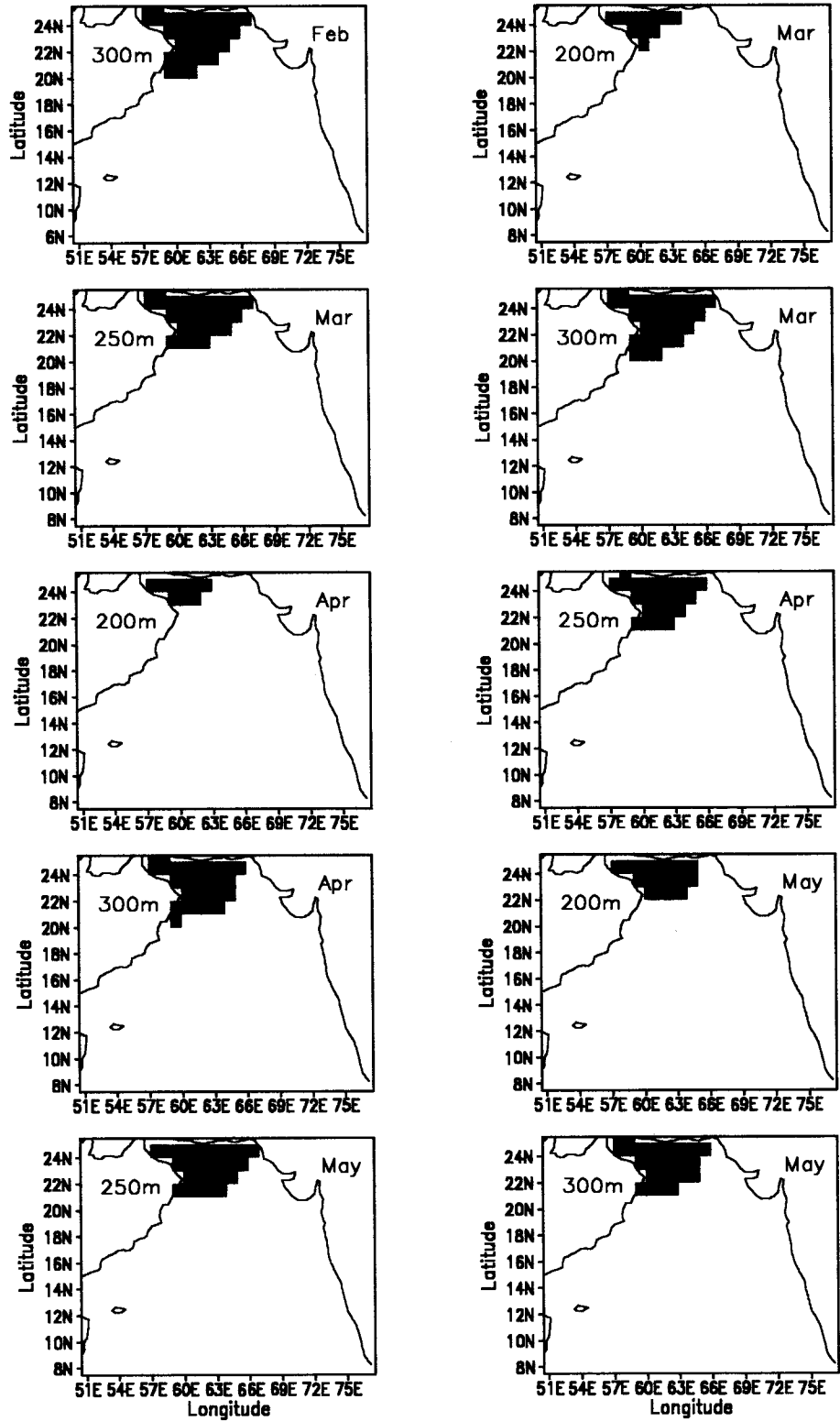


Fig.3.38 Spread of Persian Gulf Water mass
(Marroon for PGWM)

Contd...

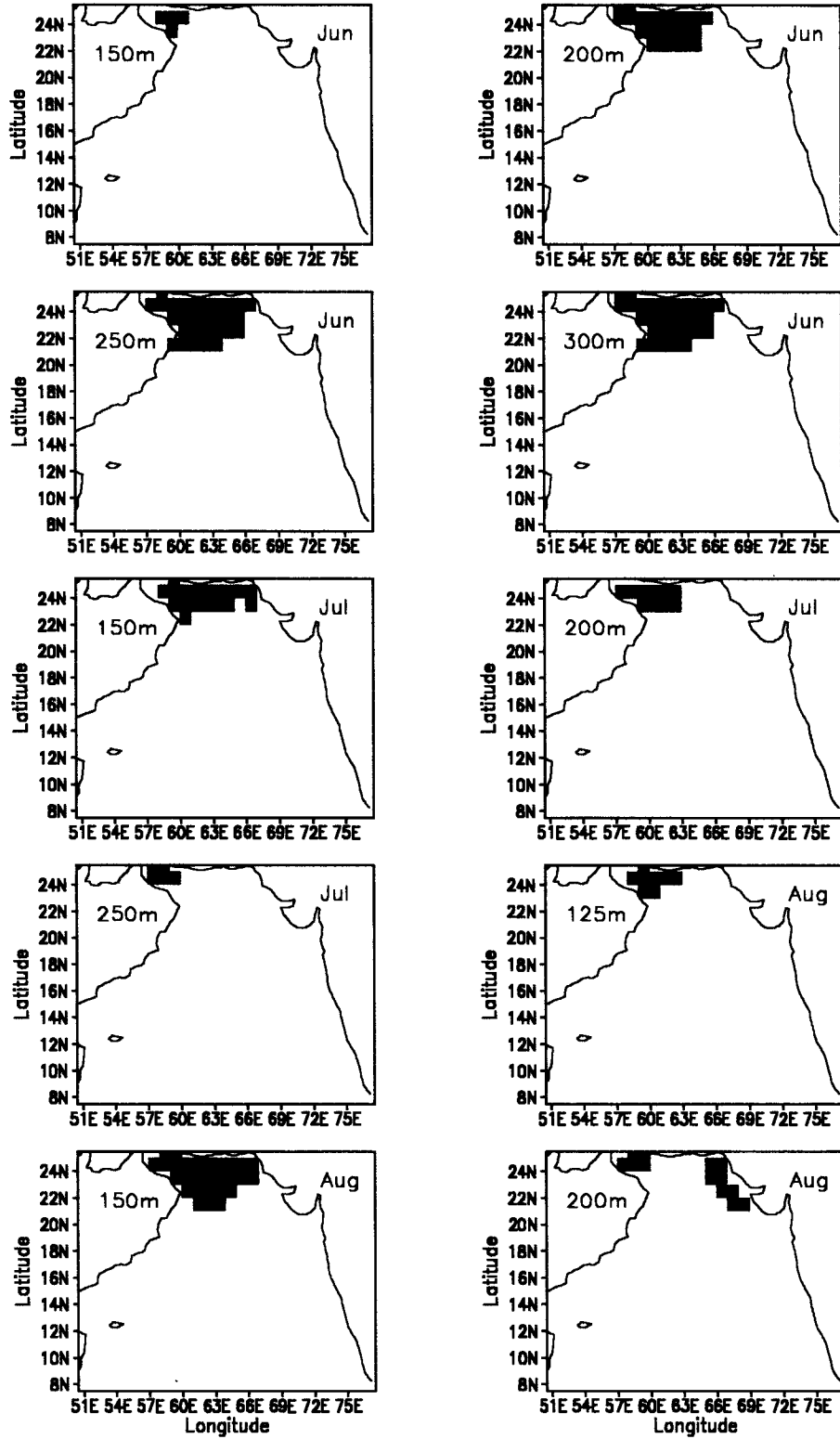


Fig.3.38 Spread of Persian Gulf Water mass
(Maroon for PGWM)

Contd...

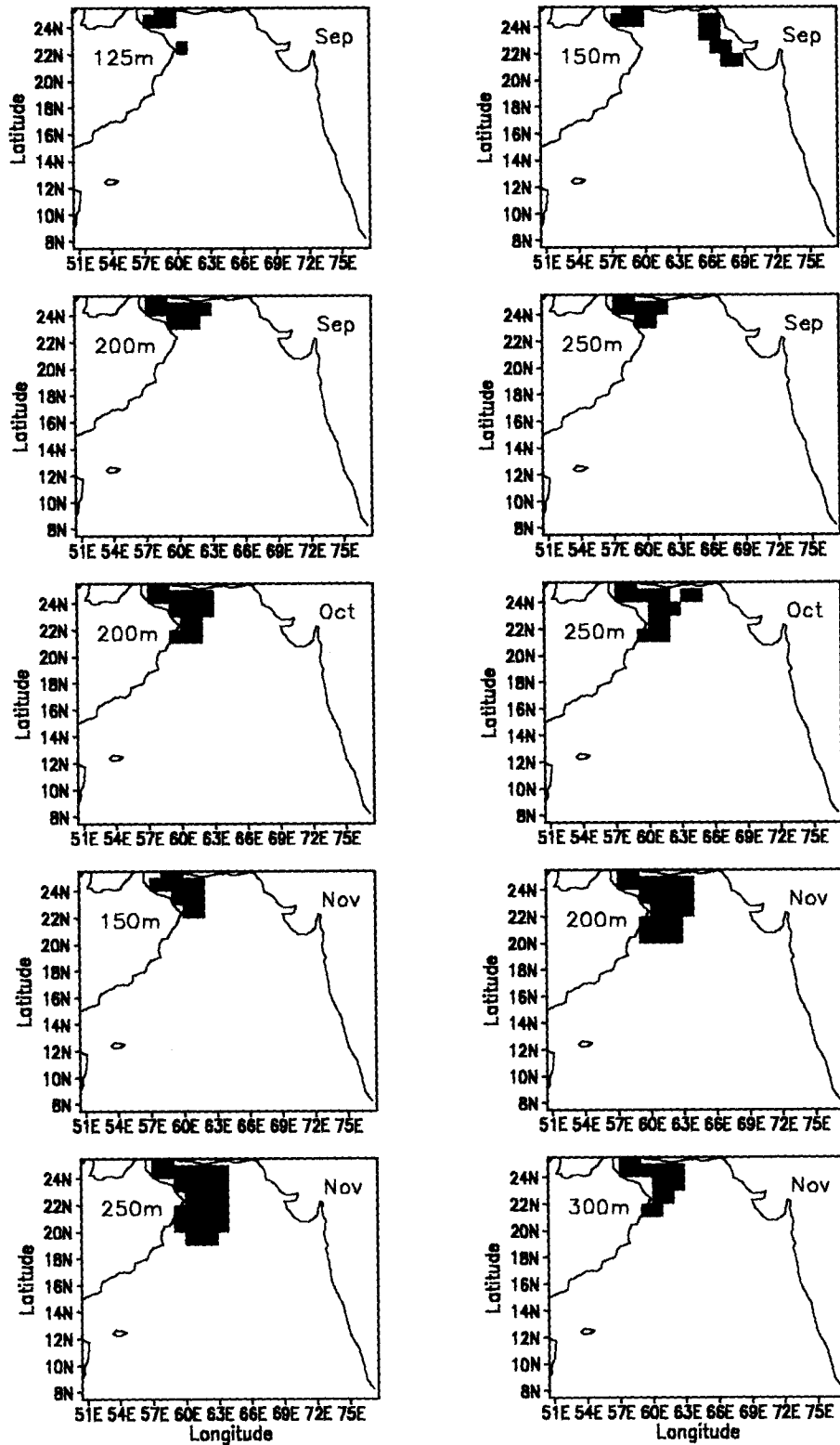


Fig.3.38 Spread of Persian Gulf Water mass
(Maroon for PGWM)

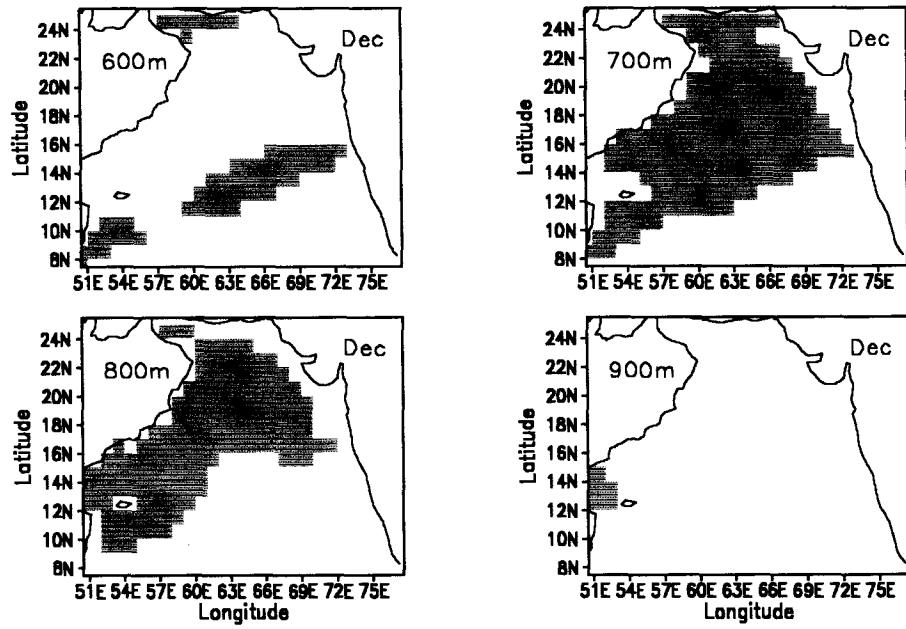


Fig. 3.39 Spread of Red Sea Water Mass
 (Grey for RSWM)

Chapter - IV

Seasonal Hydrographic Regime and stability

The strong seasonality in the atmosphere and the oceanic response are dealt with in chapter III. The dynamic nature of the region makes it imperative to study the hydrography of the region and the associated change in its stability using data of better vertical resolution. The analysis of the winds during period of observation and the hydrographic property, corresponding to year 1995 has been presented below.

4.1 Seasonal winds during 1995

Winds during different months of 1995, are shown in Fig. 4.1. Only those months which reveals significant variations and during which hydrographic observations are carried out, are presented. In January, March and December figures reveals northerly winds. The winds are strongest during January. The pattern also shows that the winds are stronger along the axis that runs from northeastern region to southeastern region. To the north of the axis, the curl is negative while to the south the curl is positive. The winds pattern shows total change from winter to summer. In July and September the winds are southwesterly. The pattern clearly depicts Findlater Jet, running from Somalia to northeastern region. The axis of the jet is characterised by zero curl. To the north of the axis positive curl exists while to its south a negative curl is evident. The stress decreases from July to September.

4.2 Hydrographic regime

The detail analysis of hydrographic properties corresponding to the

year 1995, are carried out through the vertical sections of temperature, salinity and density. The density section does not reveal any feature in addition to that from temperature and salinity sections. Therefore the results obtained from the temperature and salinity distribution along the transects –northern and southern are presented through figures 4.1 to 4.22. The details of these transects are given in chapter II and the transects are shown in figure 1. As the western region is highly tumultuous the water characteristics seen are entirely different at the western and the eastern regions of the transect. Hence, to analyse the water characteristics at the west, east and the intermediate regions of each of the transect, three stations are chosen from corresponding parts of the transect.

4.2.1 Distribution of temperature and salinity at the northern and southern transects during January

Figure 4.2 shows the temperature and salinity distributions along the northern transect during January 1995. The temperature distribution depicts a well defined mixed layer throughout the transect with a maxima (~70 m) at 725 km from the coast. The temperature of the mixed layer ranges from 24 to 27° C along the transect. The gradient of thermocline at the western part of the transect is weak ($0.02^{\circ} \text{C m}^{-1}$) compared to northeastern region. The vertical extent of the thermocline decreases from west (75 to 400 m) to east (75 to 250 m). The orientation of isotherms, show a downward slope towards the coast indicating sinking. A significant feature seen within the thermocline is a water body (21°C and 36.0 psu) between the stations N7 and N9, which is at a distance of around 900 km from the coast. It lies around 100 m depth.

The salinity section shows an irregular pattern of the Mixed layer Depth (MLD). From 450 to 750 km and between 1150 and 1350 km from the coast, the MLD is high. In these respective regions the MLD is around 70 m and 90 m. The characteristic corresponding to this layer is from 35.4 to 35.6 psu. The gradient in halocline at the west is 0.004 m^{-1} while at the east it is 0.016 m^{-1} revealing a stronger halocline at the eastern part. The salinity distribution further shows a tongue like structure in the subsurface extending to 650 km from the coast, revealing an intrusion of high saline water (36.0 psu). This in turn depicts that the region is more dynamic. A less saline water in the form of

a core is seen around 150 m depth and at a distance of 850 km from the coast.

Figure 4.4 shows the distribution of properties, along the southern transect, during January 1995. A well defined mixed layer is evident throughout the transect with a maximum depth of 90 m at 750 km from the coast. Unlike the earlier section the gradient ($0.05^{\circ} \text{Cm}^{-1}$) in thermocline gradually increases to the east of 300 km. At 200 m in the western region, warm waters are evident from the orientation of isotherms.

The salinity distribution shows a high saline water in upper 100 m and at 250 m, at the west, depicting an exceptionally dynamic nature. The salinity of the waters at the subsurface ranges from 35.9 to 36.2 psu and extends up to 250 km from the coast. Between 300 and 1300 km from the coast, the mixed layer is prominent with a maxima (80 m) around 1200 km. The halocline is stronger at the east (0.07 m^{-1}) than that at the west (0.004 m^{-1})

Figure 4.4 depicts the presence of three water bodies. One at the coastal station (N2) and the middle region (N6) at 200 m, and the third is a weak one at approximately 200 m at the east (N11). The corresponding characteristics are 18.5°C , 36.2 psu, 16°C , 35.9 psu and 15°C , 35.5 psu, respectively. The T-S distribution further shows neutrally stable water mass between 50 and 109 m at the western station, from 44 to 153 m at the middle and approximately 60-180 m at the east. At N11, around 550 m a secondary maxima in salinity is seen. However, such a distinct increase is not evident at the other two stations.

The T-S characteristics of the three stations of the southern transect are shown in Fig. 4.4. The profile clearly depicts a water mass around 250 m with temperature of around 17°C and salinity 36.2 psu at the coastal station (S2). Surface waters are characterized by low salinity (36.2 psu) than subsurface (36.6 psu) at this station. Compared to the characteristics of waters near the coast, the water column shows less variation in salinity at the central region. A high saline (35.7 psu) water body with temperature of 16 is evident at 260 m at S8. Also at this station, stability is higher than the coastal station in

the upper 200 m. At the farthest station the profile shows a water body with temperature of around 16 and 35.7 psu salinity at 84 m and a subsurface salinity maxima (36.3 psu). The drastic variation in the surface salinity is associated with the intrusion of Bay of Bengal water. Also, the characteristics reveal near-neutral stability between 64 and 183 m. The central and farthest stations do not reveal high salinity water in the depth range of 200 to 300 m. From 400 to 600 m, increase in salinity is seen at S13 and S15. Such a distinct increase is not evident at the coastal stations (S2).

4.2.2 Distribution of temperature and salinity at the northern and southern transects during March

The hydrographic characteristics along the northern transect corresponding to March is shown in Fig. 4.5. The depth of mixed layer at the western part is 60 m, while at the central part (575 km from coast), it is 125 m. The eastern region depicts a uniform temperature up to 100 m. The deepening of mixed layer reveals the intensity of winter convection. The depth of Mixed Layer, in general, increases up to 600 km from the coast and further eastward, it decreases drastically due to the presence of low saline waters at the surface on eastern side. At the easternmost region of transect, the presence of less saline water (36.2 psu) is a clear indicator of the influence of poleward flow during the winter monsoon. This flow traps the high saline central Arabian Sea water (36.5 psu) at the subsurface. A tongue like structure with salinity between 35.9 and 36.5 psu is sandwiched between the halocline and the lower uniform water at the west resulting in the upslope of isohalines towards the coast. The thermocline and halocline are weaker at west than east.

Figure 4.6 shows the southern transect of study area during March-April 1995. Orientation of isotherms shows erosion of MLD in the west and east. As in the northern transect, thermocline at the western part is weaker ($0.05^{\circ}\text{C m}^{-1}$) than that at the east ($0.09^{\circ}\text{C m}^{-1}$). A water body with temperature ranging from 25 to 28°C is seen at subsurface from 850 km to 1375 km away from the coast.

The salinity distribution shows an MLD with properties 35.4 to 35.6

psu. The mixed layer is deeper in the central region than the rest. The salinity corresponding to the water body between 750 and 1200 km at 100 m depth is 36.4 psu. Moreover, the distribution manifests a weak tongue like structure with salinity greater than 35.9 psu spreading towards east. East of 850 km from the coast, the surface water is characterized by low salinity (35.4 psu). Further, high saline water is sandwiched between the surface low salinity water and the halocline.

Fig. 4.7 shows that in March, there is demarcation of a water body (18° C and 36.4 psu) at a depth of 200 m near the coast (N2). The waters below 228 m, does not show any deviation in its properties from January. The water column up to 109 m is neutrally stable. The intermediate station shows a water body at 260 m. The corresponding properties are 16° C, 36.1 psu. Moreover, a neutrally stable water body is well depicted from 42 to 121 m at N2 and between 90 and 190 m at N5. T-S characteristics representing the eastern most region of the transect reveals the presence of subsurface salinity maxima of 36.5 psu and with a temperature of 26° C at 50 m depth. Between 60 and 161 m, the water column is neutrally stable. Further at around 270 m a water body with temperature of 14 and salinity of ~ 35.6 psu is evident from N8 to N11. Below 500 m high salinity signatures are seen at N8, N9, N10 and N11.

The T-S profiles at southern transect, near the coast, shows a water body of high salinity (35.8 psu) and temperature of 16° C at 200 m (Fig. 4.7). The surface waters depict a lower salinity (36.3 psu) than at 82 m (36.4 psu). from 100 to 150 m the water column shows near-neutral stability. A high saline water is seen at 30 m while another is depicted at 250 m. The corresponding properties are 28° C, 36.5 psu and 15° C and 35.7 psu. The characteristics show a neutrally stable water column from 100 to 150 m depth. At the farthest station, though there is drastic variation in characteristics in the upper 150 m, the trend is subsurface characteristics is maintained. The surface waters show low salinity (~ 35.2 psu) leading to salinity maxima at 90 m. At 250 m, the increase in salinity is weakly manifested from 90 to 190 m neutral stability is seen. Though signature of high saline water are seen below 500 m at S15, it is not distinct at the coastal (S2) and central (S8) stations. Stations S2, S3, S12 to S15 show high salinity below 500 m.

4.2.3 Distribution of temperature and salinity at the northern and southern transects during July-August

Distribution of properties corresponding to summer season (July 1995) along the northern transect is shown in figure 4.8. The region is characterised by a weak mixed layer (~20 m) at the east with temperature between 27 and 29° C while it is absent in the rest of the transect. Surfacing of the isotherms near the coast and the presence of uniform water body between 100 and 1100 km from the coast, at a depth of 50 m, are prominent features. The gradient of thermocline at the west is 0.07° C m⁻¹ while it is 0.1° C m⁻¹ at the east.

The MLD at the easternmost station is characterised by salinity between 36.6 psu and 36.7 psu. The uniform water body seen in temperature section is characterised by salinity between 36.4 and 36.5 psu. A high (36.5 psu) cellular structure is seen at a depth of 50 m near the coast. The halocline (0.004 psu m⁻¹) at the west is poorly manifested due to the upwelling and the presence of high salinity water within it. This high saline water (36.5 psu) is seen at subsurface between 200 and 300 km from the coast. Further to the east, at a distance of 700 km from the coast, low saline water in the form of a core is seen at a depth of 100 m. The subsurface high salinity tongue extends to 600 km from coast.

The properties along the southern transect characterizing hydrography during July-August 1995 are shown in Fig. 4.9. Surfacing of isotherms extend to 600 km from coast with highest intensity near the coast revealing intense upwelling there. This result in less vertical variation of properties of the water column at the west and at the central part. East of 600 km from the coast, depth of mixed layer increases and is maximum (95 m) at the farthest station.

The salinity distribution is the replica of the features seen in the temperature distribution. The distribution reveals a tumultuous nature of the western region compared to east. Upwelling near the coast and a strong halocline at 800 km from the coast with further increase in its gradient towards east are characteristic features of the transect. Upwelling is well depicted by the upward movement of the subsurface water (35.7 psu) and erosion of

halocline till 600 km. Orientation of isohalines in the vertical direction, around 200 km away from the coast, shows a convergence zone (upwelling front). Further to the east at a distance of 450 km from the coast, a cellular structure of high salinity is seen at a depth of 50 m. The boundary between the low salinity (36.0 to 36.1 psu) water at west and the high salinity water (36.1 to 36.4 psu) east of it, causes a haline front around 600 km from the coast. These fronts extend vertically up to 120 m.

Fig. 4.10 shows temperature-salinity profiles during July corresponding to the northern transect. There is a well defined body of water at 220 m depth with properties 18° C and 36.4 psu at N2. Also the upper 200 m shows large fluctuations in salinity. At the central region, at a depth of 250 m, a water body with properties 16° C and 35.8 psu is seen. T-S distribution at the easternmost extent of the transect shows a high saline water body at a depth of 200 m. The corresponding properties are 16.5° C and 35.8 psu. The water column extending up to 150 m represents a neutrally stable condition in the middle and the northeastern regions. Below 500 m an abrupt increase in salinity is seen from N8 to N11. However, to the west of this stations no such distinct increase is seen.

The T-S properties along the southern transect during July- August is shown in figure 4.10. Unlike January and March distributions, the T-S characteristics at the stations near the coast show a highly complicated pattern. There is a manifestation of water body at 270 m. The corresponding temperature-salinity values are 15° C and 35.9 psu. T-S distribution in the central portion shows a neutrally stable water column from 100 to 160 m. At 250 m, a water body characterized by 16° C and 36.0 psu is seen. Between 160 and 254 m, the water column is highly stable. T-S characteristics at the farthest station show that the water column is highly stable below 215 m compared to the upper water while from 84 to 200 m, it is neutrally stable. High salinity water is seen at southern stations below 500 m. This signature is very distinct towards south (S13).

4.2.4 *Distribution of temperature and salinity at the northern and southern transects during August-September*

Fig. 4.11 shows the distribution of properties along the northern transect during August. The orientation of the isotherms reveal a strong upwelling at the western part of the transect. This results in less variation in the vertical gradient of temperature of the water column at the west. The mixed layer is present to the east of 500 km from coast and it gradually increases towards east. Similar to the distribution during July, an intensified wavy nature of isolines below 100m is seen near the coast.

At the west of transect there is one to one correspondence between the features seen in temperature and salinity sections. A high saline water with a horizontal spread at 200m is seen at the west. This in turn causes the erosion of the halocline at the west. To the west of 800 km the water column shows less vertical variations. The mixed layer depth at the eastern part of the transect is 50 m.

The distribution of properties during August – September 1995 along the southern transect shows a mixed layer that develops to the east of 800 km from the coast with further increase to 40 m at the east (Fig. 4.12). Surfacing of thermocline is evident to the west of 800 km. The gradient in thermocline at the west is $0.04^{\circ}\text{C m}^{-1}$ and at the east is $0.07^{\circ}\text{C m}^{-1}$.

The halocline is absent till 800 km from the coast due to upwelling. This further results in lesser variations in salinity of the water column with more vertical extent at the west. But from the east of 800 km, the halocline develops and the gradient increases towards farthest station (0.07 m^{-1}) Another characteristic feature of the region is the presence of low saline water at the west and a high saline water at the east at the surface.

The T-S relation along the transect during August is shown in figure 4.13. A water body is seen around 280 m with properties 17°C and 36.5 psu. Low salinity is evident in the upper 40 m. The central region (N6) shows the presence of water body characterized by 16°C and 35.9 psu at 250 m depth. From 50 to 90 m the water column is neutrally stable. The T-S profiles at the

eastern station depicts similar characteristics as that of July. A water body at 220 m depth with a characteristic of 16° C and 35.7 psu is clearly seen. The water column in the upper 140 m is neutrally stable in the eastern region of the area. High stability below 140 m is a characteristic feature of the eastern region. The high salinity signature is seen below 500 m, eastwards of N9.

The T-S characteristics of the southern transect during August-September. The T-S relation at the coastal station clearly reveals high fluctuations in properties and distinct water body (Fig 4.13). The characteristics of these water bodies are 16° C, 35.75 psu at 160 m. The central and eastern regions of transect show a large range in salinity in the upper 500 m compared to the coastal station. Presence of water body with properties 16° C and 36 psu is clearly depicted at 250 m in central region while the farthest station do not show any signature at this level. The water column in the middle region is neutrally stable from 90-180 m while that at the east it is from surface to 215 m. Below 500 m, at the southernmost stations of the southern transect, high salinity signature is distinctly seen.

4.2.5 Distribution of temperature and salinity at the northern transect during December

The temperature and salinity distributions at the northern transect during December are shown in figure 4.14. An important feature seen in the temperature section is the regeneration of mixed layer (~20 m) to the east of 400 km from the coast. The gradient of thermocline is stronger at the east ($0.065^{\circ}\text{C m}^{-1}$) than at the west ($0.03^{\circ}\text{C m}^{-1}$). The presence of warm water body (18-20° C) within the thermocline at the west causes the reduction in gradient of the thermocline. The thickness of the uniform layer of water body decreases compared to that along the transect during the previous month. The downward sloping of the isotherms towards the coast reveals sinking.

Similar to the temperature section, mixed layer is prominently seen in the salinity section at the eastern part of the transect. A high saline water in the form of a tongue protruding from the west extends to 300 km in the

subsurface region. The salinity of the core of the tongue is 36.6 psu. Though there is a well defined halocline, its strength increases from west to east. The high saline water (36.7 psu) seen at the surface throughout the transect is the result of intense evaporation during this season.

Fig. 4.15 shows the property distribution along the southern transect during December 1995. The distribution of properties along the transect shows certain remarkable feature which are different from that during previous months. A mixed layer (40 to 70 m) is depicted in the transect. The thermocline is uniform throughout the transect with strongest gradient ($0.09^{\circ} \text{C m}^{-1}$) at farthest station.

The salinity at the surface, along the transect, increases towards east from 36.4 to 36.7 psu. Up to 600 km from the coast, a high saline water is seen in the subsurface region. Further, this region shows development of halocline that strengthens eastward. The detail analysis further shows that the halocline further widens at 1250 km from the coast depicting the presence of uniform low saline water (36.4 psu)

T-S profiles along the northern transect is shown in figure (4.16). The T-S relationship shows a well defined water body around 230 m. It's properties are 17.5°C and 36.7 psu. A water body with high salinity are seen at the central portion at 225 m. The characteristics of this water body are 16°C and 36.0 psu. At the eastern region of the transect a water body is seen at a depth of 190 m (16°C and 35.8 psu). The water column is neutrally stable up to 50 m at the western region while it is between 44 and 130 m at the central and eastern regions. The salinity increase is seen below 500 m from stations N9 to N11.

The T-S characteristics at southern transect during December shows that water column between 20 and 65 m is stable at the west and between 44 and 84m in the central region with an exception at the east, where the water column is stable between surface to 170 m. Moreover, the T-S diagram shows the existence of high saline water bodies existing at 300 m at west and 250 at central region. The easternmost and westernmost stations also show increase in salinity below 400 m while such a feature is absent at central and western stations.

4.3 *The water column stability in response to the seasons*

The analysis of the hydrographic properties along the two transects reveal a high degree of anomaly at the western region compared to the eastern region. This anomaly is depicted as a weak/absence of thermocline and halocline, which are responsible for development of high stability of the water column. Thus the anomaly is represented by the decrease in stability of the water column. Hence, to quantify this, the stability parameter is examined throughout the two transects. However from each transect only those stations are presented that show peculiarity in stability of water column. On the basis of the analysis of stability, the water column can be divided into three zones – the upper neutral zone, a layer of high variation in stability below it and a near neutral zone beneath the high variation zone.

Figure 4.17 shows the variations of stability at different stations of the northern and southern transects during January. The vertical distribution of stability at the western station (N2) shows neutral stability in upper 60 m. Beneath it, up to 250 m depth, the stability between the different layers highly fluctuates. The stability ranges from 0 to 6000 units. The depth of neutral stability in upper layer increases towards east (110 m) till N11. The zone of high fluctuations in stability decreases from western station (75 to 300 m) decreases towards east (100 to 200 m) with an exception at N7 (80 to 250 m). Here the stability do not show drastic decrease with depth, instead a secondary peak is seen at 225 m. The maximum stability at the west is 7000 while at the east it is 20000.

The stability of the water column along the southern transect are distinct compared to the northern transect. Unlike the coastal region at the northern transect the upper water at the respective region (S2) of southern transect do not show neutral stability over considerable depth in upper waters. The zone of high fluctuations decreases eastward till station S13 indicating an increase in stability. The maximum stability is low (4000) at coastal stations and increases to 16000 at S13. Southward of it the fluctuations is over a larger layer and the stability decreases to 7000 units. This indicates four fold increase in stability at S13 than the west.

The vertical variations of stability along the northern and southern transects during March-April are given in figure 4.18. The stability near the coast is highly irregular and increases to the center with further decrease towards east. The upper layer does not show neutral stability except at central region (N5). The vertical extent of the zone of high fluctuations of stability decreases towards center while further eastward it intensifies. Within this zone degree of fluctuations are more at the western and at the eastern region. At the west the maximum stability is less than 4000 while at the center it is 8000. Along the southern transect, the upper layer of neutral stability is absent. The zone of high fluctuations, seen at the subsurface, decreases away from the coast. Within the zone of high fluctuations a region of weaker stability exists between 75 and 110 m at central region (S10). The maximum stability at the west is 5000 while at the east it is 8000.

The vertical profile of stability at northern and southern transects during July-August are shown in figure 4.19. The zone of neutral stability is lower at coastal station (30 m) than at the eastward station (125 m). Below the neutral stability, throughout the section, there is a large fluctuation in the stability. The maximum stability at the coastal station is 20000 while at the eastern station it is 16,000.

The stability profiles at the southern transect is different from that of northern transect. At the coastal station the neutral stability is absent in upper layer while it is 100 m and 75 m at central region (S6) and southernmost station (S15). The vertical extent of the zone of fluctuations decreases from west to east. The maximum stability at the west is 8000 while at the east it is 16000.

The vertical profiles of stability at the northern and southern transects during August-September are shown in figure 4.20. The western region (N2) of the northern transect shows a high variation in stability in the vertical direction. This zone decreases towards east. Towards eastern region (N11) the upper layer show neutral stability while a highly stable layer is present beneath it. Further below it the variations decreases. Along the southern transect, at the western region (S3), the upper waters do not show neutral stability. The neutral stability develops and increases to the east (S15). The zone of high

fluctuations decreases eastward. At the west the stability ranges from 0 to 4000 while at the east it is 0 to 6000. As in the southern transect, high fluctuations are seen from surface extending to deeper region compared to that at northern transect.

The stability profiles along the northern and southern transects during December are shown in figure 4.21. The neutrally stable layer in upper water increases eastward. Below it, there is a zone of high fluctuations. It shows lesser variations at the west than at east. This is the only month wherein the variations at the west are less than that at east, at this transect. The maximum stability value at west is 20000 while it is 16000 at east. At southern transect, there is a neutral stability layer in upper 60m at west and increases to 150m at east. Beneath it, the zone of high fluctuations is seen to be decreasing towards the east. The maximum stability is 7500 at west (S2) while at east it is 8000 (S14) and at the central region it is 17000 (S11).

4.3 Seasonal impact on hydrography in terms of water type density

An important tool to analyse the water properties and identification of water mass is the T-S diagram. This tool does not reveal the fine structure (mode water) within the water column. The details of estimation of Water Type Density (WTD) are given in methodology. The WTD have been presented from few stations of both northern and southern transects that depicts the presence of mode water.

Figure 4.22. shows the vertical profile of WTD. During January, at S15, low WTD is seen between 60 to 80 m and in March, at N11 and S11, the vertical profiles of WTD reveals smaller variations from 25 to 50 m and between 80 and 120 m. The profiles of WTD, during summer, at stations N1 and N7 shows low variations (Fig. 4.22). The respective depth zones are 120 to 150 m, 50 to 90 m. At station N11, such a feature is depicted between 30 to 55 m. During December, low variations in WTD is absent in the subsurface region throughout the two transects.

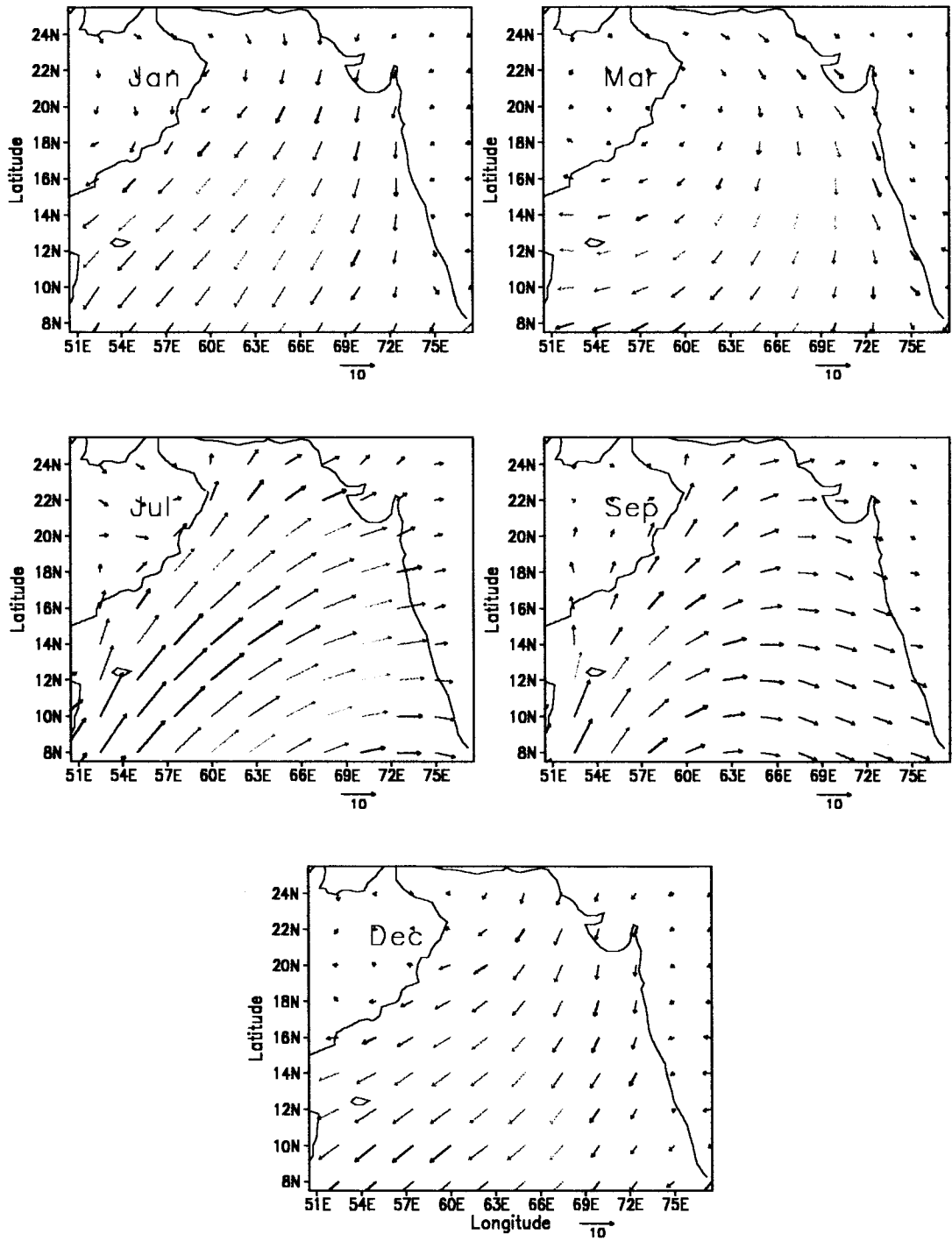


Fig.4.1 Winds speed (m/s) during 1995

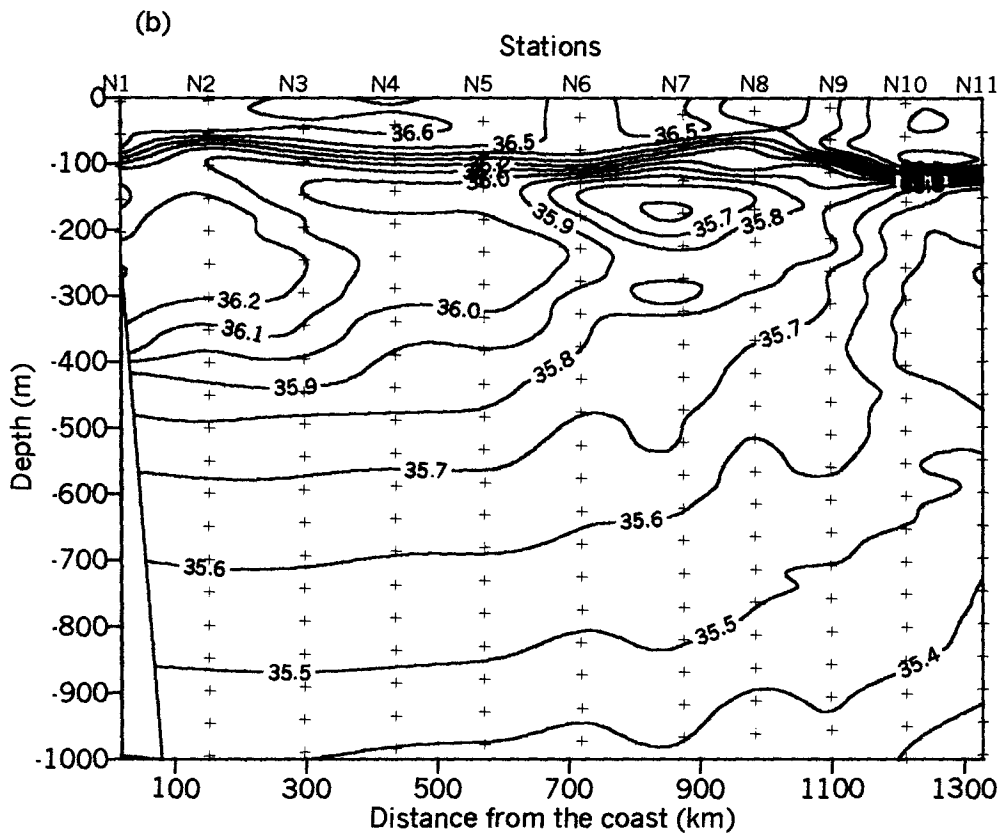
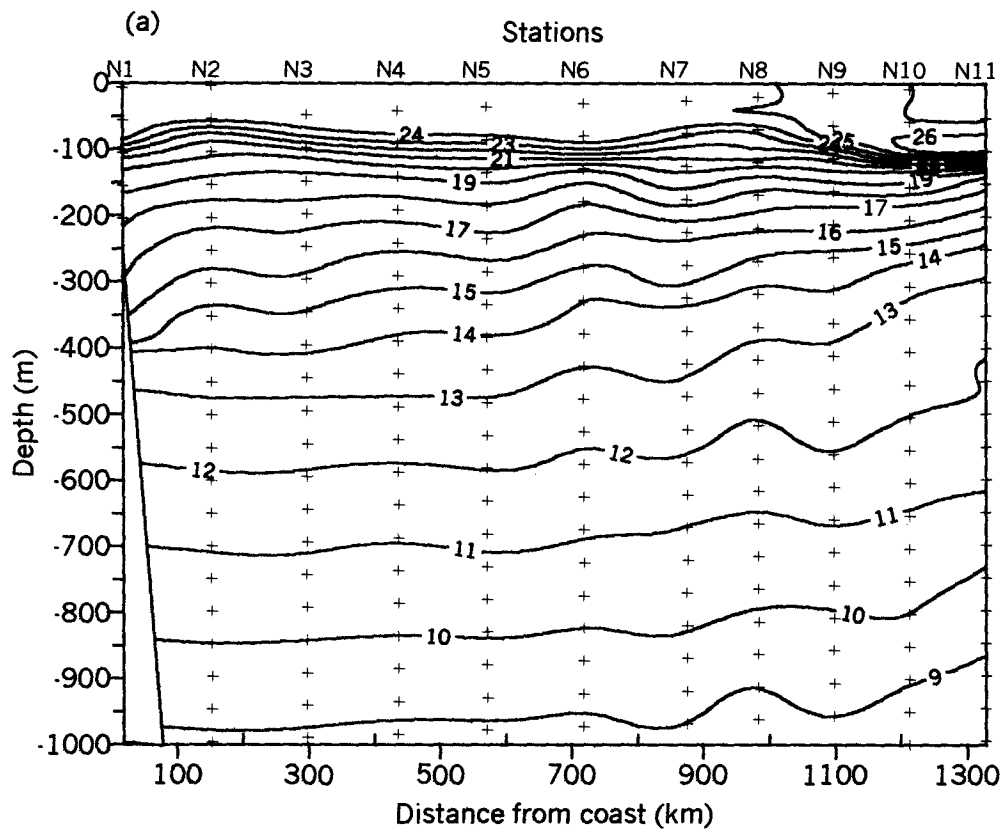


Fig 4.2 Vertical sections of (a) Potential temperature and (b) Salinity along northern transect during January

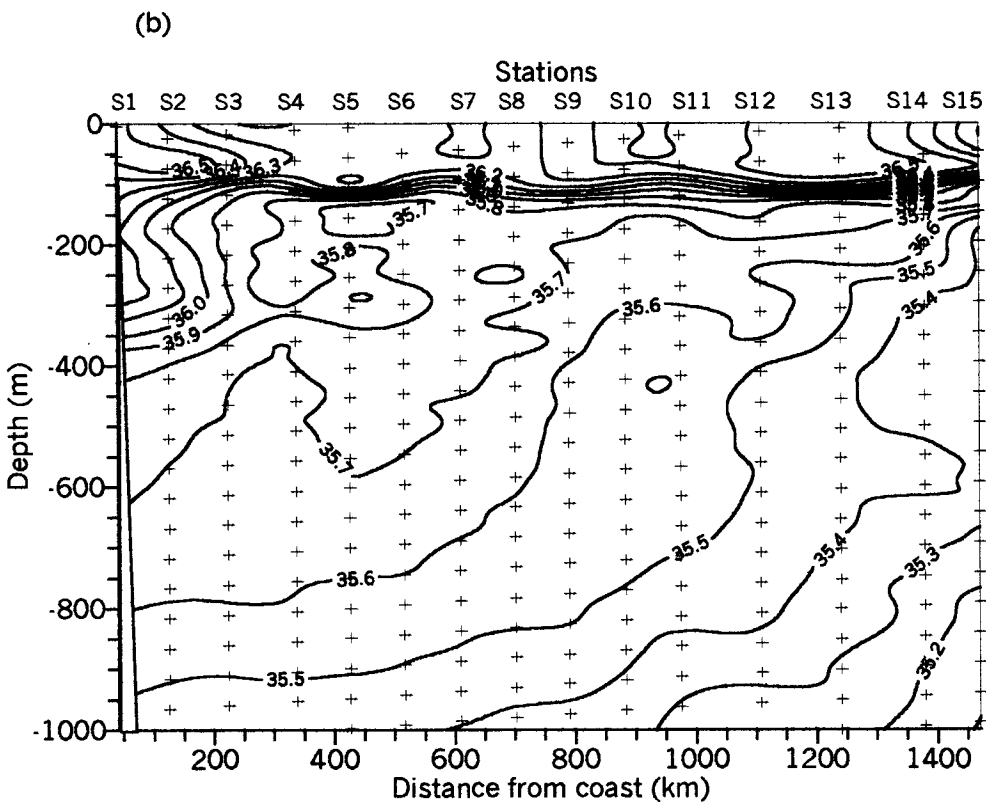
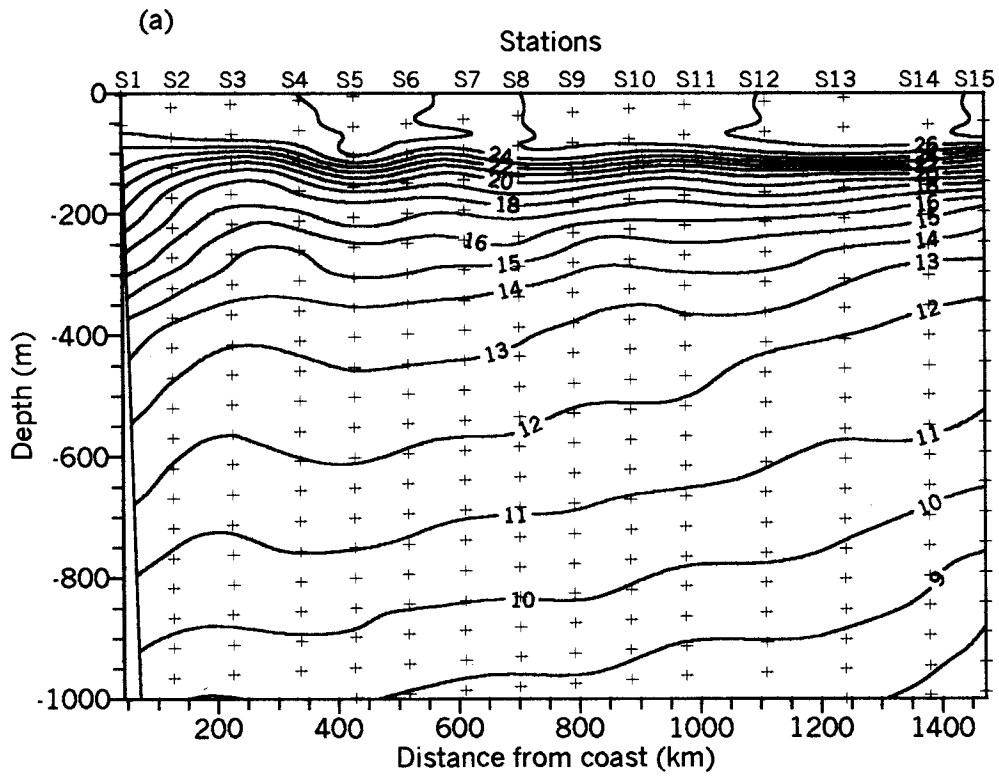


Fig. 4.3 Vertical sections of (a) Potential temperature and (b) Salinity along southern transect during January

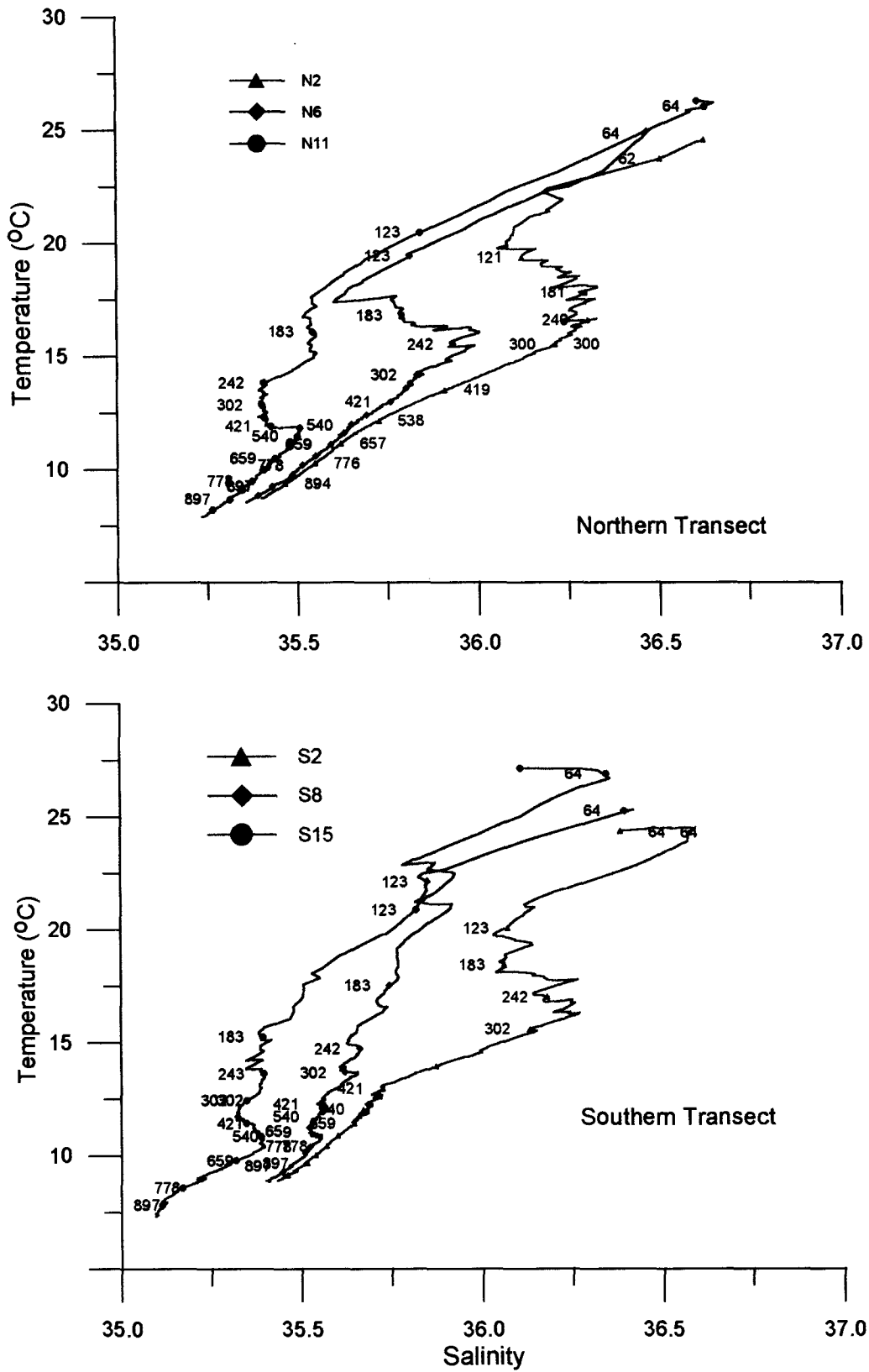


Fig 4.4 T-S profiles at different stations along the two transects during January

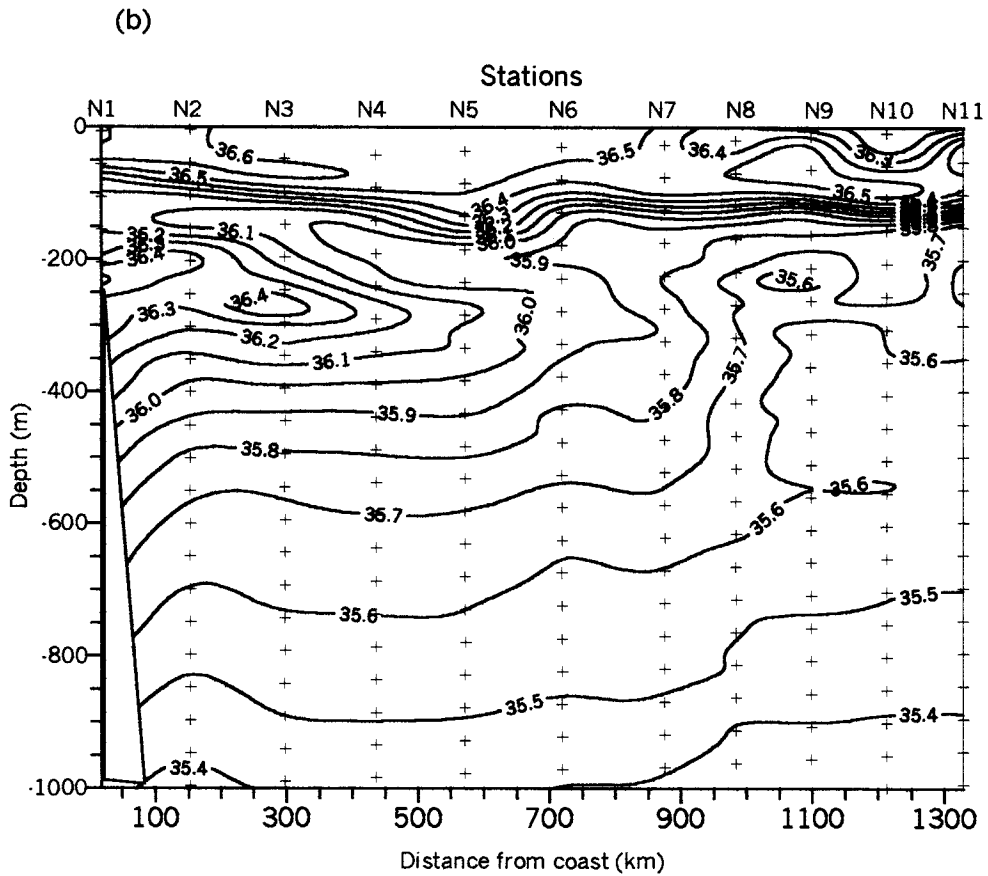
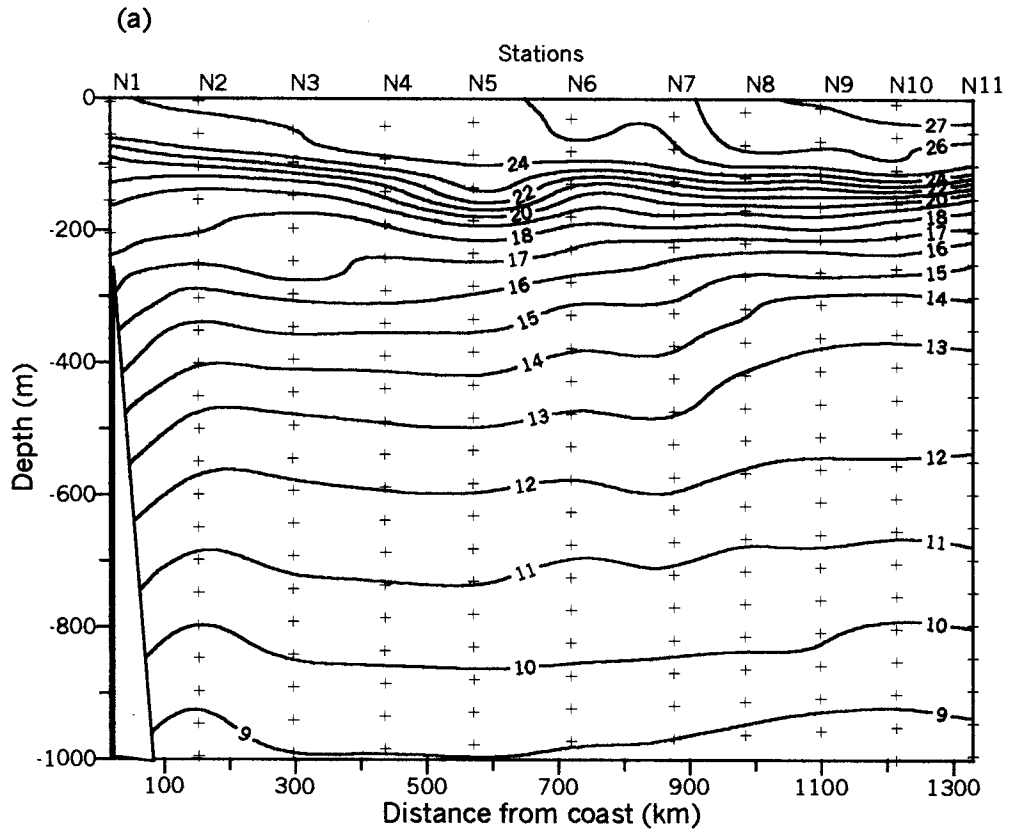


Fig. 4.5 Vertical sections of (a) Potential temperature and (b) Salinity along northern transect during March

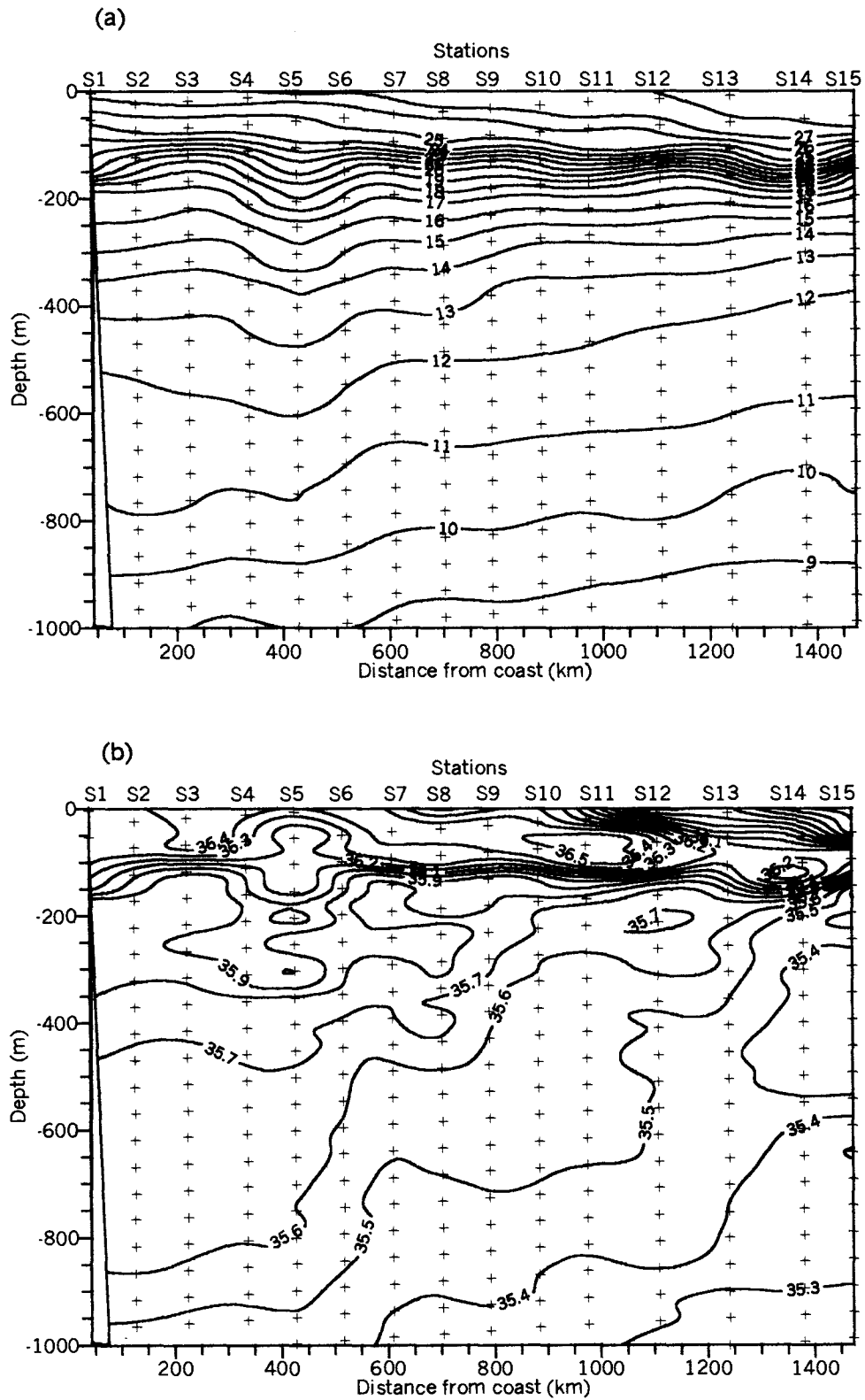


Fig. 4.6 Vertical sections of (a) Potential temperature and (b) Salinity along southern transect during March-April

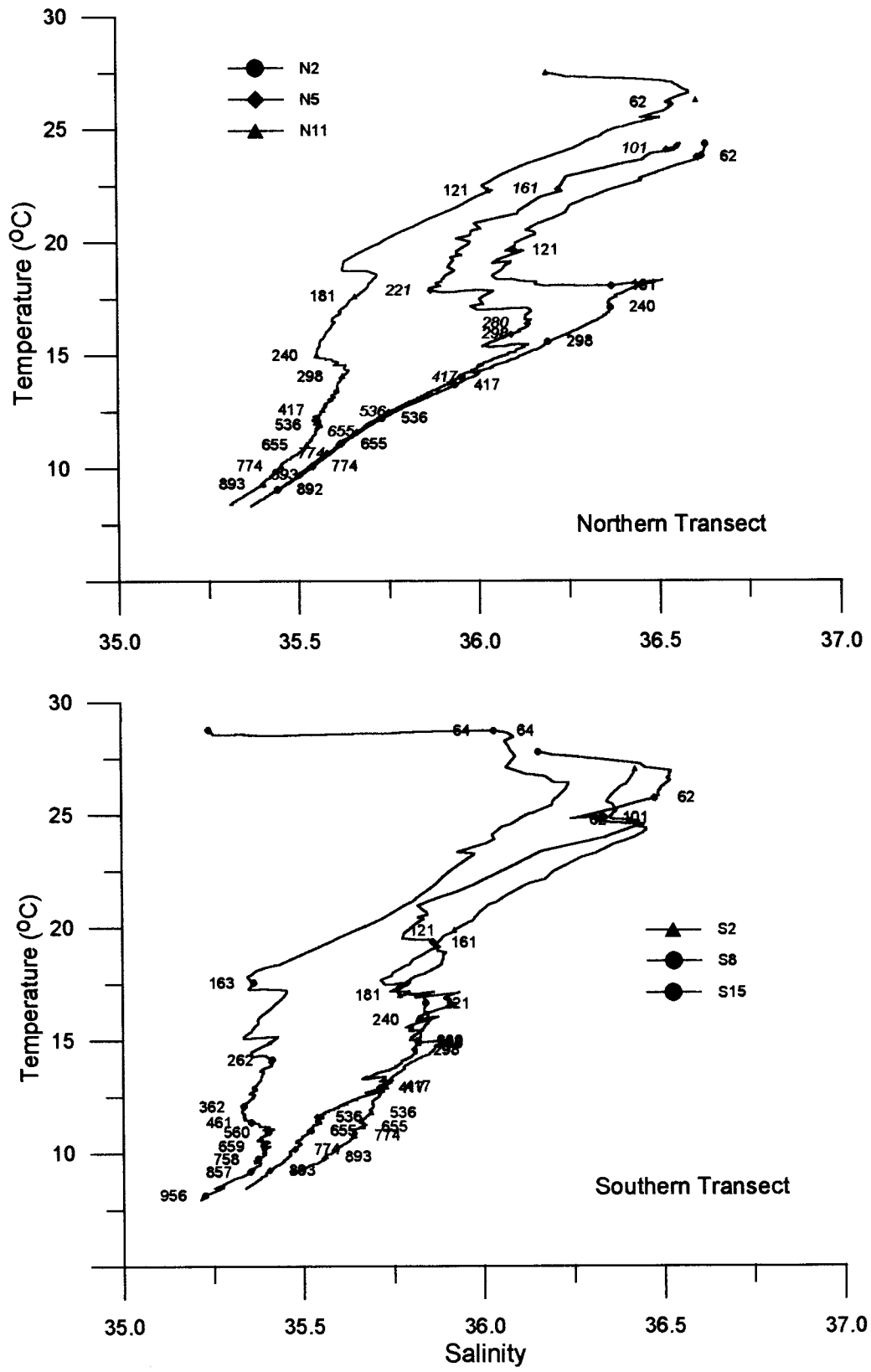


Fig 4.7 T-S profiles at different stations along the two transects during March-April

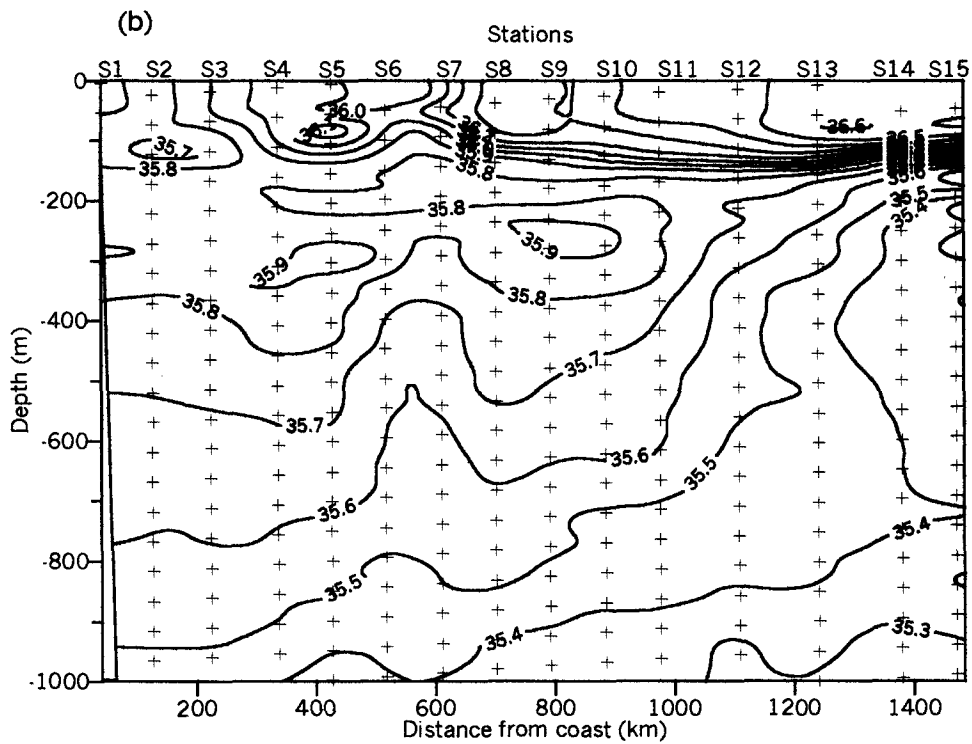
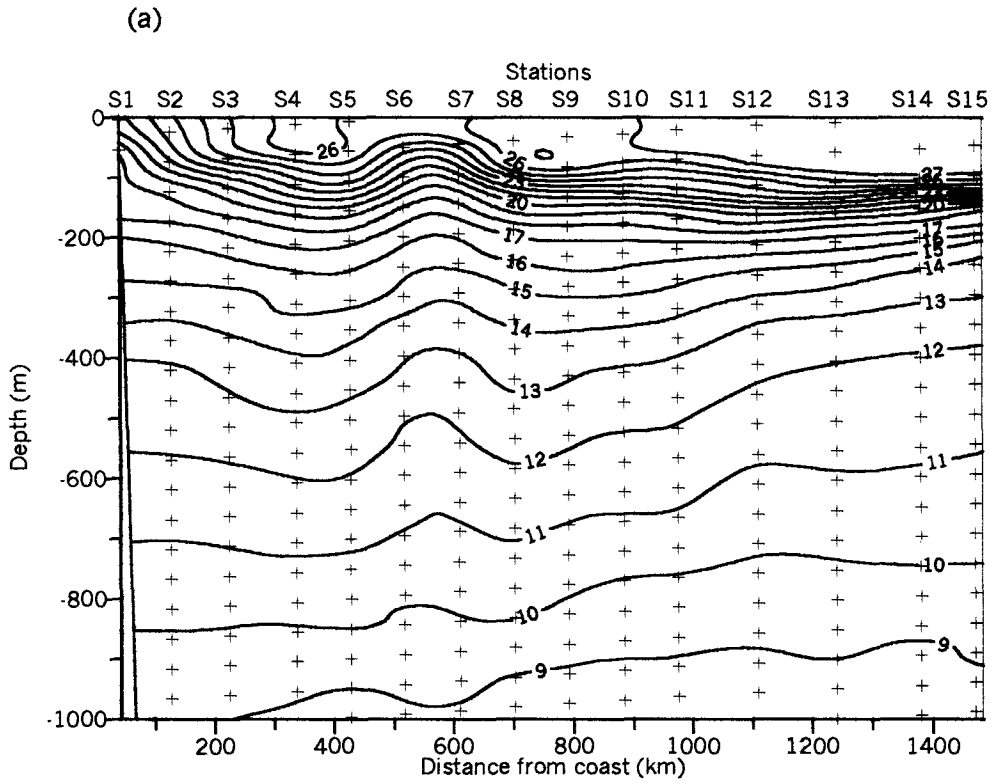


Fig. 4.9 Vertical sections of (a) Potential temperature and (b) Salinity along southern transect during July-August

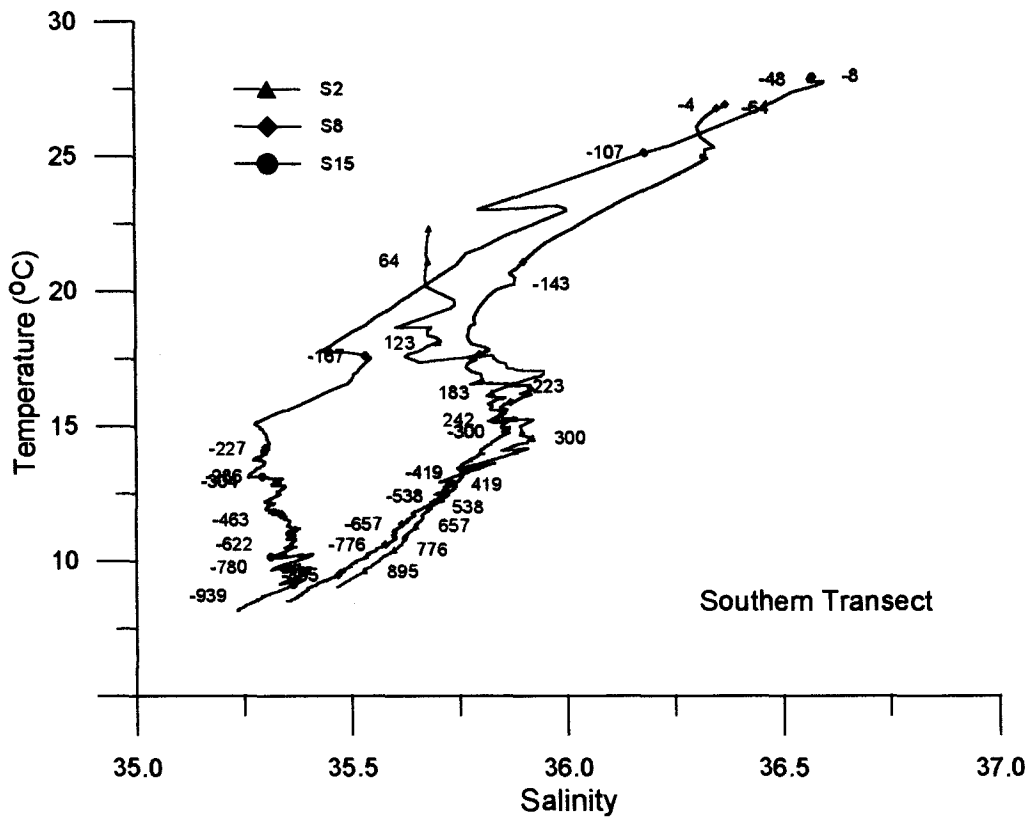
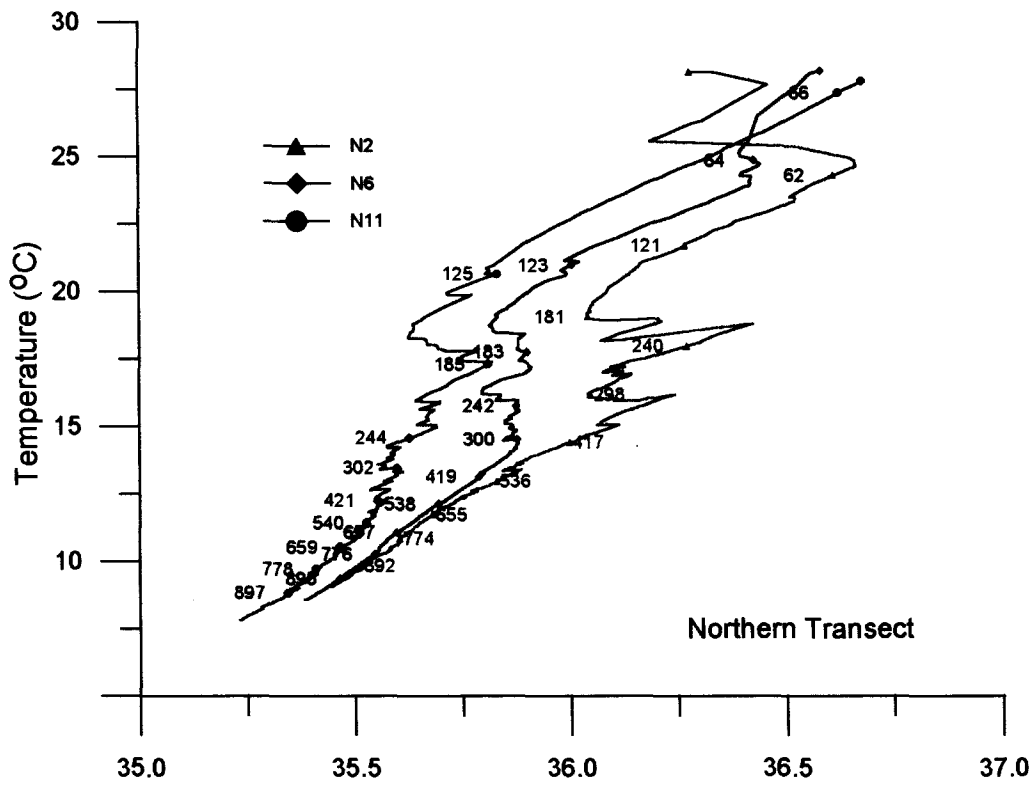


Fig 4.10 T-S profiles at different stations along the two transects during July- August

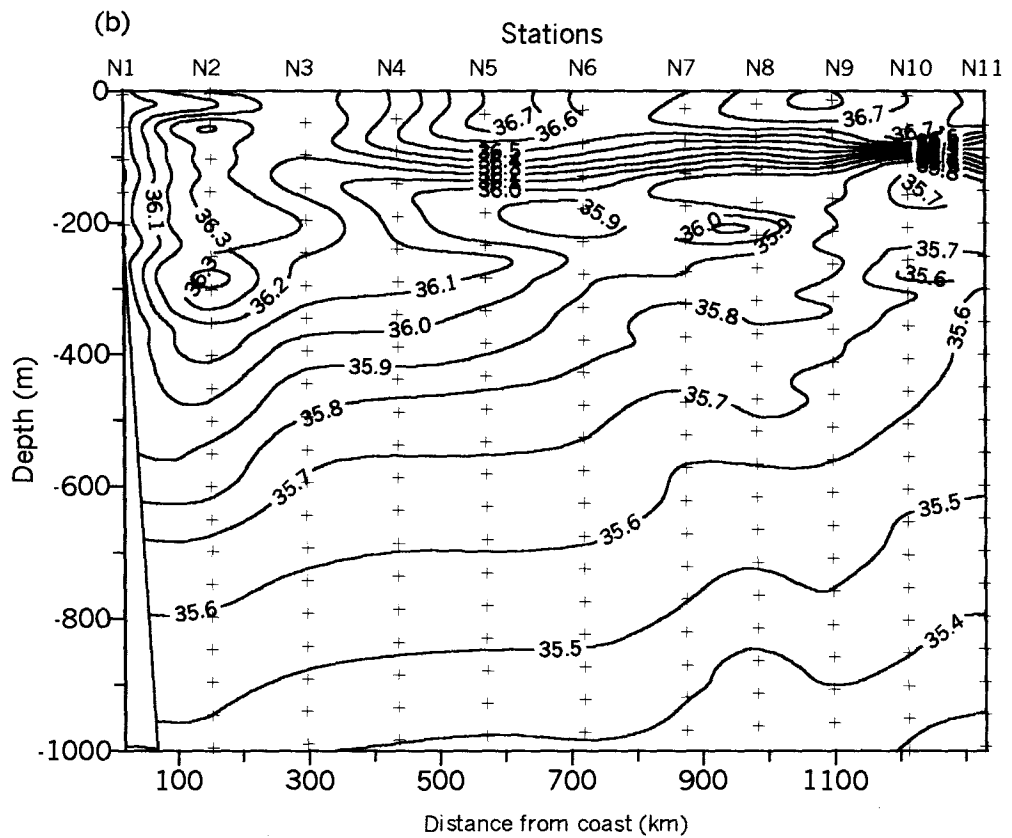
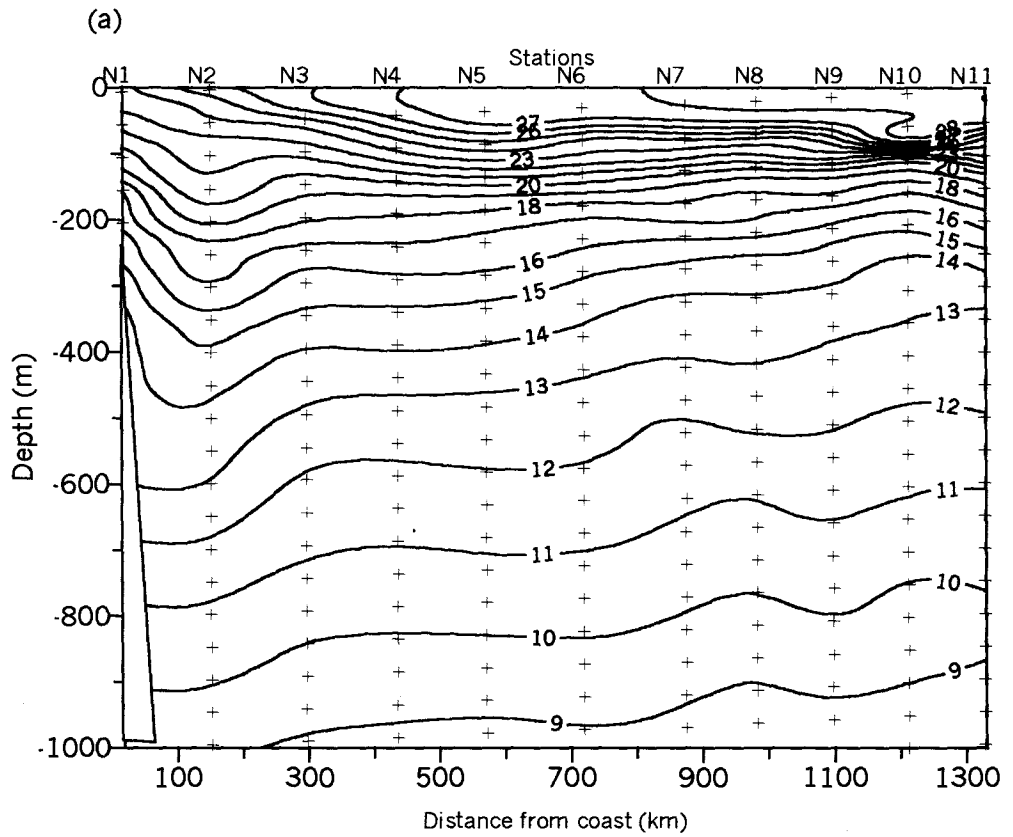


Fig. 4.11 Vertical sections of (a) Potential temperature and (b) Salinity along northern transect during August

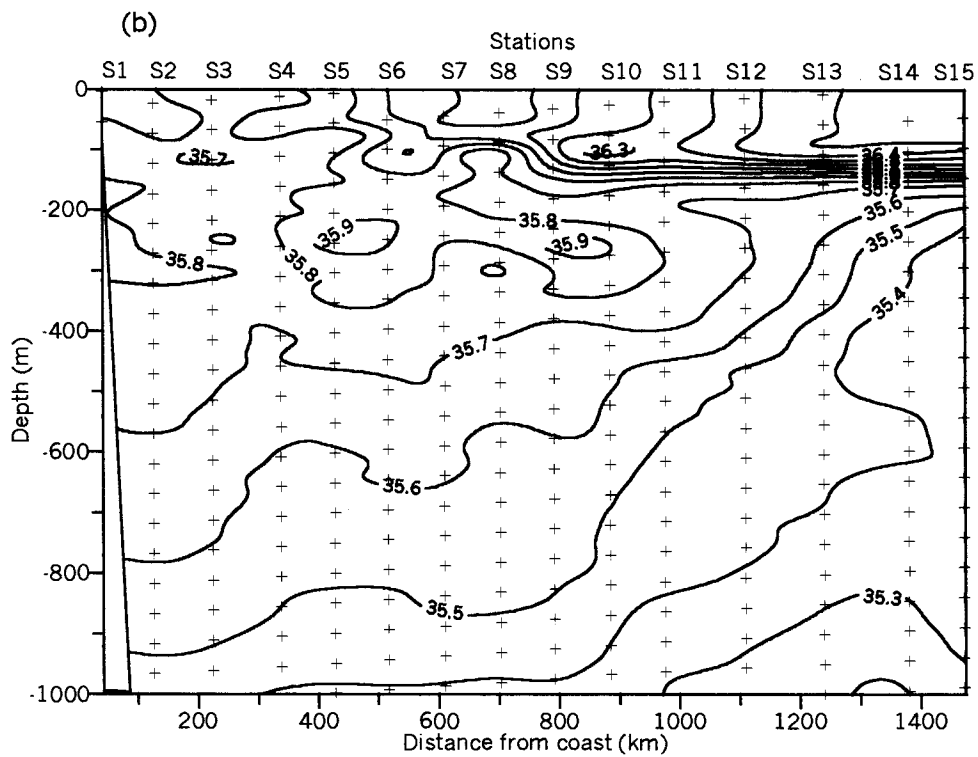
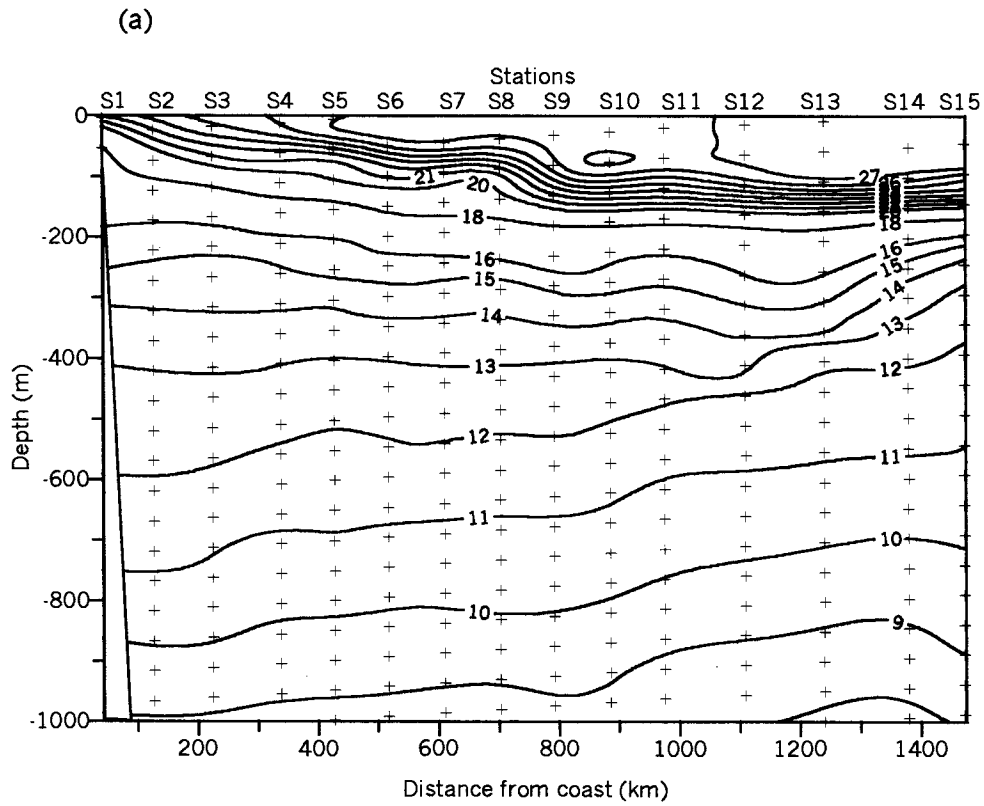


Fig. 4.12 Vertical sections of (a) Potential temperature and (b) Salinity along southern transect during August-September

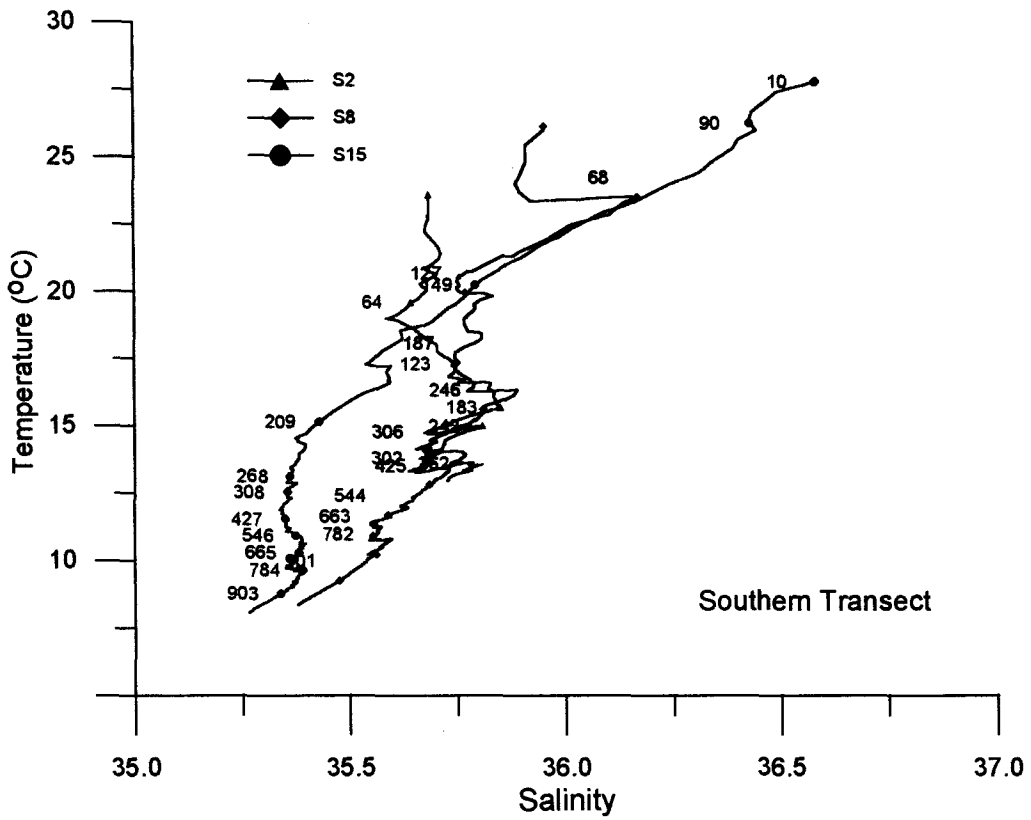
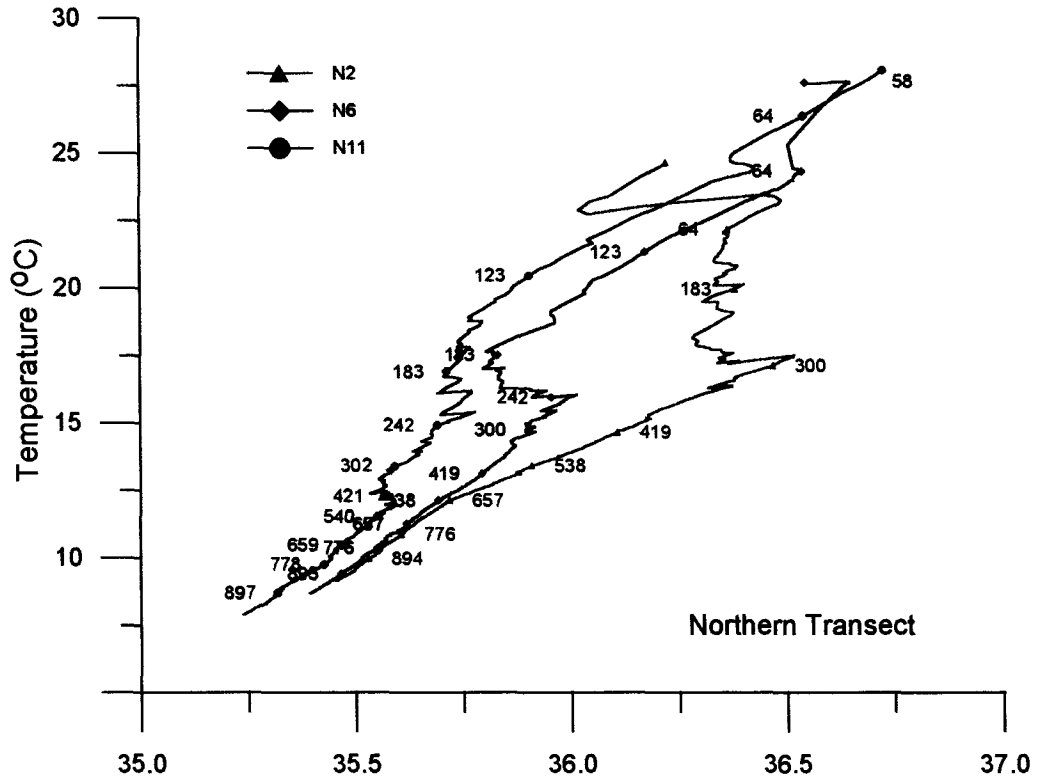


Fig. 4.13 T-S profiles at different stations along the two transects during August-September

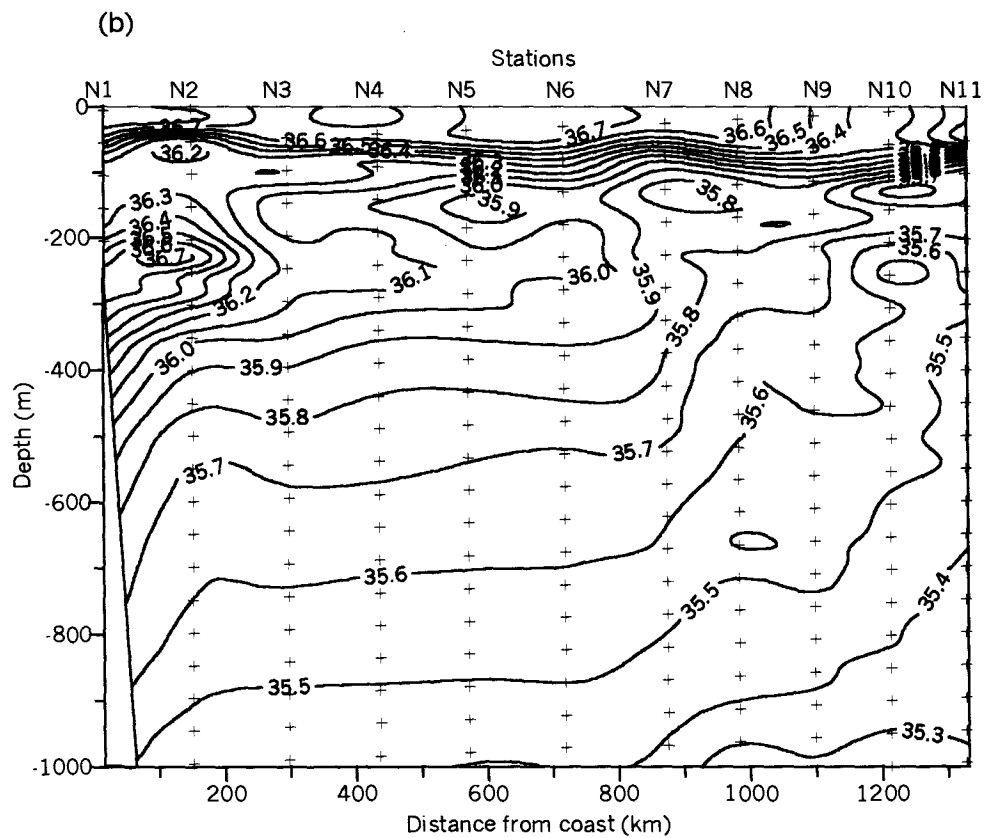
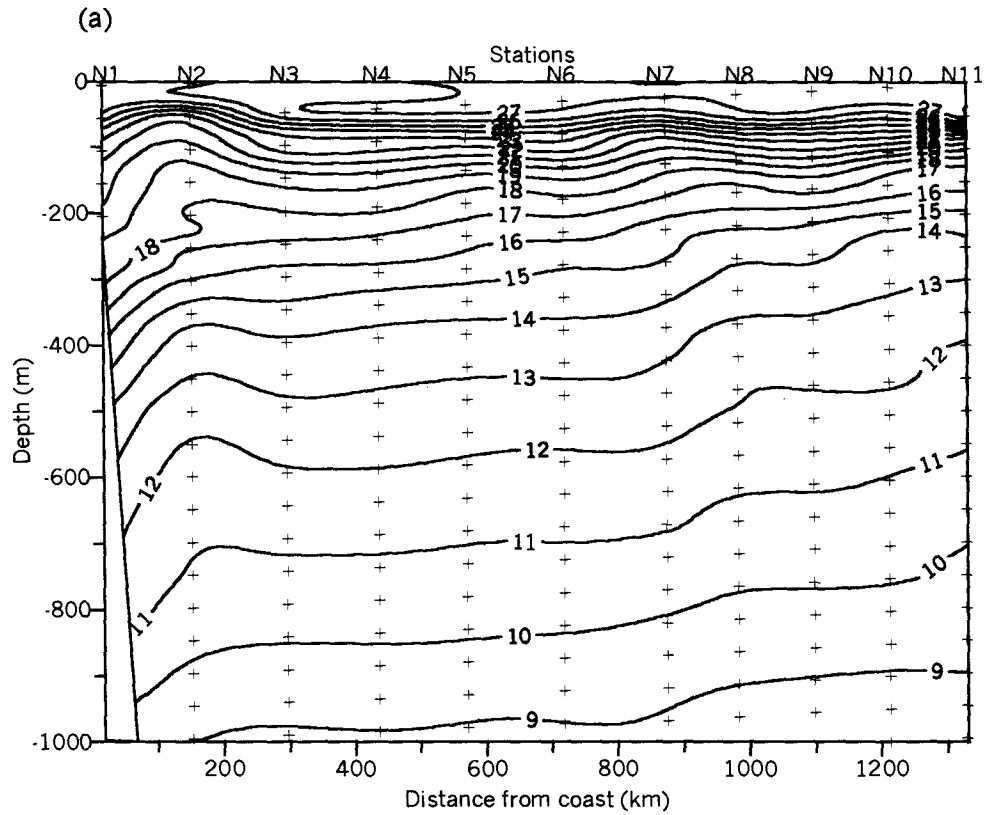


Fig. 4.14 Vertical sections of (a) Potential temperature and (b) Salinity along northern transect during December

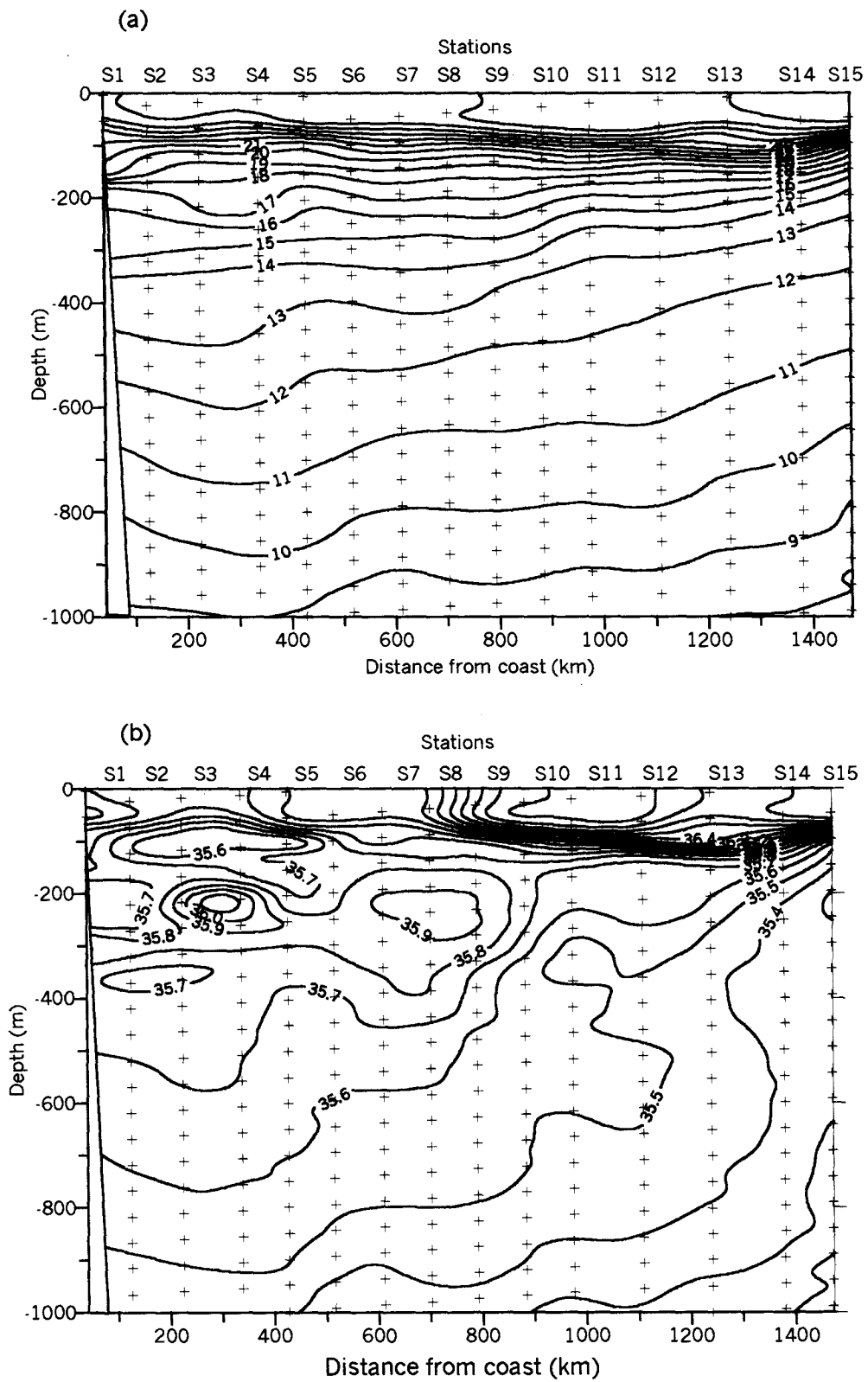


Fig. 4.15 Vertical sections of (a) Potential temperature and (b) Salinity along southern transect during December

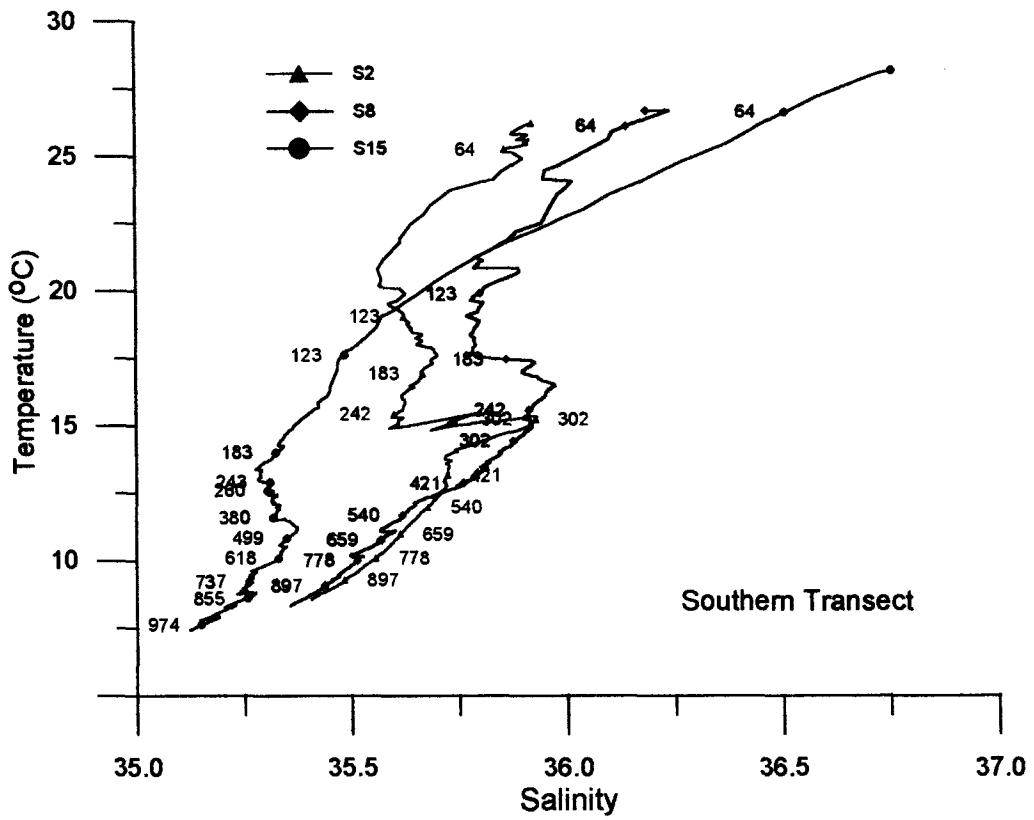
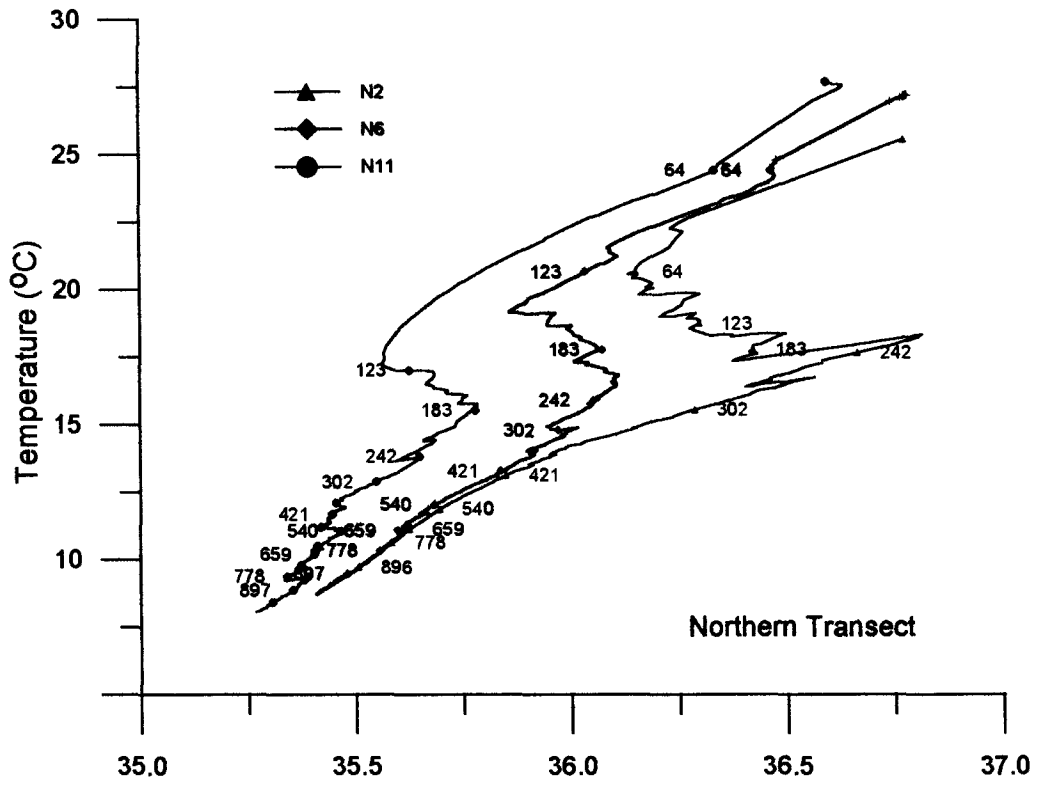


Fig 4.16 T-S profiles at different stations along the two transects during December

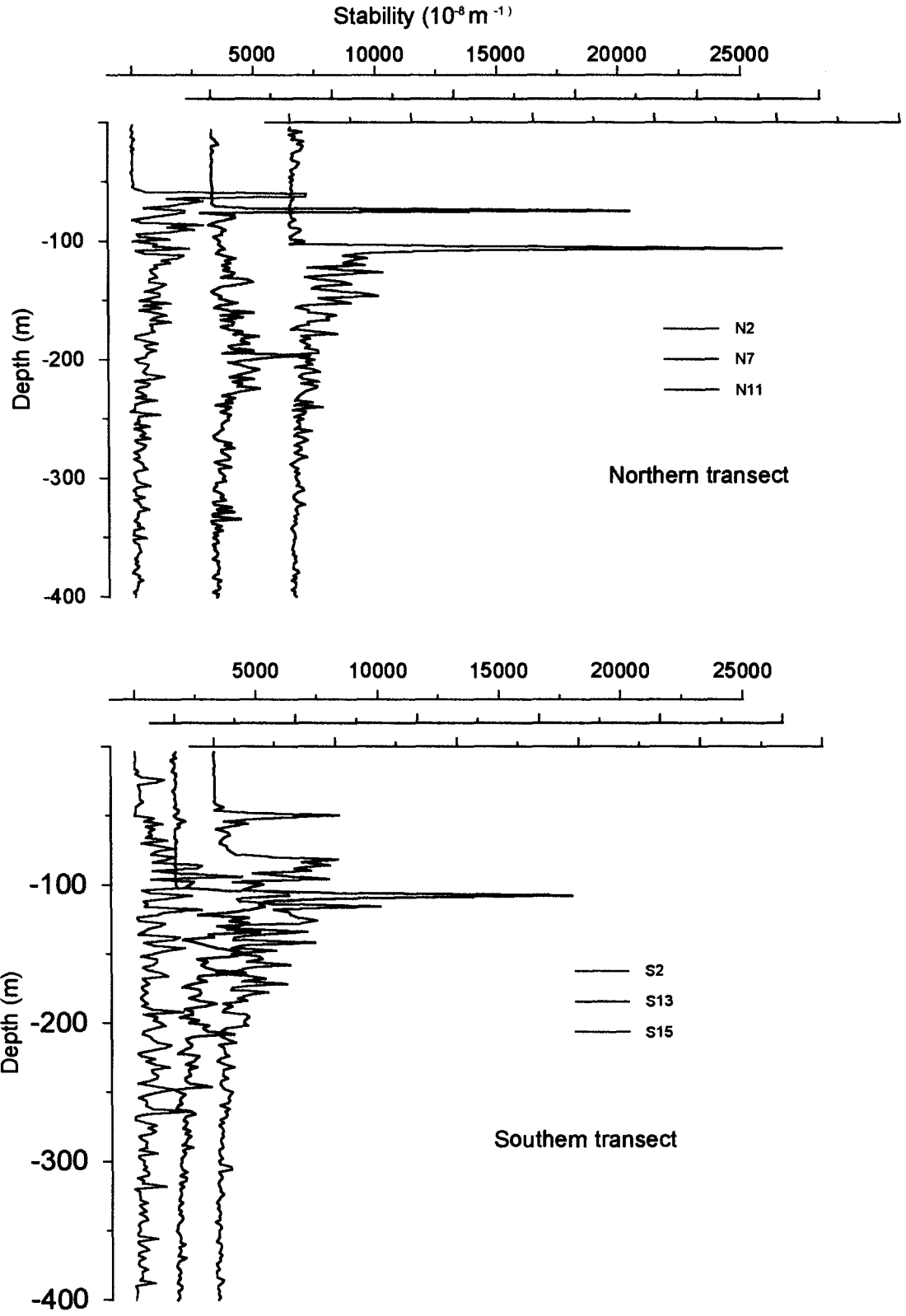


Fig. 4.17 Stability of water column at different stations during January

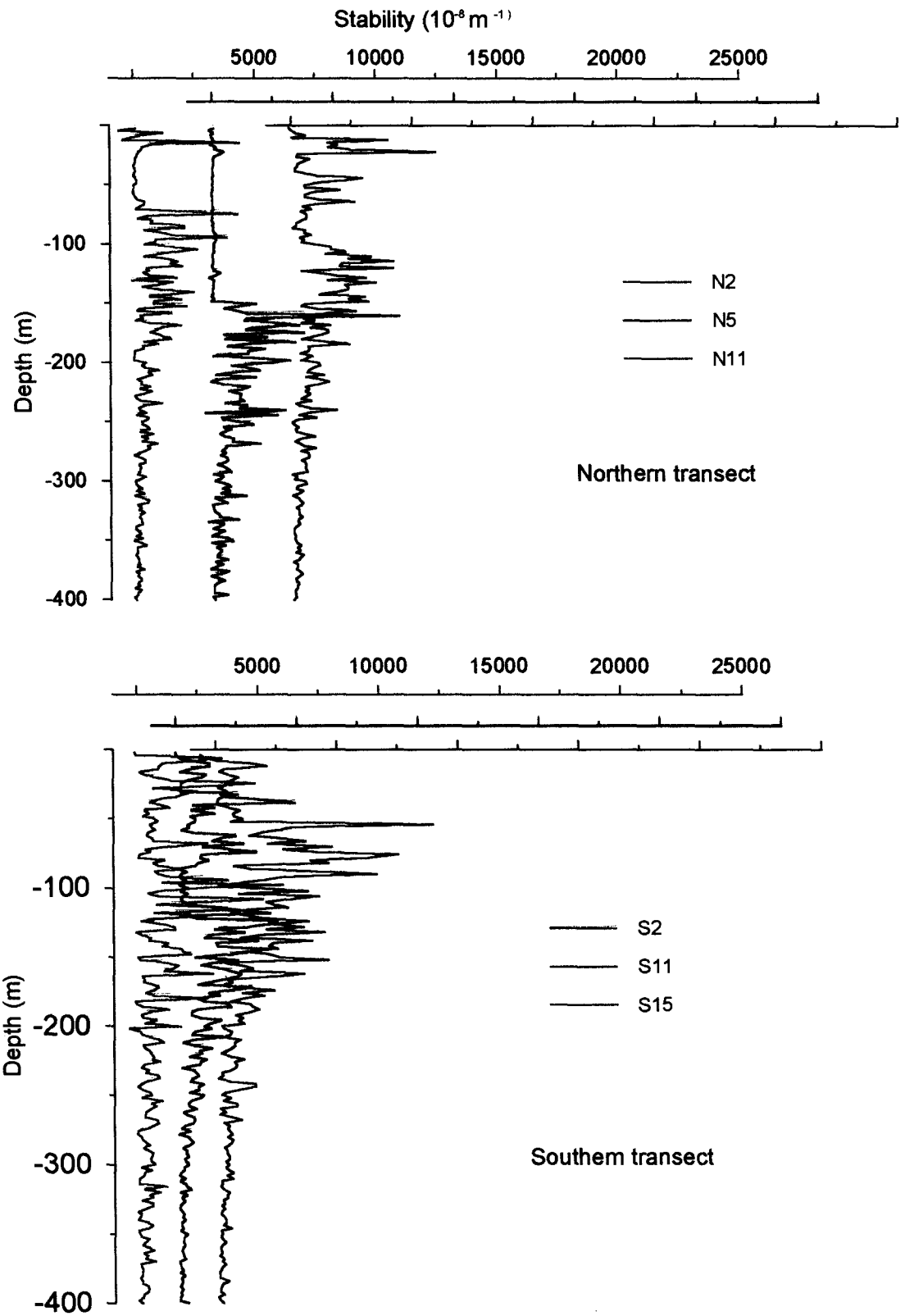


Fig. 4.18 Stability of water column at different stations during March-April

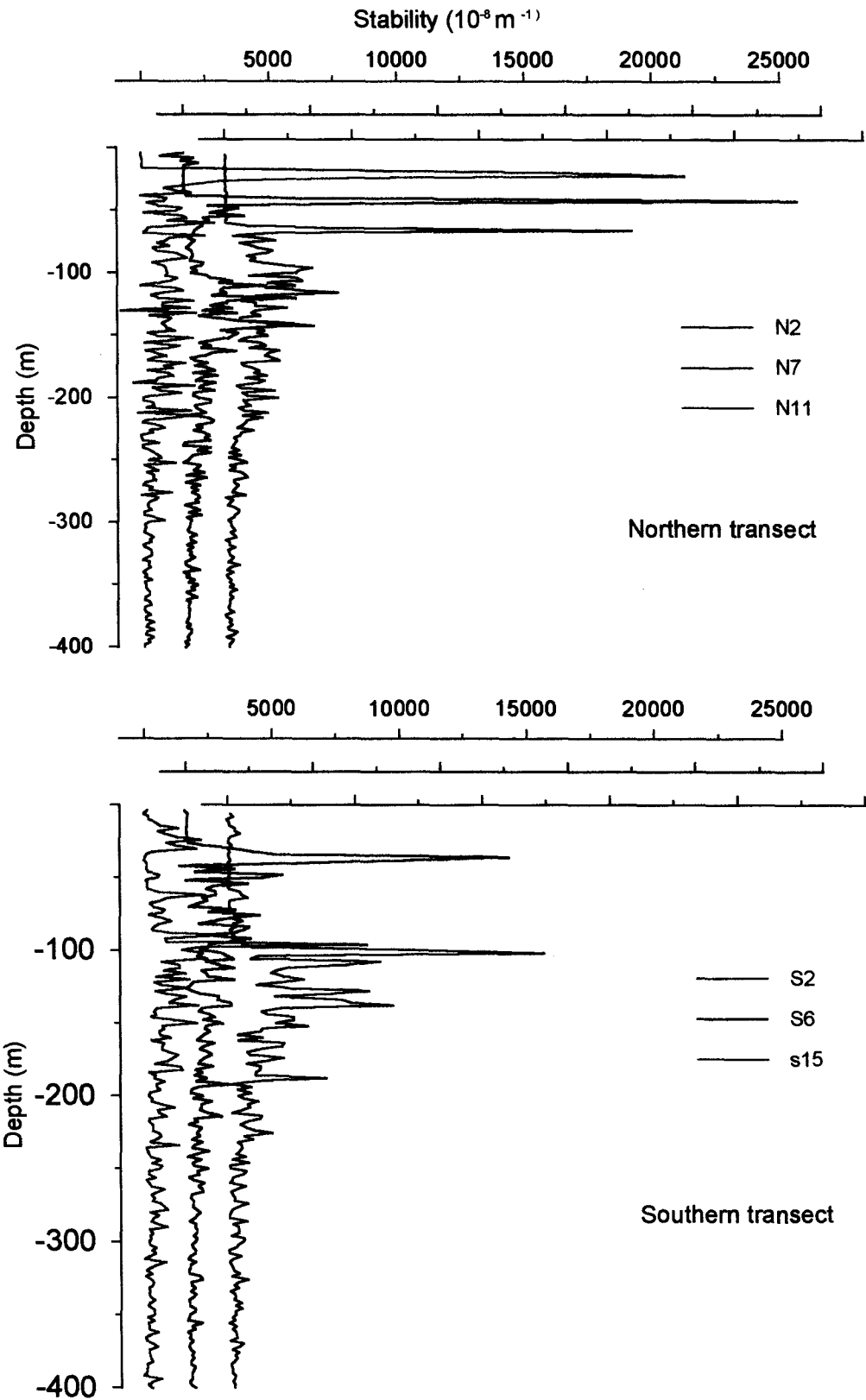


Fig. 4.19 Stability of water column at different stations during July-August

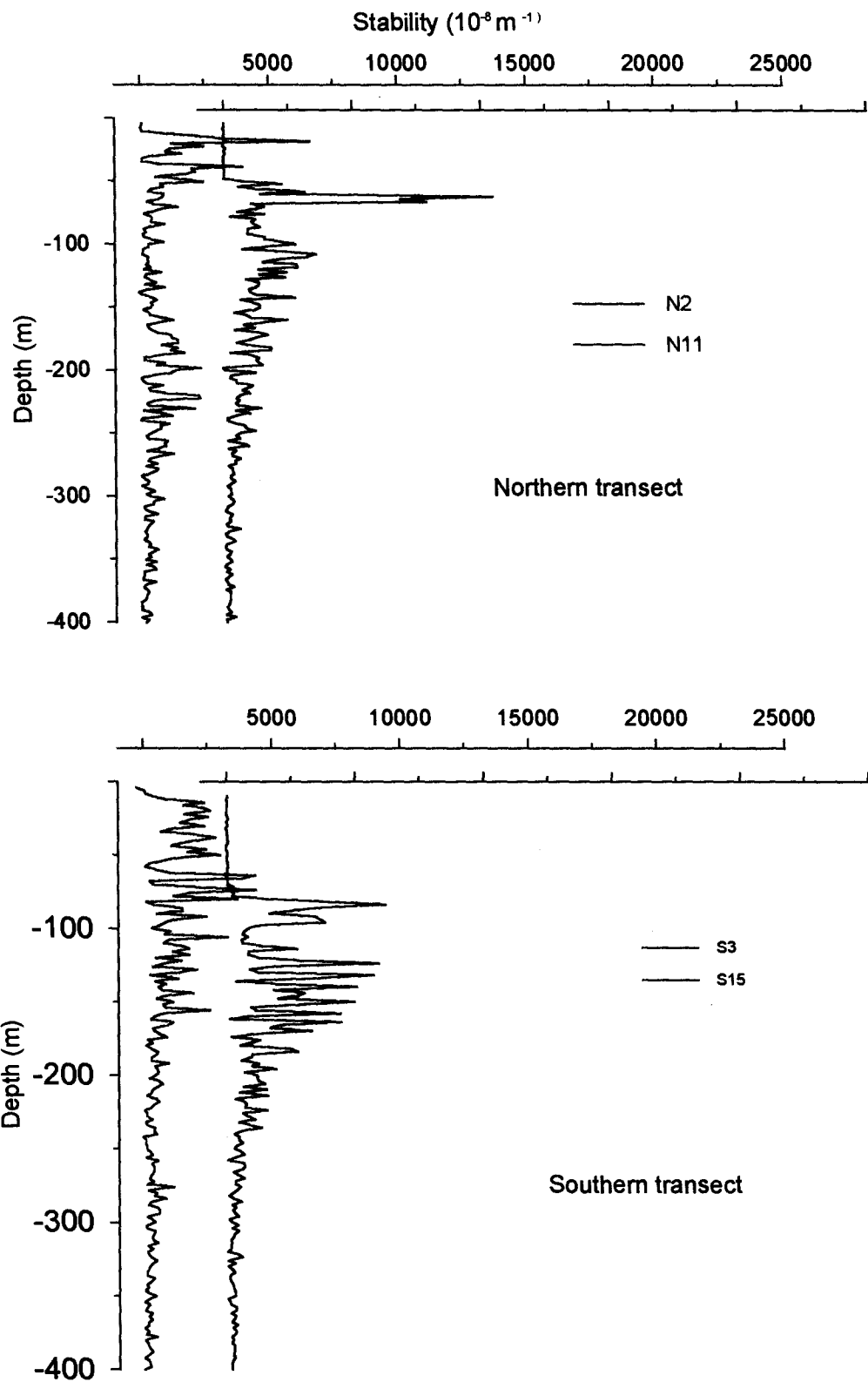


Fig. 4.20 Stability of water column at different stations during August-September

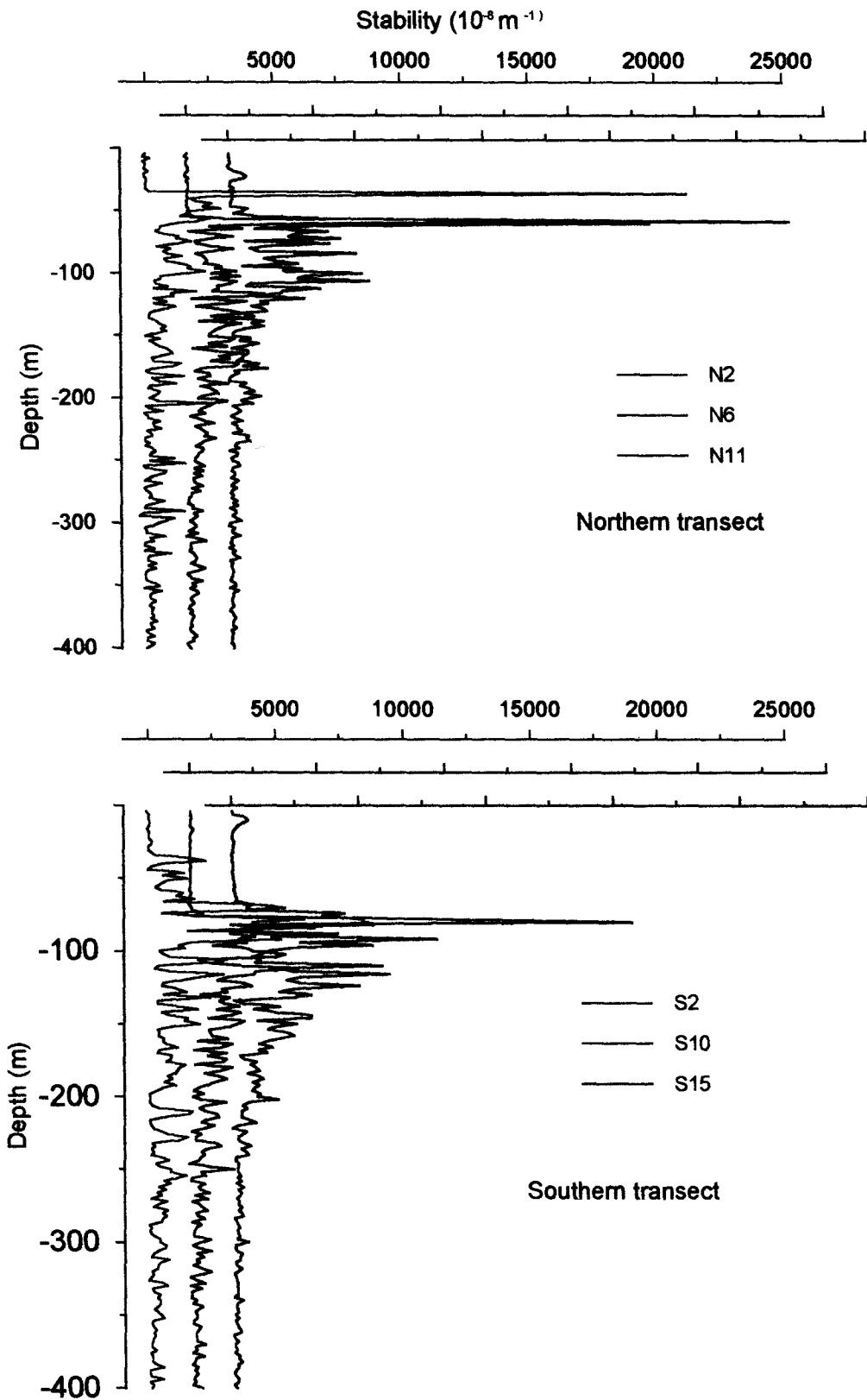


Fig. 4.21 Stability of water column at different stations during December

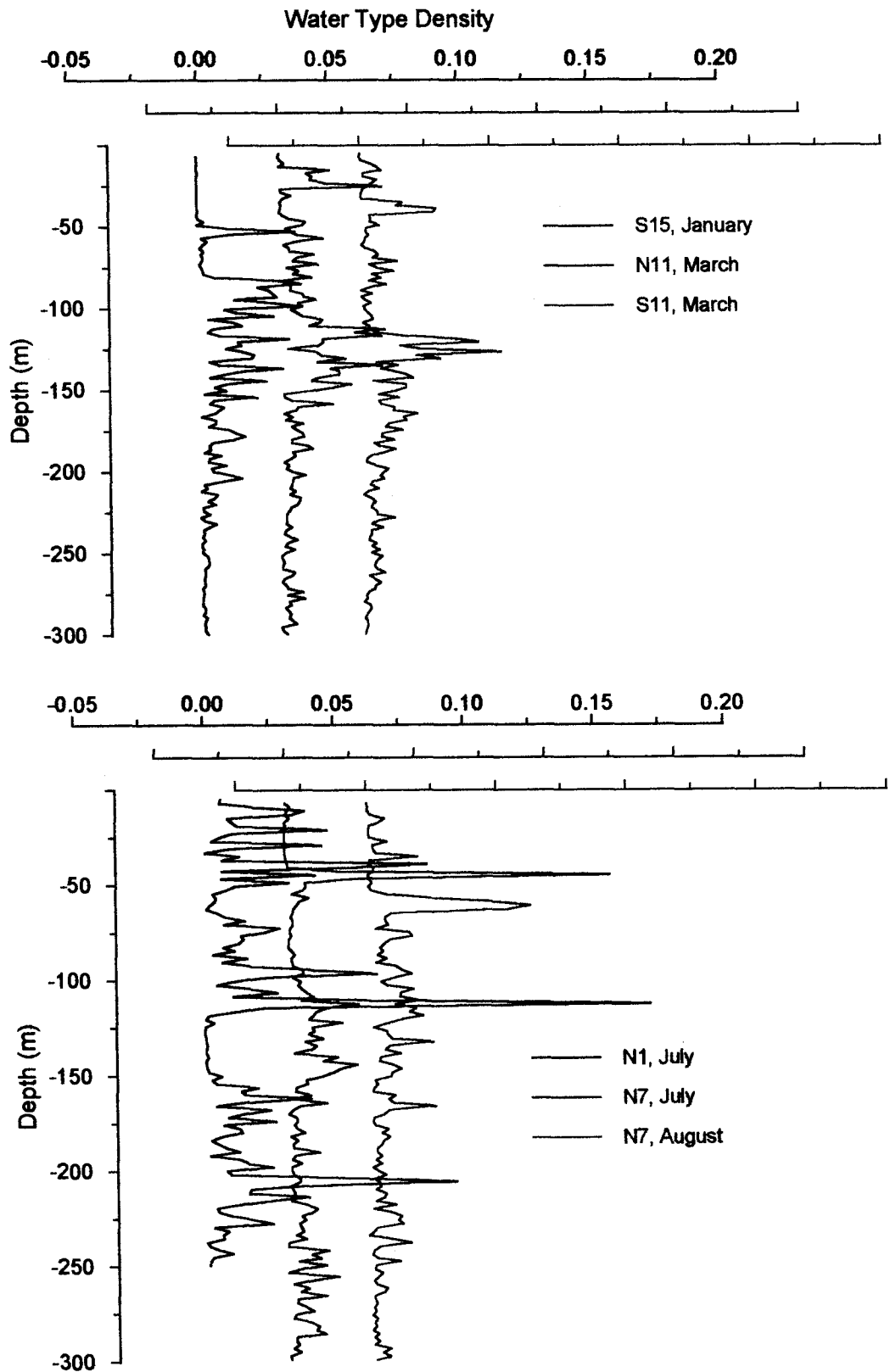


Fig. 4.22 Water Type Density at different stations

Chapter - V

Sea Surface Height Anomaly, surface Flow Characteristics and Kinetic Energy from Satellite Altimeter

Satellite observations give synoptic coverage of the sea surface thereby providing invaluable information. The present chapter deals with variations in sea level anomaly, geostrophic circulation and kinetic energy for mapping the currents and delineating energy rich zones. This study is carried out using TOPEX/POSEIDON derived sea level anomaly data of the year 1995 corresponding to cycle from 84 to 121. Each cycle has a duration of ten days. Due to instrumental failure, the data from 27th November to 6th December 1995, corresponding to the cycle 118, are not available. Observations corresponding to the cycles 84 and 121 covering few days of the year 1995 and extending to the years 1994 and 1996, respectively, have also been included in the study. Observations from cycles 119 to 121 and from 84 to 93 correspond to winter season. Cycles from 94 to 99 and 100 to 111 are of premonsoon transition and summer monsoon, respectively, while cycles from 112 to 117 is for post-monsoon transition. The periods of the cycles are presented in table II of chapter II.

5.1 Sea Level Anomaly, Circulation and Kinetic Energy during winter

Figure 5.1 shows variations in sea level anomaly (SLA) corresponding to January, February, March and December 1995. Since there is similarity in variation of SLA during the above months, the results of December 1995 are presented along with that of January, February and March 1995 as features of winter season. Cycles 84 to 93 correspond to January to March 1995. During

cycles 84 and 85 at the southeastern region, the positive SLA increases (+6 cm) and is depicted in the form of a core while at the southwestern region the negative SLA decreases (-14 cm). In association with these variations, the positive anomaly increases along the eastern and northern boundary. Cycle 86 shows a decrease in the positive anomaly at the southeastern region. Though the intensity of the negative anomaly (-12 cm) at the southwestern region is same, the area experiencing lower sea level increases. Further, the northward extent of the positive anomaly along the eastern boundary is less in comparison with cycle 85.

From cycle 87 to 89, the positive SLA at southeastern boundary increases. However, the positive anomalies along the eastern boundary do not spread in the northward direction. The negative SLA at the southwestern region decreases to -6 cm from cycle 87 to cycle 89 and extends offshore in the northeast direction. Also during cycle 89, positive anomaly develops off Oman and strengthens in the subsequent cycle. Cycle 90 shows entirely different variations in anomaly than the earlier one wherein a large area depicts positive anomaly. The negative anomaly seen at the southwestern region is absent. The westward spreading of positive anomaly is conspicuous by the extent of +4 cm contour. The negative anomaly, seen at 11°N and 60°E, is weak. From cycle 90 to 91 the high positive anomaly at the southeastern region further weakens and does not exhibit a core like structure. At the southern boundary, positive anomaly increases and propagates westward. From cycle 91 to 92 the high seen at the southeastern boundary propagates poleward. All along the boundaries the positive anomalies are evident while a weak negative anomaly is restricted to the central region. The SLA decreases poleward along the eastern boundary.

Cycle from 119 to 121 corresponds to December 1995. A negative sea level anomaly everywhere except at the southeastern region where a higher sea level exists during cycle 119. The southcentral region shows maximum negative anomaly (-18 cm). This negative anomaly extends to southwestern region and decreases as seen in cycle 121 (-9 cm). From cycles 119 to 121 the negative SLA decreases and is more pronounced towards west. At the southeastern region, the positive anomaly increases till cycle 121 and shows a

poleward and westward shift. In the rest of the region, negative anomaly weakens. During cycle 121, along the northern boundary, a positive sea level anomaly is depicted.

Figure 5.2 shows the geostrophic circulation from cycle 84 to 93. The prominent features seen are the cyclonic flow at the southwestern region and a poleward flow at the central part of the equatorward and eastern boundaries. The poleward flow forms an offshore limb of the anticyclonic eddy at the southeastern region and intensifies from cycle 84 to 88. Further, the eddy shifts in the poleward direction as seen in cycle 92. The currents at the equatorward boundary increases from 84 to 89 and it weakens till 93. The central and southwestern region show a cyclonic movement (cycle 87). The western and southern limbs of this cyclonic flow are strong and depict an equatorward and eastward flow. This flow starts weakening from cycle 87 to 93.

The negative SLA at the central and western side of the equatorward boundary and the high at the southeastern region are the major features associated with the geostrophic circulation during December. From cycle 119 to 121, the circulation pattern shows an anticyclonic nature at the southeastern region and a poleward flow along the eastern boundary (Fig. 5.1). This poleward flow associated with the offshore limb of the anticyclonic movement intensifies from cycle 119 to 121. Further to the west of 63°E, in the equatorward region, a westward flow is evident. This flow weakens and its eastward extent reduces from cycle 119 to 121.

From the cycle 119 to 121, the kinetic energy (KE) associated with the flow during winter is shown in figure 5.4. The pattern in the variation of kinetic energy is similar. The energy at the southwestern region is around 200 cm^2/s^2 , while it is 75 cm^2/s^2 at the offshore limb of the eddy at southeastern region. Further, the high kinetic energy (~ 10) shifts in the poleward direction and weakens, from 84 to 91. During 92 and 93 the flow manifest high kinetic energy at the equatorward region.

5.2 *Sea Level Anomaly, Circulation and Kinetic Energy during winter to summer transition*

The sea level anomaly during the winter to summer transition phase is shown in figure 5.4. The high, seen at the southeastern region, propagates northwestwards and weakens from cycle 94 to 97 and is absent in cycle 98. Along the southwestern region and Oman coast the positive anomalies intensify and spreads along the western boundary and the offshore region.

The general flow pattern is weaker than that during winter season (Fig. 5.5). The surface currents decrease from cycle 94 to 96 and subsequently increase as shown in cycle 99. The geostrophic current pattern shows a weaker anticyclonic rotation at the southeastern region (cycle 94). Moreover, the western limb of this rotation is in the poleward direction. This flow weakens from cycle 94 and is absent during cycle 97. At the southwestern region the cyclonic circulation pattern is associated with an equatorward flow along the Somali coast. Another important feature is the development of an anticyclonic gyre during cycles 98 and 99 and the associated equatorward flow along the eastern boundary. Further the equatorward region shows a reversal in current direction compared to winter season (cycles 96 to 99).

The KE during the transition period reveals a higher value at the equatorward region and off Somalia (Fig. 5.6). The eastern, northern and central regions depict low values. In general the KE is weaker than the winter season.

5.3 *Sea Level Anomaly, Circulation and Kinetic Energy during summer*

The variation of SLA during summer is given in Fig. 5.7. It shows a negative SLA from cycle 100 to 111 at the southeastern region. This negative anomaly shows its prominence till cycle 111 and spreads poleward and westward. The westward extent is the highest at the southern boundary. The high positive anomaly, seen off Oman during cycle 100, shifts eastward and form a core during cycle 103. The core further shifts in southwesterly direction and negative SLA develops off Oman. These negative anomalies subsequently increases till cycle 111. The northern region do not show high variability in SLA.

The geostrophic current elucidated from the altimeter during summer 1995 is given in figure 5.8. As seen from cycles 100 to 111, the general pattern of circulation in the Arabian Sea is anticyclonic covering the entire region. Embedded in the flow are the two weak anticyclonic features at 10°N , 58°E and 15°N , 61°E . The anticyclonic flow at 10°N , 58°E is seen only during cycles 102 and 103. The northern eddy like structure forms the core of the gyre during the rest of the season. With the advance of the season, it moves southwestwards. The flow pattern further reveals strengthening of the currents along the western boundary as seen from the cycles 100 to 108. Off Somalia, the development of a poleward flow is vivid in cycle 102 and shows maximum intensity during cycle 108. At the southeastern region a cyclonic flow is evident from 101 to 111. The flow along the eastern boundary is equatorward and is associated with cyclonic eddy.

The variations in kinetic energy during the summer are shown through cycles 100 to 111 (Fig. 5.9). At the southwestern region, the KE is high and decreases eastward and northward. The decrease in the eastward direction is gradual while it is drastic in the northward direction. At the southwestern region, the higher KE exists up to 16°N as seen from cycles 100 to 103. The higher KE values are seen at greater northward extent at the western region in comparison with the eastern region. In general the KE at the southwestern region increases (200) from cycles 100 to 108.

5.4 Sea Level Anomaly, Circulation and Kinetic Energy during winter to summer transition

The variations in the sea level anomaly, during October and November 1995, are depicted in cycle 112 to 117 (Fig. 5.10). Off Oman, there is a decrease in the negative sea level anomaly from cycles 112 to 116. The high seen off Somalia, as a prominent feature during summer, weakens from cycles 112 to 116 and shifts southwestward till cycle 115 and subsequently it is absent. The strong negative SLA seen at the southeastern region intensifies and propagates westward from cycles 112 to 117. Subsequently the entire equatorward region shows high negative SLA with maximum at 65°E (-18cm).

Figure 5.11 shows surface geostrophic currents during summer to winter transition. The eddy structure at the western region, westward flow at the southern region and the development of poleward flow along the eastern boundary forms characteristic features during this period. The poleward current at the southeastern boundary strengthens as seen in cycle 117. The anticyclonic eddy associated with this current, a characteristic feature of summer season, weakens from cycle 112 to 115 and in subsequent cycles it is absent. South of 12°N , a strong westward flow is evident in the central and western regions.

The variations in KE during the summer to winter transition are given in figure 5.12. South of 12°N , the region depicts higher kinetic energy. The currents are stronger at the southeastern and southwestern parts of the region. The southwestern region experiences high kinetic energy from cycle 112 to 114 and subsequently it decreases.

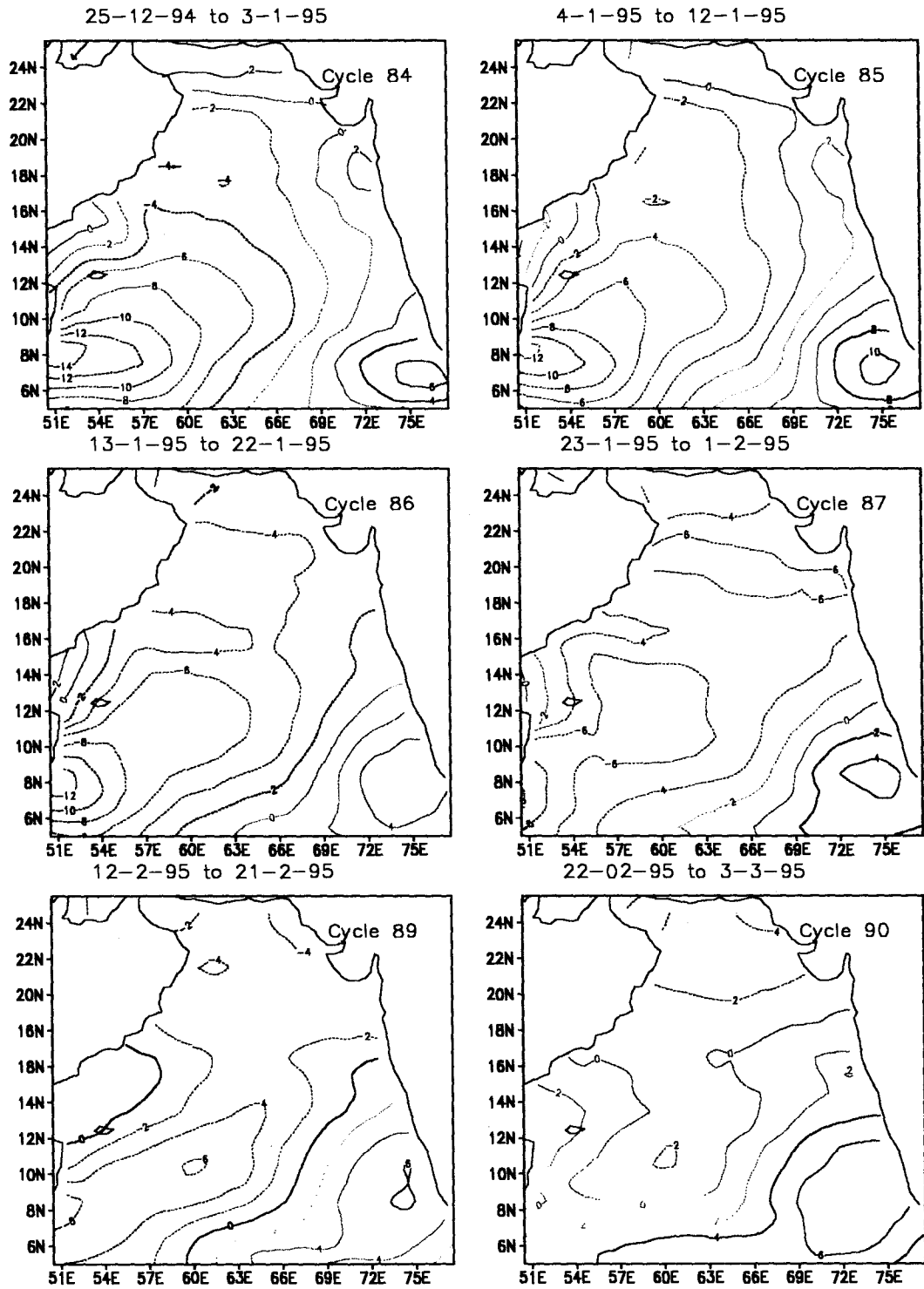


Fig. 5.1 Sea Surface Height Anomaly (cm) during winter

Contd...

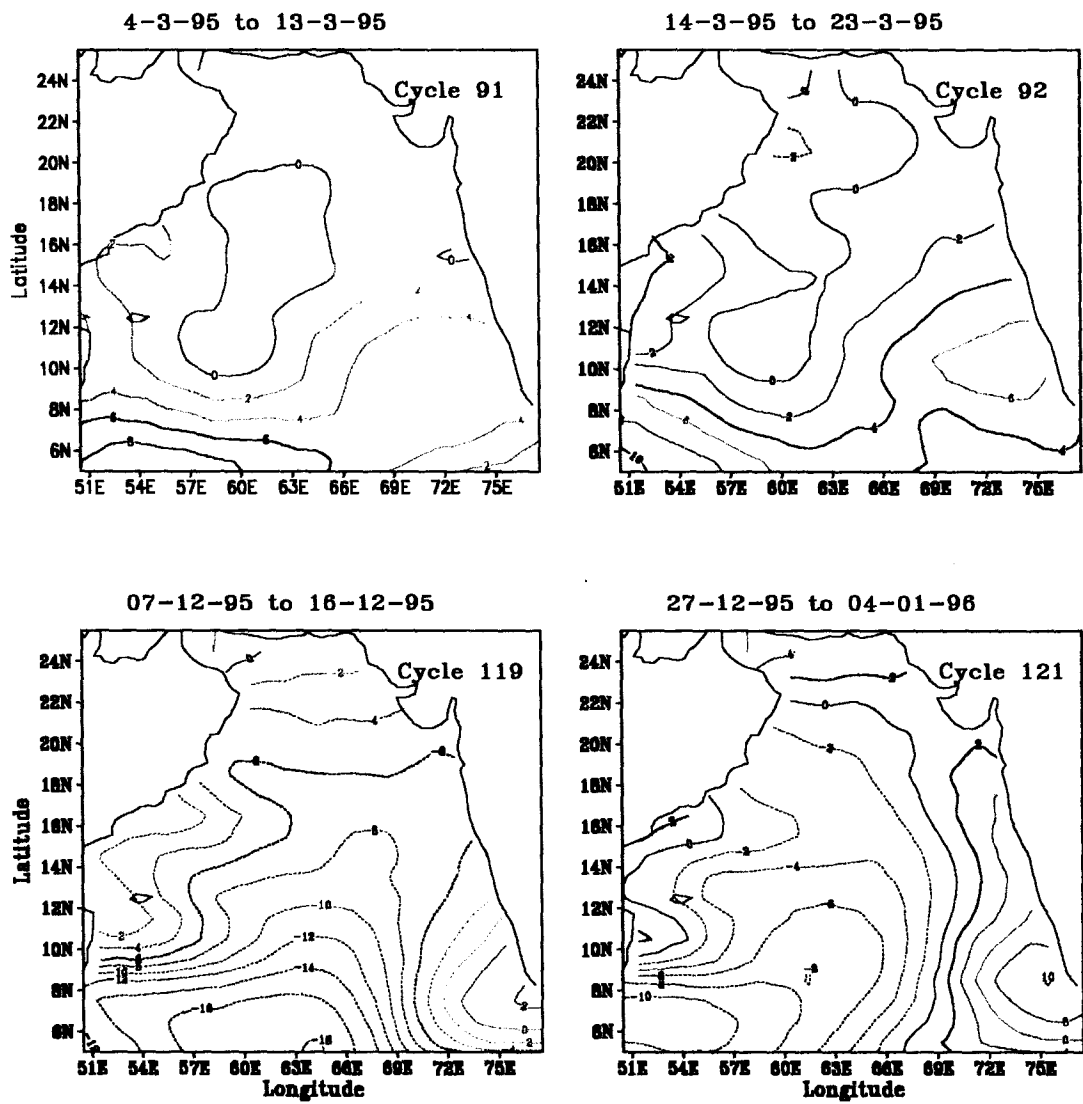


Fig. 5.1 Sea Surface Height Anomaly (cm) during winter

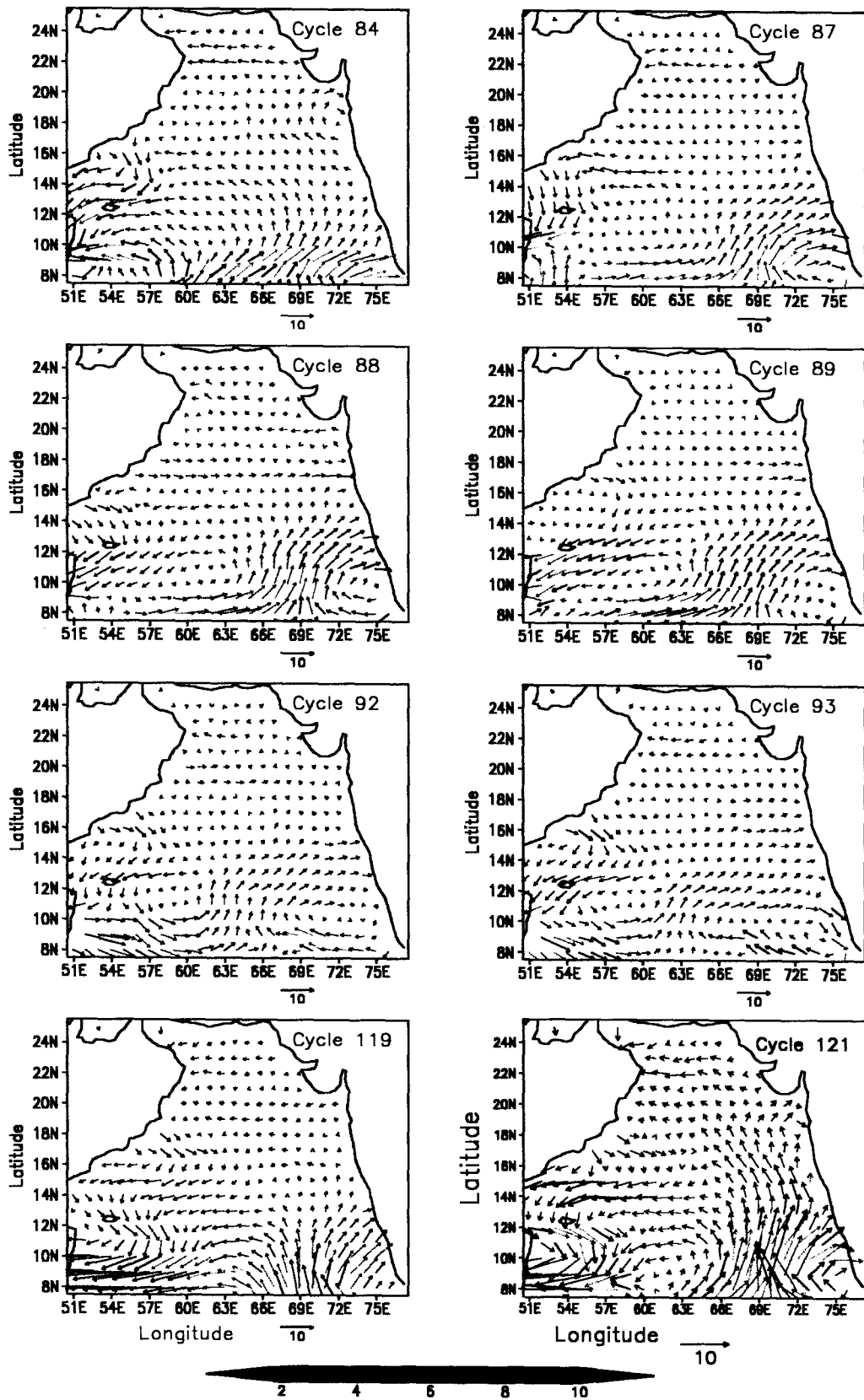


Fig. 5.2 Geostrophic Velocity (cm/s) during winter

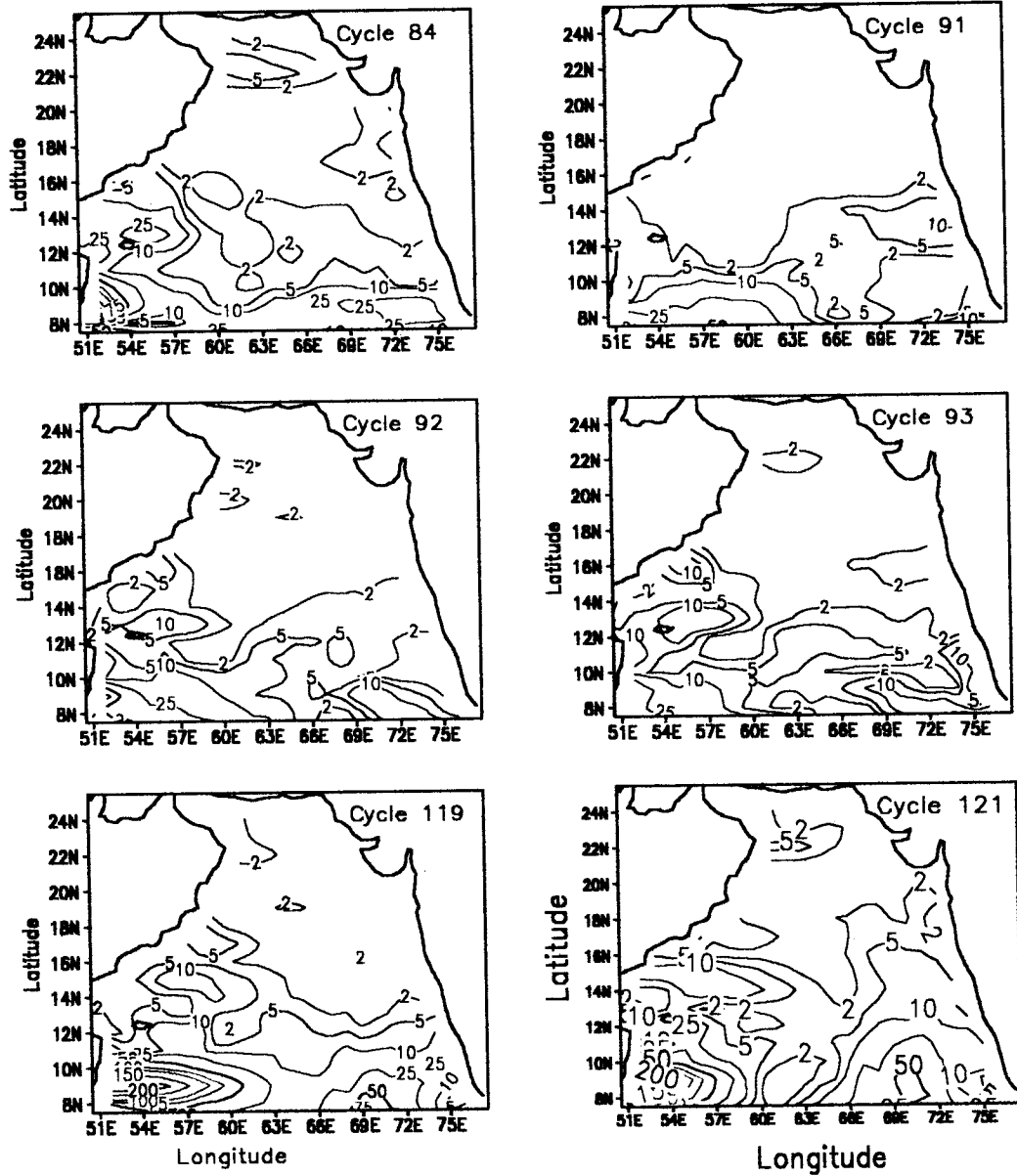


Fig.5.3 Kinetic Energy (cm^2/s^2) during winter

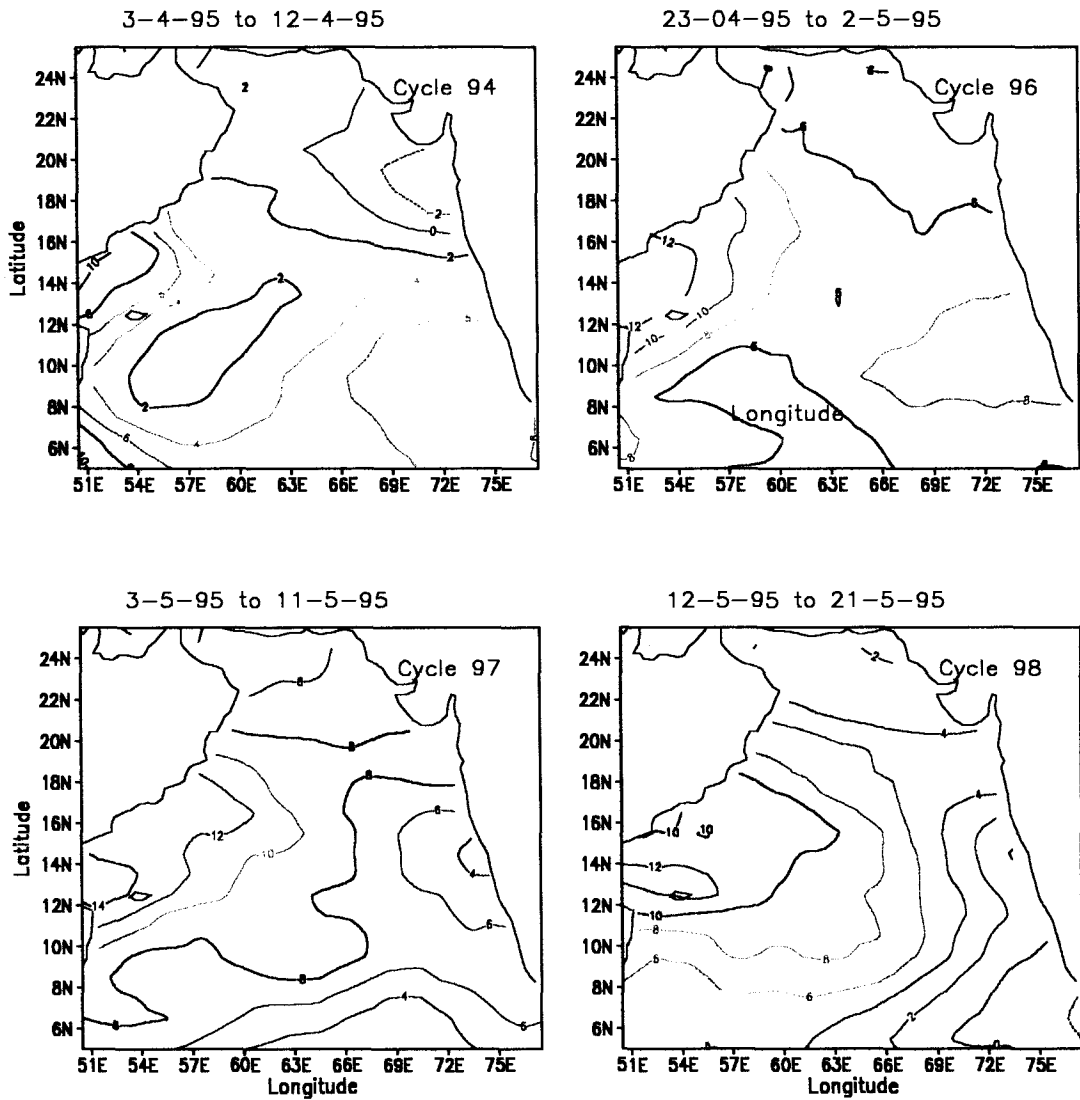


Fig 5.4 Sea Surface Height Anomaly (cm) during winter to summer transition

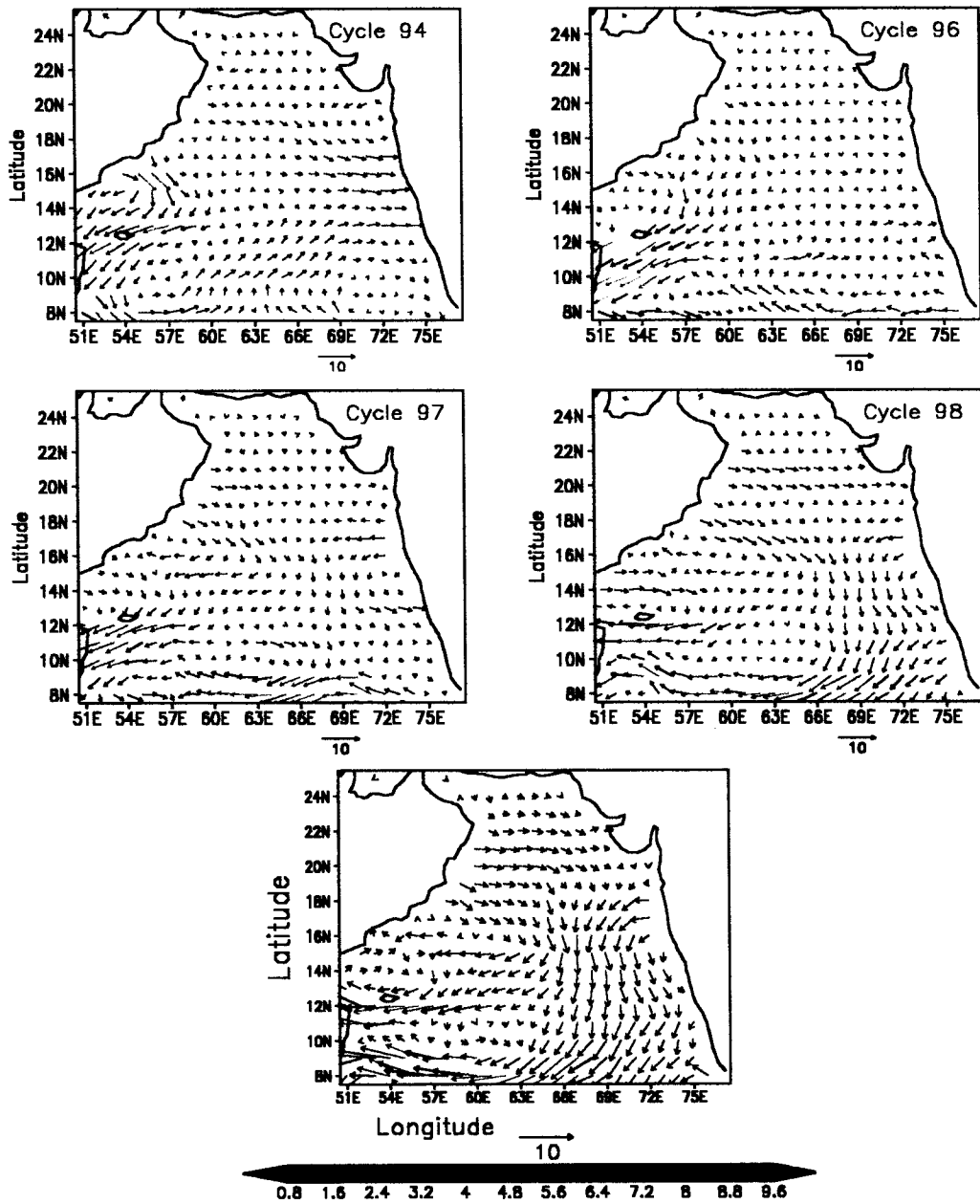
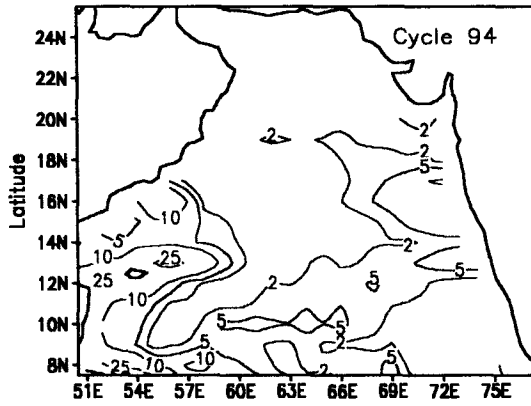
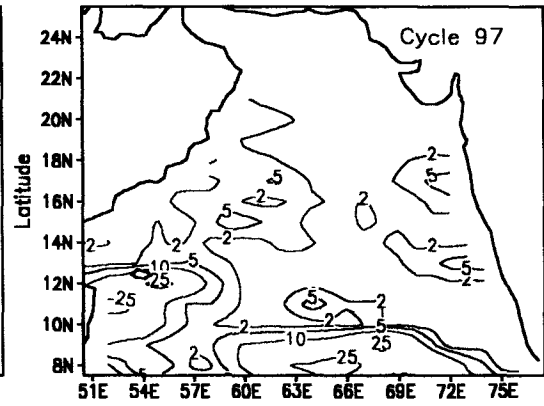


Fig. 5.5 Geostrophic Velocity (cm/s) during winter to summer transition

3-4-95 to 12-4-95



3-5-95 to 11-5-95



22-5-95 to 31-5-95

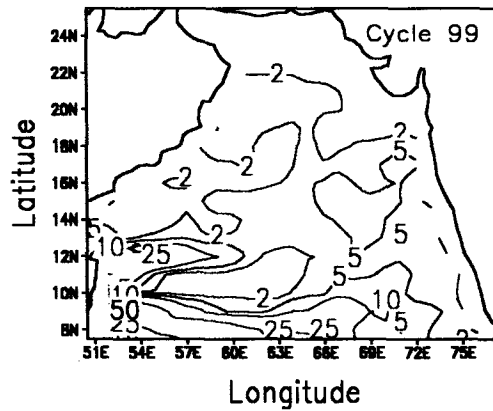


Fig.5.6 Kinetic Energy (cm²/s²) during winter to summer transition

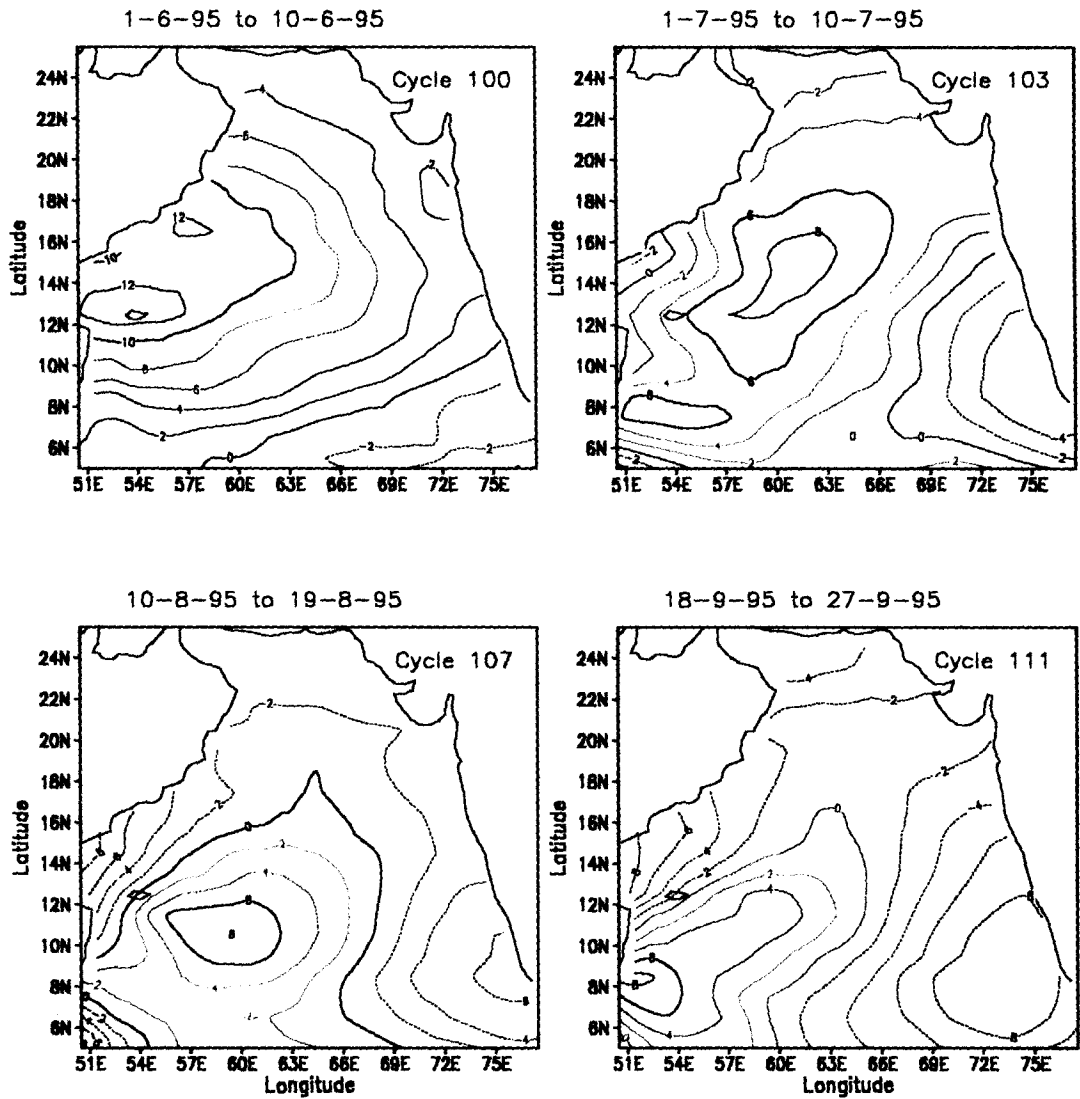


Fig 5.7 Sea Surface Height Anomaly (cm) during summer

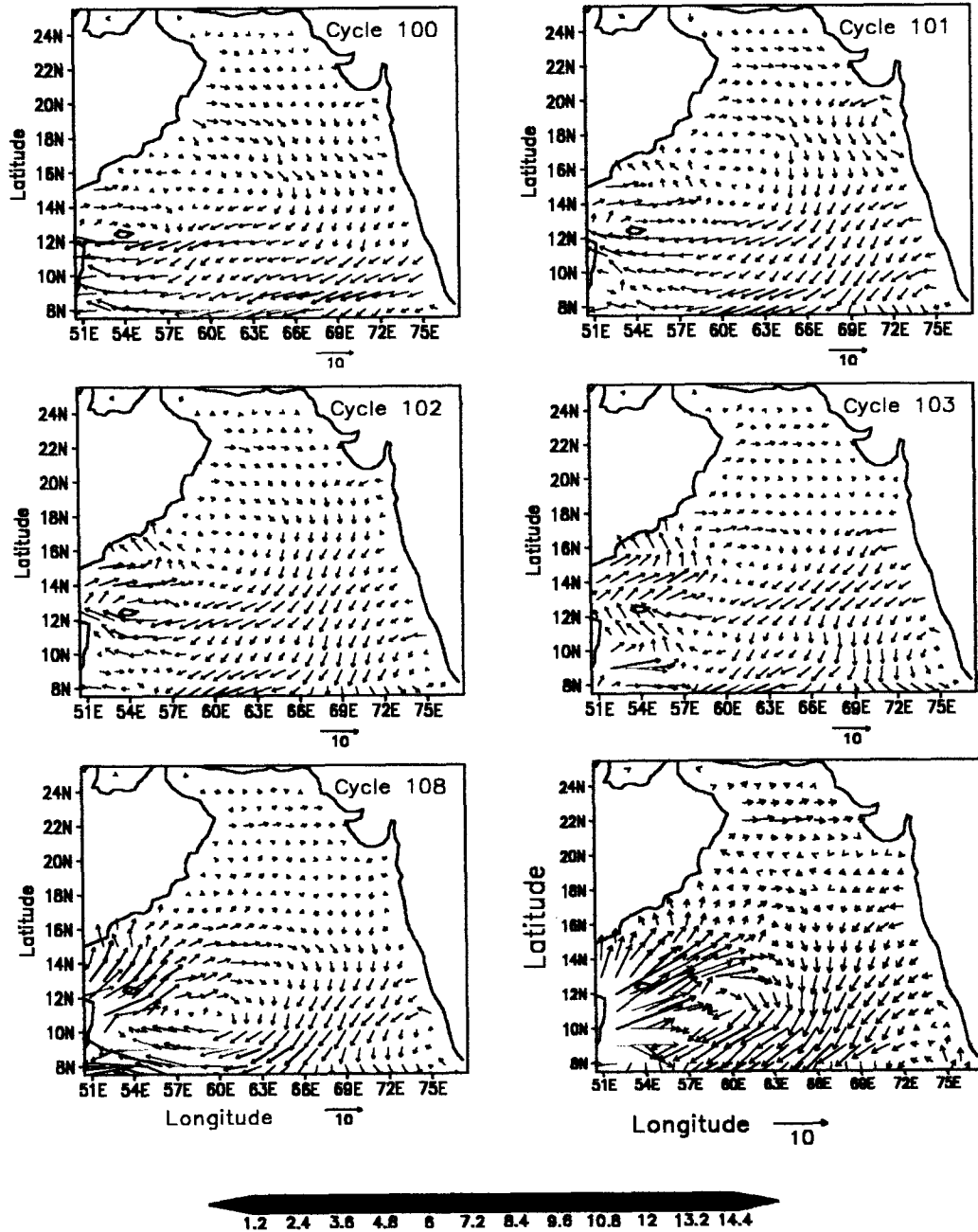


Fig. 5.8 Geostrophic Velocity (cm/s) during summer

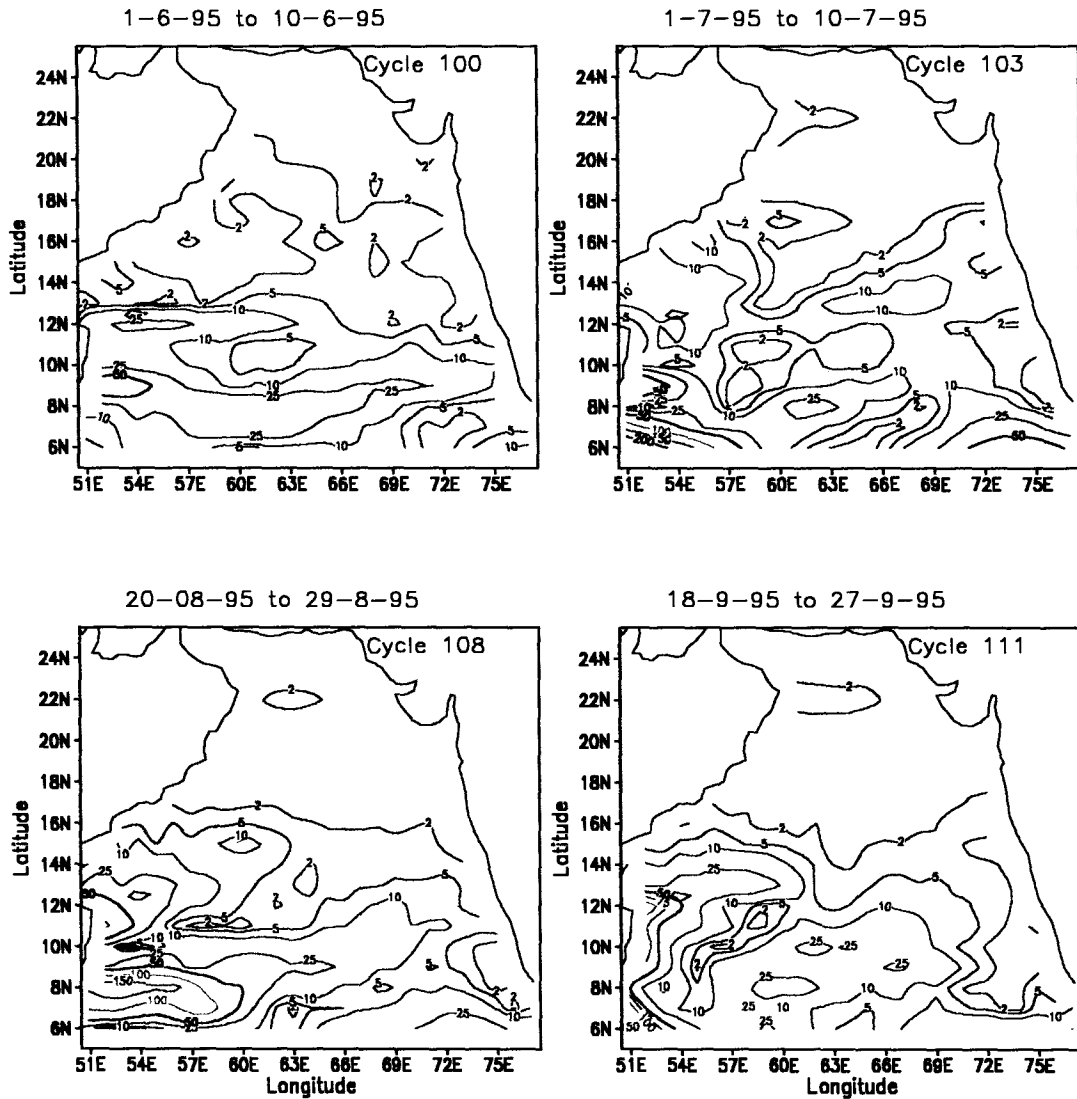


Fig.5.9 Kinetic Energy (cm^2/s^2) during summer

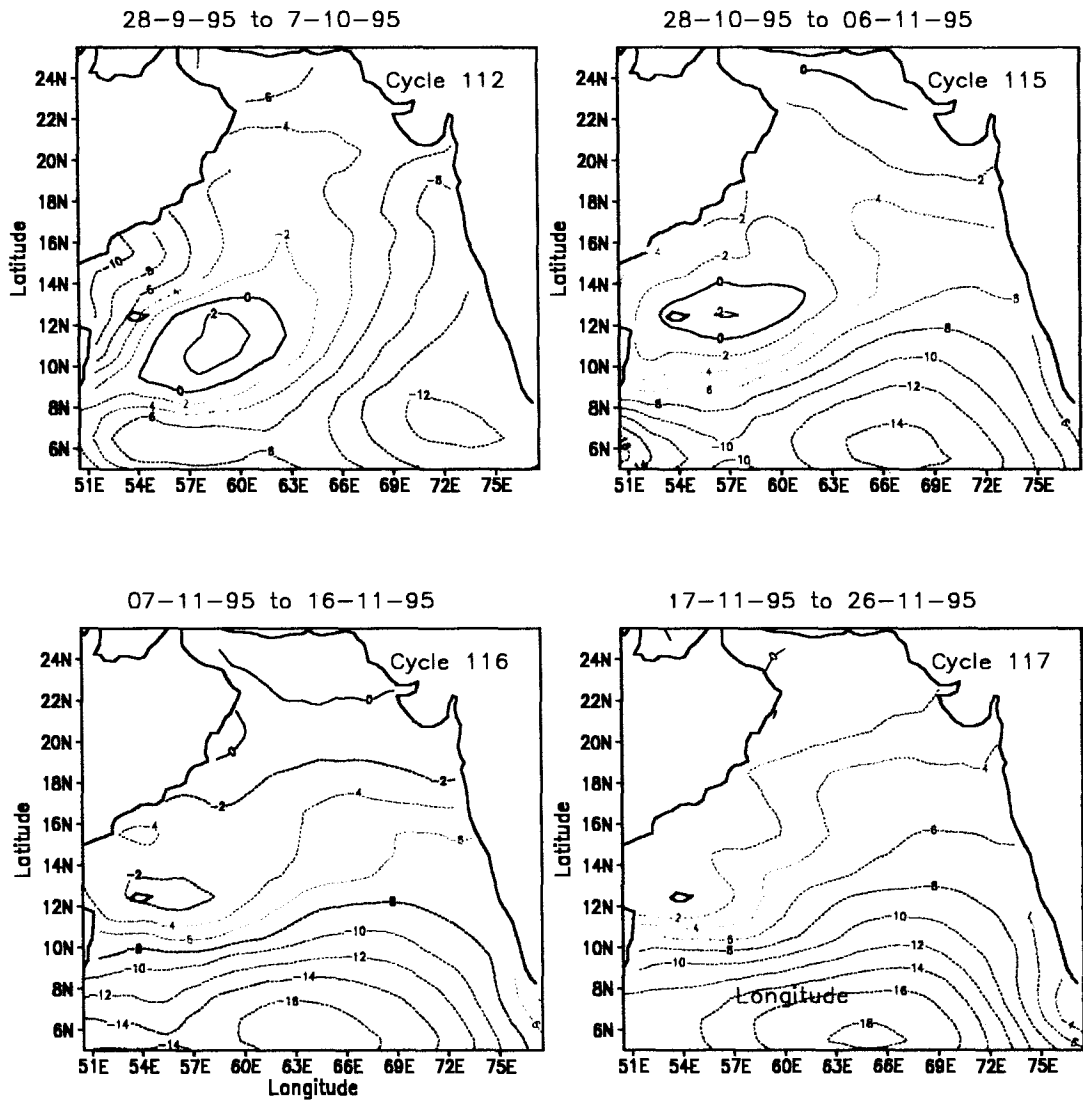


Fig. 5.10 Sea Surface Height Anomaly (cm) during summer to winter transition

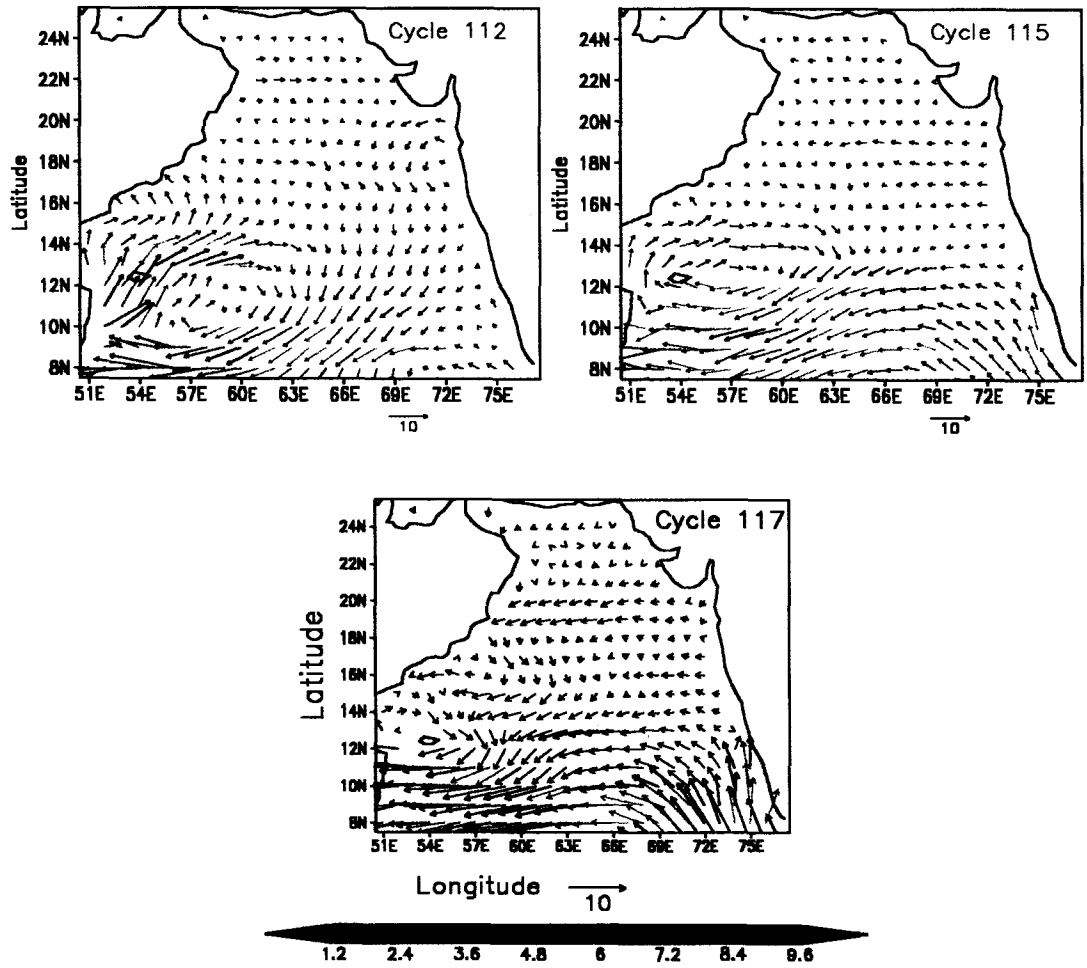
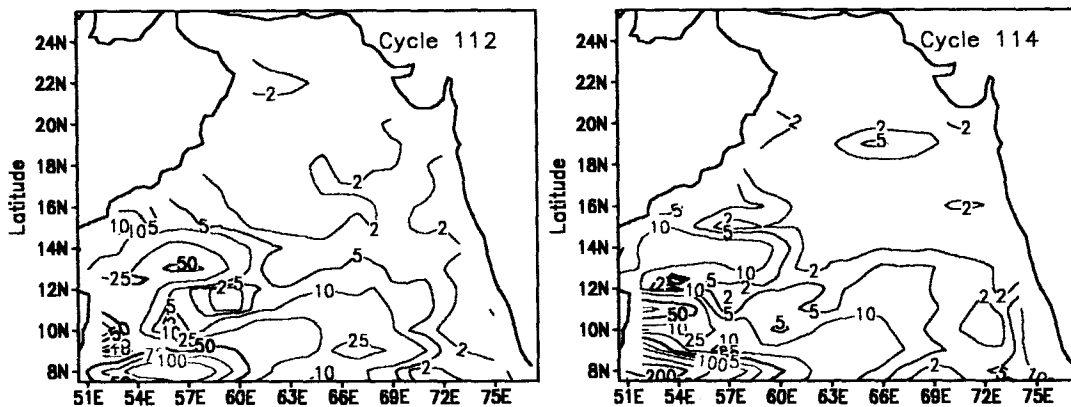


Fig.5.11 Geostrophic current (cm/s) during summer to winter transition

28-9-95 to 7-10-95

18-10-95 to 27-10-95



17-11-95 to 26-11-95

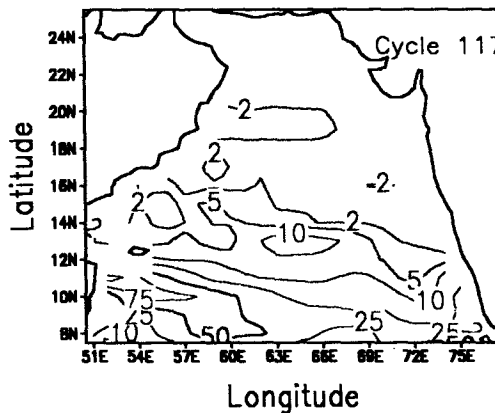


Fig.5.12 Kinetic Energy (cm^2/s^2) during summer to winter transition

Chapter - VI

Discussion

The tumultuous nature of the region manifests the response of the different forcings of the study area. The meteorological and remote forcings along with the influence of marginal seas play a vital role in ocean dynamics. The response of Arabian Sea to these forcings is discussed. In addition to qualitative analysis, quantitative investigation of the spatio-temporal variability of water masses is also carried out. As the processes in the area show intraseasonal variability, the feature has been investigated explicitly in respective months using climatological data. The system is further analysed for its stability, hydrography, mode water and the sea level variability and the role of eddies in the surface circulation.

The hydrographic data during winter and summer shows that major renewal of water occurs in the subsurface and intermediate depths of the area. The presence of ASWM and the BBWM are highly seasonal in nature while PGWM and RSWM are present throughout the year (Figs. 3.37, 3.38 and 3.39). Hence analysis of the Persian Gulf and Red Sea Water Mass is discussed separately.

The distribution of characteristics of Arabian Sea Water Mass (ASWM), points toward the head of Arabian Sea as core of the source of water mass. The surface water becomes cooler and high saline and sinks to a maximum depth of 100 m during winter (Fig. 3.37). The Bay of Bengal Water Mass (BBWM) has its influx to the study region from southeastern side while the Persian Gulf Water Mass (PGWM) and Red Sea Water Masses (RSWM) have their origin in the respective marginal seas. During winter, the water column is divided by the thermocline with a mixed layer in the upper few meters and a layer of weak gradient in the properties below it. The high saline cooler waters spread equatorward below the warmer surface waters. The coastal boundaries of the study area are subjected to upwelling during summer. Also along the

western region (west of 700 km from coast) of the study area, the thermocline surfaces and the halocline erodes due to upwelling. Upwelling and Persian Gulf waters influences the stability of water column. The uniformity in property over substantial vertical extent away from the surface represents the mode water. The mode water, of Arabian Sea origin, depicts a strong seasonality indicating the role of monsoonal forcings.

The air-sea interaction at the northern region, in December, imparts its signature that are characterized by surface temperature and salinity ranging from 25 to 27° C and 36.4 to 36.7 psu in the upper 30 m. The triggering and intensity of oceanic convection during winter are connected to meteorological forcings. The surface heat flux and the resultant sea surface temperature is an index of the measure of cooling. The winds blowing over the area are dry, weak and northeasterly (Fig. 3.1). The short wave radiation decreases from 180 to 150 Wm⁻², in poleward direction while the flux of long wave radiation is between 66 and 71 Wm⁻² (Figs. 3.2 and 3.3). The heat flux due to evaporation reveals that it ranges from 155 to 170 Wm⁻², in the northern region while the loss of heat by conduction ranges from 9 to 14 Wm⁻² and is meager compared to the loss due to evaporation (Figs. 3.4 and 3.5). Therefore, the net heat flux is a loss that ranges from 90 Wm⁻² near equator to 125 Wm⁻² at the northern region (Fig. 3.6). In an attempt to understand the oceanic coupling with the atmosphere through an integrated approach, distribution of buoyancy flux is also looked into.

The buoyancy flux is a loss (8 - 14 kg m⁻¹s⁻³) over the northern and central region, with a maximum off Gujrath (Fig. 3.8). This further reveals that densification of the surface water occurs during December and leads to genesis of Arabian Sea Water Mass Fig. 3.37). Based on 2° x 2° grid data, Prasanna Kumar et al. (1999) inferred that the Arabian Sea Water Mass (ASWM) starts forming in the Northern Arabian Sea during November and continues till February. It spreads equatorward. Using a novel approach, area and volume occupied by the water mass at depth of prominence (depth at which the water mass occupies highest area in that month) has been computed. The depth of prominence is 50 m and the water mass extends, vertically, to 75 m (Fig. 3.37). The total volume occupied is 234*10⁵ km³ while

the area at the depth of prominence is $412 \times 10^3 \text{ km}^2$. The BBWM enters the study region from southeastern sector. The area covered decreases poleward and with depth. The area occupied by the water mass at the depth of prominence (10 m) is $249 \times 10^3 \text{ km}^2$ while the total volume is $74 \times 10^5 \text{ km}^3$.

During December 1995, mixed layer depth (MLD) regenerates (Figs. 4.14 and 4.15). The mixed layer is deeper at the equatorward side while it is lower near the coast. The highest homogenization depicts weakest variation in stability of the water column. A high degree of homogenization in upper waters occurs at southern region due to the less influence of PGWM. The eastern region does not depict such a feature. The dynamic topography during December 1995, depicts a high at southeastern region and a low at the southcentral region (Fig. 5.1). Bruce et al. (1994) has drawn attention to this and attributed its cause to impact of strong wind stress curl off the southern tip of India due to strong funneling of the northeast monsoon between India and Sri Lanka. They further concluded that the feature is generated by wind forced, downwelling, coastal Kelvin wave that leaked energy offshore via westward propagating Rossby waves (Bruce et al., 1998). The present findings also agree with that of Shankar and Shetye (1997) wherein offshore propagation is depicted. The high spreads northwestwards and shows strengthening with the progress of the month, while the low weakens and propagates westward.

The high drives an anticyclonic eddy and the low drives a cyclonic eddy. The offshore limbs of the anticyclonic eddy and the cyclonic eddy drive a poleward current that carries the BBWM to the northern Arabian Sea (Fig. 5.2). This water mass is clearly seen as low salinity waters at the easternmost part of central-eastern region. The western limb of the cyclonic eddy drives the equatorward flowing Somali current. Thus the mesoscale phenomenon such as eddies act like a catalyst to the general flow. The current carries the high saline surface waters from northern region to the equator and thus influences the hydrography. The region of Somali current and the eastward limb of cyclonic eddy possess high kinetic energy (Fig. 5.3). Flagg et al. (1998), on the basis of ADCP data, indicated the dominance of the velocity field by eddies and identified that the region along Arabia possesses high KE.

In January the northern and central regions are characterized by a uniform pattern of distribution extending up to 75 m (Figs. 3.9). The associated properties are 23.5 to 25° C and 36.4 to 36.7 psu, indicating the presence of ASWM. These properties reveal cooling and the salinity pattern shows an increase in area covered by high saline water (> 36.4 psu) from that of December. This is further explained through wind, heat budget and buoyancy flux. The cool dry northeasterly winds lead to intense evaporation and the associated flux from the ocean is 125-165 Wm⁻² (Figs. 3.1 and 3.5). This is approximately same as that of December. The sensible heat flux (10 – 12 Wm⁻²) and the flux associated with long wave radiations (75-83 Wm⁻²) are similar to that in December (Figs. 3.3 and 3.4). These lead to a loss in net heat flux (75-125 Wm⁻²), which is lower than that in December (Fig. 3.6). This gives an impression that densification of surface water in January is less than that in December. However the cooling that occurs in December continues to January thereby augmenting the densification process and formation of water mass (Fig. 3.37). This is further evident from the shallowing of depth of prominence to 10 m, increase in area (1022*10³ km²) at depth of prominence and more volume (754*10⁵ km³) occupied by the water mass.

During winter, the area at depth of prominence and total volume occupied is highest in January. This reveals that the formation of the water mass is intensified in January. Though the entire region experiences northeasterly winds the eastern region is warm (25-28° C) and less saline (34-35 psu) while the western region is cold with temperature ranging between 23.5 and 26.0° C and higher salinity ranging from 35.6 to 36.6 psu (Figs. 3.9 and 3.13). These characteristics reveal a pattern, which is different than that would result only due to the dry winds. The distribution is as a result of the intrusion of warm less saline Bay of Bengal water along the eastern boundary. Shetye et al. (1991), in their studies, attribute the flow of Bay of Bengal water to the poleward limb of North Equatorial current. The vertical extent of the water decreases towards the pole.

The mixed layer, in January, is lower near the coast than the offshore part of the northern region and in the northeastern part. Lower MLD is also

seen near the coast of central-western region compared to the offshore and southern regions. Morrison et al. (1998) showed that the highest MLD occurs in late NEM. The variation in stability is weak near the surface thereby revealing the homogenized nature of the water column. The northernmost region of the southern part and the easternmost region of the central-eastern part depict the highest vertical extent of homogenization in comparison with other regions (Fig. 4.17). This is because of surface cooling and subsequent convection and absence of PGWM in the subsurface.

The positive Sea Level Anomaly (SLA) at southeastern region and negative anomaly at southwestern region strengthens till first twenty days of January 1995. The negative signal propagates westward in the equatorward region and the positive signal northward along the eastern boundary. These results are in agreement with that of Prasanna Kumar et al (1998), who depicted the presence of depression at the west and elevation at the east. These anomalies are associated with currents that are similar to December. These currents associated with eddies strengthens till first 20 days of January and later shows weakening phase. During the strengthening phase the equatorward moving Somali current extends northward till 16°N. Off Somalia and the southeastern region depict high kinetic energy. During the last phase of January, drastic changes occur. The high weakens and propagates northwestwards. The positive anomaly spreads westward in the southern region and the low weakens and moves to central Arabian Sea. The decrease in the intensity of eddies weakens the Somali current at the southwestern region and the poleward current at the eastern region.

During February shows that the area covered by ASWM decreases as a result of influence of warm, low saline Bay of Bengal water (Fig. 3.38). The properties in the northern region are 23.0 to 26.0° C and 36.2 to 36.6 psu (Figs. 3.10 and 3.14). Examination of meteorological forcings reveal that the loss due to evaporation is in the range of 100 to 130 Wm^{-2} while the sensible heat flux is in the range of 5 to 8 Wm^{-2} which is less than that in January (Figs. 3.4 and 3.5). Also, the short wave radiations (205 to 235 Wm^{-2}) increases with respect to the previous month resulting in the reduction in net heat loss (0 to 20 Wm^{-2}) as shown in figures (3.2 and 3.6). The Buoyancy flux still shows loss

from ocean but it is lower than the previous month (Fig. 3.7). Thus the conditions prevailing at the sea surface has changed. In February, though high evaporation occurs, an increase in salinity due to the effect of evaporation is not seen as it is overshadowed by the influx of Bay of Bengal water. Thus the forcings are less favorable leading to a decreased spatial extent of ASWM and fragmentary spatial nature (Fig. 3.37). Thus the BBWM restricts the equatorward spread of ASWM. Unlike January, the maximum spreading is not at 10 m but at 50 m with an area of coverage $624 \cdot 10^3 \text{ km}^2$. The total volume occupied by the water mass is $433 \cdot 10^5 \text{ km}^3$ is less than that during January.

In March the surface properties at the northern region are 24 to 25.5° C and 36.4 to 36.7 psu (Figs 3.11 and 3.15). Though the temperature at the head region is higher than the previous month, it is less compared to rest of the area. Thus, the cooling and increase in salinity is restricted to the head of the region. Moreover, a large area is covered by high saline water compared to February. This could be due to either evaporation, advection or both. To delineate the cause, different forcings are assessed. The short wave radiations ($235 - 205 \text{ Wm}^{-2}$) show an increase while sensible heat flux ($5 - 2 \text{ Wm}^{-2}$) shows a loss that decreases compared to February (Figs. 3.2 and 3.4). Also the winds over the area are weaker and northeasterly (Fig. 3.1). On examining the variation of latent heat flux, it is seen that there is a drastic reduction in loss from February to March (Fig. 3.5). These result in the gain of heat to most of the region. Thus, evaporation is not the major factor for the increase in salinity. Therefore, the role of advection is examined through the property distribution.

The comparison of surface properties with previous month show, an increase in salinity and a decrease in temperature revealing retreat of less saline BBWM along the eastern boundary (Fig. 3.37). Hence, advection is the major factor for increase in salinity. This is further evident from the spreading of ASWM (Fig. 3.37). At the depth of prominence (50 m), the area ($587 \cdot 10^3 \text{ km}^2$) and total volume ($395 \cdot 10^5 \text{ km}^3$) occupied by the ASWM decreases from that of February. However, the spread at upper 20 m level is larger than that in February. The vertical extent of BBWM also shows temporal variability. It extends to 50 m in January and February and 30 m in December, March and

April. The area occupied at the depth of prominence increases from 249×10^3 km² to 506×10^3 km² in March. However, the volume occupied shows drastic increase from 74×10^5 km³ in December to 165×10^5 km³ in January. Subsequently it decreases to 145×10^5 km³ in March. This water mass restricts the equatorward movement of the ASWM and is responsible for reduced formation of the ASWM during February. At the depth of prominence the highest spread is seen during March (506×10^3 km²). The water mass is seen to be extending to 16°N.

In March the winter convection and retreat of Bay of Bengal Water results in increase in MLD at northern and central-eastern regions than in January (Fig. 4.5). These regions also exhibit higher MLD than that at the central-western and southern regions. The reduction in MLD at the southernmost part of the southern region is due to flow of low saline waters over the high saline waters, from equatorward side (Fig. 4.6). The poleward flow is associated with the offshore limbs of anticyclonic and cyclonic eddies (Fig. 5.1) During March 1995 the highest vertical extent of homogenization (150 m) is seen at the central region (N5) of northern Arabian Sea (Fig. 4.18). This is due to the intense surface cooling and subsequent convection occurring there while rest of the regions are predominantly influenced by the upthrust due to PGWM (as is evident from the weakening of thermocline and halocline) or flow of low saline waters of lower latitude.

The water mass formed in the Arabian Sea is not dense enough to sink to great depths. Moreover, the region is influenced by seasonal forcings. Therefore, the mode waters have very low vertical extent and are not present throughout the study region. The mode water seen during March at the easternmost station is due to the trapping of the high saline cooler water below the warmer less saline poleward flowing waters.

The properties of surface waters during April show warming (26 to 30° C) and increase in salinity (34.2 to 36.8 psu) in comparison with March, while in May further increase in temperature (28 to 31° C) and salinity (34.8 to 36.8 psu) is seen (Figs. 3.16 to 3.19). The wind is weak and exhibits a change in the direction from northeasterly in March to northerly in April (Fig. 3.1). The

latent and sensible heat fluxes show reduction in loss during April compared to that in March (Fig. 3.5). The short wave radiations increase in April (Fig. 3.3). Therefore, there is a gain in net heat flux to ocean, which increases towards pole (Fig. 3.6) and the buoyancy flux is a gain in the range of 5 to 12 $\text{kgm}^{-1}\text{s}^{-3}$, which is higher than that in March (Fig. 3.7). This is ultimately manifested in the form of an increase in sea surface temperature while the absence of Bay of Bengal water along with evaporation causes an increase in salinity.

In May the southwesterly winds that blow are stronger than in April (Fig. 3.1). The increase in short wave radiations ($240\text{-}360 \text{ Wm}^{-2}$) and reduction in long wave radiation ($41\text{-}49 \text{ Wm}^{-2}$) are associated with reduction in gain of sensible heat flux to ocean with respect to April (Figs. 3.2 to 3.4). The latent heat flux (60 to 130 Wm^{-2}) increases with respect to April while spatial analysis shows a poleward decrease. This results in the net heat gain to the ocean that is larger and therefore ASWM is not formed in April and May. On the contrary, the ASWM is eroded in upper layer as a result of higher solar influx and the resultant buoyancy gain. The erosion of the water mass extends up to 20 m in May. However the water mass is seen to be dominant at deeper levels in comparison with winter months due to sinking. The depth of area of prominence is 75 m. But the area at this depth is lesser in May ($587 \times 10^3 \text{ km}^2$) than in April ($648 \times 10^3 \text{ km}^2$). The ASWM shows highest equatorward extent of 12°N at 75 m in April. This clearly indicates that the spreading continuous in transition months. The volume occupied decreases to $318 \times 10^5 \text{ km}^3$ in April and it increases in May due to greater spread at 100 m (Fig. 3.37).

From March to April drastic retreat of BBWM takes place. The properties of the water mass near the surface gets eroded and the water mass is evident at 20 and 30 m with higher area covered at later depth level.

The area covered by salinity greater than 36.4 psu is almost constant from March to May and is depicted in the form of a tongue like structure. This feature in the surface salinity, during March, could be ascribed to the combined effect of evaporation and a poleward flow along the eastern boundary. In April and May the region experiences less evaporation and retreat of Bay of Bengal water leading to continued existence of tongue like

structure of high salinity.

The high seen at the southeastern region propagates westward in the southern region and reaches the western boundary, in February and March. Subsequently, it moves poleward in April and May and a low develop at the southeastern region weakens (Fig. 5.4). The anticyclonic and cyclonic eddies dissipate by end of April. However by mid May, Somali current still reverses (Fig. 5.5) while the current at the eastern region moves equatorward. The higher kinetic energy is in equatorward and southwestern regions (Fig. 5.6).

The temperature off Somalia is less than that off Oman indicating a stronger upwelling off Somalia (Figs. 3.20 to 3.27) from June to September. The displaced water associated with upwelling converges with the ambient waters leading to the formation of an upwelling front. Examination of gradient in properties across the front reveals a thermal front rather than a haline front. This clearly shows that over a substantial vertical extent, the waters are characterised by uniform salinity that are associated with open ocean characteristics. The vertical extent of the thermal front extends to 125 m in June, 150 m in July and 200 m in August and September, from the surface.

The coastal and offshore upwelling along the western boundary is due to the poleward flow and the associated alongshore component of wind while the offshore is in response to positive wind stress curl of 4 Nm^{-3} (Fig. 3.2). In coastal upwelling the alongshore winds cause divergence of surface waters at the boundary forcing cold subsurface waters to the surface and to offshore and a lower sea level at the coast. Manghnani et al., (1998) studied the sea surface temperature, sea level anomaly, currents and the winds over the western region to describe the influence of 1995 monsoon on the upwelled waters off Oman. They found that the sea level structure in the region is modified by the spatial distribution of the wind stress field during the southwest monsoon and the coastal divergence are responsible for the depression of sea level in this area. To analyse the intensity of upwelling with advance of season, the horizontal thermal gradient at a depth of 20 m has been further examined. This reveals that from June to August, there is a frontogenesis while from August to September a frontolysis. This indicates strengthening and

weakening of upwelling along the western boundary. The head region experiences upwelling only during August. Brock and McCain (1992) showed that the offshore upward Ekman pumping influences the shallow hydrography to depths greater than 250 m in August and September at the northwestern Arabian Sea.

Similar to western boundary, the eastern boundary also experiences upwelling during summer. But the front associated is of thermohaline nature (Figs. 3.20 to 3.27). The vertical extent of front is 50 to 75 m in June, 10 to 125 m in July, and between surface and 150 m in August and September. To analyse the monthly variation of upwelling along the eastern boundary, the gradient of the front at the 50 m is examined. It is evident that the upwelling intensifies from June to August and remains same in September. The northward extent of the front increases from June to August and subsequently it retreats. There is a decrease in intensity of upwelling towards the pole as revealed by the decrease in gradient of the front.

While comparing the upwelling phenomenon at the west and the east, it is evident that the process is stronger at the west than at the east. This is due to the strong poleward moving Somali current that are associated with favorable southwesterly winds at the west while a weak equatorward flow at the east. The cold waters upwelled at the western and the eastern boundaries trap the water at the central region as manifested by the warm, high saline water between 63-69° E (Figs. 3.22 and 3.23). The solar influx reduces in summer and is least in July and August (Fig. 3.2). The long wave radiations decreases till August and further it increases (Fig. 3.3). There is a gain in sensible heat flux on western side that experiences strong upwelling while on eastern side loss occurs (Fig. 3.4). These variations are highest in August while the loss by latent heat flux is least in September (Fig. 3.5). There is a gain of net heat flux along boundaries and loss in central regions during June and July while in August and September throughout the region there is a net gain (Fig. 3.6).

The upwelling region experiences gain in buoyancy flux to the ocean. The western region shows a higher gain of buoyancy flux than the eastern

region (Fig. 3.7). The central region experiences a loss in June ($0-6 \text{ kgm}^{-1}\text{s}^{-3}$), it weakens in July ($0-2 \text{ kgm}^{-1}\text{s}^{-3}$) and subsequently the entire region experiences gain in August ($0-14 \text{ kgm}^{-1}\text{s}^{-3}$) and September ($3-12 \text{ kgm}^{-1}\text{s}^{-3}$).

Upwelling influences the change of depth of prominence. In the initial phase of summer (June), upwelling erodes the property of the ASWM and the maximum spread is seen at 50 m (Figs. 3.20, 3.24 and 3.37). With further advance of the season (July), the water mass is eroded due to upthrust from bottom and due to wind mixing at top. Therefore, the depth of prominence is at 50 m. Simultaneously, there is also surface cooling and increase in salinity at head of the region and the central northern region with respect to June (Figs. 3.21 and 3.25). However, in August, winds remain strong and upwelling extends to the head region and is clearly depicted at 30 m (Fig. 3.22). The intense upwelling at eastern and western regions and weaker upwelling at northern region advects the high saline waters to the open ocean where it leads to convergence.

The high saline water of the northern region mixes at the offshore and acquires properties similar to ASWM. Vertically, the area occupied is highest at 50 m. These processes lead to decrease in area covered from June ($435 \cdot 10^3 \text{ km}^2$) to July ($247 \cdot 10^3 \text{ km}^2$), and subsequently the area increases in August ($342 \cdot 10^3 \text{ km}^2$). The weakening of upwelling during September does not lead to formation of water properties similar to ASWM. The water with properties of ASWM is seen at northeastern region. The volume occupied by ASWM decreases from May to June ($201 \cdot 10^5 \text{ km}^3$). It further shows drastic reduction in July ($106 \cdot 10^5 \text{ km}^3$). From July to August the volume increases ($156 \cdot 10^5 \text{ km}^3$).

The upwelling at the northern and central-western regions lead to total erosion of mixed layer during summer (Figs. 4.8, 4.9, 4.11 and 4.12). The highest MLD is seen in September and occurs in southern region. This is due to the less influence of upwelling and wind mixing. This is further evident in terms of less variation in stability (Figs. 4.19 and 4.20). The upwelling leads to surfacing of the thermocline and erosion of halocline and therefore less variation in the properties between the surface and the subsurface regions.

Therefore, in the upwelling regions high fluctuations in the stability is seen.

In summer season, the high SLA along Arabia coast (Fig. 5.7) moves offshore and from mid July it moves southwestwards. The negative SLA at southeastern region propagates poleward along eastern boundary and westward along the southern region. The westward propagation is coupled with intensification. The coastal regions are characterised by negative anomaly which is intense in strong upwelling regions. The eastern region is influenced by equatorward flow while at southeastern region an anticyclonic eddy is seen. At the western region, in June, an anticyclonic eddy develops off Arabia while in July two anticyclonic eddies are seen. These eddies merge and a strong eddy- Great Whirl, develops (Fig. 5.6). The whirl is also depicted in the work of Prasanna Kumar et al (1998). The Great whirl influences the surface circulation pattern in the major part of the region. Its western limb is associated with stronger poleward current – Somali current, while the eastern limb is associated with equatorward current. This current possesses high KE (Fig. 5.9). The Great Whirl in western region and the equatorward current at the eastern region weakens in September and by the end of the month, an anticyclonic eddy develops off southeastern region. The coastal limb of this eddy drives a poleward current

From September to October, there is drastic reduction in upwelling. In October and November the presence of cold water in the subsurface region along the eastern and western boundary is due to upwelling during the previous summer (Figs. 3.28 to 3.31). The vertical extent of these cold waters decreases from October to November. The uniform pattern of hydrographic properties seen up to 10 m in October and 30 m in November indicating the penetration of atmospheric influence.

The wind during October is northerly while in November it is northeasterly (Fig. 3.1). Wind stress further shows a negative curl (0 to $8 \cdot 10^{-7}$ Nm^{-3}) in northern region and a positive curl (0 to $6 \cdot 10^{-7}$ Nm^{-3}) in the southeastern region. The short wave radiations is lesser compared to September and the influx is least in November ($195\text{-}230 \text{ Wm}^{-2}$) while the long wave radiation increases (Fig 3.3). In October and November the ocean losses

heat also in form of sensible heat flux and is higher in November. Though the latent heat flux reduces from September to October, higher flux is seen in November. The buoyancy flux distribution clearly shows that the gain ranges from 3 to 8 $\text{kgm}^{-1}\text{s}^{-3}$ in October and is less than that in September. Along the boundary the gain is higher (8 $\text{kgm}^{-1}\text{s}^{-3}$). In November large part of the ocean shows loss while a small southeastern region shows gain. The loss from the ocean increases poleward (Fig. 3.7). Thus in November, the forcings resemble to that of the winter season. The warm water at southeastern region is associated with the warm less saline waters of North Equatorial Current, these waters move in the northwesterly direction.

The pockets of water at central eastern region, at the subsurface, show similarities in properties to that of ASWM. In October maximum horizontal spread of $116 \times 10^3 \text{ km}^2$ is seen at 75 m while in November it is $152 \times 10^3 \text{ km}^2$, at 50m (Fig. 3.37). The absence of ASWM in September and its presence in October and further intensification in November indicates that upwelling is also responsible for formation of water properties akin to the ASWM. Vertically the displacement of ASWM occurs in eastward direction (Fig. 3.37), This is due to the presence of lower dense water on the eastern region compared to the western region during all the months (Fig. 3.36). The presence of Bay of Bengal Water mass is vivid in November and occupies an area of $178 \times 10^3 \text{ km}^2$ at the depth of prominence (10 m) while the total volume occupied is $40 \times 10^5 \text{ km}^5$.

The negative anomaly seen at the southeastern region propagates westward and intensifies while the high seen in summer at southwestern region dissipates (Fig. 5.10) in the transition period of summer to winter. By the end of October, the equatorward flow at the eastern boundary is absent. On the contrary a poleward flow develops. The Great Whirl also dissipates during this period and at the equatorward region a strong westward flow develops and intensify in November.

During the winter season, cool subsurface waters seen off Oman coast, result in the formation of a front. With the advance of the winter, the vertical extent of the front decreases (Figs. 3.8 to 3.11). Based on the property

distribution off Oman coast during summer and post summer transition, the cold waters can be attributed to the remnant of upwelled waters of the previous season. In May the front is seen, between 75 and 125 m, with a horizontal gradient greater than that in April (Figs. 3.16 and 3.17). An increase in gradient of the front is due to the reinforcement of properties of the remnant water by the initial phase of the upwelling. The upwelling signature along the western boundary at the subsurface region is evident in temperature distribution and not in salinity. This is due to the fact that, along the western boundary the water in the subsurface region is high saline as a result of the influence of marginal seas. The summer to winter transition period also shows the impact of the upwelling off Oman.

The spreading of ASWM and BBWM are discussed in the earlier sections while that of PGWM and RSWM are discussed below. The PGWM and RSWM enter the Arabian Sea through narrow Strait of Hormuz and Bab-al-Mandeb with a sill depth of approximately 80 m and 160 m, respectively (Bower et al., 2000). The warm high saline water exit the strait as dense bottom currents cascading down the continental slope and entraining less dense water until they reach neutral buoyancy and spread laterally into the Arabian Sea. The lateral and vertical extent of PGWM shows a marked variability with season. Morrison et al. (1998) concluded that the salinity maximum of the PGWM is associated with the suboxic portions of the Arabian Sea's oxygen minimum zone.

During December and January, the water mass is discernible between 150 and 300 m while in February and March the vertical extent reduces and the water mass is between 200 and 300 m (Fig. 3.38). The reduction in the vertical extent is due to the influence of waters that form at the surface and sinks during the winter season. In January the area occupied at 150 m is smaller than that in previous month. Thus there is a reduced replenishment of PGWM at 150 m. The deepening of the depth of prominence (depth at which the water mass has maximum area covered for that month) from 250 m in December and January to 300 m in February and March indicates the increase in the influx of PGWM to Arabian Sea and further sinking as season advances. An analysis of the area occupied at the depth of prominence shows an

increase from December ($308 \times 10^3 \text{ km}^2$) to March ($612 \times 10^3 \text{ km}^2$). This further reveals the increase in flow of the PGWM. The total volume occupied by PGWM shows an irregular pattern. The total volume increases from December ($487 \times 10^5 \text{ km}^3$) to January ($612 \times 10^5 \text{ km}^3$). However, due to the reduced vertical extent of the PGWM, the volume decreases to $445 \times 10^5 \text{ km}^3$ in February. Further, the increase of volume in March ($514 \times 10^5 \text{ km}^3$) is mainly due to the consolidation of the PGWM.

The lateral spread of PGWM indicates its presence at the northern part of the study region. The density of the ambient waters, upwelling, presence of cooler dense water at the surface and the flow determines the spreading and the direction of spread. The water mass spreads equatorward along the western boundary and attains neutral buoyancy. The warm, high saline, less dense waters on the western side than on the eastern side result in the spread of PGWM along the western boundary (Figs. 3.36 and 3.38). The maximum equatorward extent of 19°N is seen in January at 250 m.

In April and May, the vertical extent of PGWM is same as that of March (200-300 m). The depth of prominence is 300 m in April while in May it is 250 m. Moreover the area occupied at the depth of prominence decreases from $331 \times 10^2 \text{ km}^2$ to $308 \times 10^2 \text{ km}^2$. The equatorward spread occurring along the western boundary shows a decrease from April to May. This variability is due to the upward thrust as a result of initial phase of upwelling in May and the associated erosion of the properties of PGWM at 300m. This upward thrust being weak does allow the spread of properties above 300m and therefore an increase in volume occurs from April ($444 \times 10^5 \text{ km}^3$) to May ($497 \times 10^5 \text{ km}^3$).

The dynamic nature of summer monsoon is well delineated in the variability of PGWM. The upthrust associated with the upwelling results in the presence of water mass from 150 m to 300 m in June with the depth of prominence at 300 m, which is deeper than in May indicating a greater flux of the PGWM in June compared to May. With the advance of the season, the water mass is further displaced upwards and manifests in the vertical range of 125 to 250 m in July (Fig. 3.38). The upward displacement is evident from the increase in the area covered at 150 m in comparison with that in June. The

decrease in the area covered at 200 and 250 m with respect to June and the near absence at 300 m in July further indicates the stronger upthrust due to upwelling. At 150 m, the water mass shows its presence at the northernmost extent indicating the influence of the poleward flow along the western boundary. The depth of prominence shallows to 150 m in July revealing a dominant upward thrust in July compared to that in June. The total volume occupied by the water mass increases from May to June ($585 \cdot 10^5 \text{ km}^3$) while it decreases in July ($188 \cdot 10^5 \text{ km}^3$). The increase in the area occupied at 125 m in August in comparison with July reveals continuous upward thrust due to upwelling. Further, higher equatorward and eastward extent is seen in August. The depth of prominence is similar to that in July and the volume increases to $466 \cdot 10^5 \text{ km}^3$. The highest eastward and equatorward extents are at 200 m. As this spread is greater than that in July, it indicates increase in influx of PGWM during August.

In comparison with the area covered during August, a drastic decrease in area is evident in September. However, the depth of prominence (150 m) and the vertical extent (125 - 250 m) are same. The presence of the water mass at the eastern boundary, the reduction in area covered, the lesser equatorward extent and decrease in volume ($210 \cdot 10^5 \text{ km}^3$) are attributed to the impact of upwelling. During summer the highest impact is in September. The PGWM do not depict uniformity in properties over large vertical extent, except at N11 and N7 in July, where it is seen as mode water between 120 to 150 m and 50 to 90 m at N7.

From September to October the vertical extent (200 – 250 m) of the PGWM decreases and it deepens to acquire stability as is evident from deeper depth of prominence. There is an increase in the area covered by water mass and the depth of prominence (250 m). This also leads to increase in volume ($228 \cdot 10^5 \text{ km}^3$) with respect to September. Further the increase in equatorward extent is also discernible in October. The variability reflect the reduced effect of upwelling and the water mass starts acquiring neutral buoyancy at deeper level. From October to November an increase in vertical extent (150-300 m) is evident. Though the depth of prominence is same as that in October, the area covered shows a significant increase leading to increase in volume ($525 \cdot 10^5$

km³). Moreover the extent of PGWM is more towards equatorward direction. This reveals the continuous influx of the PGWM.

From the CTD data, the PGWM is seen in northern region as a tongue of warm high saline water between 150 and 350 m (Fig. 4.2) while its weak influence is seen at central-western region. The salinity at the core of tongue is highest (36.4 psu) in March, July, August and December, in the northern region and higher salinity is seen near the coast at central-western region during December and January (Figs. 4.8, 4.14). During July and August the tongue at the northern region shows discontinuity near coast, due to upwelling. The variation of salinity within the tongue reveals that PGWM spreads equatorward with its core near the western boundary. At the central-western region the salinity variations in the subsurface reveals that the water mass is present near the coast. At the easternmost station the influence of PGWM is negligible. The water mass is also absent to the south of S12 and east of N8 (Fig. 4.4). The upwelling erodes the water mass and restricts its spread in Arabian Sea and therefore the eastward and equatorward extent is lower during SWM (Figs. 4.11, 4.12, 4.14, 4.15).

The presence of PGWM leads to large variation in stability of water column. In comparison with southern and central-eastern regions that are not strongly influenced by PGWM, the western region shows stability fluctuations over a greater vertical extent at the depth zone where PGWM is present. This reveals that with the spread of PGWM, the waters in layer above it is stability while those below are less stable than the overlying waters (Fig. 4.17).

Thus during summer to winter transition, winter and winter to summer transition periods the consolidation of the PGWM occurs and this phase is waxing period. During the summer, the water mass is eroded and hence the period is waning.

The spreading of RSWM is towards north. This is due to the presence of less saline cold waters at the equatorward side compared to the northern region. The cold waters are denser than the waters at the head region and hence the RSWM spreads poleward. The signal due to Red Sea water mass

in the T-S diagrams that are plotted using CTD data is distinct only at the eastern and southern region. Shapiro and Meschnov (1991) observed that in winter the Red Sea water propagates southward along Somali Coast whereas in Summer, the eastward propagation intensifies.

The volume occupied by the ASWM and BBWM is highest in January. These reflect that the extreme climatic conditions of winter are in January. The volume occupied by PGWM is maximum in January and minimum in July. This clearly shows penetration of the monsoonal forcings to these depths. The volume occupied by RSWM shows an irregular pattern. It is maximum in March and minimum in September. However, no definite pattern is seen.

Chapter - VII

Summary and Conclusions

The study of ocean dynamics forms an integral part of investigations on climate and biogeochemical cycling. The role of Arabian Sea dynamics on the biogeochemical aspects, monsoon and global climate has given impetus to the research during last decade.

The exchange of heat and mass between the interacting regimes such as marginal seas, open ocean and the atmosphere play a vital role in the hydrodynamics of the region. The importance of water mass has been recognized for understanding ocean's role in climate change as they act as reservoirs for heat, salt and dissolved gases. Hence, study of water mass and circulation has been indispensable for understanding the ocean as an integrated system.

The thesis is an outcome of a modest attempt by the author to enhance the knowledge of Arabian Sea dynamics. The entire region is analysed for climatological monthly evolution of hydrography, identification of different water masses, quantification of their spreading and delineation of the responsible mechanisms. The area and volume occupied by individual water mass is determined and hence their contribution to entire Arabian sea has been worked out. Further, the stability of water column is examined to quantify dynamic nature of the region during different periods of the year 1995. The western region is found to be more dynamic than the eastern region. The hydrography associated with the circulation, during 1995, emphasizes the generation, intensification and dissipation of eddies. The nature of circulation and kinetic energy reveals the role of eddies in the surface geostrophic flow

and in the distribution of Arabian Sea Water Mass (ASWM) and Bay of Bengal Water Mass (BBWM). The outflow from Persian Gulf in subsurface region and upwelling influences the stability. Based on the investigations and subsequent discussion the main conclusions drawn are given hereunder.

The head of Arabian Sea is the core of the source of Arabian Sea water mass. The water mass formation initiates in December. Among the different forcings the most dominant fluxes are the latent heat and solar fluxes. The short wave radiations range from 150 to 300 Wm^{-2} and are lowest in December. The latent heat flux exceeds 120 Wm^{-2} and is highest at the head region in December.

The water mass sinks to a maximum depth of 100 m in April, May and June. It spreads equatorward and sinks on the eastern side due to less dense waters at the east than the west. The southward extent is restricted by the poleward flow of Bay of Bengal water. In January, the depth of prominence is shallow while in subsequent months it is deeper. Also, the maximum horizontal spread ($1022 \times 10^3 \text{ km}^2$) is in January and occurs at 10 m. The water mass occupies maximum volume ($754 \times 10^5 \text{ km}^3$) in January. Except in September, the water mass is present throughout the year with varying spatial extent. Therefore, in addition to winter convection, the mixing at the subsurface is also responsible for the formation of the water mass during non-winter period.

The Bay of Bengal water mass is prevalent in the study area from November to March and is restricted along eastern boundary. The water mass extend from surface to of 50 m from November to March while it is in the subsurface region during April. In January the water mass spreads over a larger area ($434 \times 10^3 \text{ km}^2$) at depth of prominence (10 m) and the volume ($165 \times 10^5 \text{ km}^3$) it occupies is maximum.

The Persian Gulf Water Mass (PGWM), Red Sea Water Mass (RSWM) are present throughout the year. In January, the volume occupied by PGWM is maximum ($612 \times 10^5 \text{ km}^3$) while in July it is minimum ($198 \times 10^5 \text{ km}^3$). The water mass is present at the deeper levels in winter while in summer, due to influence of upwelling, it is lifted up. The vertical migration is maximum in

August and September revealing the influence of monsoonal forcings up to 400 m. The seasonal migration of Persian Gulf water mass can lead to change in oxygen concentration which is essential for the biota. The water mass spreads equatorward along the western boundary due to presence of high dense water at the eastern region. The spread is higher in winter than in summer. The Red Sea water mass shows highly irregular variation in the volume.

The region experiences extreme seasonal conditions with varying in magnitudes. The thermohaline structure of the western region gets highly perturbed during summer affecting the vertical stability of the water column. The coastal and northern regions experience most intense upwelling in August-September. The upwelling leads to formation of thermohaline front at the east while at the west it is a thermal front. The associated wind curl ranges from 0 to 8 Nm^{-3} . Another factor affecting the stability is the Persian Gulf water mass. During summer, stability at the coastal region fluctuates over a large vertical zone while at the eastern region the fluctuation is confined to less vertical extent. In addition to the affect of upwelling, the stability increases due to PGWM.

In the study region the Mixed Layer Depth (MLD) is governed by winter convection, wind stress curl, warm high saline subsurface water, advection of low saline water and eddies. The MLD is the highest at central-eastern region during winter while at the coast it decreases due to the upthrust by PGWM. In summer the MLD at the coastal region is absent due to strong upwelling. The MLD is also affected by the poleward flow of water from low latitude and Bay of Bengal. It is weak at southern region and eastern region during winter.

The mode water, present within the upper waters, is subjected to the strong monsoonal forcings. Moreover, the mode water do not have large vertical extent. Hence it lacks longevity and is not found everywhere though high dense water is formed in the region.

The surface circulation of the study region is governed by eddies generated by both meteorological and remote forcings. Eddies with laterally

inverted nature are present at southeast and southwest region during the two seasons. The warm water eddy at southeastern region, during winter, is stronger than the cold-water eddy during summer and influences the poleward flow of BBWM. The cold-water eddy at the southwestern region drives equatorward flow - Somali current. These eddies intensify till mid January and dissipates by the end of April.

In summer the eddy structure reverses. At the southeastern region there is a cold-water eddy while at the southwestern region, coalescing of two eddies generates a strong warm water eddy - Great Whirl. The highest sea level depression (-9 cm) and elevation (+8 cm) associated with cold-water eddy and Great Whirl are in September.

In winter, the North Equatorial Current ($25 \text{ cm}^2\text{s}^{-2}$) and Somali current ($100 \text{ cm}^2\text{s}^{-2}$) has maximum kinetic energy while in summer, it is associated with the poleward Somali current ($150 \text{ cm}^2\text{s}^{-2}$). The southwestern region is the zone of higher kinetic energy.

The confluence of extreme atmospheric forcings and remote forcings underscores the need for greater focus on interdisciplinary investigation of this region so as to have a base line information to investigate the broader aspects such as role of Arabian Sea in global climate.

Bibliography

- Ali, M. M. (1990). Estimation of the horizontal velocity of the Socotra eddy and some observations of sea surface thermal features using INSAT-1B. *Int. J. Remote Sens.*, 11(1), 41-47.
- Babu, V. R., J. S. Sastry, V. V. Gopalkrishna and D. V. R. Raju (1991). Premonsoonal water characteristics and circulation in the East Central Arabian Sea. *Proc. Ind. Acad. Sci. (Earth Plan. Sci.)*, 100(1), 55-68.
- Basu, S., S. D. Meyers, and J. J. O'Brien. 2000. Annual and interannual sea level variations in the Indian Ocean from Topex/Poseidon observations and ocean model simulations. *J. Geophys. Res.* 105:975-994.
- Bauer, S., G. L. Hitchcock and D. B. Olsen (1991). Influence of monsoonally-forced Ekman dynamics upon surface layer depth and plankton biomass distribution in the Arabian Sea. *Deep Sea Res.*, 38, 531-533.
- Beal, L. M., A. Field, and A. L. Gordon (1999). Spreading of Red Sea overflow waters in the Indian Ocean. *J. Geophys. Res.*, in press.
- Bower, A. S., H. D. Hunt and J. F. Price (2000). Characters and dynamics of the Red Sea and Persian Gulf outflows. *J. Geophys. Res.*, 105, NO. C3, 6387-6414
- Brewer, P. G., A. P. Fler, S. Kadar, D. K., Shafer, and C. L. Smith (1978). Chemical oceanographic data from the Persian Gulf and Gulf of Oman, Tech. Rep. WHOI-78-37, 105, Woods Hole Oceanogr. Inst., Woods Hole, Mass.
- Brock, J. C., C. R. McInain, and W. W. Hay (1992). A Southwest monsoon hydrographic climatology for the northwestern Arabian Sea. *J. Geophys. Res.*, 97, 9455-9465.
- Bruce, J. G., D. R. Johnson and J. C. Kindle (1994). Evidence for eddy formation in the eastern Arabian sea during the northeast monsoon. *J. Geophys. Res.*, 99(C4), 7651-7664.
- Bruce, J. G., J. C. Kindle, L. H. Kantha, J. L. Kerling and J. F. Bailey (1998). Recent observations and modeling in the Arabian Sea Laccadive high region. *J. Geophys. Res.*, 103(C4), 7593-7600.
- Chao, S. Y., T. W. Kao, and K. R. Al-Harli (1992). A numerical investigation of circulation in the Arabian Gulf. *J. Geophys. Res.*, 97(11), 219-11, 236.

Currie, R. J. (1992). Circulation and upwelling off the coast of South-East Arabia. *Oceanol. Acta*, 15(1), 43-60.

Cutler, A. N., and J. C. Swallow (1984). Surface currents of the Indian Ocean (to 25° S, 100° E). *Institute of Ocean Science Technical Report*, 187

Da Silva, A., C. Young and S. Levitus (1994). Atlas of surface marine data 1994, vol. 1: Algorithms and procedures. NOAA Atlas NESDIS 6, U. S. Dept. Commerce, Washington, D. C.

Duing, W. and A. Leetma (1980). Arabian Sea cooling: a preliminary heat budget. *J. Phys. Oceanography*, 10, 307-312.

Flagg, C. N. and H. S. Kim, (1998). Upper Ocean currents in the northern Arabian Sea from shipboard ADCP measurements collected during 1994-1996 U. S. JGOFS and ONR programs. *Deep Sea Res. II*, 45, 1917-1959.

Fieux, M. and H. Stommel, (1977). Onset of the South west Monsoon over the Arabian Sea from marine reports of surface winds: structure and variability. *Monthly Weather Review*, 105, 231-236.

Findlater, J. (1969). A major low-level air current near the Indian Ocean during the northern summer. *Q. J. R. Meteorol. Soc.*, 95, 362.

Fischer, J., F. Schott, and D. Quadfasel, (1996). Variability of the Northern Somali Current System. Supplement of EOS, Transactions of the American Geophysical Union 77, 382.

Fofonoff, N. P. and R. C. Millard Jr. (1983). Algorithms for computation of fundamental properties of seawater. UNESCO technical papers in marine science. 44, UNESCO.

Hastenrath, S. and L. Greischar (1991). The monsoonal current regimes of the Tropical Indian Ocean: Observed surface flow fields and their geostrophic and wind-driven components. *J. Geophys. Res.*, 96(12), 619-633.

Hellerman, S. and M. Rosenstien, (1983). Normal Monthly wind stress over the world ocean with error estimates. *J. Phys. Oceanogr.*, 10, 1611-1651.

Horton, C., M. Clifford, J. Schmitz, and B. Hester, (1994). SWAFS: Shallow Water Analysis and Forecast System Overview and Status Report, NAVOCEANO Report, 54, U.S. Nav. Oceanogr. Off.

John, V. C., S. L. Coles and A. I. Abozed, (1990). Seasonal cycles of temperature, salinity and water masses of the Western Arabian Gulf, *Oceanol. Acta.*, 13, 273-281.

Knox, R. A. (1987). The Indian Ocean: interaction with the monsoon. In: *Monsoons*, Fein, J., Stephens, P. (Eds.) Wiley, New York, 365-379.

Krishnamurti, T. N. (1987). Monsoon models. In: *Monsoons*, Fein, J.,

Stephens, P. (Eds.), Wiley, New York, 467-522.

Kumar, P. V. H., and N. M. Kumar (1996). On the flow and thermohaline structure off during pre-monsoon season. *Continental shelf Res.*, 16(4), 457-468.

Lagerloef, G. S. E., G. Mitchum, R. Lukas and P. Niiler, 1999: Tropical Pacific near-surface currents estimated from altimeter, wind and drifter data, *J. Geophys. Res.*, 104, 23,313-23,326.

Levitus, S. and T. Boyer, (1994a). World Ocean Atlas 1994 Volume 4: Temperature. NOAA Atlas Nesdis4, U. S. Department of Commerce, Washington, D. C.

Levitus S., R. Burgett and T. P. Boyer (1994b). World Ocean Atlas 1994 Volume3: Salinity NOAA Atlas NESDIS 3. U. S. Dept. of Commerce, Washington, D. C.

Lighthill, M. J. (1969). Dynamic response of the Indian Ocean to the onset of southwest monsoon. *Phil. Trans. Roy. Soc. London*, A265, 45-92.

Luther, M. E. and J. J. O'Brien (1985). A model of the seasonal circulation in the Arabian Sea forced by observed winds. *Progress in Oceanography*, 14, 353-385.

Luyten, J. R. (1982). Equatorial current measurements. I: Moored observations. *J. Mar. Sci.*, 40, 19-41.

Manghnani V., J. M. Morrison, T. S. Hopkins and E. Bohm (1998). Advection of upwelled waters in the form of plumes off Oman during the Southwest monsoon. *Deep Sea Res. II*, 45, 2027-2052.

McCreary, J. P. and P. K. Kundu (1989). A numerical investigation of sea surface temperature variability in the Arabian Sea. *J. Geophys. Res.*, 94, 16097-16114,

Molinari, R. L., J. Swallow and J. F. Festa (1986). Evolution of near-surface thermal structure in the western Indian Ocean during FGGE, 1979. *J. Mar. Res.*, 44, 736-762.

Molinari, R. L., D. Olsen, and G. Reverdin (1990). Surface current distributions in the Tropical Indian Ocean derived from compilations of surface buoy trajectories. *J. Phys. Res.*, 95, 7217-7238.

Morrison, J., L. A. Codospoti, S. Gaurin, B. Jones, V. Manghnani, and Z. Zheng (1998). Seasonal variation of hydrographic and nutrient fields during the USJGOFS Arabian Sea process study. *Deep Sea Res. II*, 45, 2053-2101.

Murray, S. P., and W. Johns (1997). Direct observations of seasonal exchange through the Bab el Mandab Strait. *Geophys. Res. Lett.*, 24, 2557-2560.

Perigaud, C., and P. Delecluse. 1993. Interannual sea level variations in the tropical Indian Ocean from Geosat and shallow water simulations *J. Phys. Oceanogr.* 23:1916-1934.

Prasanna Kumar, S. and T. G. Prasad (1996). Winter cooling in the northern Arabian Sea. *Curr. Sci.*, 71, 834-841.

Prasanna Kumar S., H. Snaith, , P. Challenor, and H. T. Guymer, H. T. (1998). Seasonal and inter-annual sea surface height variations of the northern Indian Ocean from the TOPEX/POSEIDON altimeter. *Ind. J. Mar. Sci.*, (27), 10-16.

Premchand, K., J. S. Sastry, and C. S. Murty (1986). Water mass structure in the western Indian Ocean, part 2, the spreading and transformation of the Persian Gulf Water. *Mausam*, 37, 179-186.

Prell, W. L. (1984). Variation in monsoonal upwelling: A response to changing solar radiation, In: *Climate processes and Climate Sensitivity*, Hansen, J., Takahashi, T. (Eds.), American Geophysical Union, Geophysical monograph Series 29, 48-57.

Privett, D. W. (1959). Monthly charts of evaporation from the Indian Ocean, including the Red Sea and the Persian Gulf, Q. J. R. *Meteorol. Soc.*, 85, 424-428.

Qasim, S. Z. (1982). Oceanography of the northern Arabian Sea. *Deep Sea Res. Part A*, 29, 1041-1068.

Quadfasel, D. R., and F. Schott (1982). Water mass distributions at intermediate layers off the Somali Coast during the onset of the southwest monsoon, 1979. *J. Phys. Oceanogr.*, 12, 1358-1372.

Rameshbabu V., M. S. Rao and M. V. Rao (1992). Heat budget parameters for the southwestern Arabian Sea during monsoon – 88 experiment. In: *Oceanography of the Indian Ocean*, B. N. Desai (ed.). Oxford and IBH, New Delhi, India.

Rao, R. R., R. L. Molinari and J. F. Festa (1989). Evolution of the climatological near-surface thermal structure of the tropical Indian Ocean. I. Description of mean monthly mixed layer depth and sea surface temperature, surface current, and surface metrological fields. *J. Geophys. Res.*, 94, 10801-10815.

Rochford, D. J. (1964). Salinity maxima in the upper 1000 meters of the north Indian Ocean. *Aust. J. Mar Freshwater Res.*, 15, 1-24.

Rudnick, D. L., R. A. Weller, C. C. Eriksen, T. D. Dickey, J. Marra, and C. Langdon, (1997). Moored instruments weather Arabian Sea monsoons, yield data. *EOS*, 78, 117 and 10-121.

Sarma, Y. V. B., V. S. N. Murty, D. Panakala Rao, and J. S. Sastry (1986). Circulaiton and water mass structure in the central Arabian Sea during

December 1982. *Ind. J. Mar. Sci.*, 5, 234-240.

Schott, F. 1983. Monsoon response of the Somali Current and associated upwelling. *Prog. Oceanogr.*, 12, 357-381.

Shankar, D., and S. R. Shetye (1997). On the dynamics of Lakshadweep high and low in the southeastern Arabian Sea. *J. Geophys. Res.*, 102(C4), 12551-12562.

Shenoi, S. C., K. Antony, and D. Sunder, D. (1988). Nature of the oscillatory flows in the shelf waters of the western continental shelf of India. *J. Coastal Res.*, 4(4), 617-626.

Shetye, S., R. (1984). Seasonal variability of the temperature field off the south west coast off India. *Proc. Ind. Acad. Sci. (Earth Plan. Sci.)*, 93, 399-411.

Shetye S. R. and S. S. C. Shenoi (1988). Seasonal cycle of surface circulation in the coastal North Indian Ocean. *Proc. Ind. Acad. Sci. (Earth and Planetary Science)*, 97, 53-62.

Shetye, S. R., A. D. Gouveia, S. S. C. Shenoi, D. Sundar, G. S. Micheal, A. M. Almeida, and K. Samtanam. (1990). Hydrography and circulation of the west coast off India during the southwest monsoon 1987. *J. Mar. Res.*, 48, 359-378.

Shetye, S. R., A. D. Gouveia, S. S. C. Shenoi, G. S. Micheal, D. Sundar, A. M. Almeida and K. Samtanam. (1991). The coastal current of western India during the northeast monsoon. *Deep Sea Res.*, 38, 1517-1529.

Shetye, S. R., A. D. Gouveia, S. S. C. Shenoi, D. Sundar, G. S. Micheal, A. M. Almeida, and K. Santanam (1990). Hydrography and circulation of the west coast of India during the Southwest Monsoon 1987. *J. Mar. Res.*, 48, 359-378.

Shetye, S. R., A. D., Gouveia, S. S. C. Shenoi (1994). Circulation and water masses of the Arabian Sea. In: Lal, D. (Ed.) *Proc. Ind. Acad. Sci.*, Lotus Printers, New Delhi, India, 9-25.

Smith, S., M. Roman, I. Prusiva, K. Wishner, M. Gowing., L. A. Codispoti, R. Barber, J. Marra, and C. Flagg (1998). Seasonal response of zooplankton to monsoonal reversals in the Arabian Sea. *Deep Sea Res. II*, 45, 2369-2403.

Stramma, L., J. Fischer and F. Schott (1996). The flow field off southwest India at 8N during the southwest monsoon of August 1993. *J. Mar. Sci.*, 54, 55-72.

Shapiro, G. I., and S. L. Meshchanov (1991). Distribution and spreading of Red Sea Water and salt lens formation in the northwest Indian Ocean. *Deep Sea Res. Part A*, 38, 21-34, 1991.

Swallow J. C. and J. G. Bruce (1966). Current measurements of the Somali

Coast during the southwest monsoon of 1964. *Deep Sea Res.*, 13, 861-888.

Swallow, J. C. (1984). Some aspects of the physical oceanography of the Indian Ocean. *Deep Sea Res.*, 31, 639-650.

Tchernia, P. (1980). Descriptive regional oceanography, Pergamon Press, Oxford, England, p.253.

Tomczak, M. and J. S. Godfrey (1994). Regional Oceanography: An introduction. Pergamon, Oxford. pp. 422.

Tomczak, M. (1999). Some historical, theoretical and applied aspects of quantitative water mass analysis. *J. Mar. Res.*, 57, 275-303.

Varma, K. K., V. K. Das, and A. D. Gouveia (1980). Thermohaline structure and water masses in the Northern Arabian Sea During February-April. *Ind. J. Mar. Sci.*, 9, 148-155.

Webster, P. J. (1987). The elementary monsoon. In: *Monsoons*, Fein, J., Stephens. P. (Eds.), Wiley, New York, 3-32.

Weller, R. A., M. F. Baumgartner S. A. Josey, A. S. Fischer, and J. C. Kindle, (1998). Atmospheric forcing in the Arabian Sea during 1994-1995: observations and comparisons with climatology and models. *Deep Sea Res. II*, 45, 1961-1999.

Wyrtki, K. (1971). Oceanographic Atlas of the International Ocean Expedition. *Nat. Sci. Found.*, Washington, D.C., 531

Wyrtki, K. (1973). An equatorial jet in the Indian Ocean. *Science*, 181, 262-264.

